Summer 2016

The Role of Diagenesis in Reservoir Development of the Big Clifty (Jackson) Sandstone in South-Central Kentucky

Kort H. Butler
Western Kentucky University, kort.butler390@topper.wku.edu

THE ROLE OF DIAGENESIS IN RESERVOIR DEVELOPMENT OF THE BIG CLIFTY (JACKSON) SANDSTONE IN SOUTH-CENTRAL KENTUCKY

A Thesis
Presented to
The Faculty of the Department of Geography and Geology
Western Kentucky University
Bowling Green, Kentucky

In Partial Fulfillment
of the Requirement for the Degree
Master of Science

By
Kort Hewitt Butler

August 2016

THE ROLE OF DIAGENESIS IN RESERVOIR DEVELOPMENT OF THE BIG CLIFTY (JACKSON) SANDSTONE IN SOUTH-CENTRAL KENTUCKY

Date Recommended June 30, 2016

Michael T. May

Dr. Michael T. May, Director of Thesis

Fredrick D. Siewers

Dr. Fredrick D. Siewers

John M. Andersland

Dr. John M. Andersland

Dean, Graduate School

7/15/16

Date

Acknowledgments

Firstly I'd like to thank my progenitors and vaccines for my existence. To my and others' ancestors who were positively selected for FOXP2 and other genes related to speech and language, thank you for making complex forms of communication such as written theses possible. Words cannot describe my gratitude for this fortune. To my parental figures, your lessons in integrity, intellectual inquisitiveness, magnanimity, patience, and modesty are ones I value greatly and will continue to pursue and foster in actions and words. Your support, encouragement, and assistance editing this document were vital. To my elder sibling whom I've always admired, and whose pursuit in science encouraged my own, thank you for being a role model and making me a better person.

I could not have completed this thesis without my advisor, Dr. Michael May, whose consultations on decapitating the tangential heads of this project, as well as avoiding ingestion of *Conium maculatum* tinctures, were most invaluable. Additionally thank you for the suggestion of a diagenetic-related thesis topic on the Big Clifty it proved challenging and rewarding, and for the many lessons in geology and writing. I would like to thank Dr. John Andersland for his numerous lessons in microscopy, both electron and optical. Thanks for the criticism, edits, and reminders in fields of views. I'd also like to thank Dr. Fred Siewers for his suggested use of cathodoluminescence microscopy for this study, as well as for edits. Thank you, Dr. Andrew Wulff, for your availability, good humor, advice, and his thoughts on retrograde Pb-biomagnification in anti-knocking agents in urban ecosystems it was enlightening.

I am grateful to the Western Kentucky University Graduate School for the research grant and to National Petrographic of Houston, TX, for the thin section services

despite being sent challenging heavy-oil saturated samples. This study would have not have been possible without either. Additionally, I am appreciative of Dave Harris, Head of the Energy & Minerals Section of the Kentucky Geological Survey in Lexington, KY, for the opportunity to conduct optical cathodoluminescence microscopy, and for entrusting me with access to the instrumentation. Thank you Patrick Gooding, Ray Daniel, and Ryan Pinkston of the Well Sample and Core Library of the Kentucky Geological Survey in Lexington for the permission and assistance in sampling cores. I also wish to thank Nicolas Roduit for developing and sharing his software, JMicroVision. It proved incredibly valuable being able to map thin sections and rectifying images of key locations from multiple microscopes.

Finally, my deepest gratitude to my friends, both autochthonous and allochthonous with respect to Kentucky, thank you. The steadfast support, wise counsel, and good humor shown to me during the pursuit of this degree were immeasurably valuable. To a certain Brazilian lass with whom I shared an improbable introduction, thank you for everything after all this time.

TABLE OF CONTENTS

LIST OF FIGURES

LIST OF TABLES

THE ROLE OF DIAGENESIS IN RESERVOIR DEVELOPMENT OF THE BIG CLIFTY (JACKSON) SANDSTONE IN SOUTH-CENTRAL KENTUCKY

Kort H. Butler August 2016 260 pages

Directed by: Michael T. May, Fredrick D. Siewers, John M. Andersland

Department of Geography and Geology Western Kentucky University

The Big Clifty is a Chesterian-age Mississippian sandstone member of the Golconda Formation that extends from south-central Kentucky into adjacent Illinois and Indiana. Asphaltic deposits and conventional petroleum plays are distributed along the Pennyrile Fault System and Plateau in the southeastern portion of the Illinois basin. In south-central Kentucky anomalous oil-saturation geometries are observed in cored sections of Big Clifty from wells in Warren and Butler counties along the margin of the Pennyrile Plateau. Petrographic study of the cores has revealed several diagenetic processes that have contributed to, or are directly responsible for, the anomalous oil saturation geometries and resultant reservoir partitioning.

This study utilizes standard transmitted and reflected light microscopy, UV-epifluorescence, optical cold-cathode cathodoluminescence microscopy, scanning electron microscopy, and alizarin red S and potassium ferricyanide staining in petrographic examination. Raman microscopy, energy-dispersive X-ray spectroscopy, transmitted electron microscopy, and X-ray diffraction assisted in identification and compositional analysis of minerals. Quantification of framework grains and cement compositions, porosity, and grain-size distributions was also conducted. This study's data classifies the Big Clifty as a fine to very-fine grained, quartz arenite with predominantly siliceous and phyllosilicate cements and a mean of porosity of 7%.

Oil-saturation geometries concordant to rock fabric are due to compaction, weathering of labile grains, and precipitation of authigenic cements (mainly quartz, kaolinite, and pyrite). A paragenetic sequence, established from textural evidence, places quartz, kaolinite, and pyrite phases early in paragenesis with labile grain dissolution, compaction, precipitation of ferroan carbonate cement, and development of vugular porosity occurring later during burial. These phases and processes enhanced preexisting porosity and permeability heterogeneities within the rock. Nodular pyrite, oil emplacement, and precipitation of poikilotopic calcite are the latest diagenetic events. Nodular pyrite and poikilotopic calcite are responsible for oil-saturation geometries distinctly discordant with rock fabric. Poikilotopic calcite forms interstratal seals, occluding porosity, replacing framework grains and cements, and overprinting primary rock fabric. This study's preliminary research into the poikilotopic calcite suggests its occurrence is possibly associated with the cored wells' shallow depths less than 500 feet (150 meters), and proximity to near-vertical faults and waters from drainage systems of karstified carbonate aquifers updip.

Chapter 1: Introduction

1.1 Introduction

Unconventional hydrocarbon reservoirs associated with diagenetic seals may be considered by many as novel rather than being pursued as an important hydrocarbon trap. Difficulty recognizing diagenetic alteration of primary mineralogy from well logs, in addition to delineation of subsurface extent, has impeded exploitation of such diagenetically encased reservoirs. Hydrocarbons in south-central Kentucky occur within several carboniferous siliciclastic strata within the Illinois Basin. The Big Clifty (Jackson) Sandstone member of the Golconda Formation is one of the oldest of these units and hosts both conventional and unconventional oil. Bitumen and asphalt rock in Kentucky are distributed along the margin of the Pennyrile Plateau and are commonly associated with the Pennyrile Fault System, but have been studied little in the context of petrophysics and diagenetic mineralogy. Conventional (low viscosity) oil reservoirs of the Big Clifty and other Chesterian and Pennsylvanian strata are located basinward and produce from structural-stratigraphic traps (May, 2013).

Several cores of Big Clifty Sandstone recovered along the basin periphery display anomalous variation in oil saturation and geometries (Figure 1.1). Examination of these cores at the Kentucky Geological Survey (KGS) in Lexington revealed multiple reservoir-seal contacts with variation in hydrocarbon saturation noted from sub-centimeter to decimeter scale, as well as contacts being concordant to discordant with respect to bedforms. An experienced KGS worker familiar with Big Clifty cores from both conventional fields and asphalt rock in the basin remarked never having seen such discordant reservoir-seal contacts or extensive replacement textures influencing oil

emplacement in their career within the basin (D. Williams, 2013, personal communication). Heretofore, there have been no published reports of such anomalous oil saturations occurring within the Big Clifty along the southeastern edge of the basin.

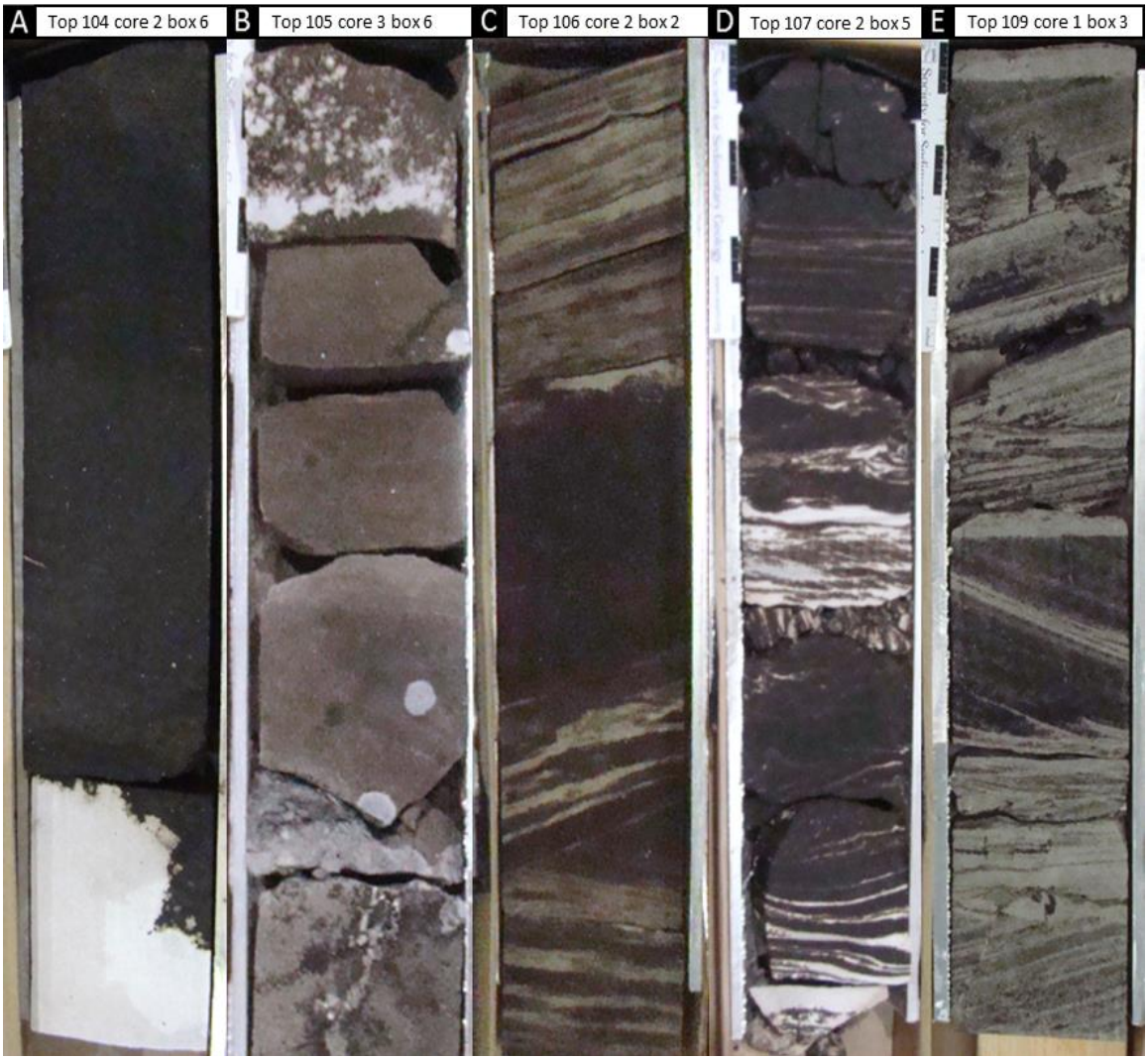

Figure 1.1. Distinct, variable, oil-saturation geometries in cores from several wells concordant and discordant to bedforms. Cores displayed: 104 core 2 box 6 (A), 105 core 3 box 6 (B), 106 core 2 box 2 (C), 107 core 2 box 5 (D), and 109 core 1 box 3 (E).

Diagenesis pertains to all mineralogical, physical, and chemical changes undergone by sediment following deposition short of metamorphism. Any alteration to porefluid chemistry or changes in subsurface environment can alter rock texture, fabric,

and affect subsequent diagenesis (Ali et al., 2010). Such changes in the subsurface environment are significant in petroleum exploration and extraction, but also in well siting for geothermal resources, CO_2 sequestration, contaminant prediction and remediation, and aquifer response models.

1.2 Purpose

The purpose of this study is to provide an accurate petrographic characterization of the Big Clifty Sandstone in south-central Kentucky. Multiple cores are studied to elucidate current and previous subsurface conditions. More specifically, the goals of this study are twofold:

1) Identify the fabric and non-fabric selective compartmentalization controls within the reservoir and seal of the Big Clifty Sandstone;

2) Establish paragenesis and reservoir-seal evolution through detailed examination of framework grains, cement, porosity, and alteration and associations of these sandstone architectural components relative to oil-saturation geometries and core position.

Petrographic observations in this study rely primarily upon transmitted and reflected light microscopy. Raman microscopy, scanning and transmission electron microscopy (SEM and TEM, respectively), X-ray diffraction (XRD), optical cold-cathodoluminescence microscopy (OM-CL), ultraviolet (UV) epifluorescence microscopy, and thin-section staining were employed to supplement standard light microscopy. These other forms of microscopy provided discrete and bulk mineral information and corroborative identification. This research involved comparison of observed textures in Big Clifty cores along the basin edge, which contain unconventional

resources, and an investigation of whether or not the diagenetic textures associated with the observed interstratal traps are the result of regional or localized processes. Providing accurate information of this kind is directly applicable to the detection, development, and stimulation of crude oil resources the Big Clifty at or near the cored locations and, potentially, elsewhere in the basin. Despite the KGS acquiring the cores in 2012, and interest in petrography and core analysis as evidenced by the absence of several core sections on loan to oil companies, there has not been any publication or publically available study regarding the cores and associated documents following their release by Petro River Oil, formerly known as Gravis Oil, and known as MegaWest Energy at the time of coring.

Chapter 2: Geologic Background

2.1 Illinois Basin Development

The Illinois Basin is an interior continental basin that extends from western Illinois to southwestern Indiana and western Kentucky (Figures 2.1 and 2.2). Initial accumulation of sediments began in the late Precambrian or early Cambrian within the then actively rifting New Madrid rift complex that includes the Reelfoot Rift and the obliquely-connected Rough Creek Graben (Ervin and McGinnis, 1975; Heigold, 1990; Kolata and Nelson, 1990a). Thermal cooling of the failed rift and the granite-rhyolite basement rocks, as well as the uncompensated isostatic mass in the lower crust, created a broad, gradually-subsiding embayment throughout the Paleozoic (Kolata and Nelson, 1990b). This vertical compressional regime, from excess mass, caused episodic subsidence of the proto-basin during the Paleozoic with several major unconformities demarcating eustatic and tectonic influences (Kolata and Nelson, 1990a, 1990b; Macke, 1996). Subsidence and sedimentation was most active during the Paleozoic as uplift and orogenic activities outside the proto-basin provided weathering surfaces and sediment sources, in addition to constraining the basin's geometry (Buschbach and Kolata, 1990; Kolata and Nelson, 1990a; Leighton and Kolata, 1990). Compressional stresses associated with the Alleghenian Orogeny resulted in localized deformation producing many of the structural traps (Kolata and Nelson, 1990a; Seyler and Cluff, 1990; Bethke et al., 1990; Lewan et al., 2002). Since the early Triassic, uplift and erosion have removed an estimated two to three kilometers of sedimentary rock from the southeastern margin of the basin in Kentucky (Cluff and Byrnes, 1990; Kolata and Nelson, 1990a). As a result, the Pennsylvanian is the youngest-preserved Paleozoic rock in much of the basin. The

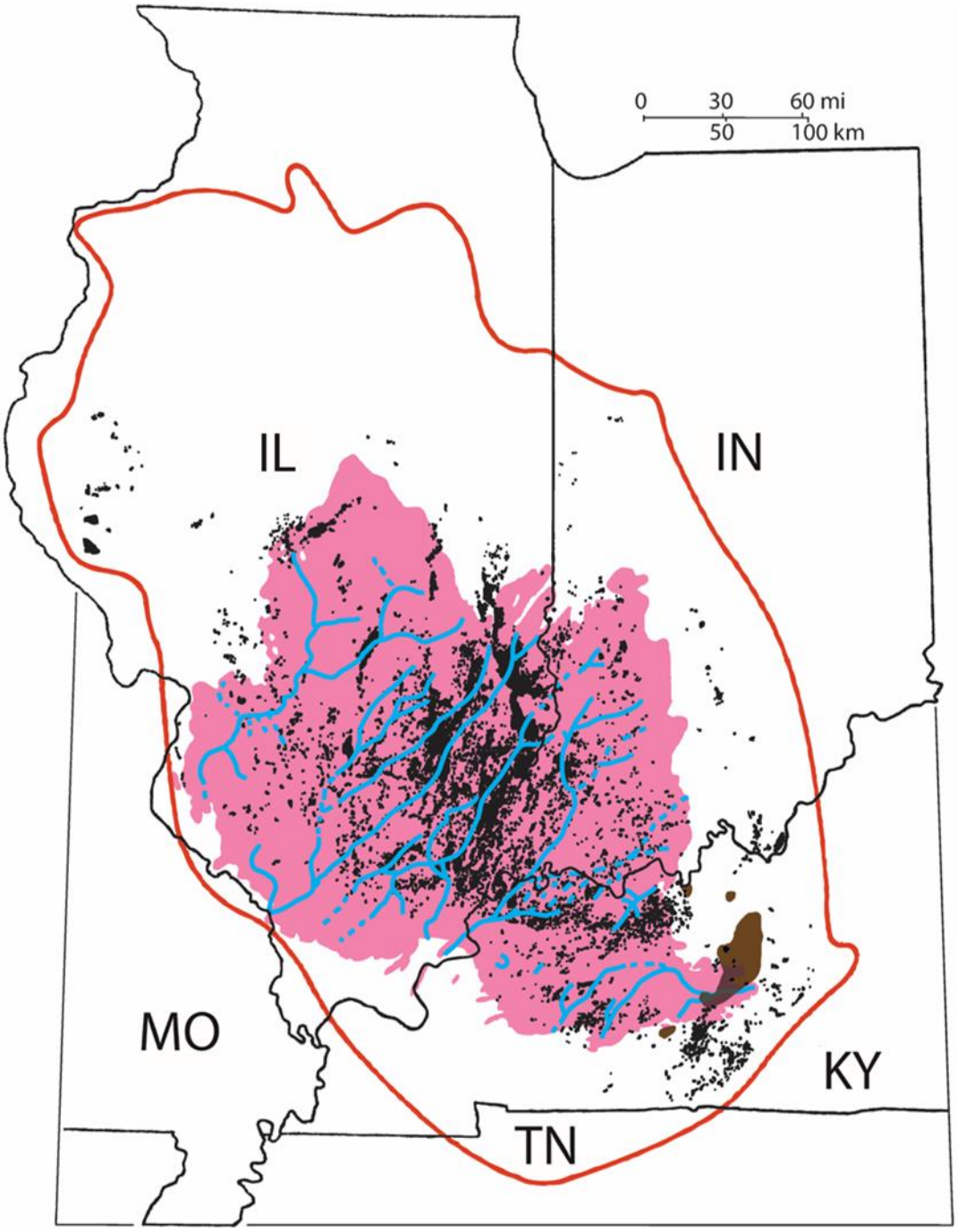

Figure 2.1. Illinois Basin map showing extent of Chesterian Series rocks. Displayed are the areal extent of Chesterian Series (pink), major sub-Absaroka sequence boundary paleovalleys (blue), conventional oil and gas fields (black), and generalized areas of asphaltic rock and bitumen impregnated sandstone (brown). Basin outline (red) and conventional field distribution modified from Buschbach and Kolata (1990), Chesterian rock extent modified from Lewan et al. (2002), paleovalleys modified from London (2014), and unconventional resources modified from May (2013).

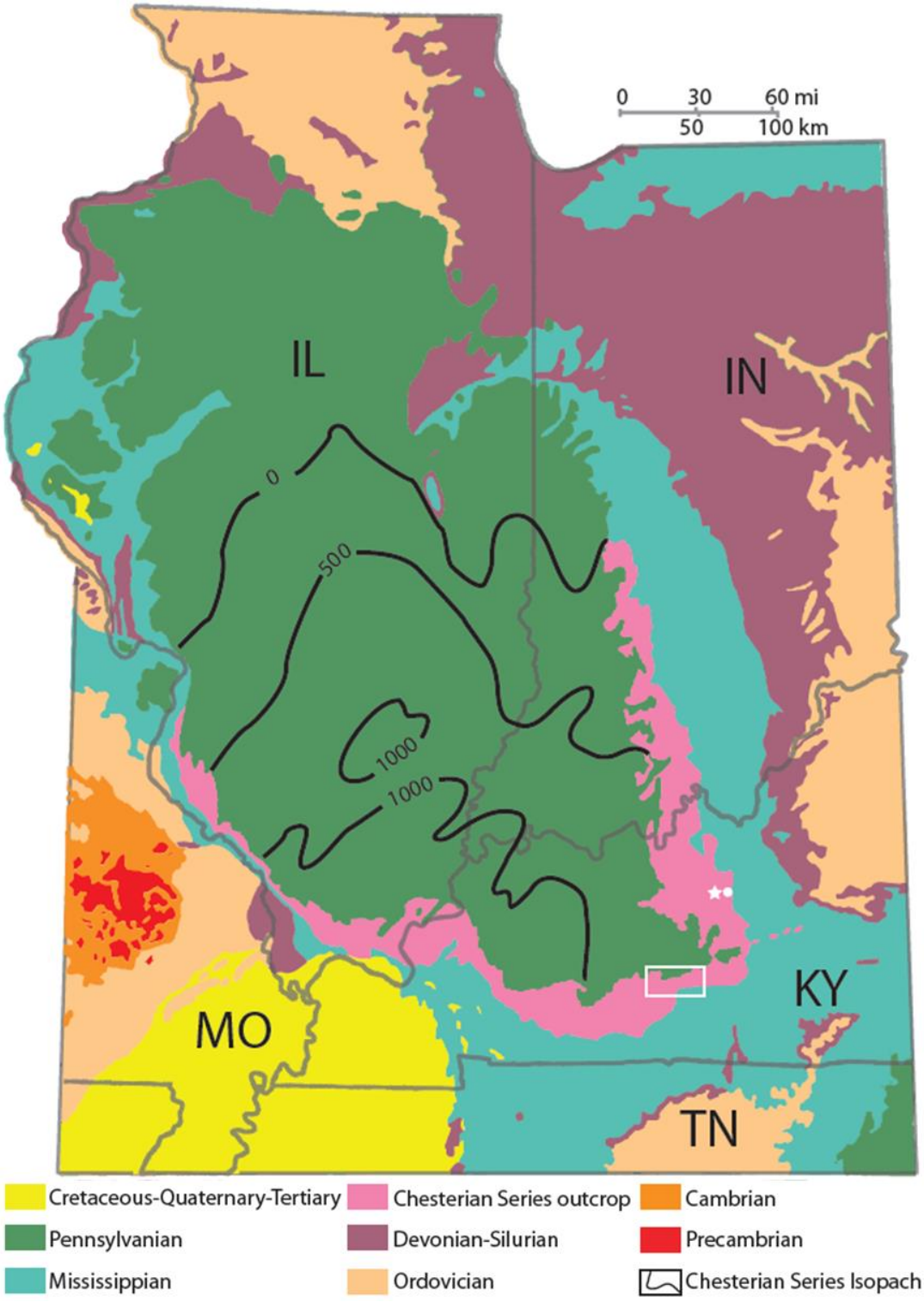

Figure 2.2. Generalized geologic map of the Illinois Basin. Isopach values are gross thickness in feet of the Late Mississippian Chesterian Series in the subsurface. The Big Clifty type section, and "Roadcut" sample location are indicated by a white star and circle, respectively. White rectangle is study area and approximate areal extent of Figure 2.10. Modified from Pryor et al. (1990).

exception to the generalization of Pennsylvanian strata being the most recent Paleozoic rock preserved in the Illinois Basin, is in a down-dropped fault block in Union County, Kentucky, where strata of Lower Permian age is preserved (Kehn et al., 1982; Nelson et al., 1990; Rowan et al., 2002).

2.2 Source Rock

Despite the presence of numerous hydrocarbon-bearing strata within the Illinois Basin, few shale or limestone strata contain greater than the minimum total organic carbon (TOC >1.0–2.0 % by weight) required for catagenesis to produce the thermal maturities and gradients capable of expelling hydrocarbons (Cluff and Byrnes, 1990; Lewan et al., 2002; Rowan et al., 2002; Strąpoć et al., 2010). The New Albany Shale is a Middle and Upper Devonian to Lower Mississippian unit that is the dominant source rock of the Morrowan-Chesterian reservoirs in the Illinois Basin (Figure 2.3) (Schwalb, 1975; Sedimentation Seminar, 1978; Cluff and Byrnes, 1990; Barrows and Cluff, 1984; Jobe and Saller, 1995). This generative shale is correlative with the Ohio and Marcellus shales of the Appalachian Basin, the Antrim Shale of the Michigan Basin, the Chattanooga Shale of the Black Warrior Basin, and the Woodford Shale of the Arkoma Basin (Barrows and Cluff, 1984; Strąpoć et al., 2010). The New Albany, Antrim, Ohio, Marcellus, and Chattanooga shales were the basinal succession of the Catskill delta complex, where dysoxic to anoxic conditions, within a stratified water column, inhibited aerobic metabolism of organic matter by the benthic fauna (Catacosinos et al., 1990; Devera and Hasenmueller, 1990; Strąpoć et al., 2010). At its depocenter, the New Albany Shale reaches a thickness of 450 ft (~137 m) near the border of Kentucky and southeastern Illinois (Devera and Hasenmueller, 1990). South of the Pennyrile Fault

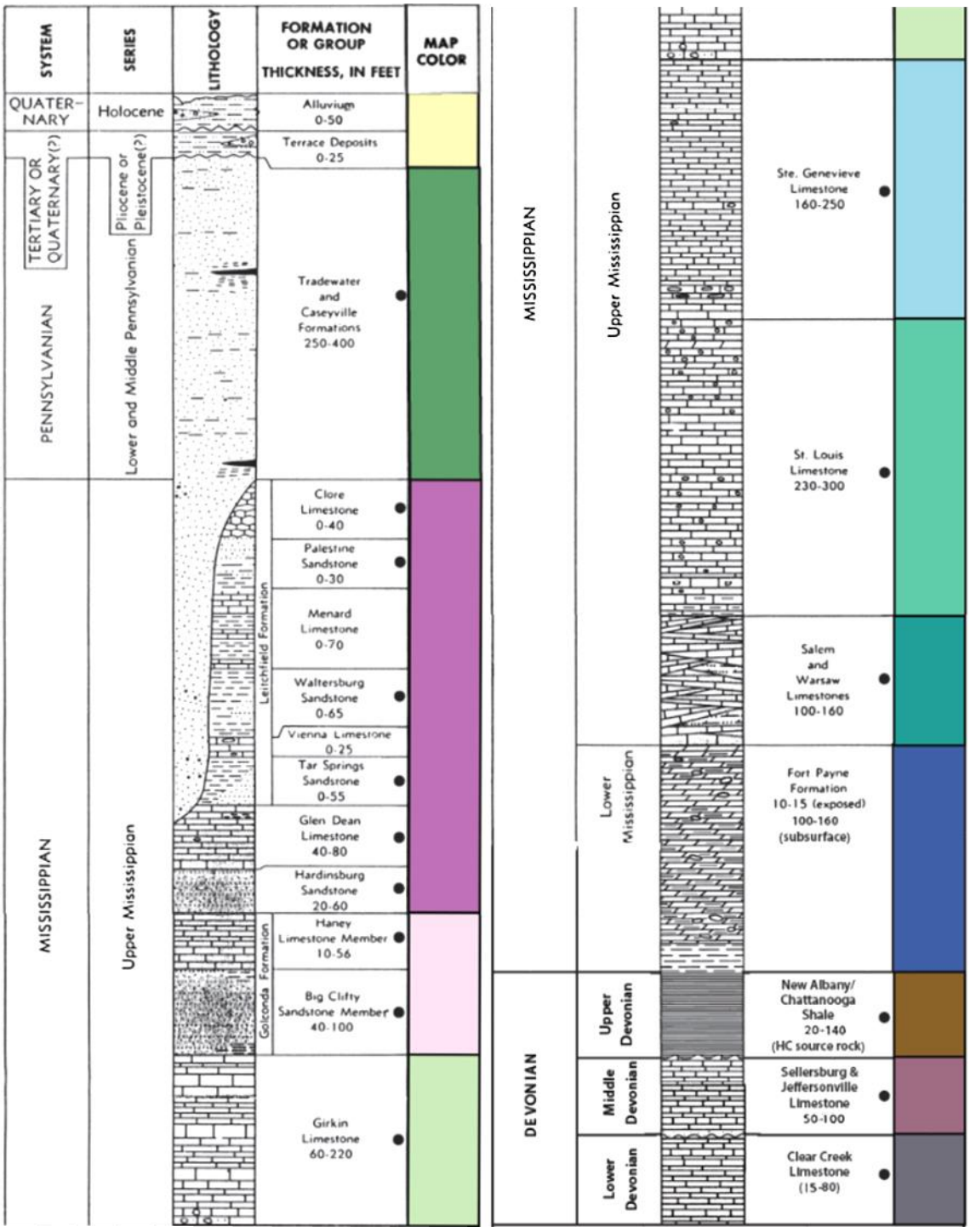

Figure 2.3. Generalized stratigraphy of northern Warren and southern Butler counties, Kentucky. Geologic unit colors match those as displayed on the study area location map (see Figure 2.10). Black circles denote productive oil units. Subsurface thickness values of the Fort Payne and older units are based on CONSUNA charts of Treworgy and Devera (1990) and Mikulic (1990). After Butler and May (2013), modified column from McGrain and Sutton (1973).

System in south-central Kentucky this formation varies 10–140 ft (~3 to 43 m) in thickness (Treworgy and Devera, 1990).

2.3 Late Paleozoic Tectonism and Reservoir Sedimentology

From the Late Mississippian through the Permian, compressional tectonic stresses associated with the convergence of Gondwana and Laurentia resulted in widespread deformation and uplift of crustal blocks producing new fault zones and positive structures, especially in the western portions of the basin (Figure 2.4) (Schwalb, 1975; Sable, 1979; Kolata and Nelson, 1990a). Similar faulting and structural relief occurred in

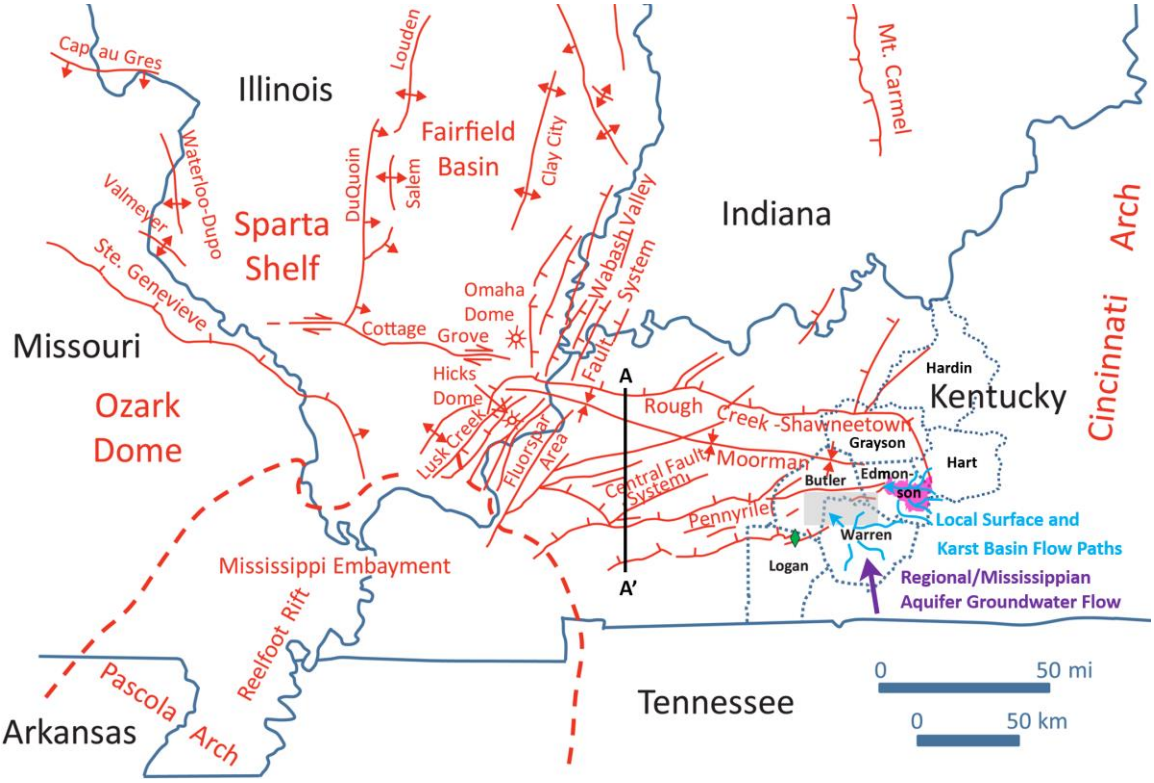

Figure 2.4. Major regional structural features of the southern portion of the Illinois Basin. Counties from which core was retrieved and nearby counties that contain asphalt rocks are outlined (blue dashed). Gray rectangle is the areal extent shown in Figure 2.10 and pink shape is the location of Mammoth Cave National Park. The location of Stampede Asphalt Rock Mine is indicated by green diamond, in Logan County, Kentucky. Transect of Rough Creek Graben (A–A') cross section is shown in Figure 2.5. After May (2013), modified from Nelson (1990), with flow paths based on Ray and Currens (1998) and Lloyd and Lyke (1995).

the northern portion of the basin (not shown). In the eastern and central portion of the basin, transferred stress produced bifurcated, high-angle, wrench, and en echelon faults within the southwest-to-northeast-trending Pennyrile Fault System and the unnamed fault system to the south (Nelson, 1990; Kolata and Nelson, 1990a). A majority of these en echelon faults are high-angle and normal dip-slip defining horsts and grabens (Figure 2.5) (Nelson, 1990). Ancillary to the uplift and compressional stresses in the Illinois Basin was the penecontemporaneous uplift of the Canadian Shield to the north (Swann, 1963; Sable, 1979; Treworgy, 1988, 1990; Treworgy and Devera, 1990; Kolata and Nelson, 1990a; Smith and Read, 2001). This combination of uplift in and around the embayment and at the sediment source favored deposition of predominantly siliciclastic sediments, especially on the proto-basin's margins, during the Late Mississippian (Kolata and Nelson, 1990b). Deposition continued through the Permian, however, uplift and erosion in the basin have removed sedimentary rocks younger than the Permian and older than the Cretaceous (Kolata and Olive, 1990; Kolata and Nelson, 1990b).

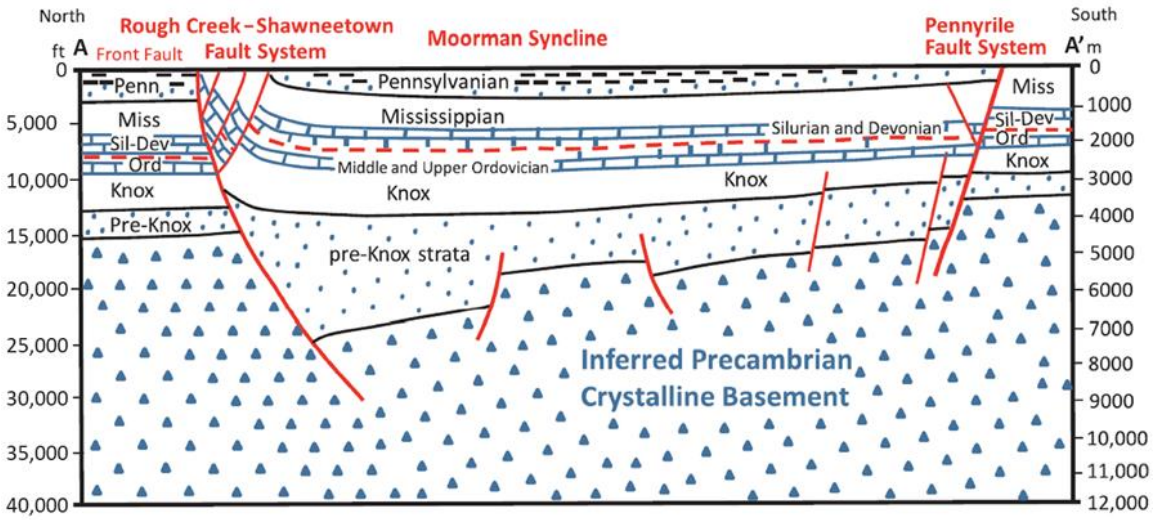

Figure 2.5. Cross-sectional interpretation of the Rough Creek Graben based on seismic reflection profile in western Kentucky. See Figure 2.4 for transect location. After May (2013), and modified from Nelson (1990).

In south-central Kentucky, near the basin margins, the Chesterian is a transitional series between the carbonate-dominant Valmeyeran Series of the Lower Mississippian and the siliciclastic-dominant Morrowan Series of the Lower Pennsylvanian (Swann, 1963; Treworgy and Devera, 1990; Smith and Read, 2001). The Chesterian Series encompasses from the base, the Girkin Limestone to the uppermost part of the Leitchfield Formation in Figure 2.3. The Valmeyeran and Morrowan series consist of the Fort Payne through the Ste. Genevieve limestones, and the siliciclastic-rich Caseyville and Tradewater formations, respectively (Treworgy and Devera, 1990; Mikulic, 1990). Similar to the Valmeyeran and Morrowan series that precede and follow it, Chesterian strata display repetitive successions of lithologies relating to basin-wide transgression and regression (Figure 2.6) (Kolata, 1990). The Chesterian siliciclastics of Kentucky crop out along the southeastern and eastern margins of the Illinois Basin and contain shallow marine, deltaic, and tidal influences consistent with a near-shore, marine, depositional environment (Figure 2.7) (Swann, 1963; Sable, 1979; Noger, 1987; Treworgy, 1988, 1990; Smith and Read, 2001).

Sediments comprising the Big Clifty Sandstone were deposited in a highstand systems track possessing abundant sediment supply. The ancient Michigan River transported siliclastics and sedimentation resulted from the migration of laterally-extensive distributary mouth bars and amalgamated channel sands (Swann, 1963; Treworgy, 1988; Smith and Read, 2001; Nelson et al., 2002). During normal regression, these sands downlapped into the basin and the upslope facies equivalent, periestuarine clay and silt were deposited at the basin margin (Treworgy, 1988; Pryor et al., 1990;

Smith and Read, 2001). In the southern and eastern portions of the basin, the Big Clifty forms a broad belt of bituminous quartzose sandstone.

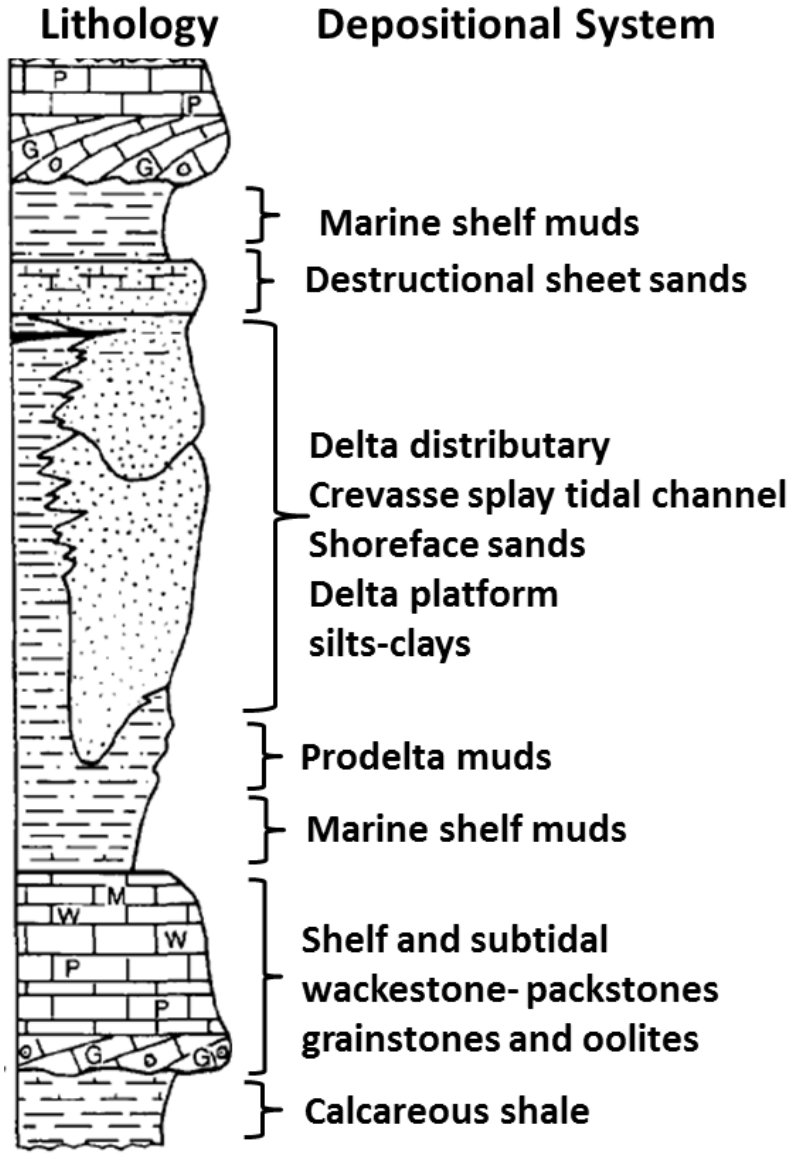

Figure 2.6. Idealized Chesterian regressive depositional cycle. Modified from Pryor et al., (1990).

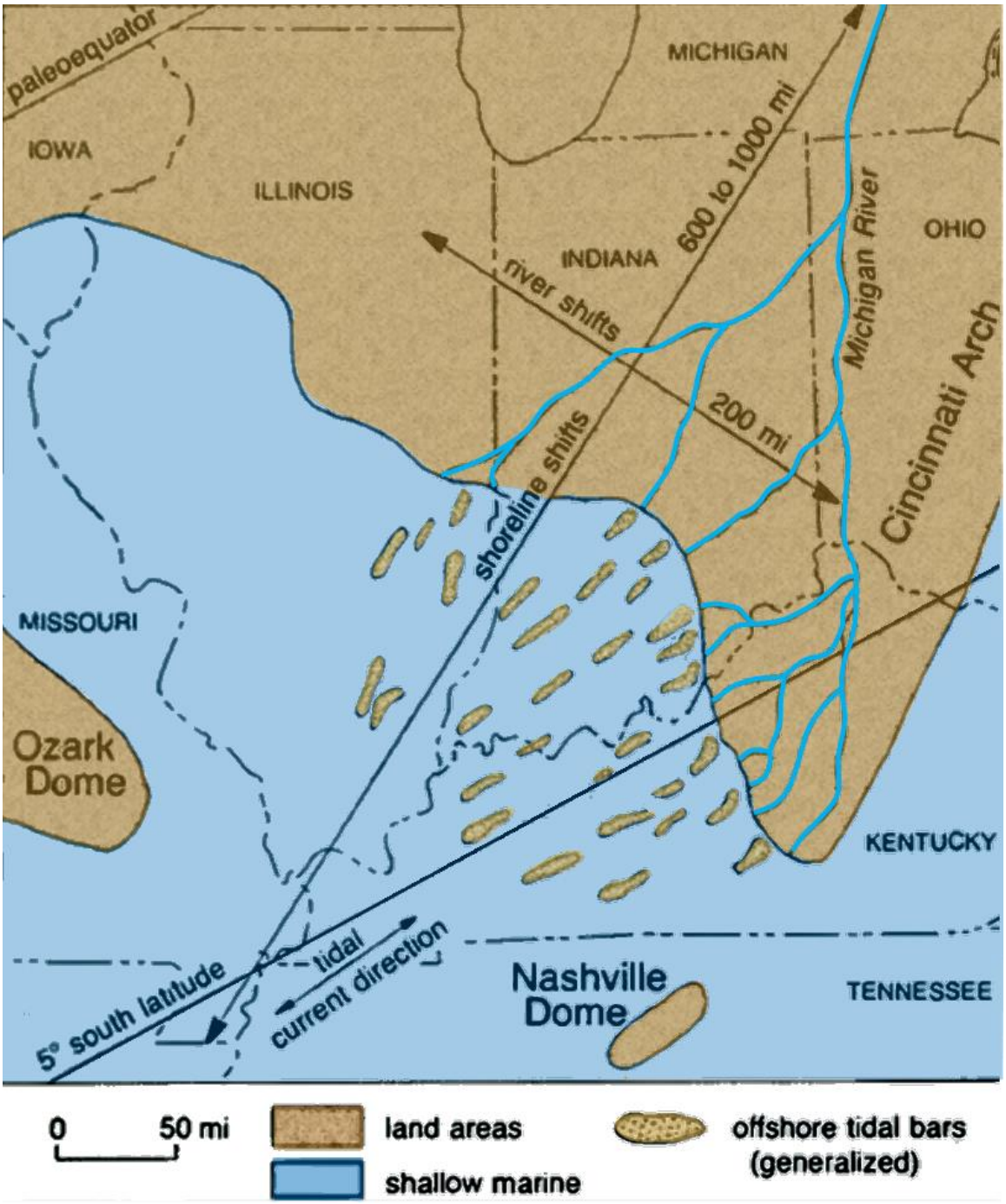

Figure 2.7. Schematic paleogeographic view of the Illinois Basin during deposition of the Fraileys/Big Clifty. Modified from Treworgy (1988), based on Swann (1963).

The sand was deposited in a marginal-marine to lower-deltaic environment that prograded basinward from the eastern and southeastern margin of the Illinois Basin. The bitumen content is the result of petroleum emplacement after deposition (Swann, 1964; Mack et al., 1981; Droste et al., 2000). Silt and carbonate content in the unit increases to the west and, in the basin's west and northwest, the Big Clifty is known as the Fraileys Shale (Treworgy, 1990). In south-central Kentucky, the Big Clifty conformably overlies the Beech Creek Limestone Member of the Girkin Formation and is conformably overlain by the Haney Limestone Member of the Golconda Formation (Figure 2.3) (Potter, 1962; Swann, 1963; Noger, 1987). Thin shale and mudstone layers are commonly found between the contacts of these limestone units with the main body of sandstone exhibiting a typical regressive-transgressive depositional cycle (Noger, 1987; Pryor et al., 1990).

2.4 Trapping Mechanisms and Diagenesis

Trapping mechanisms for reservoirs are commonly defined as: 1) stratigraphic, 2) structural 3) combination structural-stratigraphic, or 4) hydrodynamic (least common) (Biddle and Wielchowsky, 1994). Stratigraphic traps produced by post-depositional diagenetic alterations enhance and/or reduce porosity and permeability and, thus, create conditions favorable for the retention of petroleum (Cant, 1986; Pryor et al., 1990; Seyler and Cluff, 1990). Stratigraphy and structure greatly influence secondary petroleum-migration pathways (e.g., faults and joints, karstified carbonates, and permeable sedimentary beds) and the emplacement and trapping of oil following expulsion from the generative hydrocarbon "kitchen" (Hunt, 1987; Bethke et al., 1990; England et al., 1991; Lewan et al., 2002). Chesterian reservoirs are also associated with productive Pennsylvanian-aged oil and gas fields. Approximately 60% of all oil produced within the

Illinois Basin is from Chesterian reservoirs (Pryor et al., 1990; Lewan et al., 2002). These reservoirs are commonly targeted within the basin, given their broad distribution, continuity, and multiple pay-zone potentials (May, 2013).

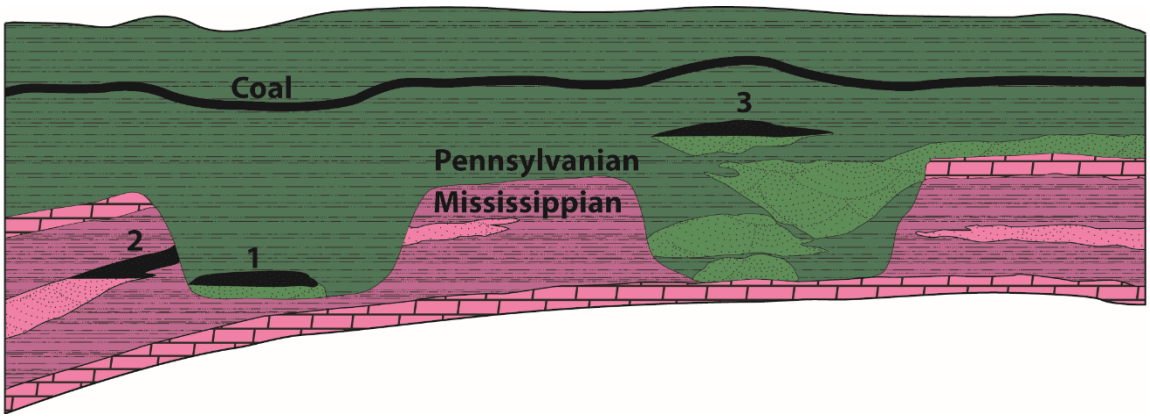

Figure 2.8. Stratigraphic trapping mechanisms associated with Kaskaskia-Absaroka sequence boundary in the Illinois Basin. (1) basal Pennsylvanian fluvial sandbars deposited on paleovalley floor with compaction syncline in overlying coal; (2) pre-Pennsylvanian reservoir terminating in shale infilling paleovalley; and (3) compaction anticline resulting from shales compacting multistoried sandstone packages deposited inside and above the paleovalley. No scale implied. After May (2013), and modified from Howard and Whitaker (1988).

Structural-stratigraphic combination traps are common in the widespread Chesterian. Oil is trapped by shale and fine-grained limestone that encloses sandstone at structural highs and/or at compaction anticlines (Figure 2.8) (Noger, 1984; Seyler and Cluff, 1990; Howard, 1990; May, 2013). Folding and faulting, in response to orogenic activity, influence sedimentation and hydrocarbon migration and preservation, particularly in fault-related paleovalleys (Nelson, 1990; May et al., 2007). According to Lewan et al. (2002), 66% of the petroleum in Chesterian reservoirs is sourced from the locally-generative rock below (New Albany Shale with potential contributions from the Late Ordovician Maquoketa Shale). Maximal expulsion of oil in southern Illinois occurred in the Late Pennsylvanian and Early Permian, during which time many of the

structural traps developed (Figure 2.9) (Lewan et al., 2002). Buoyant ascension, along faults and joints, are probably paths for oil movement over short distances with migration updip within carrier beds being responsible for emplacement of oil in reservoirs. Such reservoirs may be hundreds of miles distant from their source rocks (Bethke et al., 1990). Conventional crude oil plays within Chesterian sandstone are still targeted in the deeper portions of the basin as well as in updip locations, primarily in Indiana and Illinois, where erosion and incisement have removed little of the overlying strata (Figure 2.1).

Similar to younger Chesterian sandstone and Pennsylvanian-aged sandstone, the Big Clifty contains both conventional oil reservoirs within the basin and unconventional "tar sands" (these sediments are lithified and, technically, are not sand) and heavy oil along the southeastern basin margin (May, 2013). Many of these heavy-end hydrocarbons are trapped within the sub-Pennsylvanian (sub-Absaroka) paleovalleys along the Pennyrile Fault System (Noger, 1984; Howard and Whitaker, 1988; May et al., 2007). Chesterian and Pennsylvanian bitumen-rich rocks crop out along or near the southeastern basinal margin in western Kentucky (Figures 2.1 and 2.2). These resulted from devolatilization and degradation of lighter-end hydrocarbons, possibly with microbial assistance (Weller, 1927; Russell, 1933; McFarlan, 1943; Lewan et al., 2002; May, 2013).

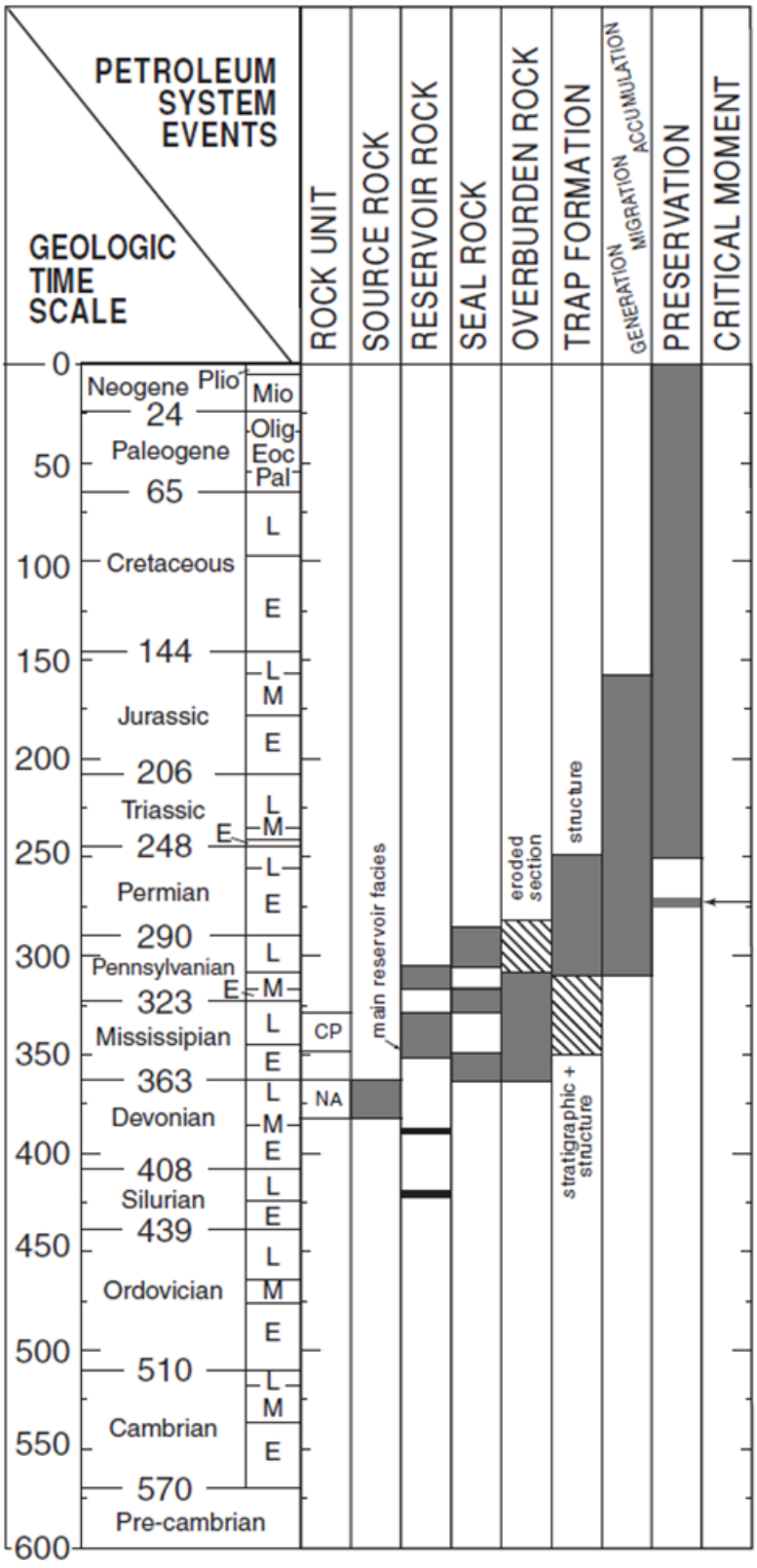

Figure 2.9. Sequence of events in the development of the Illinois Basin Chesterian petroleum play. From Lewan et al. (2002).

Diagenetic processes are broadly divided into three groups as related to the environmental conditions and timing in the post-depositional stages of sedimentation. Eogenesis encompasses alterations to pore fluids, organic matter (if present), cements, and sediments immediately following deposition (Schmidt and McDonald, 1979; Choquette and James, 1987; Pryor et al., 1990). Eogenesis is greatly controlled by sediment fabric, mineralogy, and interstitial waters at the time of deposition, with the influence of surficial and near-surface processes diminishing with increasing depth (Wilson and Stanton, 1994; Boggs, 2005; Ali et al., 2010). Burial, physical compaction, and mesogenetic processes associated with increasing temperatures greatly reduce primary porosity, especially if early cement is dissolved or minimal (Wilson and Stanton, 1994; Boggs, 2005).

Dolomitization, aragonite/high-magnesium calcite to low-magnesium calcite alteration, decarbonatization, fluid expulsion and stylotization, mineral replacement and overgrowths, weathering of labile sediments, feldspar hydrolysis, and clay-mineral authigenesis and alterations thereof commonly occur within the mesogenetic stage (Schmidt and McDonald, 1979; Folk, 1980; Choquette and James, 1987; Pryor et al., 1990; Wilson and Stanton, 1994; Montañez, 1997; Pitman et al., 1999; Boggs, 2005). Increasing temperature generally speeds reactions and can significantly affect porosity as the mineral stabilities of cement and grains change with changing pore-fluid chemistry (Boggs, 2005).

Telogenesis pertains to alterations caused by surficial processes acting on exhumed or shallow sedimentary units following burial (Schmidt and McDonald, 1979; Choquette and James, 1987; Pryor et al., 1990). Carbonate dissolution, metal oxidation

(including, e.g., Liesegang banding), and cation-leaching of feldspars are common telogenetic alterations of subaerially-exposed sedimentary rocks (Pryor et al., 1990; Stoessell, 1992; Surdam et al., 1993; Qin and Ortoleva, 1994). Paragenesis is particularly difficult to establish when secondary porosity from diagenesis has obliterated original grains and early cements, and altered grain orientation (Schmidt and McDonald, 1979; Pryor et al., 1990; Pitman et al., 1999).

2.5 Local Geology

In order for inferences regarding paragenesis to be made or conclusions to be drawn from petrographic examination, a sample's relative stratigraphic position in the Big Clifty Member must be established prior to its comparison with other Big Clifty samples from different locations and stratigraphic positions. This study did not conduct fluid-inclusion analysis for the microthermometry or barometry of authigenic cements such as quartz or calcite. However, the interpretation of cathodoluminescent-carbonate cements and hydrocarbon emplacement necessitates minimally, a broad understanding of the local paleohydrogeology and burial history. The Green River and its tributaries have contributed to the dissolution and transport of carbonate from the karst systems of Mammoth Cave and environs, as well as those of the greater Mississippian lowland plain south of the Pennyrile Plateau, for at least three million years (Granger et al., 2001). Because of this proven ion-transport mechanism in the immediate vicinity of the cores, and it being a possible source of bicarbonate and carbonate for the studied cores, geophysical logs of other wells were correlated with cored wells and samples' depths to provide greater subsurface geologic context (see Appendix A). These correlated

geophysical well logs also serve as proxies for the MegaWest core wells as the geophysical well data from these cores is not publicly available.

All but one of the samples used in this study are from six MegaWest wells cored along the Pennyrile Fault System in northern Warren and southern Butler counties (Figure 2.10). Many of these cored wells are located near proven Chesterian oil and gas reserves drilled on Quaternary-Tertiary alluvium and terrace deposits or directly on bedrock such as the basal Pennsylvanian Caseyville Formation. Core 106 is the exception and was drilled on the Menard Limestone. Many of the modern wells have casing extending several hundred feet below the surface as is commonly done in karst terrain such as that in southern Warren County. This is done to protect groundwater resources. Many domestic water wells on the Pennyrile Plateau draw from perched aquifers within the Chesterian strata (Maxwell and Devaul, 1961; Fetter, 2000). Although most of these wells have sufficient yields for domestic use, the Green River is the regional base level (Maxwell and Devaul, 1961). In addition to railroads, the Green River was also utilized in the transportation of mined asphalt rock during the first half of the 20th century (May et al., 2007). The Green River Asphalt Company had a mine at Youngs Ferry, less than three miles west and downriver of the location of Core 108. The mine was located on Pennsylvanian conglomerate with minimal overburden (Walcott, 1901).

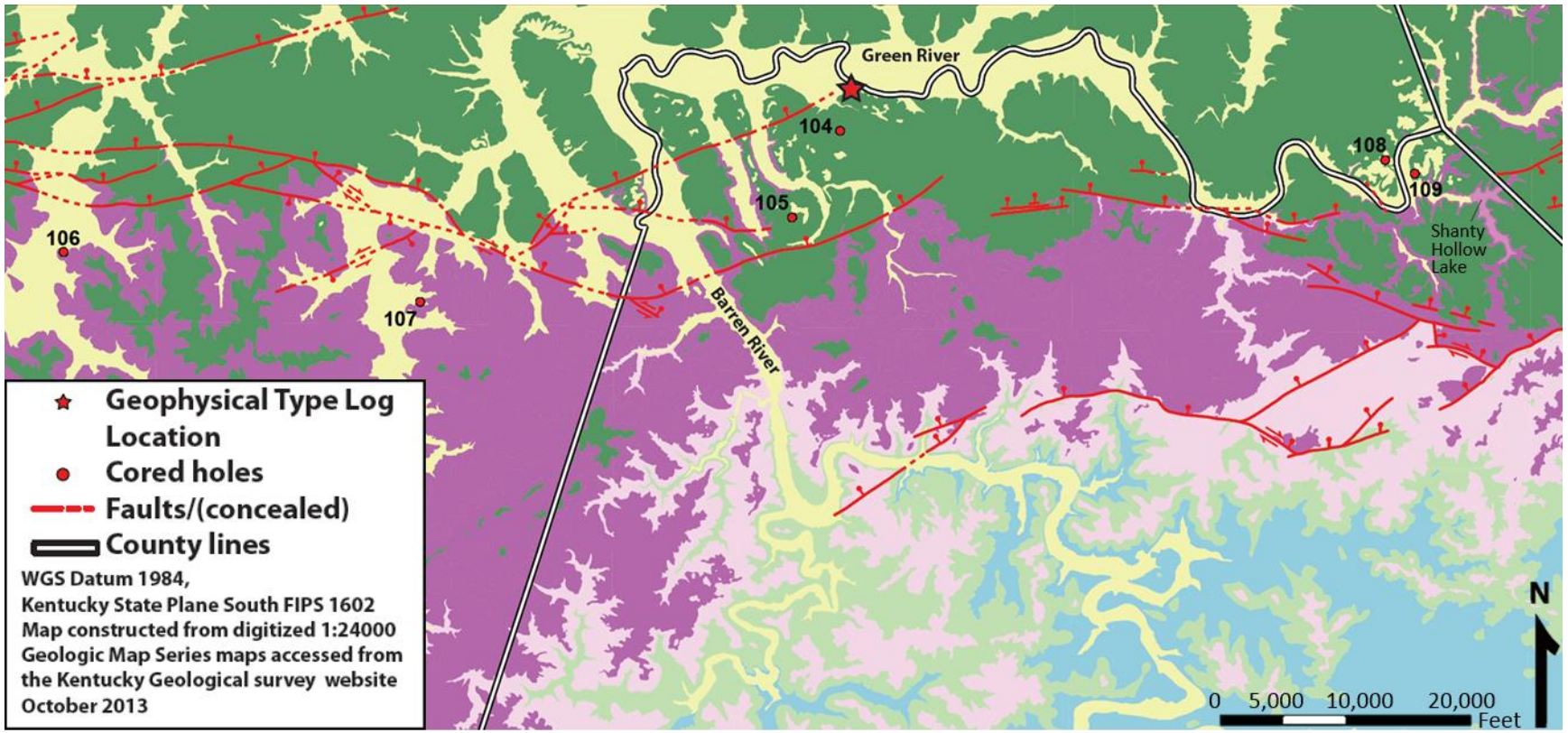

Figure 2.10. Generalized geologic map and core locations of Big Clifty Sandstone in northern Warren and southern Butler counties. The areal extent and regional structural context of this map can be seen in Figure 2.2 as the white box and Figure 2.4 as the gray box. To preserve continuity across the extent of the mapped area, geologic units were grouped and assigned the corresponding color as shown in Figure 2.3. Red star denotes location of geophysical type log (see Figure A.2 in Appendix A). The Pennyrile Fault System bisects the study area and defines the southern edge of the Rough Creek Graben with a series of en echelon north-dipping normal faults. After Butler and May (2013), map constructed from KGS compiled spatial data of Davidson (2002), Mullins (2002a–d), Thompson (2002), Mullins (2006), Toth (2006a–c).

Chapter 3: Methodology

3.1 Sample Collection

This petrographic study mainly employed standard light and cold-cathode cathodoluminescence optical microscopy to establish paragenesis with additional instrumentation and analytical techniques being used for certain samples (Table 3.1). Twenty-two of the twenty-three samples studied were taken from split-cores of six holes cored by MegaWest Energy and donated to the Kentucky Geological Survey in Lexington, KY, in 2012. Sample collection initially made use of thirteen sample billets of core sections (Figures 3.1A–G and 3.1N–S), made by earlier researchers, of which only four had been thin-sectioned. The nine billets that had not been thin-sectioned were sent to a contracted petrographic service laboratory for thin-sectioning and preparation. Samples obtained earlier from the MegaWest cores had proved difficult to thin section because immobile hydrocarbons resisted epoxy impregnation, thus preventing thin-sectioning. For this reason, a petrographic service laboratory familiar with thin-section preparation of rock hosting heavy-end hydrocarbons was contracted. Prior to shipment to the contracted laboratory, multiple attempts were made to remove the immobile hydrocarbons with organic solvents (acetone, petroleum ether, methylene chloride, and toluene). Despite these pretreatments many of these cores required multiple solvent treatments from the laboratory which the laboratory graciously did without additional charge due to the academic nature of this research.

To expand the research beyond the initial thirteen samples taken from MegaWest cores 104, 105, and 109, six additional core sections of interest were identified for sampling in cores 106, 107, and 108 (Figures 3.1H–S). From these six core sections of

Sample		KGS Oil & Gas Record #	Stained	Diamond Polished for microprobe	60 µm & double-sided polished	PPL, XPL, RFL	UV	CL	EM	XRD	Raman	Depth (ft)
Code	#											
104c1-b10	1	133678	-	-	-	X	-	X	SEM	-	X	482.3’
104Bc1-b10	1B	133678	-	-	X	-	X	-	SEM	-	-	482.3’
109c1-b2	2	136344	-	-	-	X	X	X	-	-	-	281.1’
109c1-b3	3	136344	-	-	-	X	X	X	-	-	-	283.5’
109c1-b4	4	136344	-	-	-	X	-	X	-	-	-	285.9’
109c1-b5	5	136344	-	-	-	X	-	X	SEM	-	X	289.0’
109c1-b10	6	136344	-	-	-	X	-	X	-	-	-	302.7’
109c2-b4	7	136344	-	-	-	X	-	X	-	-	X	315.8’
105c2-b5	8	136343	-	-	-	X	X	X	SEM	-	X	450.7’
105c2-b6	9	136343	-	-	-	X	-	X	-	-	-	451.6’
105c2-b7	10	136343	-	-	-	X	-	X	-	-	-	455.3’
105c2-b9	11	136343	-	-	-	X	-	X	-	-	-	462.6’
105c3-b1	12	136343	-	-	-	X	-	X	-	-	-	469.0’
105c3-b2	13	136343	-	-	-	X		X	SEM	-	-	470.8’
106c1-b7	14	133621	X	X	-	X	X	X	-	-	-	338.5’
106c1-b10	15A	133621	X	X	-	X	-	X	-	-	-	347.2’
106Bc1-b10	15B	133621	-	-	X	-	X	-	-	-	-	347.2’
107c1-b6*	16	133622	-	-	-	-	-	-	-	X	-	180.3
107c1-b7	17A	133622	X	X	-	X	X	X	-	-	-	182.3’
107Bc1-b7	17B	133622	-	-	X	-	X	-	SEM	-	-	182.3’
107c2-b5†	18	133622	X	X	-	X	X	X	SEM	-	X	210.7’
108c1-b2	19	133623	X	X	-	X	X	X	-	-	-	255.4’
Roadcut*	RC	N/A	-	-	-	-	-	-	TEM	X	-	GL

* = Samples not thin sectioned

X = Analysis preformed

– = Analysis not preformed

† = Thin section contains artifacts from residual oil resisting epoxy impregnation. Staining further compounded the sample with the stain poorly restricted to one side of the thin section leaving a residue. The acid wash may have dissolved tenuous carbonate cement in the sample, as well although the sampled section of core contains vugs.

Table 3.1. Analytical techniques and sample preparation of core and other samples. Sample codes refer to thin sections in boxes and Oil and & Gas record numbers refer to cored well the sample was taken from. All samples are of the Big Clifty except for 108c1-b2 which is of the Hardinsburg. All samples were thin sectioned with the exception of 107c1-b6 and “Roadcut”, which were shale chips from the core, and hand sample from outcrop, respectively. Samples 104Bc1-b10, 106Bc1-b10, and 107Bc1-b7 are from the same depth and location as 104c1-b10, 106c1-b10, and 107c1-b7, respectively. Billets of 106Bc1-b10 and 107Bc1-b7 have billets that mirror those of 106c1-b10 and 107c1-b7 as the initial billets sampled were cut in half. Sample 104Bc1-b10 was made from the same billet as 104c1-b10 was. The combined stains used on select samples were alizarin red S and potassium ferricyanide. Abbreviations PPL, XPL, and RFL are, plane-polarized, cross-polarized, and reflected light microscopy, respectively. UV stands for ultraviolet, CL stands for cathodoluminescence, and EM stands for electron microscopy of transmitted (TEM) and scanning (SEM).

interest five billets were made, and some shale chips were selected as samples. As per the initial sample request form, and the wishes of KGS to maintain the integrity of the core, destructive XRD analysis of core material was restricted to the shale-chip sample, 107c1-b6 (Figure 3.1J).

To provide more information about the Big Clifty, from which these billets were sampled, five of these thin sections were diamond polished and stained with alizarin red S and potassium ferricyanide to assist distinguishing carbonates and their ferroan varieties (see Table 3.1). For the purpose of fluid-inclusion analysis, three 60-µm thick, double-sided polished, thin sections were made. Unfortunately, these thick sections were insufficiently polished and began to deteriorate immediately with the sample flaking and peeling off of the slide backing. In light of these developments, and with the realization that the analysis of fluid inclusions would be extremely time-consuming and carried the risk of sample loss just by handling the thin section, this aspect of the project was abandoned to pursue more promising avenues of research. The "Roadcut" sample was not taken from the MegaWest cores and instead was retrieved from the upper section of Big Clifty near its type section in Hardin County, Kentucky (see Appendix A, section A.8). In the hand sample (Figure 3.1T), this rock contained heavy-end hydrocarbons and was used to examine clay mineralogy of the Big Clifty from a part of the basin where the Big Clifty does not possess evidence of a subaerial unconformity in its upper portion (Nelson et al., 2002).

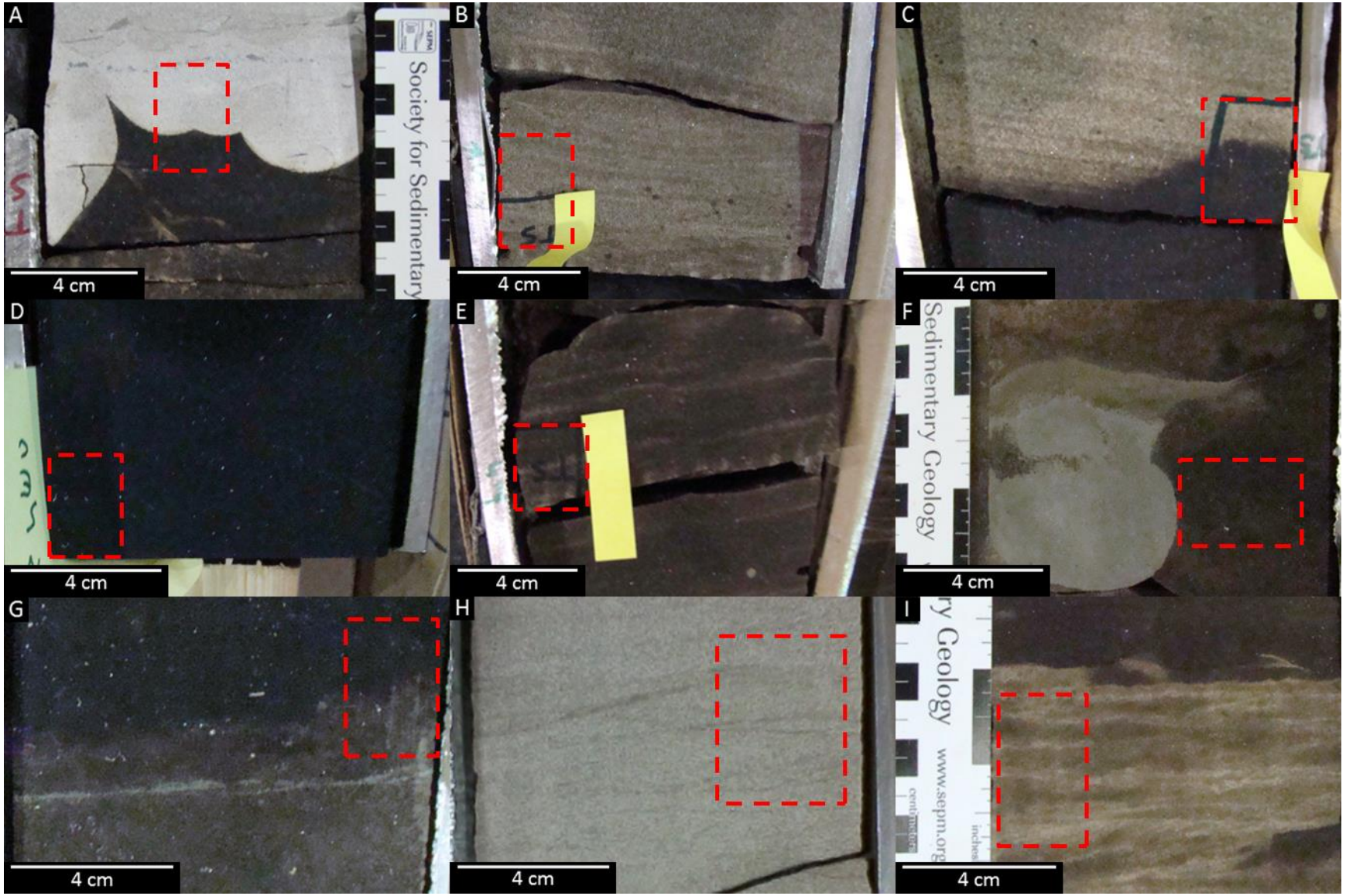
A
4 cm
Society for Sedimentary
B
4 cm
C
4 cm
D
4 cm
E
4 cm
F
Sedimentary Geology
4 cm
G
4 cm
H
4 cm
I
Geology
www.sepm.org
4 cm

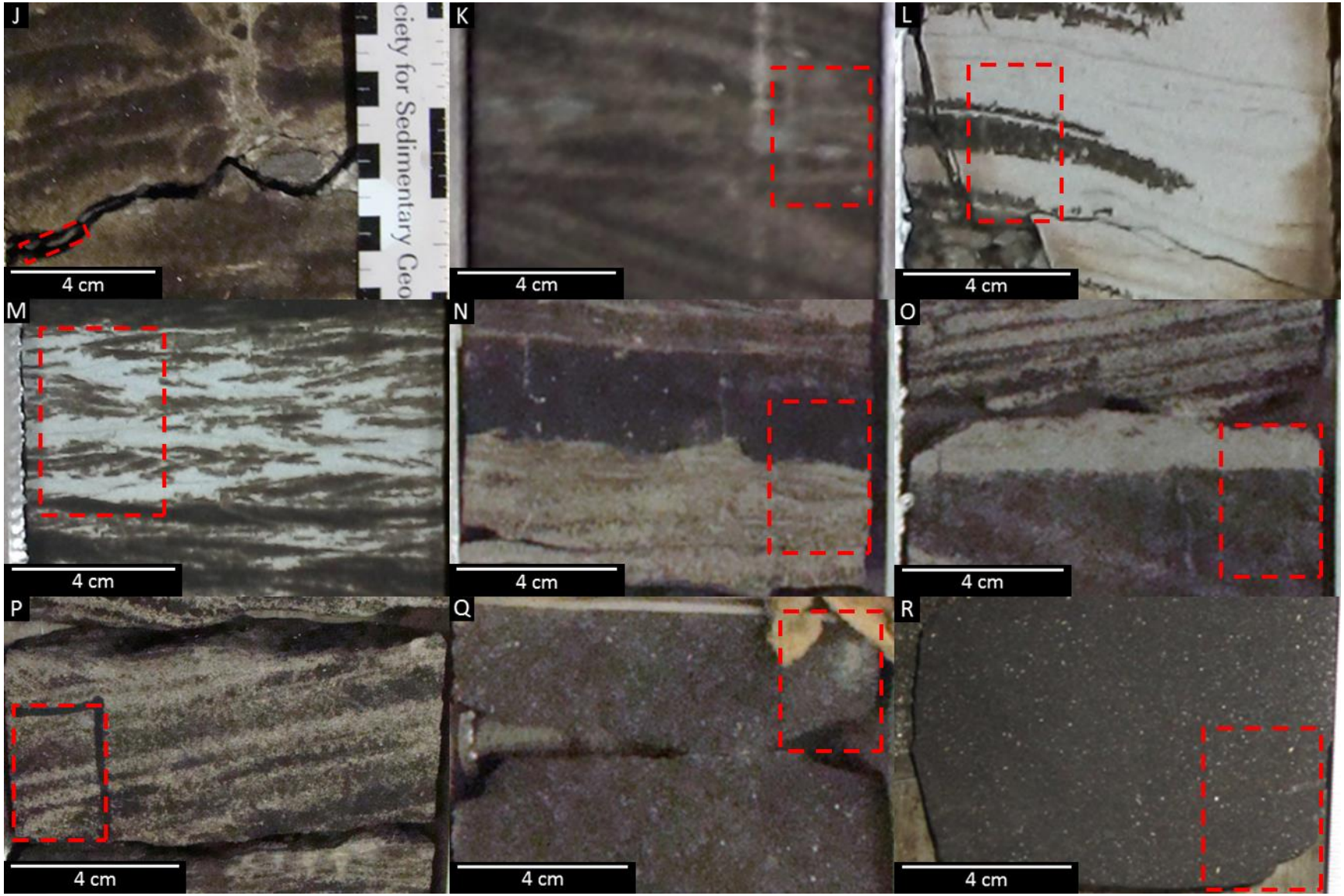
J
4 cm
K
4 cm
L
4 cm
M
4 cm
N
4 cm
O
4 cm
P
4 cm
Q
4 cm
R
4 cm

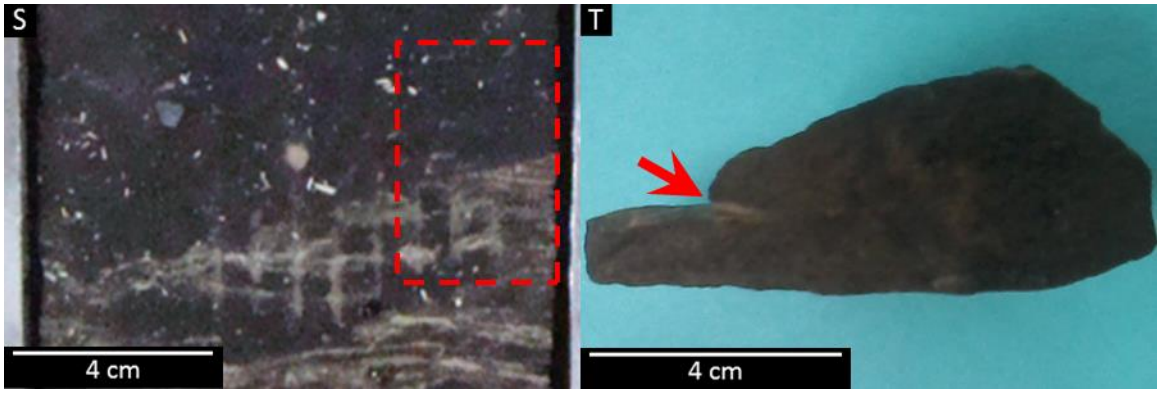

Figure 3.1 (from previous pages). Sections of rock sampled for this study. Red dashed rectangles outline locations of billeted core or shale chips sampled, red arrow denotes clay drape from which clays were isolated. Samples from displayed rocks: 104c1-b10 & 104Bc1-b10 (A), 105c2-b5 (B), 105c2-b6 (C), 105c2-b7 (D), 105c2-b9 (E), 105c3-b1 (F), 105c3-b2 (G), 106c1-b7 (H), 106c1-b10 & 106Bc1-b10 (I), 107c1-b6 (J), 107c1-b7 & 107Bc1-b7 (K), 107c2-b5 (L), 108c1-b2 (M), 109c1-b2 (N), 109c1-b3 (O), 109c1-b4 (P), 109c1-b5 (Q), 109c1-b10 (R), 109c2-b4 (S), and Roadcut (T).

3.2 Analytical Techniques

3.2.1 Overview of Techniques

The petrographic study primarily relied upon standard transmitted and reflected light microscopy supplemented with optical cold-cathode cathodoluminescence microscopy. UV-epifluorescence microscopy was also conducted to explore if there were any fluorescing hydrocarbons that were coincident with any texture or fabric. The OM-CL permitted discrimination between detrital grains and authigenic overgrowths, cement generations, and minerals that might otherwise exhibit similar optical features in standard light petrography. Electron microscopy, SEM, and TEM were employed for their high-magnification capabilities in order to resolve fine details and perform semi-quantitative elemental estimates of mineral compositions. Raman microscopy was used to: (1) confirm mineralogy of cements and grains identified via optical petrographic methods including cathodoluminescence microscopy; and (2) to determine the veracity of the carbonate stains that potentially affect the observed cathodoluminescence. The XRD was used to identify clay minerals, which are a minor constituent within the studied Big Clifty intervals and sandstone reservoir body. A more thorough explanation of the theoretical background behind cathodoluminescence, electron microscopy, Raman, and XRD and their uses in petrographic studies can be found in Appendix C.

3.2.2 Transmitted and Reflected Optical Microscopy

Most of the petrographic analysis and description of clastic textures, framework grains, cement, and porosity of the eighteen thin-sectioned core samples were conducted using research-grade petrographic microscopes (Nikon Eclipse E200 and Olympus BH-2) under standard transmitted, plane and cross-polarized (PPL and XPL), and reflected light

(RFL) (Figures 3.2A&B). Sample examination under reflected light was sourced by a Dyna Lite 150 fiber optic module. Transmitted and reflected light photomicrographs were taken with Motic 3.0 and JVC KY-F75U digital cameras. UV-epifluorescence microscopy utilized a mercury lamp for the UV light source and an Olympus BX51-P microscope to observe the fluorescence of oil. This microscope and an Olympus DP71 camera were used to capture UV-epifluorescence photomicrographs. The utility of UV-epifluorescence was limited as the observed fluorescence from hydrocarbons was weak in the few samples in which it occurred. This is not surprising as more than a year had passed between coring and billet sampling and hydrocarbons are most fluorescent from fresh cuts (Swanson, 1981). In addition, billets from the most saturated sampled sections of core had most of their mobile hydrocarbons removed by organic solvents prior to thin sectioning.

3.2.3 Optical Cold-Cathode Cathodoluminescence Microscopy

Cathodoluminescence microscopy was conducted with a Technosyn Luminescence 8200 Mk II, a cold-cathode microscope stage attachment with gun control, and a Varian SD-90 rotary pump in conjunction with a Leitz Wetzlar Orthoplan microscope (Figure 3.3). This microscopy was performed at the Kentucky Geological Survey on the University of Kentucky campus in Lexington, Kentucky. A total of eighteen samples from six cored holes were examined with OM-CL (see Table 3.1). Sample billets were impregnated with non-luminescent epoxy and backed on non-luminescent glass in thin section. Each of the five stained thin sections had one side which remained unstained. During sample examination, operating conditions were as follows: gun potential was 10–12 kV, beam current was 380–500 μAmps, and the

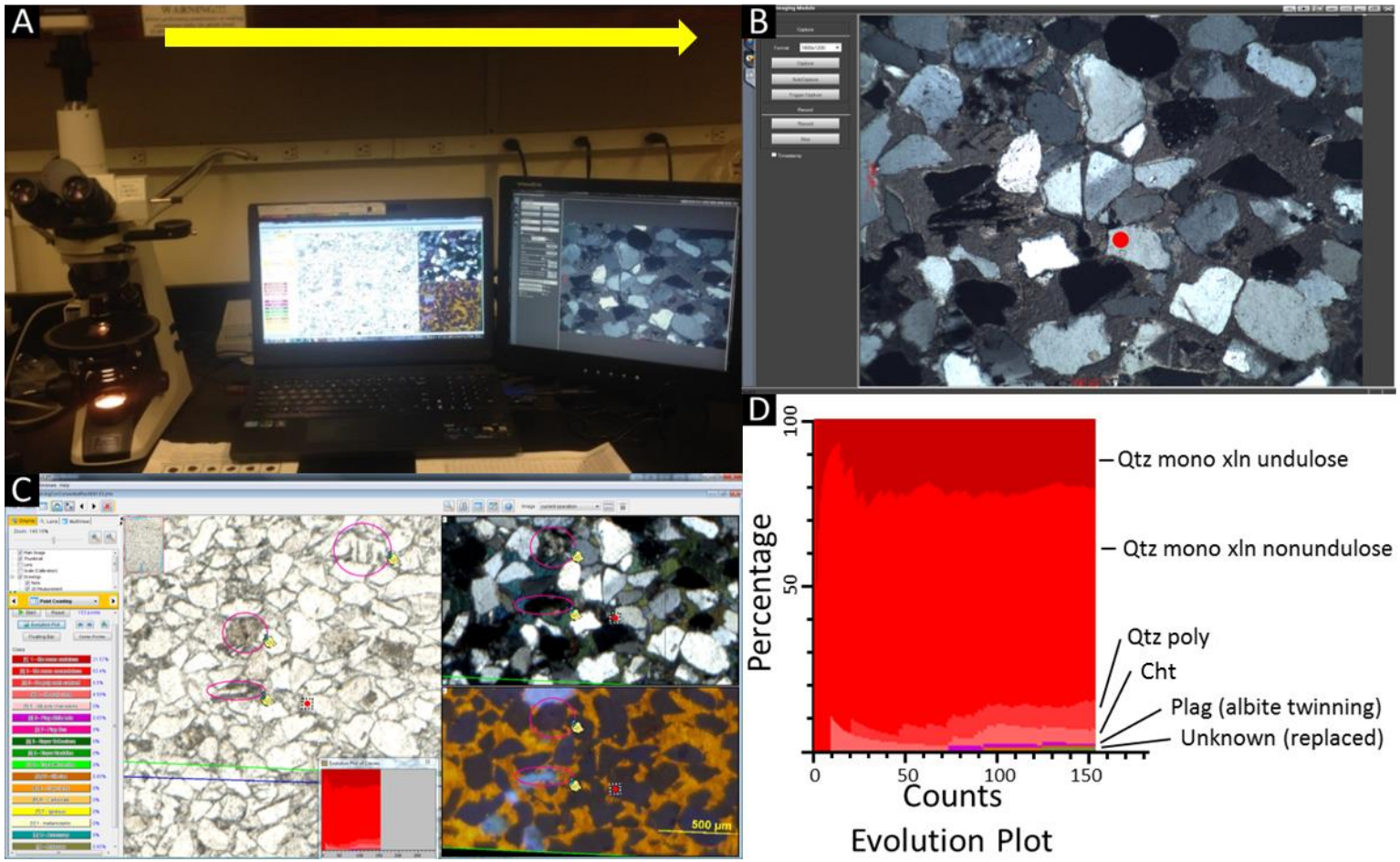

Figure 3.2. Microscope and camera setup with petrographic and image software used for grain counts and PPL, XPL, and RFL photomicrographs. A) Nikon Eclipse E200 microscope equipped with a 3.0 Motic camera was used for transmitted light and a Dyna Light 150 fiber optics unit was utilized capturing reflected light photomicrographs. B) Photomicrographs were captured using Motic Image Plus 2.0 software. C) Petrographic image software JMicroVision ver. 1.2.7 with rectified and scaled PPL and XPL thin section scans and OM-CL photomicrograph. D) Evolution plot of framework grains initially used during grain counting.

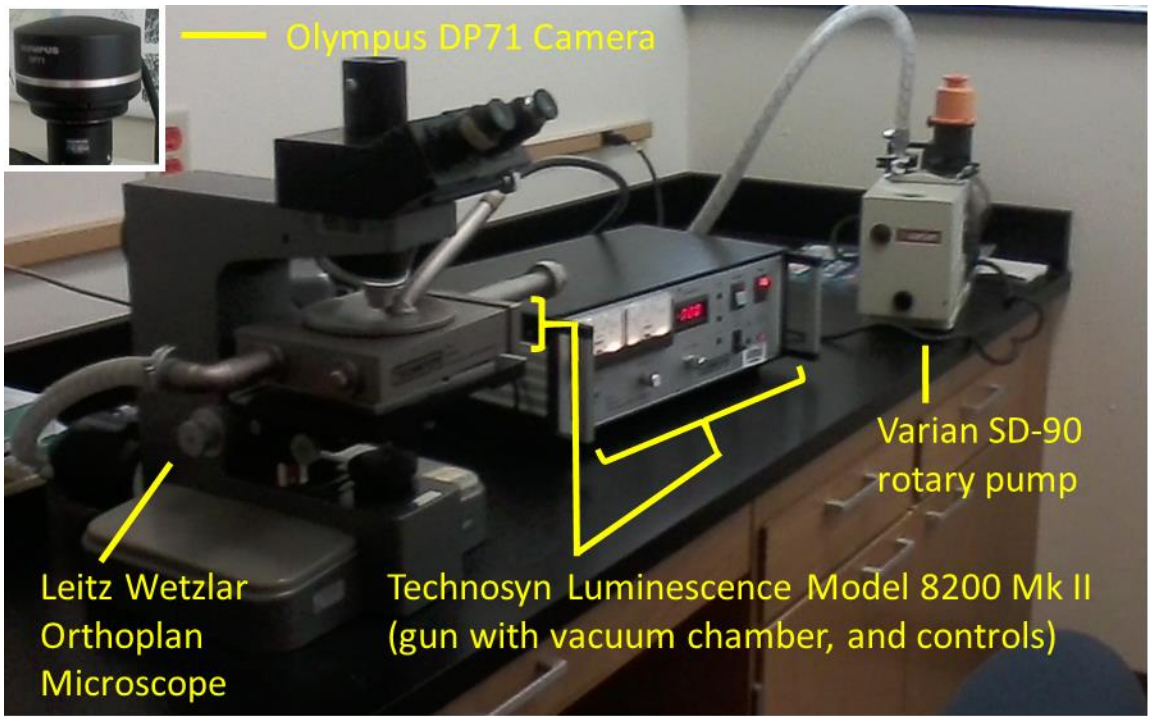

Figure 3.3. OM-CL instrumentation and camera (inset). Used to capture OM-CL photomicrographs at the KGS, University of Kentucky.

chamber pressure was maintained below 0.1 Torr. Operating procedures and conditions for the cathode lamp and vacuum chamber were followed to mitigate radiation exposure to author, beam damage to the sample, and to minimize beam current and vacuum fluctuations for photomicrograph consistency. OM-CL microscopy was performed in a dimmed room with a thick piece of cloth encircling the objective, and the top chamber window, and with a cap over the microscope's bulb below the stage. These measures were taken to prevent the introduction of outside light. A residue of back-streamed oil was apparent on the chamber's windows prior to use. This was compensated for with a white-balance auto-correction in the image-capture software. Stained and unstained portions of thin sections were photographed to gauge any observable effect the staining process had on the cathodoluminescence of carbonates in a given sample.

Exposure times for images varied depending upon the overall intensity of the CL within the field of view in an attempt to maintain the apparent differences in hue and brightness of mineral and non-mineral components as viewed through the eyepieces. Areas of interest where minerals were weakly luminescent and, thus, the overall field of view was dark, required longer exposure times for minerals to be distinguishable from images of minerals from areas that, overall, were brightly luminescent. Fields of view containing brightly-luminescent calcite cement required shorter exposure times than did the fields of view where such cement was absent. In many samples, the majority of grains and cements were weakly luminescent with a few brightly-luminescent minerals. Unstable beam current (termed "climbing") necessitated vacuum adjustment on several occasions during long exposure times of dim areas. Otherwise, optically-conspicuous features to be indistinct and blurred. Egregious differences in photographed images from observed areas were immediately noticed and photographed again, although some blurring of details and fine objects in images were not noticed until later. Despite the best efforts of the author, some photomicrographs appear more clearly than others, whether as a result of polish, exposure time, staining, transient luminescence, or a combination thereof.

Of all the forms of microscopy utilized in this study, OM-CL was the best suited for identifying siliciclastic detrital grain boundaries and distinguishing calcite and quartz-cement generations. Despite the invaluable assistance and access to equipment rendered by Dave Harris at the KGS in Lexington, KY, OM-CL was the least available form of microscopy. Access to OM-CL during grain counts would have obviated the need for robust quantification of the framework grains (mineralogy, size, and angularity/

roundness) and cements of samples; particularly those affected by replacive diagenesis where a survivor bias would be intrinsic. Notwithstanding the aforementioned difficulties, cold-cathode OM-CL provides rapid, economical, true-color, real-time observation with minimal sample preparation and with findings that can be corroborated with other forms of microscopy without interference. Consequently, to elucidate paragenesis, attention and use of OM-CL was focused on petrographic textures and cross-cutting relationships unique to CL as well as corroborating features of textural pertinence identified with other forms of microscopy.

3.2.4 Staining

Calcite has variable solubility and reactivity with alizarin red S depending upon the crystallographic orientation of the crystal. Alizarin red S stained surfaces normal to the c-axis appear lighter than those parallel to the c-axis (Dickson, 1966). The variable surface area created by the acid wash results in variable efficacy of alizarin red S (Ayan, 1965; Dickson, 1966). Alizarin red S stain ideally produces a pink color in calcite and leaves dolomite unchanged. Potassium ferricyanide may produce a blue color in ferroan calcite, turquoise or light blue in ferroan dolomite, and leave pure end-member calcite and dolomite unstained (Ayan, 1965). Lindholm and Finkelman (1972) reported that the degree of coloration of potassium ferricyanide in calcite and dolomite is proportional to Fe^{2+} content with the stain being sensitive to as little as 100 ppm in calcite. Nelson and Read (1990) noted that the acid used by Lindholm and Finkelman (1972) was weaker than the acids which the Dickson (1966) method used. Furthermore, the degree of staining for potassium ferricyanide is strongly pH-dependent as Turnbull's precipitate (the resultant blue stain) will not precipitate on a thin section unless carbonate is present

even if ferrous iron is abundant (Dickson, 1966; Nelson and Read, 1990). Dickson (1966) stated that it would be ill-advised to relate Fe^{2+} content solely on the degree of staining of Turnbull's precipitate, since ferroan calcite would be more sensitive to staining than dolomite of similar iron content. Potassium ferricyanide is capable of detecting 1% ferrous iron in calcite solid solution (Dickson, 1966). Nevertheless, Nelson and Read (1990) analyzed the Fe^{2+} content of combined alizarin red S and potassium ferricyanide-stained calcite using an electron microprobe. They found that most calcite that stained pink was non-ferroan, <1000 ppm Fe^{2+} content. Purple- or mauve-stained calcite had Fe^{2+} content that predominantly ranged between 1000-3000 ppm, and calcite with Fe^{2+} content in excess of 3000 ppm stains blue (Nelson and Read, 1990). Nelson and Read's (1990) study is the only one encountered by this author that relates Fe^{2+} content with the functional constraints of the widely-adopted Dickson (1966) staining procedures used to indicate ferroan nature in calcite and dolomite. The combined effects of these stains are summarized below in Table 3.2.

Stain	Calcite	Ferroan Calcite	Dolomite	Ferroan Dolomite
Alizarin red S	Very pale pink – dark pinkish red	Very pale pink – dark pinkish red	No effect	No effect
Potassium Ferricyanide	No effect	Light blue-dark Blue	No effect	Dark blue
Alizarin red S & Potassium Ferricyanide	Very pale pink – dark pinkish red	Pinkish purple – royal blue	No effect	Pale blue – turquoise

*Only carbonate minerals encountered in this study are included. For an overview of carbonate identification staining methods see Ayan, 1965; and Dickson, 1966.

Table 3.2 Stain effects on calcite and dolomite and ferroan varieties for identification.

The above stains have limited effectiveness on ankerite and no effect on siderite and magnesite unless specific changes are made to the procedures for dolomite and calcite staining (Ayan, 1965; Dickson, 1966). Neither ankerite nor siderite, satisfying the dominant constituent rule, or any appreciable amount, were found in either stained or unstained portions of thin sections (Hatert and Burke, 2008). Furthermore, all stained portions of the stained thin sections, where carbonates lacked stain or exhibited colors other than purple, were checked with Raman microscopy. In only a few instances was the stained calcite mistaken for dolomite. Stains fade over time, and the longer the time between staining and observation the less reliable the stain is for identification purposes. This was not an issue encountered during this research; however, any future researchers who utilize this study's stained thin sections should be aware that the original stains may no longer be visible.

Staining was not particularly useful for identifying or imaging carbonates with OM-CL. The reduced profile of the calcite from the acid etching allowed inclusions of luminescent minerals to shine through. The staining also gave black edges to the calcite borders in the OM-CL and the appearance of shadows in the SEM images. The acid etching did reveal the curved cleavage planes of baroque dolomite in one sample which had, heretofore, been unrecognized. Carbonate, with similarly-curved cleavage planes or other features such as the undulatory extinction typical of baroque dolomite, was not observed in other samples whether stained or unstained. The reduced thickness profiles of the etched carbonate minerals, particularly calcite, would also have produced a noticeable difference in the interference colors. Any change in the interference colors of calcite or dolomite were, however, obfuscated by the potassium ferricyanide and alizarin red S. The

additional iron from the potassium ferricyanide and the decrease in sample interaction volume contributed only slightly to quenching the luminescence in the crystals. The five stained samples had few carbonate minerals making it difficult to assess the consequences of staining on luminescence. The primary deleterious effect of the stains on the samples was the obfuscation of carbonate's fine features visible in transmitted light and with OM-CL as well as the obfuscation of the crystalline boundaries between carbonates and those of other minerals.

3.2.5 Electron Microscopy

Electron microscopy was used to study seven samples of Big Clifty thin sections. Samples represent four different cored well locations (cores 104, 105, 107 and 109), with cores 105, 107, and 109 each having samples from two different core intervals, and Core 104 samples (104c1-b10 and 104Bc1-b10) being made from the same billet though different in polish and thickness. Sample 107c2-b7 contains SEM photomicrographs of stained portions.

Scanning Electron Microscopy (SEM) in conjunction with Energy-Dispersive X-ray Spectroscopy (EDS) was utilized to examine the composition of important textural relationships of the thin sections. Samples were analyzed with a JEOL JSM-5400LV scanning electron microscope with an IXRF-system attachment for EDS analysis. The SEM images produced in this study are produced from backscattered secondary electrons (BSE) and such images are referred to as SEM-BSI. The accelerating voltage of the electron beam was maintained at 20 kV for all samples. The apparent differences in contrast and tonal element in photomicrographs was due to the variance in the atomic numbers of the sample materials (minerals, epoxy, and organics). SEM-EDS analysis was

used for semi-quantitative estimations of elemental compositions in minerals such as Ca, Mg, Fe, and Mn of calcite and dolomite, and K, Na, and Ca compositions of feldspar. SEM-EDS analysis, while capable of giving elemental compositions, provides a poorer analytical spatial resolution than SEM-BSI (Flegler et al., 1993).

Transmission electron microscopy (TEM) was utilized to examine clays isolated from a clay drape of bitumen-impregnated Big Clifty obtained from a hand sample of Big Clifty. This sample was exposed in a roadcut (sample designated "Roadcut") in Hardin County, Kentucky, on the south side of Wendell H. Ford (formerly Western Kentucky) Parkway, mile marker 120.1 (See Figure 2.2 and Appendix A, section A.8, for location). Clay morphology and possible mineralogy were provided by TEM and from select area electron diffraction (SAED). This work was conducted with a JEOL-100CX TEM. A clay drape was pried from hand sample after soaking the sample in acetone to remove the hydrocarbons. The fine-grained sediment was gently agitated in deionized water then successively centrifuged with the supernant decanted until no residuum was observed. A drop from the solution of clay suspensions was applied and adsorbed to Formvar-coated grids, and observed in the TEM. Clay mineral analyses from earlier researchers, Atherton et al. (1960) reported illite and kaolinite as the dominant clay minerals found within upper Chesterian sandstones. Therefore, no attempt was made to prevent swelling in the Roadcut sample given the low shrink-swell capacity of these two clays.

3.2.6 Raman Microscopy

This study utilized a confocal Thermo Scientific DXR Raman microscope with a 780-nm laser and 50-µm grating. Signal-processing, peak-area integration and mineral matching of Raman spectra were conducted with Omnic for Dispersive Raman ver.

8.2.403 software. Raman microscopy was primarily limited to the identification of stained carbonates as well as carbonates that displayed quenched luminescence or non-luminescent areas. Raman microscopy also aided in the mineral identification of grains and cements that either occurred with other amorphous phases, as did microcrystalline pyrite, or had too-fine or ambiguous mineralogical features to be resolved with standard transmitted and reflected light microscopy.

3.2.7 X-ray Diffractometry

Smear sample mounts of powdered material from two samples, 107c1-b6 and Roadcut, were analyzed with a Rigaru MiniFlex II X-ray diffractometer with Cu Kα (λ = 1.54 Å) X-ray source using PDXL software ver.1.81. Neither preparation of 107c1-b6 or Roadcut samples extended beyond the standard mortar and pestle and distilled water for the smear-sample mount method. Further sample preparation was deferred, in part, due to the lack of volcanic minerals and other labile precursors of expansive clays observed in thin section, as well as the satisfactory results and mineral-peak matches produced from the analysis of the smear-sample mounts. The mineralogy of the clays detected with XRD was corroborated by the observed clay morphologies and SAED pattern produced with TEM of clays from the Roadcut sample.

3.3 Thin-Section Analysis

3.3.1 Framework Grains

Prior to petrographic examination, a specialized scanner with polarizing films was used to produce high-resolution plane- and cross-polarized light images of thin sections. These images of thin sections served as maps allowing the matching and scaling of images following rectification with JMicroVision ver. 1.2.7 software (Figure 3.2C).

Additionally, these scanned images of thin sections were used with the built-in tools of JMicroVision for quantitative estimations (Figure 3.2D) (Roduit, 2014). Modal analysis of the framework grains required points which were specifically limited to framework grains. Limiting point counts to only grains was done for efficiency; stochastic determination of relative abundancies of porosity, matrix, and grains and cement compositions is inefficient (Pye, 2007). Framework grain composition plots require, at a minimum, three-hundred grains for reliable and statistically-valid estimations of composition (Pye, 2007; Roduit, 2014). Counting three-hundred points that coincide with framework grains stochastically would entail point counting in excess of three-hundred points and, potentially, require additional thin sections if the grains are coarse or the point count number is large (Chayes, 1956; Plas and Tobi, 1965; Garrison, 2003).

The recursive grid and evolution plot functions in the *Point Counting* tool of JMicroVision were initially used for point selection, specifically, for modal analysis of framework-grain composition. Selected grains were those that coincided with the locations of a grid point or were the nearest grain to a point. A recursive grid generates points based on a rectangular grid which is subsequently further subdivided creating more points (Roduit, 2014). Use of the *Point Counting* tool and recursive grid were not continued past the first sample (104c1-b10Seal), since each successive point generated by the software on the scanned thin-section image was located in a different part of the thin section. Locating the generated grid point proved too time-consuming to continue use of the *Point Counting* tool. Grains in subsequent samples were selected from regular, but not equally-spaced, points along traverses of the thin section. Point intervals were spaced approximately 1 mm, as were the parallel traverses upon which the points were laid. The

approximate 1-mm point interval and line spacing exceeded the apparent diameter of the largest grain, ensuring non-duplicative sampling, as well as a sufficiently large population of grains for sampling (Plas and Tobi, 1965). Sample 104c1-b10Reservoir was the exception to this spacing and a 600-µm spacing was used, though this spacing was similar to the shortest spacing of the recursive grid in sample 104c1-b10Seal, 730 µm. The point intervals and line spacing used in both 104c1-b10Seal and 104c1-b10Reservoir point counts exceed the maximum grain diameter encountered in both the reservoir and reservoir seal of 104c1-b10 thin section which was important for non-duplicative sampling (Plas and Tobi, 1965). Separate point counts were conducted in the seal and reservoir respectively of 104c1-b10. This was done to explore the possibility of a mineralogical or deposition influence on the extensive overprinting of framework grains and earlier cements by replacive calcite. Such calcite had drastically increased the surface area and angularity of detrital grains.

Mineralogy of framework grains was quantified using a modified Gazzi-Dickinson (Dickinson and Suczek, 1979) method. Detrital grain composition was plotted on a QFL (Quartz Feldspar and Lithics) ternary diagram modified from McBride (1963) in accordance with the sandstone classification-naming scheme proposed by Dott (1964) (Figure 3.4). Sandstone composition was plotted by the abundancies of the detrital constituents with respect to the poles along categorical definitions of framework grains (Figure 3.5). Heavy minerals, such as tourmaline, zircon, rutile, hematite, ilmenite, and magnetite as well as micas were excluded from plotted compositions of framework grains (Folk, 1980). No distinction was made between non-cryptocrystalline varieties of polycrystalline quartz. The abundance of such grains of plutonic or metamorphic varieties

were combined and included with the monocrystalline quartz abundance for plotting relative to the Q-pole (Figures 3.4 and 3.5). This lack of distinction is justified by the lack of foliated or granoblastic textures indicating a metamorphic source. Differentiation of polycrystalline quartz, based upon the presence of undulatory extinction of the crystal constituency of a grain, is contentious. Such differentiation would also be impractical and without statistical significance given the already low percentages of polycrystalline quartz component. Plagioclase and alkali feldspar grains comprise the F-pole. Cryptocrystalline quartz grains, and polymineralic grains comprised of silt-sized quartz, were treated as sedimentary lithic rock fragments and included with clay clasts and other lithics on the L-pole. Neither volcanic nor metamorphic lithics were observed in sample thin sections and such grains, if present, are considered to contribute little to the lithic percentage.

The maximum chord length of each accounted grain was measured to the nearest $1/100^{th}$ of a millimeter with special care taken to exclude syntaxial cements from detrital-grain measurements (Tainrui, 1991). These chord lengths are apparent grain diameters and, although studies have found that such values are closer to the diameter of the intermediate axis of grains, it is a reasonable approximation of grain size of an indurated, heavy-oil, reservoir rock in lieu of sieve analysis (Kellerhals et al., 1975). Diameters of grains <30 μm and unidentified grains were measured and included in the grain-size histograms but not in the composition plots. Matrix was excluded from both and only factored in the architectural components calculation.

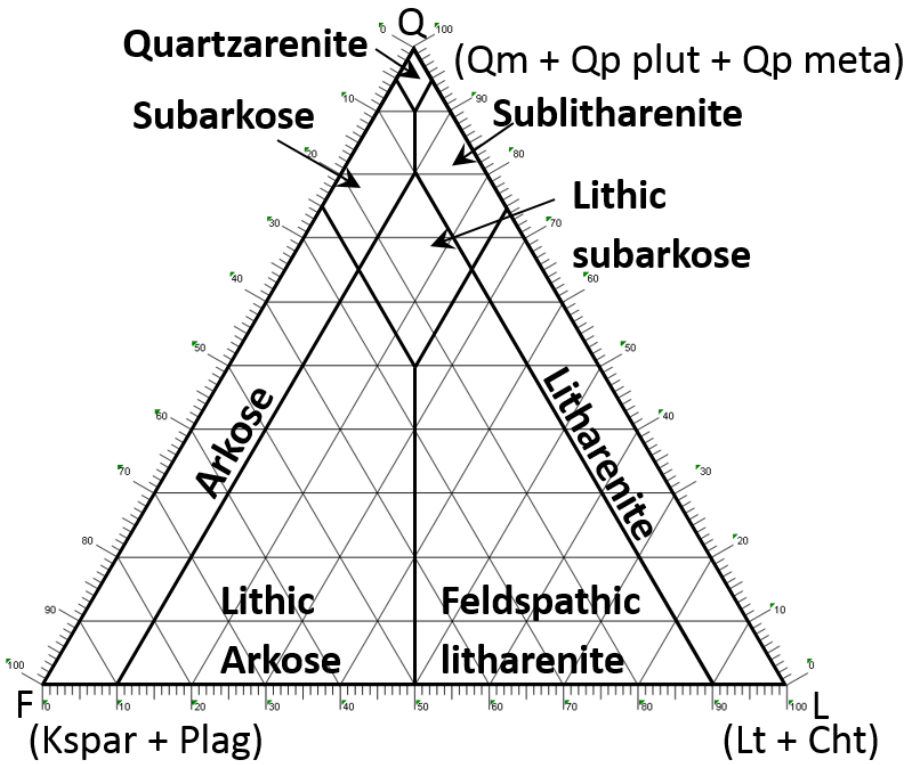

Figure 3.4. QFL-composition diagram and sandstone name classifications. Modified from McBride (1963) in accordance with sandstone name classifications proposed by Dott (1964). See Figure 3.5 for abbreviations. From McBride (1963) and Dott (1964).

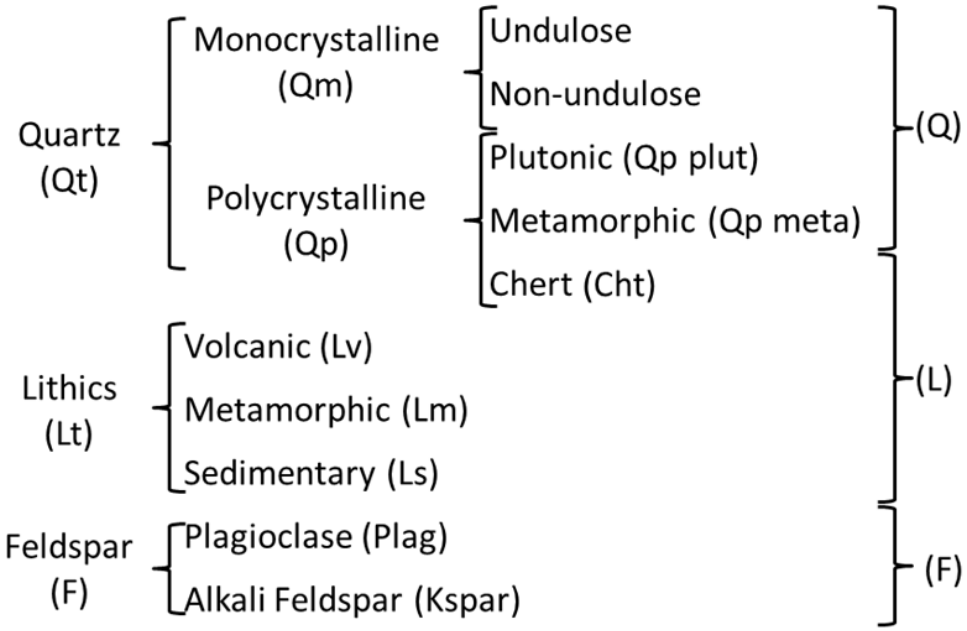

Figure 3.5. Detrital framework grain categories and abbreviations used in ternary diagrams. QtLtF poles (left) are used gauge textural maturity while, QLF poles (right) are used for provenance.

Grain counts were compiled to a sum of at least 300 identifiable framework grains of sand-size particles in each thin section sample. Angularity/roundness was visually estimated using transmitted light and grains compared to the Powers (1953) scale. Where unrestricted, syntaxial overgrowths make quartz grain boundaries appear euhedral, and when sieve analysis is not feasible, OM-CL can be used to discern between original grain boundaries and cements. Grain-size histograms of samples, as well as QFL-composition plots for separate cores, are included in Appendix D. Grain-size abundancies were graphically presented with a lower and upper interval within each Udden-Wentworth grade (Udden, 1914; Wentworth, 1922) of the sand-size particle range. This was done, in part, to better display the distinction in grain size between samples particularly those from the same core. Sieve analysis was not possible with the samples due to the non-destruction agreement with the KGS. Consequently, grain-size measurements were completed from plane view. Grain-size distribution histograms did not follow the convention of traditional sieve analyses having the bins in the phi scale and decreasing in coarseness from the left to the right (Houseknecht, 1992).

3.3.2 Cements and Porosity

In addition to detrital-grain composition, the relative percentages of cements, and matrix were estimated and recorded to the nearest $1/10^{th}$ for each counted grain. Phyllosilicate cements were distinguished using standard transmitted light petrography as well as OM-CL. Illite was distinguished by its relatively higher birefringence when compared to that of kaolinite, which is similar to that of quartz, and from glauconite which maintains its green color in PPL and XPL. Kaolinite cement appears similar to chert cement in XPL due to its low birefringence but is distinguishable by its platy

morphology and microporosity, both of which are conspicuous with blue-dyed epoxy under PPL. The dark-blue luminescence of kaolinite also readily distinguishes kaolinite from the non-luminescent chert under OM-CL. Carbonate cement was distinguished in stained samples by color. Raman microscopy was also utilized to identify ferroan dolomite and calcite, both of which appeared dark blue under PPL. OM-CL was similarly used in detecting unstained, non- or weakly-luminescent carbonates which were later identified using Raman microscopy. Very few instances of non- or weakly-luminescent carbonates were encountered in thin sections. The few locations where dolomite exists were known and marked on the scanned thin-section images with JMicroVision prior to the grain and cement quantification. Unusual and rare trace cements such as apatite and Ti-oxide were discovered and checked using OM-CL and Raman microscopy, and SEM-EDS, respectively.

Conservative porosity values of samples were estimated using the *Background* tool in JMicroVision with the blue epoxy being selected from plane-polarized scanned images. Scanned images were first cropped to exclude the epoxy border and notches from contributing to the areal percentage of porosity. Porosity was then selected from the image based on hue, intensity, and saturation that resulted in the exclusion of the darker blue hues from the stains, as well as the faint blue of the epoxy within the microporosity, but included the primary and large secondary porosity (Figure 3.6).

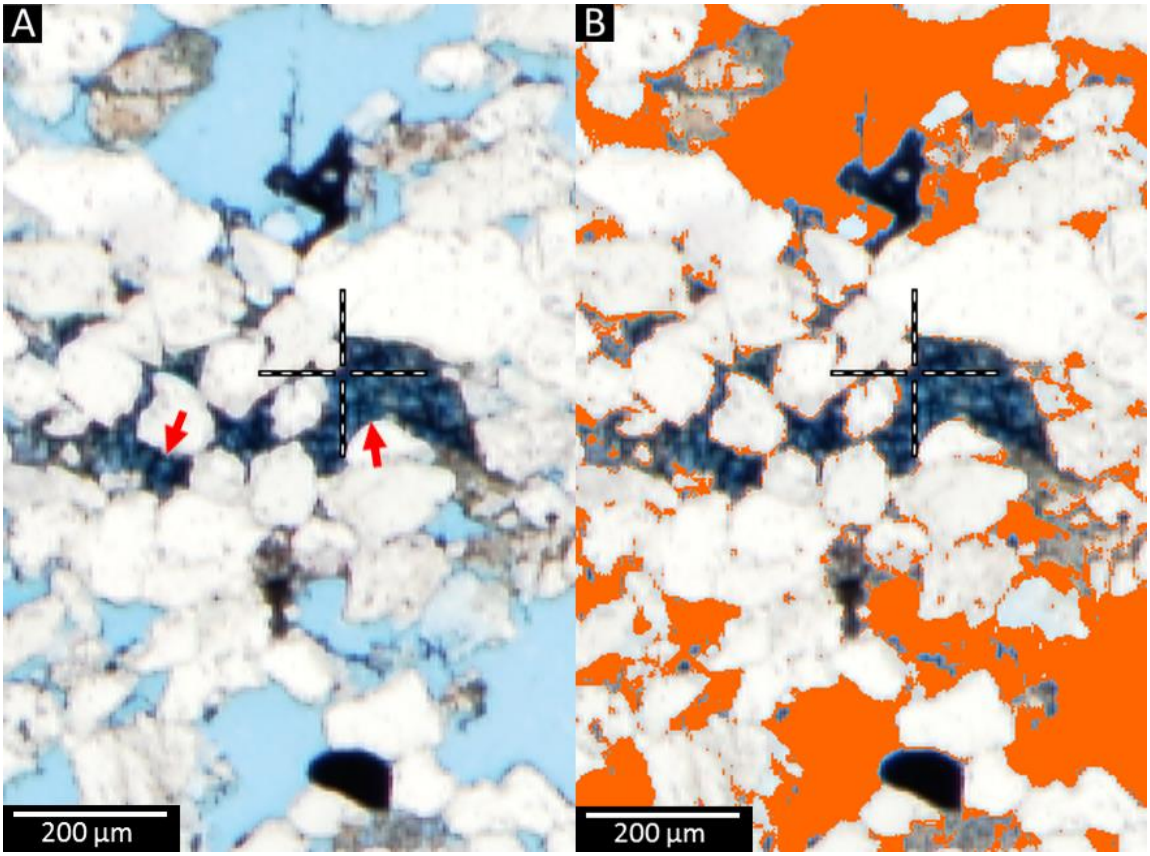

Figure 3.6. Porosity selection and estimation from PPL-scanned thin selection. A) Epoxy (light blue) is a lighter shade of blue than the stained ferroan dolomite (red arrows). B) Porosity is selected and displayed as orange in JMicroVision, while the ferroan dolomite remains blue and is not selected for porosity estimation.

Chapter 4: Results

4.1 Overview of samples

Compositional quantification of sample thin sections predominantly classify as fine- to very-fine grained, siliceous-cemented quartz arenite (Figure 4.1). This composition is consistent with compositions of Chesterian sandstones of the Illinois Basin reported by Mack et al. (1981). Most of samples are well- to moderately-sorted with less than 5% matrix. Framework grains are primarily subangular to subrounded based upon original grain boundaries of detrital grains. Angularity appears to be inversely related to grain size, however, angularity due to replacement commonly makes original grain boundaries difficult to discern even with the aid of OM-CL.

Monocrystalline quartz is the most abundant framework grain with non-undulatory variety (extinction ≤5˚stage rotation) always more common than undulatory (extinction >5˚ stage rotation) (Basu et al., 1975). Grains of polycrystalline quartz as well as chert are present in all samples, although not in particular abundance, the latter less so than the former. Feldspars comprise less than 5% of framework grains in samples from the Big Clifty. Feldspars typically exhibit bright light-blue luminescence with OM-CL in thin section except for weathered feldspars which appear green. Feldspars noted and analyzed via SEM-EDS were predominantly alkali varieties. It is suspected that some portion of ghost grains that comprise the unknown grains encountered in every sample during grain-counts were feldspars that have weathered. It is probable, therefore, that the framework-grain composition of studied samples was slightly higher (1–2%) in feldspar initially after deposition than what currently is estimated. Sedimentary lithics, besides chert and chalcedony, are primarily clasts of phyllosilicates and silt-sized grains, with

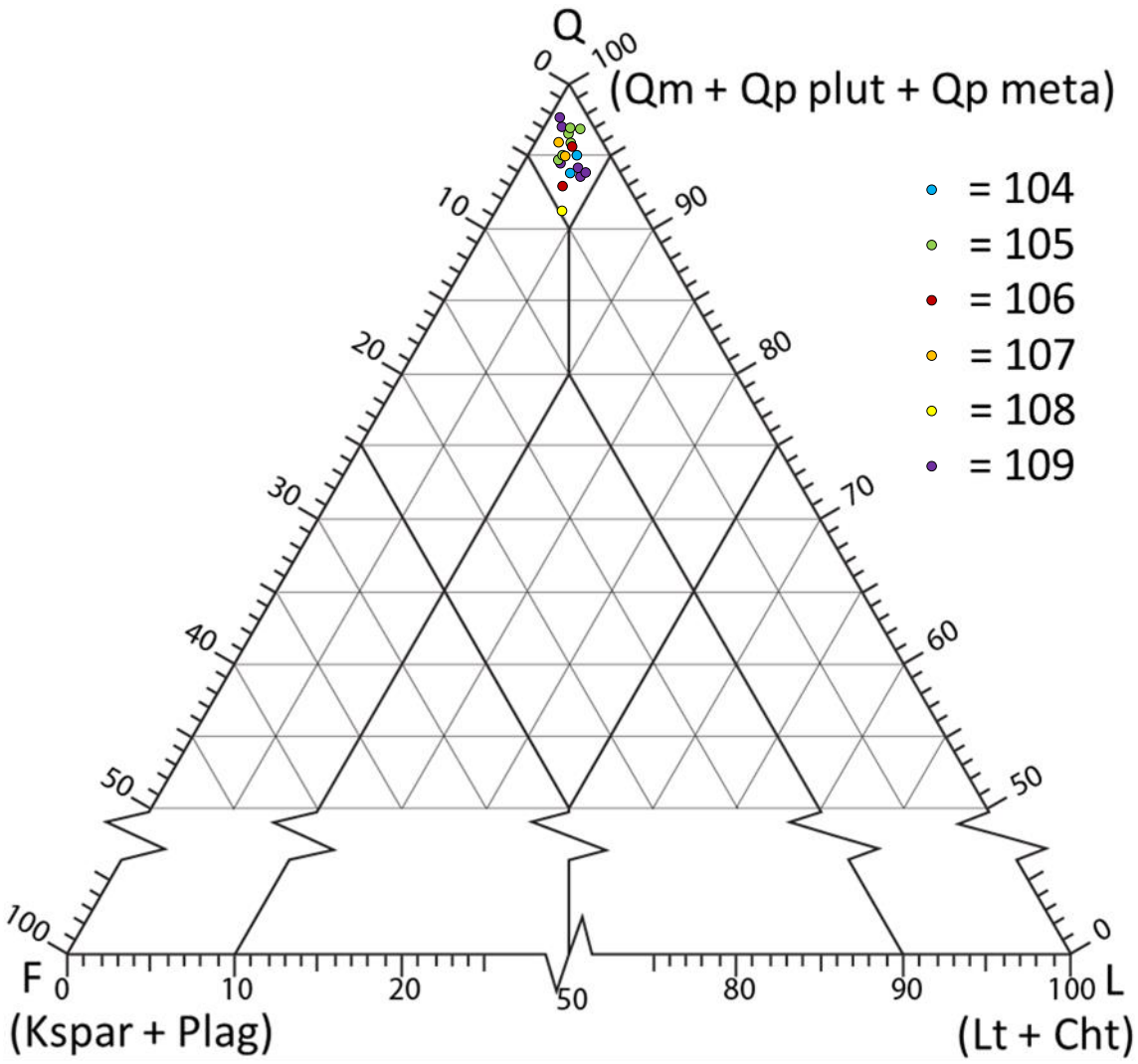

Figure 4.1. Framework grain composition plots of thin sections. Numbers in upper right correspond to sampled cores. Abbreviations at each pole are the same as those used in Figure 3.4 and defined in Figure 3.5. The sampled Big Clifty Ss. is a quartz arenite as is the sample from Core 108 which is the Hardinsburg Ss.

bioclasts being rare. Muscovite, biotite, titanite (sphene), and zircon are accessory, minerals shared by many of the samples with tourmaline, hematite, and apatite also occurring in a few places. Hematite and apatite are also observable as rare cements.

Quartz is the most abundant cement in all samples, except for the seal section of 104c1-b10 (Table 4.1). Quartz cementation is primarily syntaxial with quartz grains but also occurs as epitaxial overgrowths on chert grains and some weathered feldspars in a

Sample	Framework Grain Size (μm)		Roundness and Sorting	Framework Grains (% of 100)								Cements (% of 100)								Architectural Components (% of 100)		Porosity (% of 100)
				Quartz (Q)			Feldspar (F)	Lithics (Lt)			Detrital Accessory Minerals	Siliceous		Carbonate		Fe Cement		Phyllosilicate	Trace			
	Range	Median		Mono (Qm)	Poly (Qp plut + Qp meta)	Crypto (Cht)	(Kspar + Plag)	Lv + Lm + Ls				Qtz OG	Chert	Calcite	Dolomite	Pyrite	Fe-Oxide			Grains & Cement	Matrix	
104c1-b10 (Reservoir)	40–490	200	Subrounded – Subangular Well sorted	91	3	2	3	-	-	1	Muscovite, Zircon, Titanite	93	<1	<1	-	<1	<1	5 (Kaol~4, Ill~1, & Glau<1)		100	<1	1.7
104c1-b10 (Seal)	60–340	170	Subangular – Angular Well sorted	88	7	3	2	-	-	<1	Muscovite, Titanite, Zircon, Biotite	3	<1	94	-	1	<1	1 (Kaol~1, Ill<1, & Glau<1)	Ti-Oxide	99	1	<0.1
105c2-b5	20–410	190	Subangular – Subrounded Moderately sorted	93	2	1	3	-	-	1	Muscovite, Zircon, Titanite, Hematite	85	<1	1	-	5	<1	8 (Kaol~4, Ill~2, & Glau~2)	Apatite	99	1	12.3
105c2-b6	50–400	200	Subangular – Subrounded Well sorted	95	2	1	1	-	-	1	Muscovite, Titanite, Zircon	90	-	2	-	2	<1	5 (Kaol~3, Ill~1, & Glau~1)		99	1	12.2
105c2-b7	50-460	210	Subrounded – Rounded Well sorted	97	<1	1	1	-	-	1	Muscovite, Biotite, Zircon	92	<1	1	-	2	<1	4 (Kaol~2, Ill~2, & Glau<1)		100	<1	9.2
105c2-b9	20-370	190	Subangular – Subrounded Moderately sorted	94	2	1	2	-	-	1	Muscovite, Zircon as inclusions	84	-	1	-	2	<1	12 (Kaol~9, Ill~2, & Glau~1)		99	1	10.2
105c3-b1	50–360	170	Subrounded – Subangular Well sorted	96	<1	1	2	-	-	<1	Muscovite, Zircon as inclusions	62	-	2	-	21	<1	15 (Kaol~6, Ill~5, & Glau~4)		99	1	5.8
105c3-b2	20–470	200	Subangular – Subrounded Moderately sorted	92	3	1	3	-	-	1	Muscovite, Titanite, Zircon	67	1	17	-	1	<1	14 (Kaol~11, Ill~2, & Glau~1)		99	1	12.6
106c1-b7	40–310	130	Subangular – Subrounded Well sorted	94	2	2	2	-	-	<1	Muscovite, Zircon as inclusions	73	-	7	<1	<1	-	19 (Kaol~13 & Ill~6)		98	2	6.2
106c1-b10	30–310	120	Subangular – Subrounded Well sorted	91	2	1	4	-	-	2	Muscovite	73	-	3	<1	<1	-	23 (Kaol~14 & Ill~9)		98	2	6.9
107c1-b7	50–410	140	Subrounded – Subangular Moderately sorted	93	3	<1	3	-	-	1	Muscovite, Zircon, Titanite	62	<1	4	<1	10	<1	23 (Kaol~15, Ill~6, & Glau~2)		98	2	11.4
107c2-b5	20–280	130	Subangular – Subrounded Well sorted	88	7	1	3	-	-	1	Muscovite, Zircon as inclusions	64	1	5	<1	5	<1	24 (Kaol~17, Ill~5, & Glau~2)		98	2	22.3
108c1-b2	20–210	90	Subangular – Subrounded Well sorted	86	5	2	5	-	-	2	Muscovite, Titanite	65	2	<1	-	4	-	28 (Kaol~12, Ill~12, & Glau~4)		96	4	5.3
109c1-b2	40–310	180	Subrounded – Subangular Moderately sorted	94	3	1	2	-	-	<1	Muscovite, Zircon	84	<1	<1	-	1	-	14 (Kaol~5, Ill~4, & Glau~5)		98	2	3.0
109c1-b3	40–540	200	Subrounded – Subangular Moderately sorted	92	2	2	2	-	-	2	Muscovite, Zircon	90	<1	<1	-	1	<1	8 (Kaol~4, Ill~2, & Glau~2)		99	1	4.6
109c1-b4	40–390	200	Subrounded – Subangular Poorly sorted	94	<1	2	2	-	-	2	Muscovite	85	1	<1	-	1	<1	12 (Kaol~8, Ill~2, & Glau~2)		99	1	5.5
109c1-b5	60–390	230	Subrounded – Subangular Moderately sorted	97	1	<1	2	-	-	<1	Muscovite	96	-	<1	<1	3	<1	1 (Kaol~1, Ill<1, & Glau<1)		99	1	11.4
109c1-b10	30–370	140	Subrounded – Subangular Moderately sorted	93	2	1	4	-	-	<1	Muscovite, Titanite, Tourmaline	88	-	1	-	4	<1	7 (Kaol~5, Ill~1, & Glau~1)		100	<1	5.0
109c2-b4	30–510	150	Subrounded – Subangular Poorly sorted	91	3	2	2	-	-	2	Muscovite, Titanite	83	-	<1	-	2	<1	14 (Kaol~7, Ill~2, & Glau~5)		99	1	3.9

Table 4.1. Petrographic composition of MegaWest samples under transmitted and reflected light.

few samples. In a majority of the Big Clifty samples, and in 108c1-b2 of the Hardinsburg, phyllosilicate cement is the second most abundant type of cement. In samples 105c3-b1 and 105c3-b2, kaolinite is the third most prevalent cement. Kaolinite is present as matrix in mud laminae, and as authigenic, interstitial cement, and coatings on surfaces of labile grains. Illite is also present in mud laminae as matrix and as authigenic cement commonly associated with alteration products of labile grains and other phyllosilicates. Illite and kaolin were detected with XRD in both 107c1-b6, and Roadcut samples (Figure 4.2), corroborating the identified clays from the Roadcut sample with TEM (Figure 4.3).

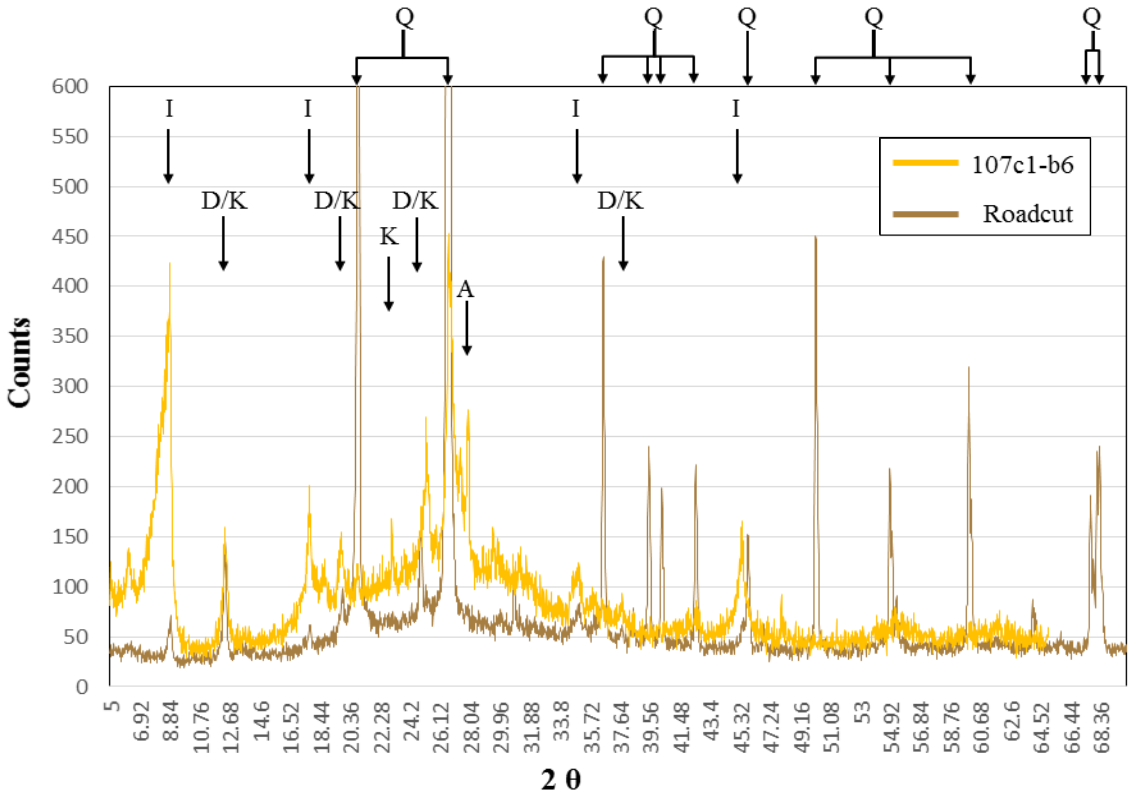

Figure 4.2. XRD of 107c1-b6 and Roadcut smear sample mounts. Mineral peak matches are quartz (Q), illite (I), dickite (D), kaolinite (K), and albite (A). Dickite and kaolinite matched for similar peaks except in one instance where only kaolinite matched. Albite and quartz were detected in the finely-ground sample material. The two center quartz peaks of the Roadcut and 107c1-b6 samples extend beyond 600 counts but the graph axis was restricted to better display the clay mineral peaks of both samples for comparison.

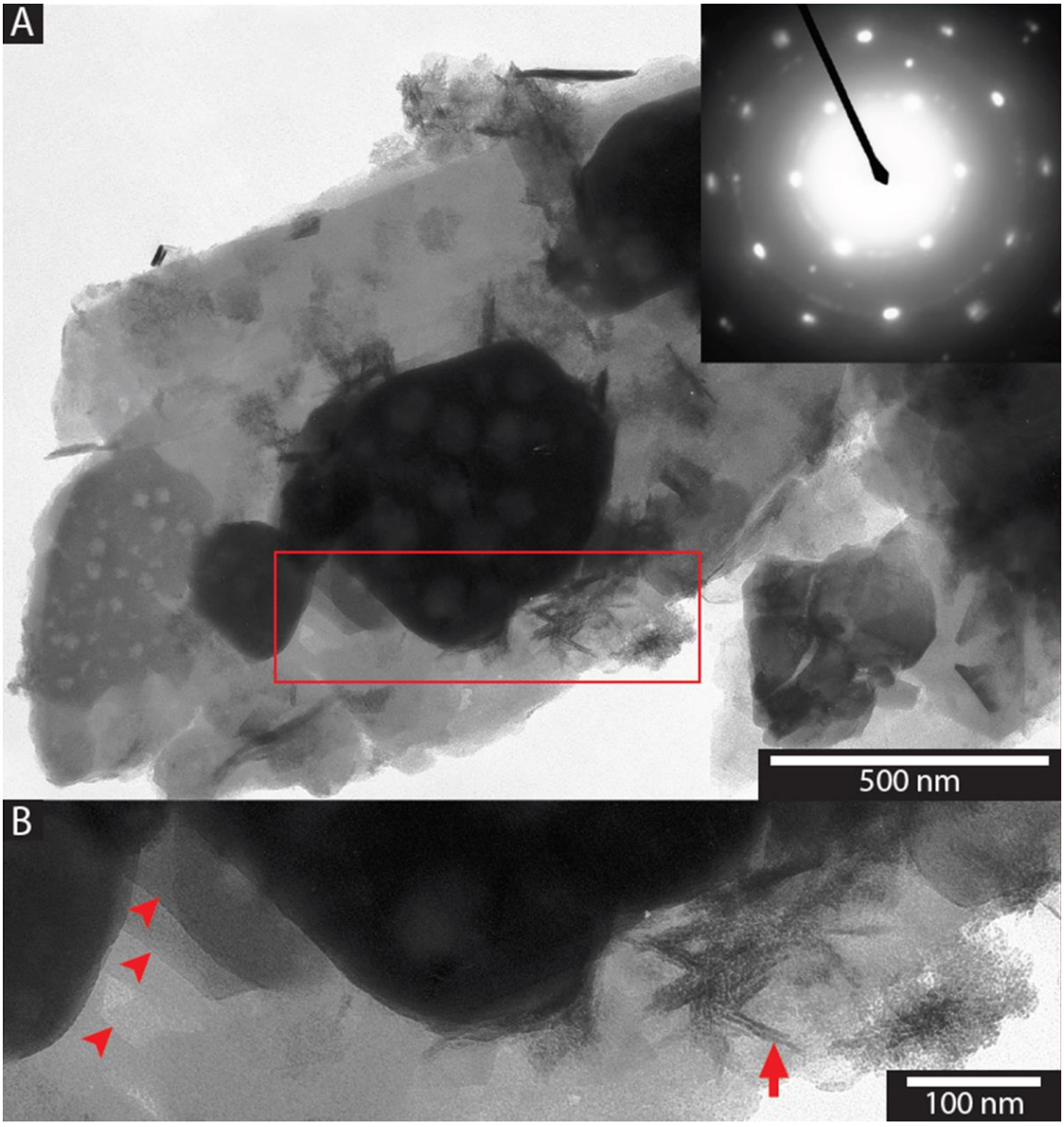

Figure 4.3. TEM photomicrograph of clay sized particles from Roadcut sample of upper Big Clifty Sandstone. Sample taken from outcrop on the Wendell H. Ford (formerly Western Kentucky) Parkway at mile marker 120.1 (see section A.8 in Appendix A for sample location, and Appendix B for sample location in the outcrop). A) Clay morphologies are psuedohexagonal platelets and lathes. Inset SAED pattern was taken from the central dark platelet and is consistent with *hk*0 diffraction patterns of kaolin. Rectangle is field of view in B. B) Multiple stacked platelets (red arrowheads) and lathes (red arrow) are visible, the presumed minerals being kaolinite, and illite, respectively.

Although the distinction between dickite and kaolinite was not made with either the XRD, or TEM, kaolinite is used for simplicity. Glauconite is also present in many, but not all, samples. Glauconite is most abundant in Core 109 and is particularly conspicuous in sample 109c2-b4 occurring along with early calcite cement and biogenic lithics (carbonate), and clay clasts. Pyrite is quite common in samples occurring as grain coats, nodules, and euhedral cement. Pyrite is most abundant and volumetrically significant in thin sections containing pyrite nodules, such as in sample 107c1-b7, or immediately proximal to them, such as in sample 105c3-b1, (see Figures 3.1K&F and Appendix B). Pyrite more commonly occurs near clay lamina and associated organics.

Carbonate cement is present in all samples with calcite being much more common than dolomite. but only making up small percentages in all but a few samples. In samples 104c1-b10 and 105c3-b2, calcite occurs in substantial amounts and is both poikilotopic and replacive. Bright, dull, and non-luminescent calcite was observed with OM-CL. Non-luminescent zones always occur near luminescent zones but have smaller areal extents than luminescent calcite. Dolomite is exclusively non-luminescent across all samples. In stained samples, ferroan calcite is indicated by appearing purple and in a few locations blue, with stained dolomite always appearing blue. Chert cement occurs in a few samples but is scarce, as is Fe-oxide (hematite) cement. Apatite cement was only observed in one sample, 105c2-b5, and was initially noticed with OM-CL. Ti-oxide cement was detected with SEM and its composition with SEM-EDS. Ti-oxide cement occurs in very minuscule amounts in the reservoir-seal portion of 104c1-b10 although the mineralogy of this cement is unknown.

Porosity is generally low in samples. Sample 107c2-b5 is unique in that it contains the greatest porosity of all the sampled cores by far at 22%, 10% higher than other samples due to vugular porosity. Unsurprisingly, 107c2-b5 is the least well cemented of the samples. Excluding 107c2-b5, mean porosity amongst samples is 7%.

4.2. Examples of Common Core Textures from Core 105

Within this study, cores 105 and 109 were the most sampled of the MegaWest split-cores. Samples from Core 105 contain more diagenetic and texturally similar features encountered in other Big Clifty samples than samples from Core 109. Consequently, Core 105 is more useful for illustrating the commonly observed diagenetic and textural features encountered in cores.

Samples 105c2-b5 and 105c2-b6 were retrieved from similar depths, 450.7 and 451.6 ft, respectively (see Table 3.1). However, hydrocarbons are still visible only in 105c2-b6 despite known occurrences within 105c2-b5 according to Loring Tarcore Labs (see Figures 3.1C&B, and see Appendix B for box-core images, and section A.1 in Appendix A for Loring Tarcore analyses relevant to this study's samples). Both samples are from a relatively clean, planar-bedded section of the upper Big Clifty. Grain contacts are predominantly long or concavo-convex with tangential contacts occurring mostly in relatively coarse or more porous areas. Quartz and kaolinite are the dominant cements with quartz preceding kaolinite which more commonly fills interstitial rather than secondary porosity (Figure 4.4). Authigenic euhedral pyrite is commonly concentrated along organic-rich clay laminae and replaces phyllosilicates and matrix (Figure 4.5). Pyrite content increases in abundance with depth in Core 105, with the greatest amount occurring in 105c3-b1 which is from a section of core containing a pyrite nodule (see

Figure 3.1F and Appendix B). Much of the pyrite in Core 105 does not appear to be syndepositional but to have precipitated after quartz cementation and some authigenic kaolinite (Figure 4.6). Trace amounts of early Fe-oxide cement occur as dust rims on quartz grains preceding quartz cementation (Figure 4.7). Potassium feldspar appears to be slightly more stable than plagioclase, although grains of both commonly exhibit signs of alteration, such as authigenic clays and development of secondary porosity which commonly is preferentially along twins (Figure 4.8). Typically feldspars with replacive textures have either been partially altered to clays prior to replacement by pyrite or calcite, or exhibit no earlier weathering prior to replacement by calcite. Sample 105c3-b1 is the least porous of Core 105's samples. Porosity destruction from cementation is mainly due to pyrite and not authigenic clays or calcite.

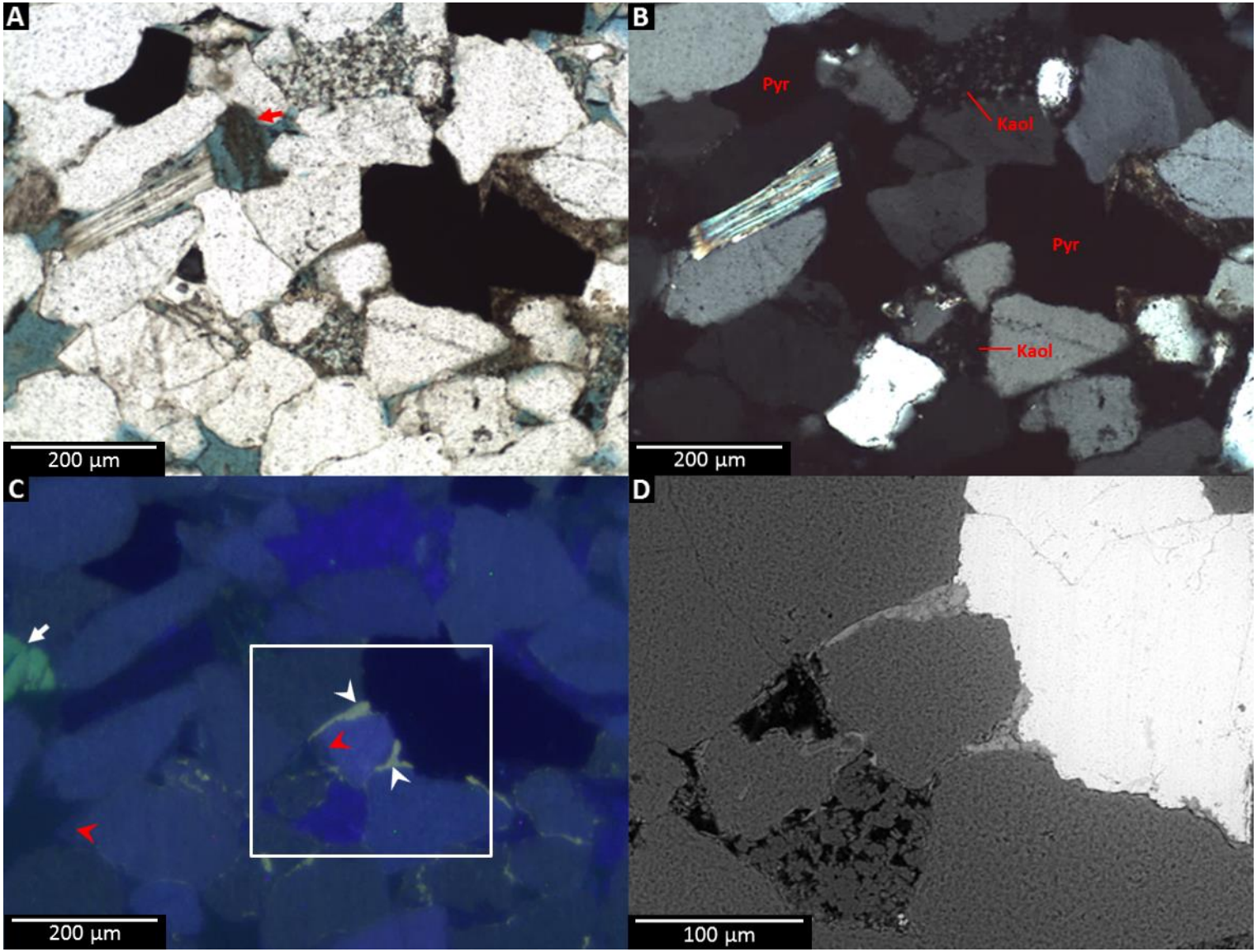
A
200 µm
B
Pyr
Kaol
Pyr
Kaol
200 µm
C
200 µm
D
100 µm

Figure 4.4 (from previous page). Common quartz, kaolinite, and pyrite cement and rare apatite cement from sample 105c2-b5. Field of view and scale is the same for photomicrographs A, B, and C; D is the area inside the white rectangle defined in C. A) Porosity (blue) is visible between grains and within in ghost grains (red arrow), PPL image. Organics bound to clays appear brown. B) Authigenic kaolinite (Kaol) and pyrite (Pyr) contributes to primary porosity loss, XPL image. C) Detrital quartz grains are distinguishable from overgrowths by luminescence, CL image. Most detrital quartz grains are weakly-luminescent appearing blueish gray while overgrowths (red arrowheads) do not luminesce and appear gray. Apatite cement (white arrows) is luminescent and appears as a similar green to weathered feldspar (white arrow). D) Apatite appears a slightly lighter gray than the quartz of the grains it cements in SEM-BSI. Porosity (black) both intercrystalline (microporosity) and interparticle, is visible within the kaolinite cement (dark gray) and between quartz grains, but completely absent where pyrite (white) cements.

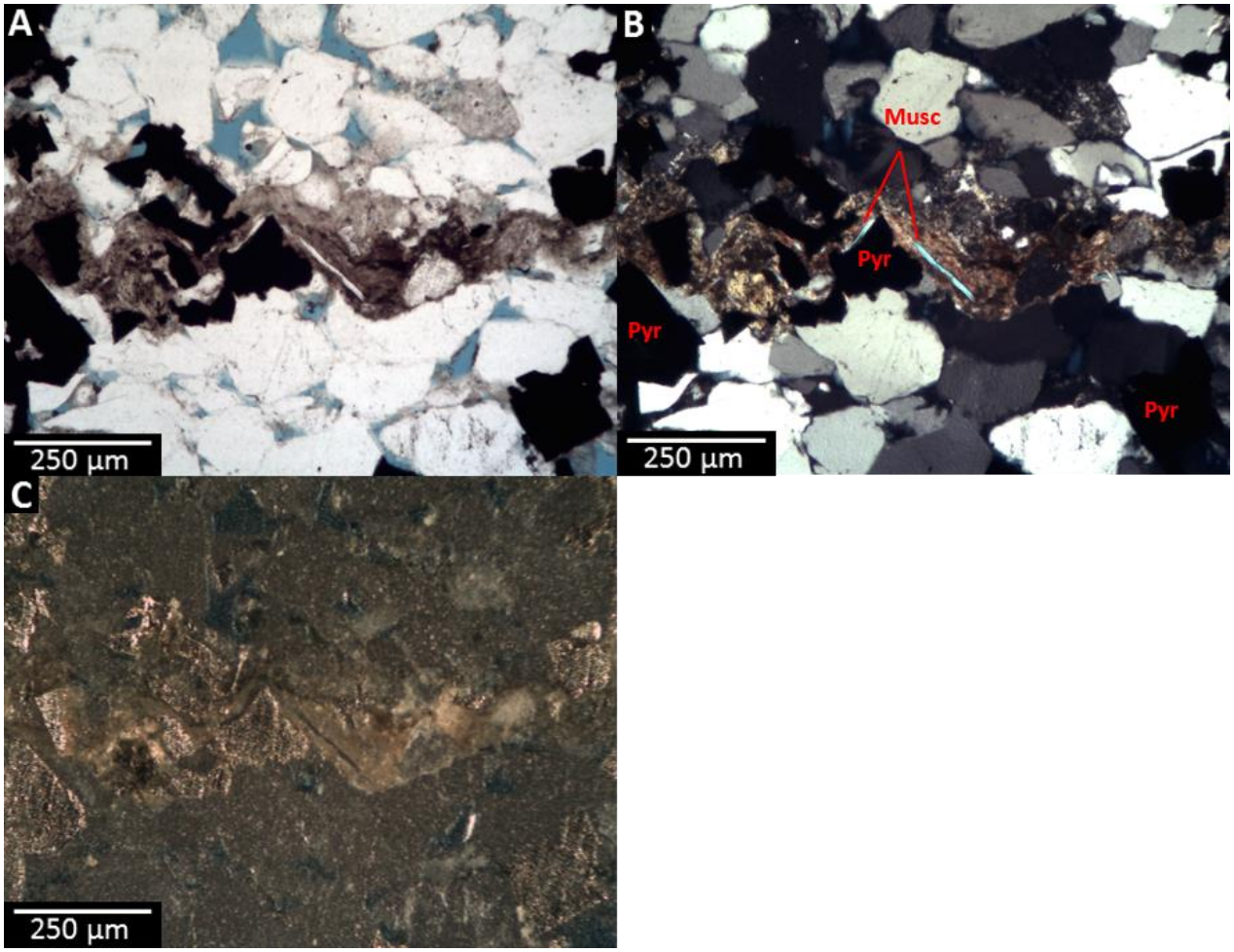

Figure 4.5. Euhedral authigenic pyrite and associated clay in laminae of sample 105c2-b5. Field of view and scale is the same in all photomicrographs. Sampled core interval had no apparent oil saturation. A) Along clay drapes compaction is greatest and porosity (blue) is reduced, PPL image. B) Laminae are discernable from organic rich phyllosilicate matrix (Pyr = pyrite; Musc = muscovite), XPL image. C) Euhedral pyrite (gold color) fills porosity and replaces phyllosilicates, RFL image.

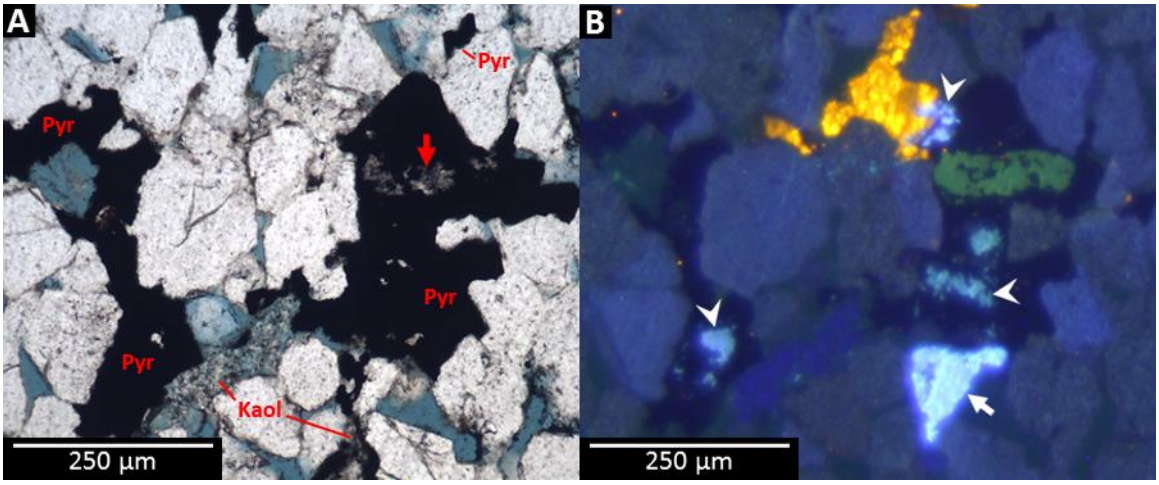

Figure 4.6. Pyrite cement and partial replacement of grain in sample 105c3-b1. Field of view and scale is the same in both photomicrographs. A) Pyrite (opaque) cement replacing labile framework grain (red arrow), PPL image. Pyrite does not replace authigenic kaolinite (Pyr = pyrite; Kaol = kaolinite). B) Partially replaced feldspars (white arrowheads) and labile grain luminesce through replacive pyrite and calcite cement, CL image. Feldspars appear light blue with replaced feldspars luminescing less intensely than the unaltered feldspar (white arrow). The unknown labile grain that appears green is likely weathered feldspar. Calcite cement is brightly-luminescent and appears yellowish orange. Non-poikilotopic calcite generally only replaces feldspar framework grains. Yellowish orange points of luminescence are potentially remnant calcite although these 'pin-pricks' are too few and small to interpret texture.

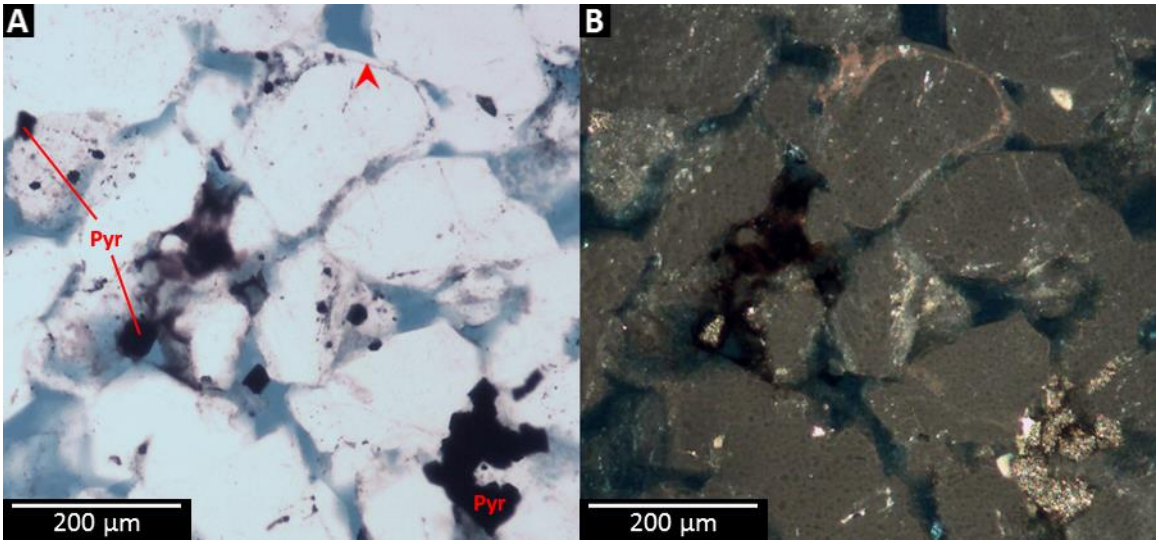

Figure 4.7. Fe-oxide dust rim and pyrite in sample 105c3-b1. Field of view and scale are the same in both photomicrographs. Fe-oxide dust rim (red arrowhead) and pyrite (Pyr = pyrite) appears opaque in plane light, PPL. B) Fe-oxide appears pinkish red between quartz grain and quartz overgrowth, RFL image.

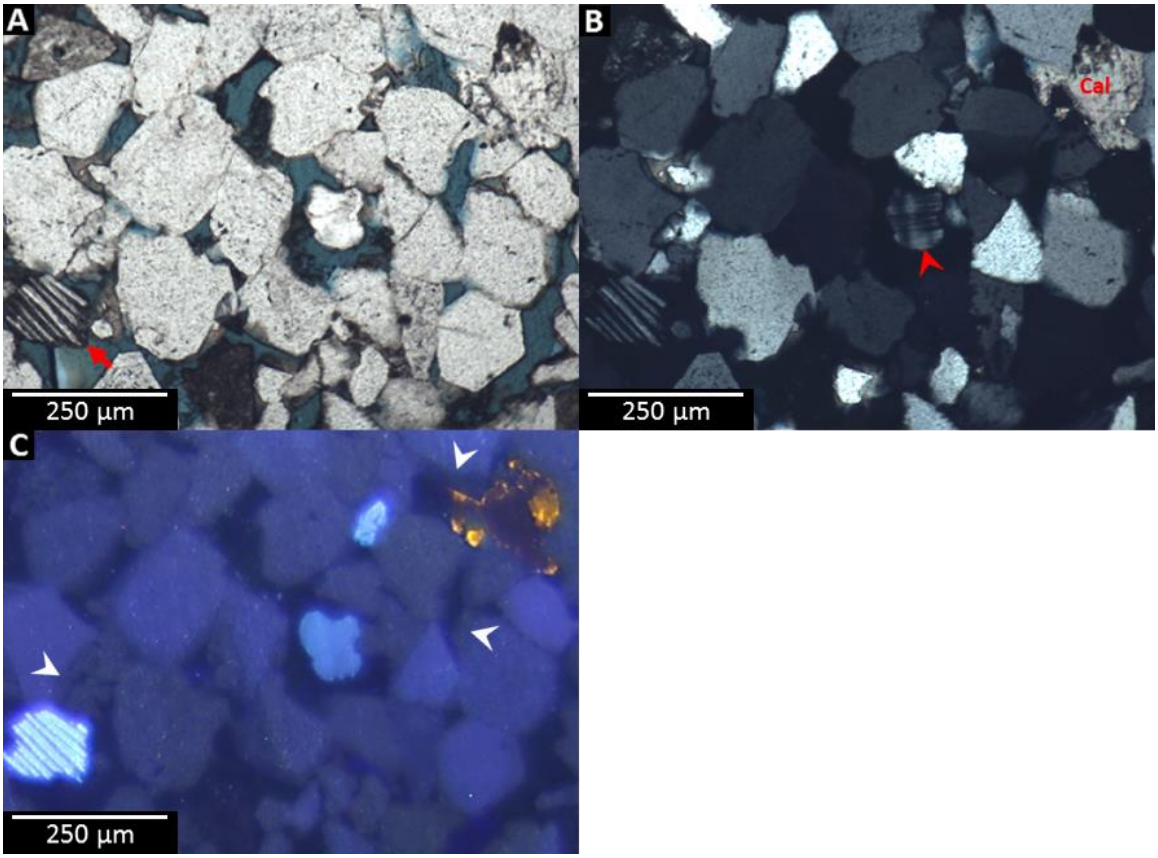

Figure 4.8. Potassium and plagioclase feldspars in sample 105c2-b6. Field of view and scale is the same in all photomicrographs. A) Plagioclase is conspicuous due to preferential alteration (red arrow) along twinning, PPL image. Calcite (Cal = calcite) is not replacive. B) Tartan twinning of microcline (red arrowhead) unaffected by diagenesis. C) Plagioclase grain is more luminescent than microcline, CL image. Calcite is predominantly dully-luminescent (orange and dark brown) and succeeds quartz overgrowths (white arrowheads).

Carbonate is scarce in all but 105c3-b2 of Core 105 samples with both dully- and brightly-luminescent calcite occurring (Figures 4.6 and 4.8). Certainly most, if not all, of the calcite cement observed in Core 105 precipitated after quartz overgrowths and pyrite. Earlier phases of calcite may have been present at one time in samples 105c2-b5 and 105c3-b1 where points of yellowish orange luminescence are observed, albeit only with OM-CL (Figure 4.6). The deepest sampled section of Core 105, sample 105c3-b2 at 470.8-ft depth, is also the most calcareous with greater abundances of calcite cement than

other Core 105 samples. Poikilotopic calcite in 105c3-b2 is more replacive than non-poikilotopic patches of calcite in other Core 105 samples, replacing labile grains as well as embaying and also replacing stable quartz grains and quartz and chert cement (Figure 4.9). Poikilotopic calcite in 105c3-b2 also exhibits both bright and dull luminescence with both types occurring, and in some places contiguous with one another (Figures 4.10 and 4.11). Brightly-luminescent calcite appears to be slightly more replacive than the dully-luminescent calcite. There are no mineral distributions or apparent textural features associated with brightly- and dully-luminescent zones to indicate separate generations between the two luminescent varieties of poikilotopic calcite of sample 105c3-b2.

Despite sedimentary structures being visible in many reservoir sections of core, stratification is difficult to see in thin sections containing very little detrital matrix such as those from Core 105. Sample 105c2-b9 is slightly graded and is moderately sorted. Grading is subtle in thin section where change in grain size is subtle and laminations or bedding are not clearly demarked by microstylolites, or increased mud content with authigenic pyrite. Sample 105c2-b9 also contains greater clay content than the sampled cores above it but is otherwise very similar to 105c2-b7 which is similar to 105c2-b6. Microstylolites and other textural features relating to diagenesis and deposition are present in Core 105 but such features, and those not observed in Core 105, are best exemplified in other samples.

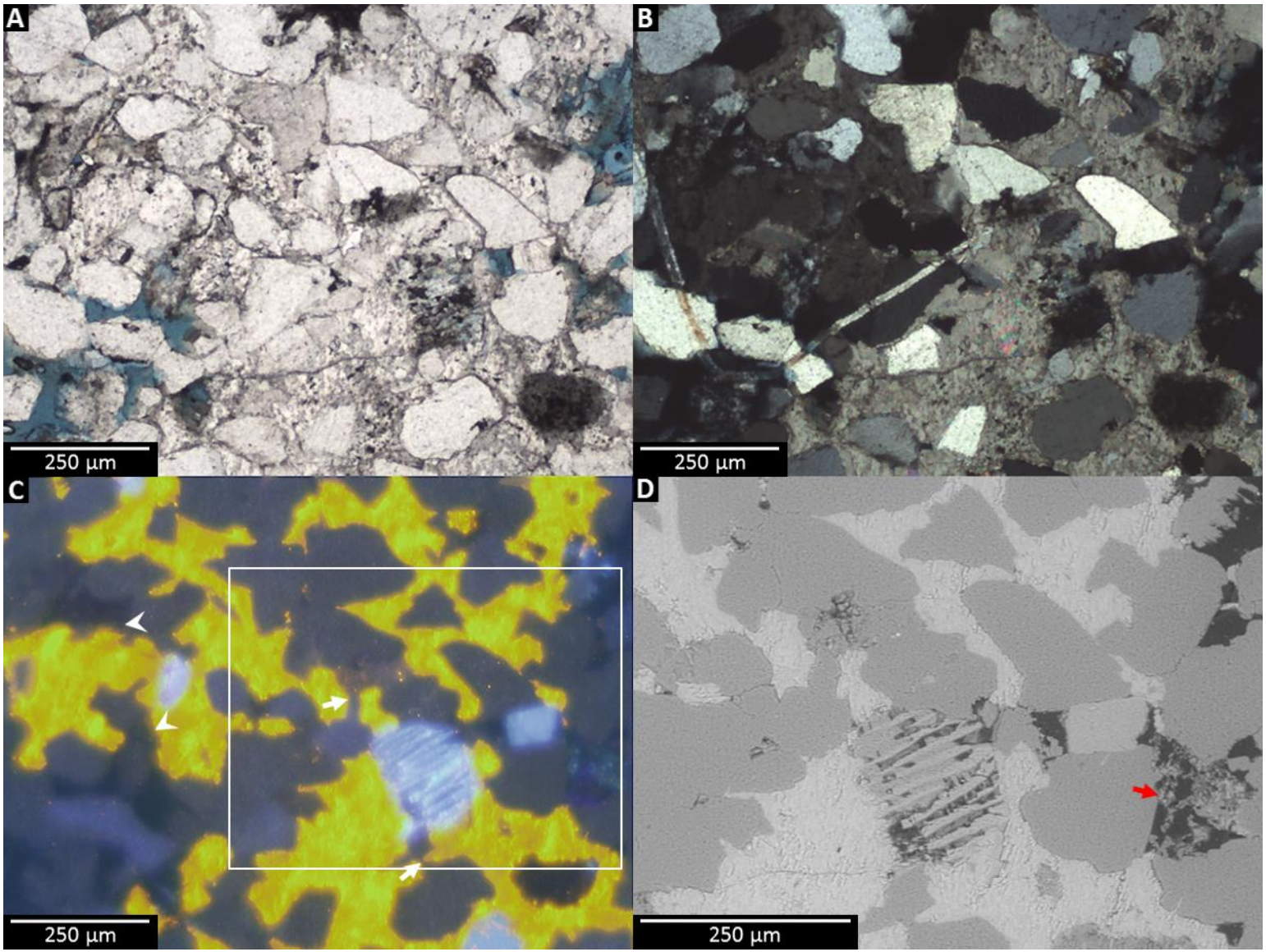
A
250 µm
B
250 µm
C
250 µm
D
250 µm

Figure 4.9 (from previous page). Replacive calcite cement in sample 105c3-b2. Scale bar and field of view is the same for photomicrographs A, B, and C; D is the area inside the white rectangle of C. A) Calcite occludes intergranular and secondary porosity (blue) in feldspar, PPL image. B) Remnants of earlier cements and fragments of partially replaced grains appear suspended in poikilotopic calcite cement, XPL image. Framework grains are predominantly monocrystalline quartz with a few feldspars displaying variable stages of weathering. C) Calcite is brightly-luminescent and appears yellow, CL image. Replacive calcite has embayed earlier cements and framework grains including chert (white arrowheads) creating several isthmus-like contacts between framework grains (white arrows). Feldspars and the preferential weathering along crystal twins is conspicuous under CL where feldspars commonly appear bright light-blue. D) Authigenic clay of ghost grain (red arrow) is visible as fine textures in a pore (black), SEM-BSI. Silica appears dark gray whereas light gray represents calcite and feldspar, calcite is slightly lighter.

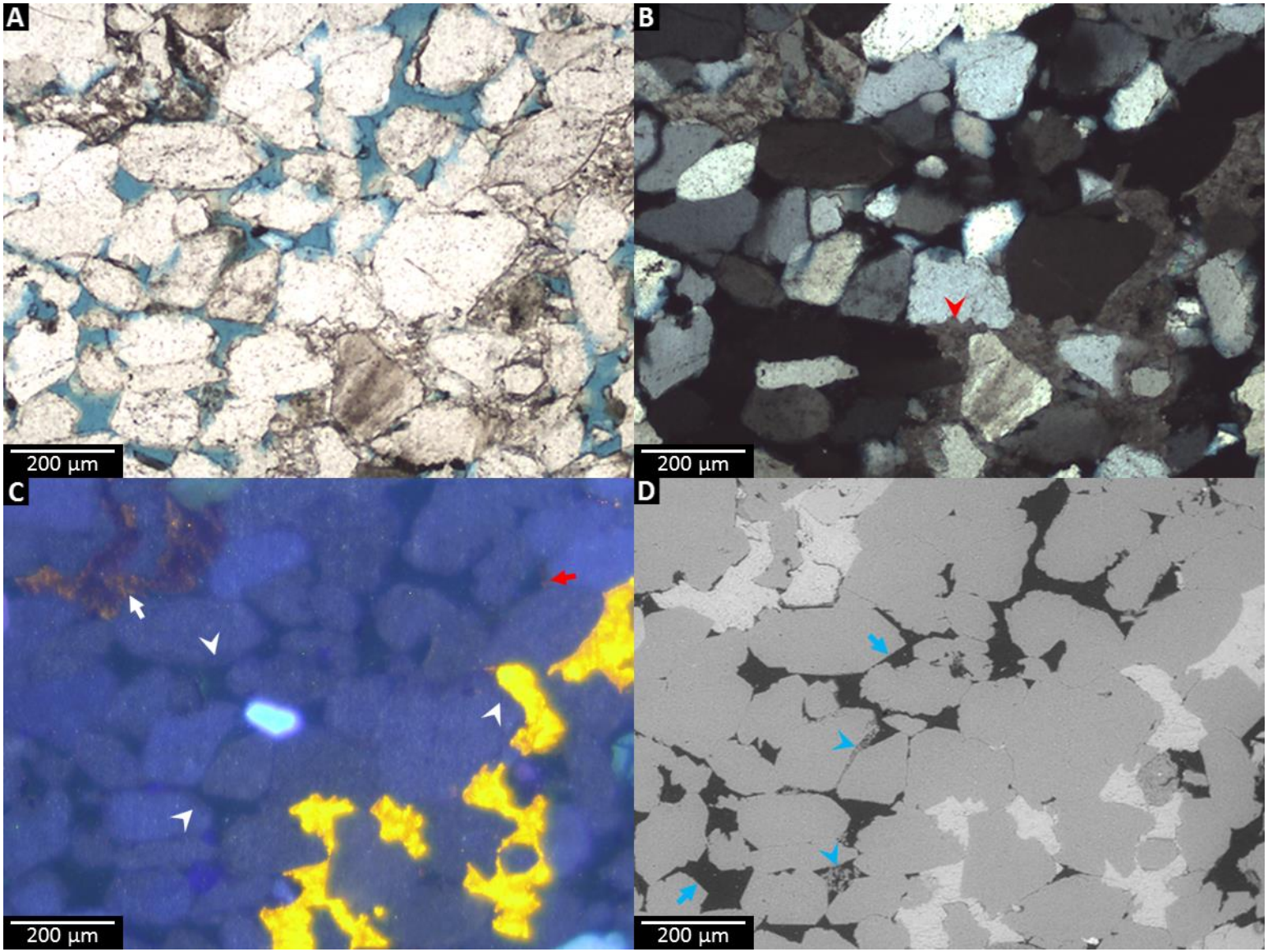
A
200 µm
B
200 µm
C
200 µm
D
200 µm

Figure 4.10 (from previous page). Non-contiguous, luminescent and dully-luminescent, poikilotopic calcite cement from sample 105c3-b2. Scale bar and field of view is the same for all photomicrographs. A) Porosity (blue) is the second most abundant of all cores sampled where calcite is absent, PPL image. B) Poikilotopic calcite minimally embays framework grains (red arrowhead), XPL image. C) Both luminescent and quenched (white and red arrows) calcite occurs in the sample post quartz overgrowths (white arrowheads), CL image. Minute dog-tooth crystals of quenched calcite (red arrow) are potentially contiguous with nearby luminescent calcite. Difference in calcite luminescence is potentially due to limitations on solute transport to crystal growth interface or changes in bulk-fluid chemistry affecting activator and quencher ion activities. D) Euhedral terminations of overgrowths on quartz grains (blue arrows) bordering pores are easily distinguishable in SEM-BSI. Authigenic clay coatings and cement (blue arrowheads) within pores is likely penecontemporaneous or soon following siliceous cementation as it occurs on both detrital grain and overgrowths based on the contrast in C.

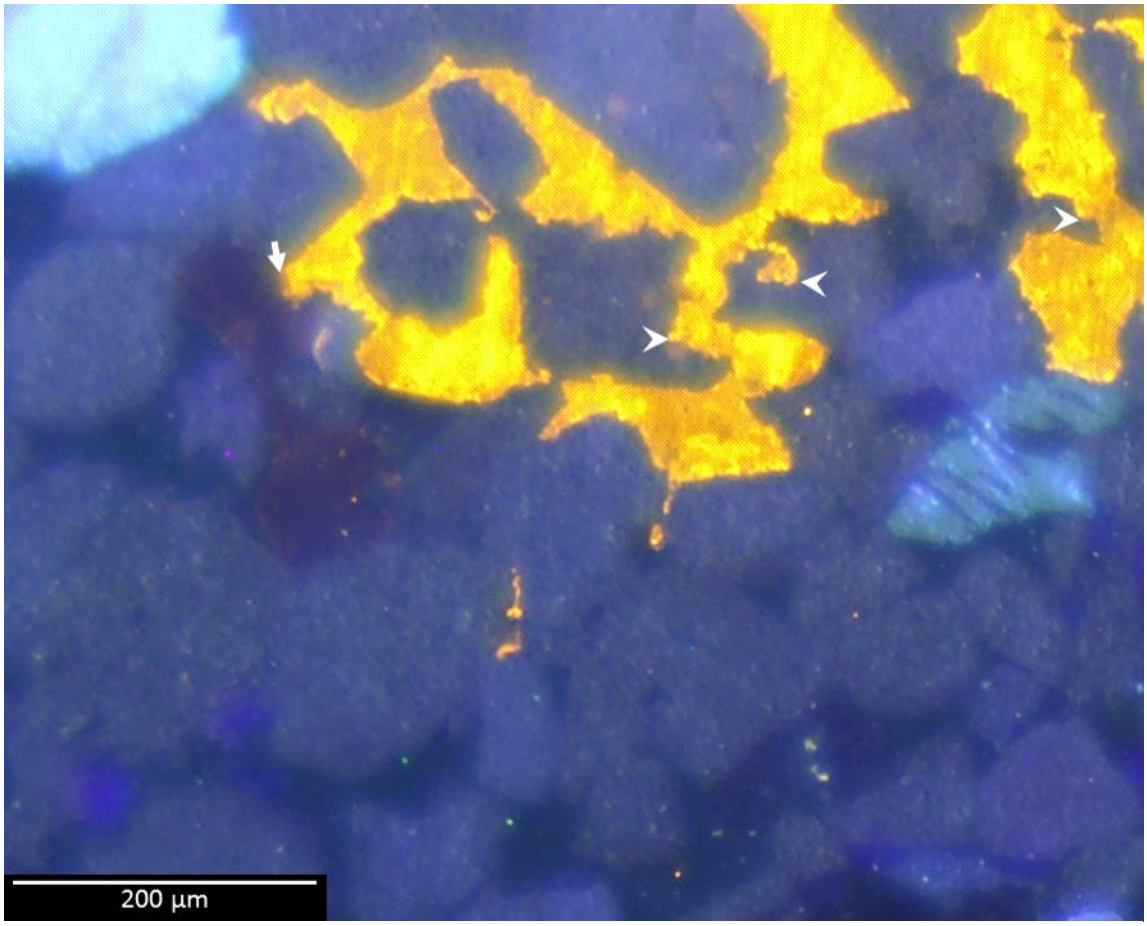

Figure 4.11. Poikilotopic calcite cement of dull and bright luminescence from sample 105c3-b2. Brightly-luminescent calcite appears yellowish orange which abruptly transitions (white arrow) to dully-luminescent calcite that appears dark brown. Brightly-luminescent poikilotopic calcite is more common and slightly more replacive of framework grains and cements (white arrowheads) than dully-luminescent calcite.

4.3. Select Pertinent Textures from Other Cores

4.3.1 Clays

Glauconite is observed primarily as an early cement alongside pyrite (Figure 4.12) although it also composes framework grains in samples. In sample 109c2-b4, glauconite occurs proximal to calcite, which may be the only occurrence of early calcite precipitation observed in all sampled cores. Glauconite is more abundant in samples with obvious marine influence, such as samples with biogenic grains. Kaolinite is a common alteration product of feldspar weathering and is most noticeable as occurring after quartz overgrowths. Authigenic kaolinite, however, is likely to have occurred throughout burial, except where immiscible oil or authigenic calcite restricts solute transport of aqueous phases (Figure 4.13). Authigenic kaolinite can also form as an alteration product from the weathering of labile minerals other than feldspars such as muscovite (Figure 4.14). Illitization of clays, both authigenic and detrital, is to be expected in Paleozoic sediments containing no volcanics and few labile minerals (Figure 4.15).

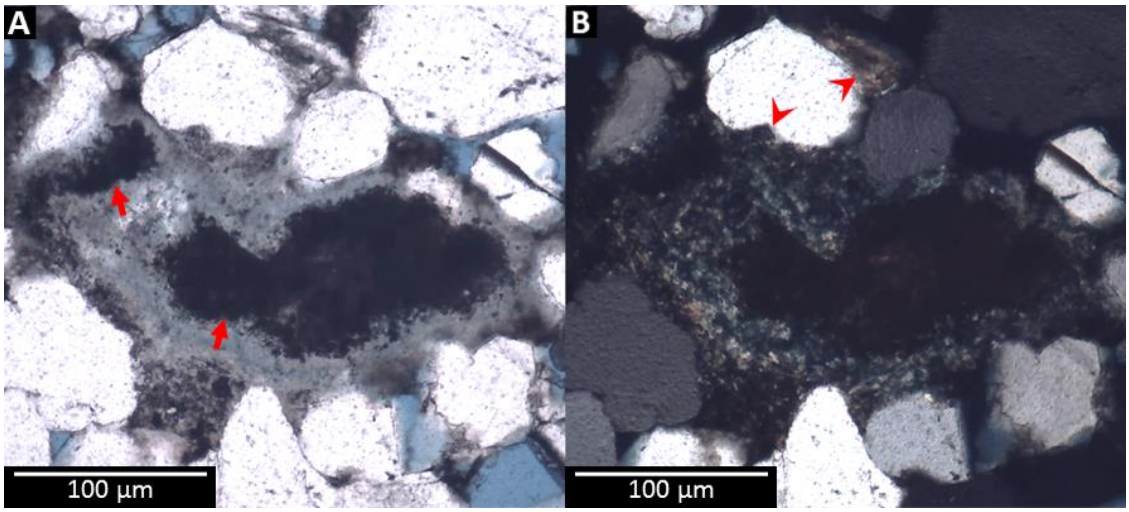

Figure 4.12. Glauconite in sample 109c2-b4. Scale bar and field of view is the same for both photomicrographs. A) Glauconite (green) is commonly associated with organic material (red arrows), PPL image. B) Glauconite appears similarly green in cross-polarized light as it does in plane light (A), XPL image. Early calcite cement (red arrowheads) is only observed in sample 109c2-b4.

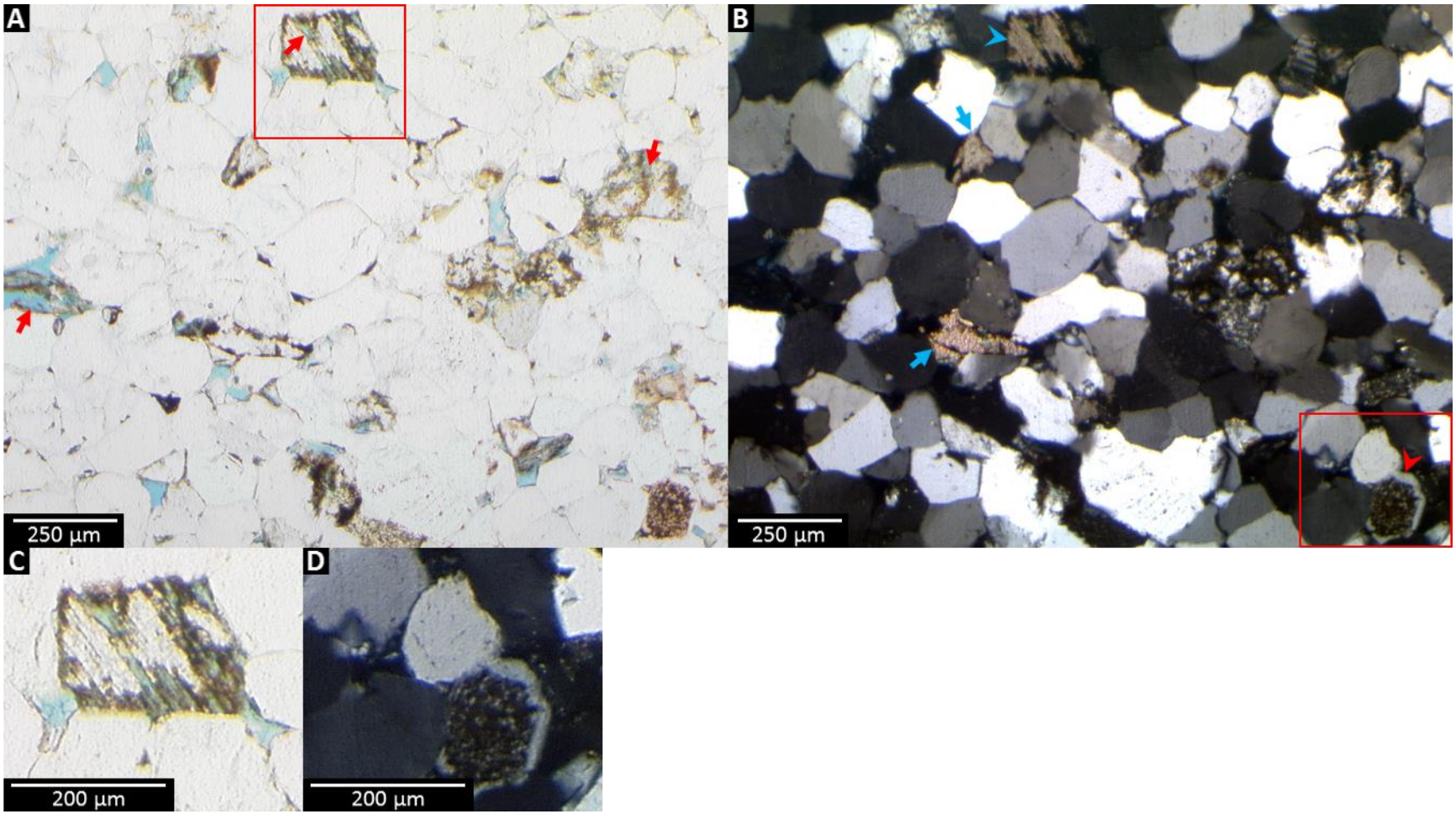
A
250 µm
B
250 µm
C
200 µm
D
200 µm

Figure 4.13 (from previous page). Feldspar alteration during different stages of diagenesis within the reservoir of sample 104c1-b10. Scale bar and field of view is the same in photomicrographs A and B; C and D are the areas inside the red squares of A and B respectively. A) Much of the porosity (blue) in the reservoir of sample 104c1-b10 is secondary porosity (red arrows), PPL image. B) Syntaxial quartz overgrowths are distinguishable from epitaxial quartz overgrowths on a weathered grain (red arrowhead), XPL image. The former grain was likely once a feldspar but has been altered to kaolinite and stained brown due to oil within micropores. Calcite is present in the reservoir prior to poikilotopic calcite as intergranular cement (blue arrow), as well as replacive cement (blue arrowhead) indicated by the intragranular porosity and ghost twinning. C) Incomplete replacement of framework grain by pre-poikilotopic burial calcite is possibly due to oil adsorption to the alteration products of the former labile grain, poisoning the crystal growth interface in calcite, PPL image. D) Incomplete coverage of epitaxial quartz overgrowths failed to prevent subsequent alteration of labile grain and infiltration of oil into micropores following oil emplacement, XPL image.

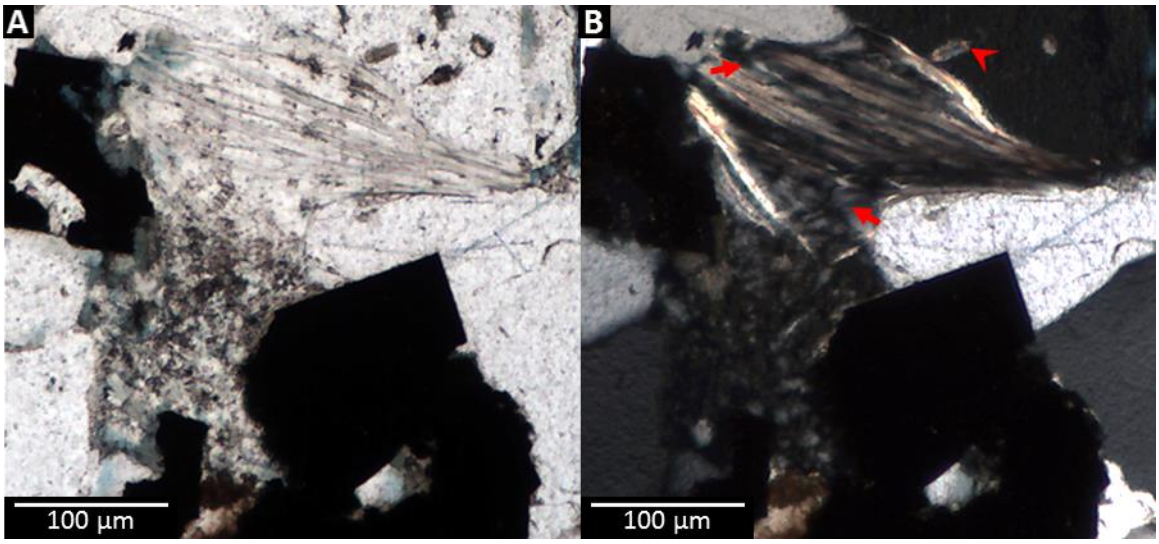

Figure 4.14. Displacement of muscovite by kaolinite in sample 105c2-b5. Scale bar and field of view is the same in both photomicrographs. A) Interparticle porosity is filled by euhedral pyrite (opaque) and authigenic kaolinite (cloudy) cement, PPL image. B) Low first-order interference colors (gray) of kaolinite are visible between mica layers (red arrows), XPL image. Zircon (red arrowhead) inclusions within quartz grains are not uncommon. Apparent length of zircon is approximately ~20 µm.

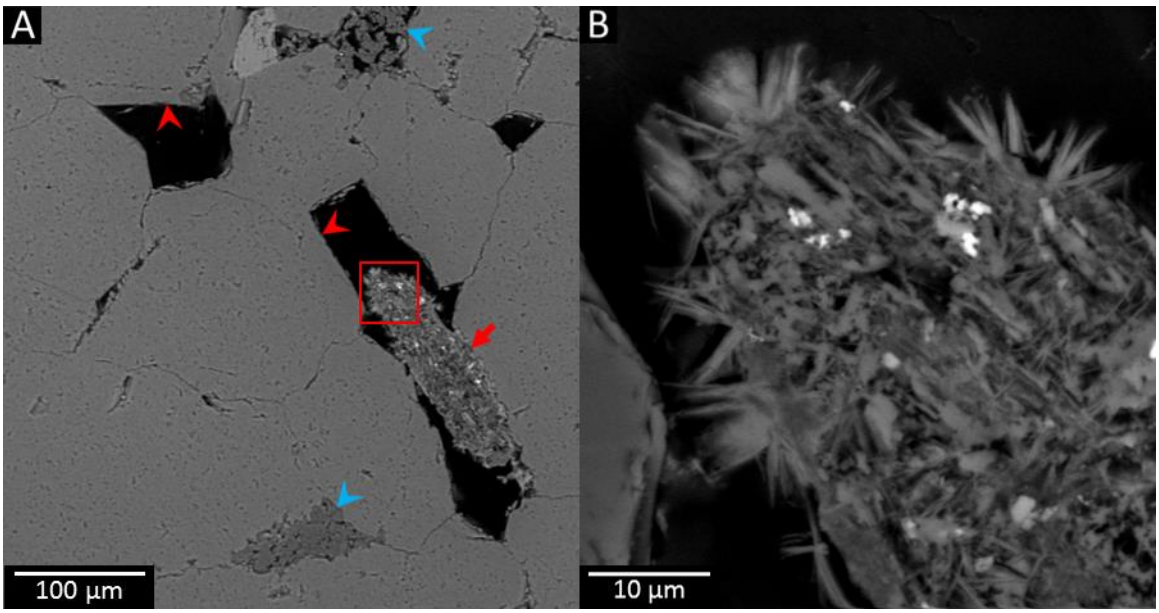

Figure 4.15. Authigenic cements in reservoir of sample 104Bc1-b10, SEM-BSI. Scale bar is different in both photomicrographs, Red square in A indicates the field of view in B. A) Quartz overgrowths (red arrowheads) are dominant cement although intraparticle kaolinite (dark gray) (blue arrowheads) exists. Terminations of quartz overgrowths are smooth where not in contact with clay clast (red arrow). B) Fibrous illite within and coating clay clast is an alteration product of existing detrital and diagenetic phyllosilicates.

4.3.2. Pyrite

Pyrite nodules are unique but not uncommon to reservoir sections of core. Nodule diameters range from 400 μm to several centimeters in size. Nodular pyrite in hand sample appears as blobs, but in thin section euhedral crystal edges are visible (Figure 4.16). Fine microcrystalline pyrite coats framework grains in the reservoir seal of 104c1-b10 (Figure 4.17). This pyrite upon cursory inspection is not associated with mud laminae or detrital clays, and provides some minimal protection from replacive calcite.

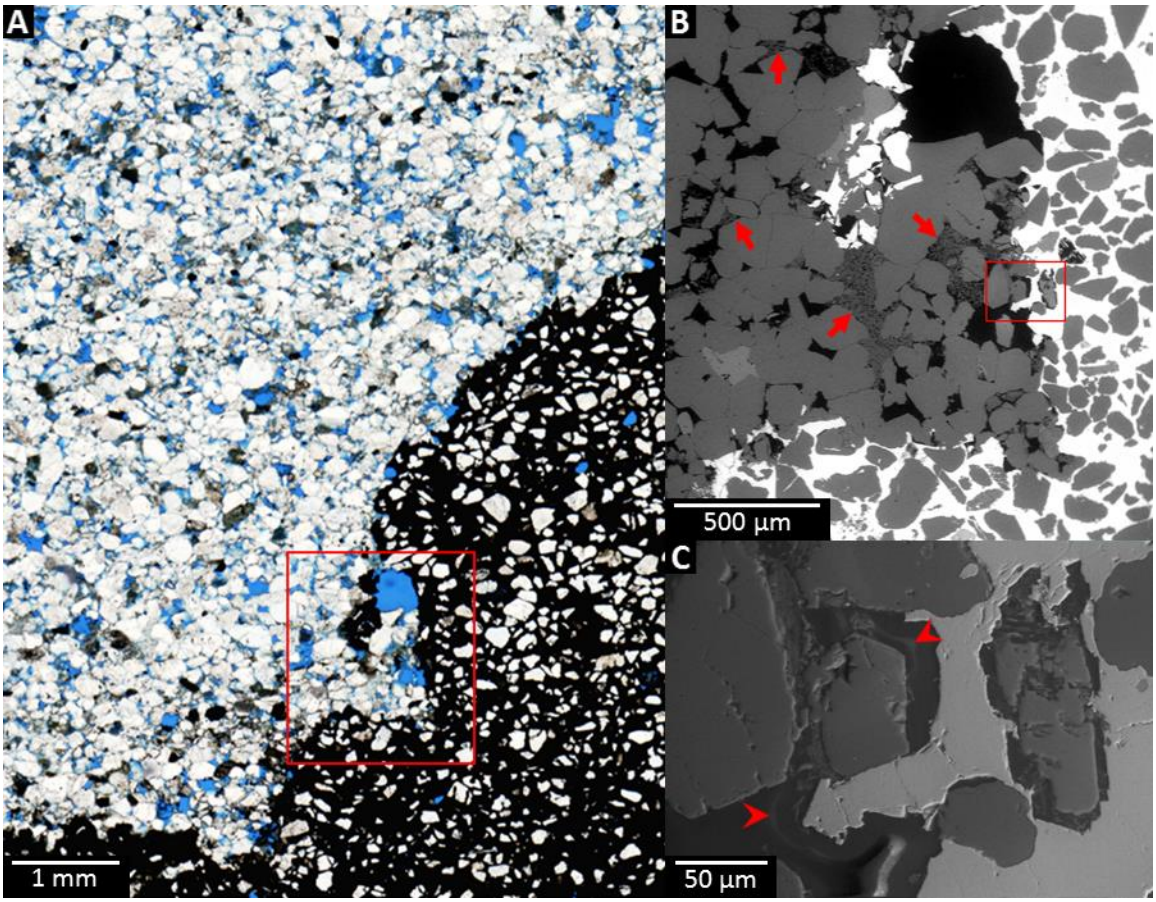

Figure 4.16. Pyrite nodule in sample 107Bc1-b7. Field of view is different for each photomicrograph, B and C are the area inside the red rectangles of A, and B, respectively. A) Authigenic pyrite engulfing many grains irrespective of lamination or sorting in general, PPL scanned image. B) Pyrite (white) and kaolinite (red arrows) cements are clearly visible, SEM-BSI. C) Displacement of oil (red arrowheads) by pyrite is visible with electron charge build-up upon the specimen due to the resistivity of the hydro-carbons, SEM-BSI (with topo inverted shadow max settings).

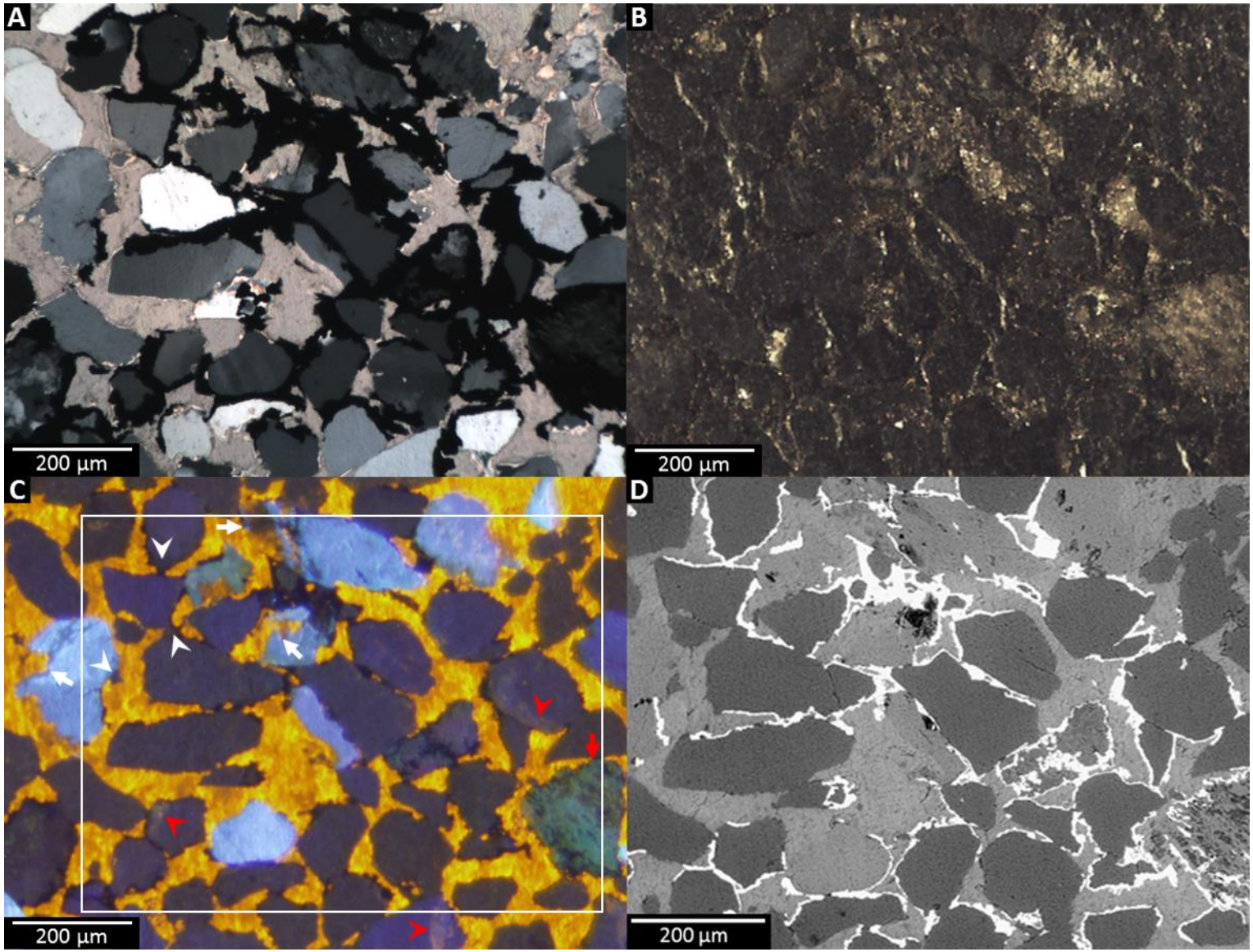
A
200 µm
B
200 µm
C
200 µm
D
200 µm

Figure 4.17 (from previous page). Calcite and pyrite cement in reservoir seal of sample 104c1-b10. Scale bar and field of view is the same for photomicrographs A, B, and C; D is the area inside the white rectangle of C. A) Poikilotopic calcite replacing grains not protected by a microcrystalline pyrite (opaque) cement coating, XPL image. Framework grains are predominantly quartz with a few feldspars. B) Pyrite cement is visible coating framework grains, RFL image. C) Grain embayment especially of feldspars (white arrows) is conspicuous under CL whereas pyrite cement on weathered feldspar is less discernable (red arrow), CL image. Remnant quartz overgrowths exist in a few locations (white arrowheads). Yellow-tinge areas (red arrowheads), are opaque in XPL.
D) Framework grains and cement contacts, particularly those with pyrite (white) are clearly identifiable in SEM-BSI. Secondary porosity (black) occurs within weathered feldspars and those being replaced. Quartz is dark gray with calcite and feldspar being a light gray with calcite being slightly lighter.

The areal extent of pyrite and other opaques observable under cathodo-luminescence is diminished compared with the opaque area observed under transmitted light (Figure 4.17). Pyrite itself is non-luminescent due to its conductive properties; however, the grains and cements below and around these coatings are visible, but, variably luminescent through these grain coatings (Figure 4.17C). The pyrite, confirmed by Raman microscopy, within the opaque coatings, is microcrystalline. Pyrite and the undifferentiated opaques contain gaps, are of insufficient thickness to absorb all emitted photons from minerals beneath, or eclipse those emitted from neighboring luminescent minerals particularly calcite. Additionally, reflected luminescence of nearby bright calcite, from the surface of opaques and pyrite coatings gives the luminescent minerals below a yellow-tinge color (Figure 4.17B&C). Neither CL through, nor reflectance of CL upon pyrite and opaque coatings occur where pyrite cement is more massive (nodular) and nearby intensely luminescent minerals are absent. The true areal extent of pyrite is more accurately assessed with SEM-BSI where high electron density from Fe and S appears light in contrast (Figure 4.17D).

4.3.3 Mesogenetic Carbonate

Calcite comprises much of the carbonate cements that precipitated during burial after quartz overgrowths, much of which is not considered to be either early (Figure 4.12), or poikilotopic (Figure 4.17). Dolomite cement, while uncommon, is present in several sampled cores. All dolomite encountered is non-luminescent under OM-CL although some locations had bright or weakly luminescent calcite nearby (Figure 4.18). In all stained thin sections, compositions of dolomite and calcite cement are ferroan as indicated by blue and purple precipitates respectively. Stained calcite consistently

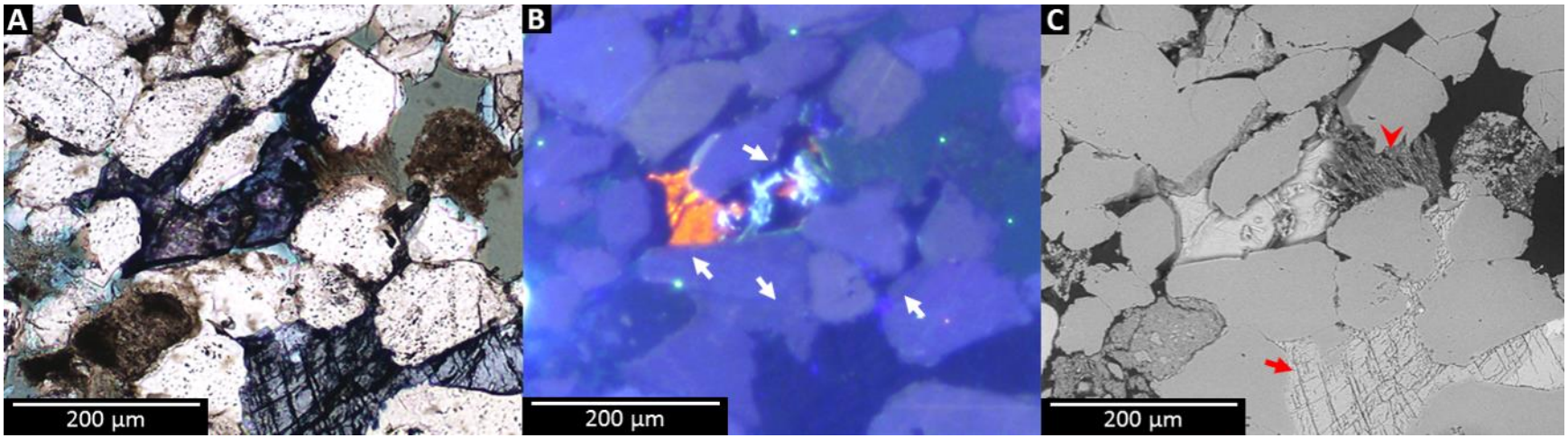

Figure 4.18. Mesogenetic ferroan calcite and baroque dolomite in sample 107c2-b5. Scale bar and field of view is the same in all photomicrographs. A) Ferroan content indicated by purple and dark-blue stain of calcite and dolomite respectively, PPL image. B) Partially replaced feldspar luminesces light-blue and is visible within luminescent ferroan calcite that appears orange in color, CL image. Dolomite however is non-luminescent. Quartz overgrowths (white arrows) precede ferroan carbonate. C) Acid etching reveals baroque nature of dolomite with curved cleavage planes (red arrow), SEM-BSI. Nearly total dissolution of feldspar is evident (red arrowhead).

appears purple, and dolomite blue with the exception of one patch that appears blue but was identified by Raman microscopy as calcite. Dolomite does not appear to be replacive, i.e. not encroaching quartz grains and overgrowths; and crystals appear clear in PPL, lacking inclusions of other minerals or indications of dissolution (Figure 4.19).

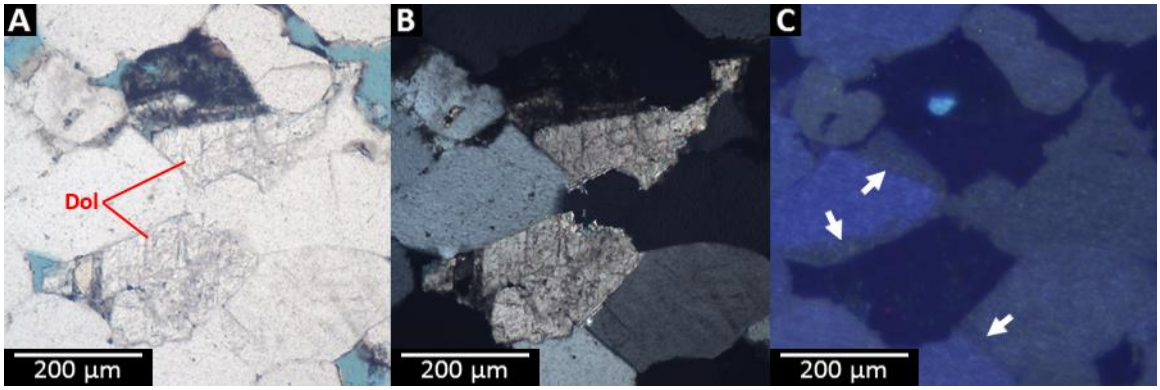

Figure 4.19. Non-replacive dolomite in sample 109c1-b5. Scale bar and field of view is the same in all photomicrographs. A) Unstained dolomite appears relatively clear with no visible inclusions (Dol = dolomite), PPL image. Brown areas in pores due to over exposure of epoxy to electron beam. B) Dolomite exhibits neither curved cleavage planes nor undulose extinction that typifies, but is not diagnostic of saddle dolomite, XPL image. C) Dolomite is non-luminescent, CL image. Quartz overgrowths are well formed (white arrows) and precede dolomite cement which precedes feldspar dissolution.

Hydrocarbon residuum, oil staining, and inclusions of partially replaced grains and cement can make recognition of calcite challenging with standard optical microscopy. This is particularly the case if the areal extent of the cement is limited (Figures 4.12 and 4.13) or has undergone major dissolution. In the latter case, OM-CL is the most useful means of detection, although only if the calcite is luminescent (Figure 4.20). Burial calcite is predominantly brightly-luminescent across all sampled cores with nearly all occurrences of such calcite exhibiting luminescence to some degree if only weakly or only from certain zones (Figures 4.21 and 4.22). Luminescence is observed in calcite from stained portions of thin sections (Figure 4.23).

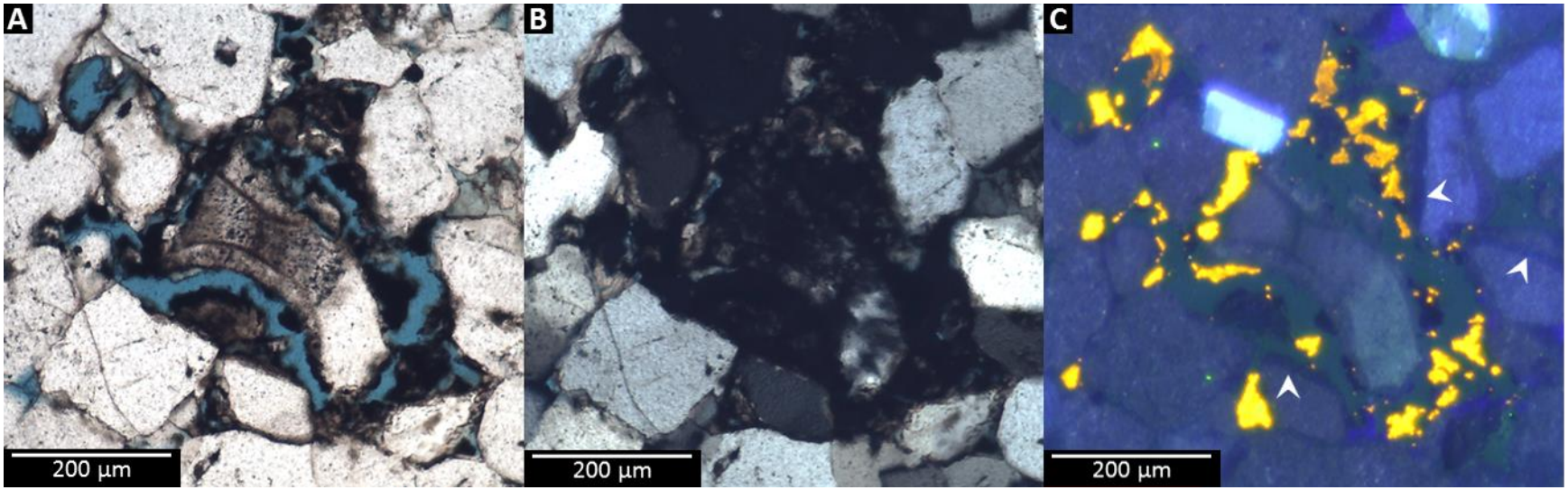

Figure 4.20. Major dissolution of burial calcite cement in sample 109c2-b4. Scale bar and field of view is the same in all photomicrographs. A) Biogenic grain (center) is poorly cemented, PPL image. Bitumen appears opaque in pores and oil stains grains and clay a brown color. B) Biogenic grain is likely allochthonous as chalcedony replacement is not observed elsewhere in thin section or those from other cores, XPL image. C) Remnant calcite is brightly-luminescent and appears yellow, CL image. Dissolution of earlier calcite cement has restored some primary porosity. Quartz overgrows (white arrowheads) precede calcite cement.

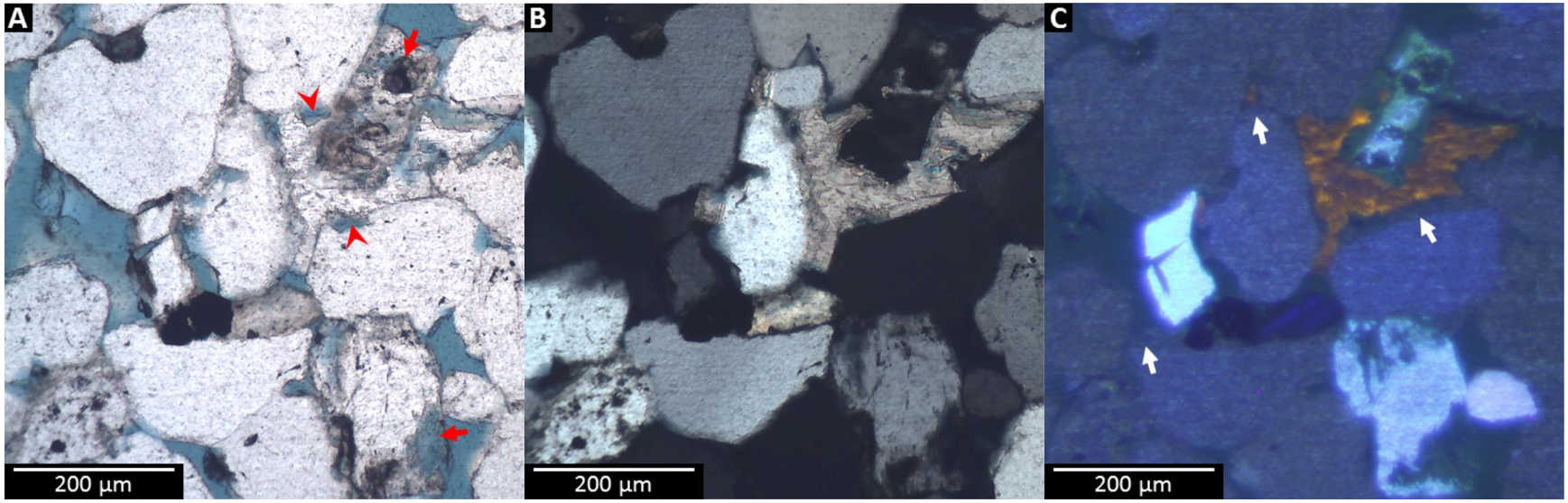

Figure 4.21. Minor dissolution of burial calcite cement in sample 109c1-b5. Scale bar and field of view is the same in all photomicrographs. A) Secondary porosity develops within non-quartz grains (red arrows) and cements (red arrowheads), including replacive calcite, PPL image. Minimal pyrite (opaque) cement is concentrated near clay clast. B) Calcite slightly replaces and embays weathered feldspar (upper right) but has not embayed or replaced quartz grains and cement, XPL image. C) Luminescent feldspar (upper right) is visible within dully-luminescent calcite cement, CL image. Feldspars generally luminesce light blue and their alteration products, dark green. The degree of feldspar alteration can sometimes be visually judged from CL with decreasing intensity and an apparent shift in color from bright light-blue luminescence to weak dark-green luminescence with progressive weathering. Luminescent calcite appears dark orange to brown in color. Quartz overgrowths (white arrows) are more apparent on grains with contrasting luminescence.

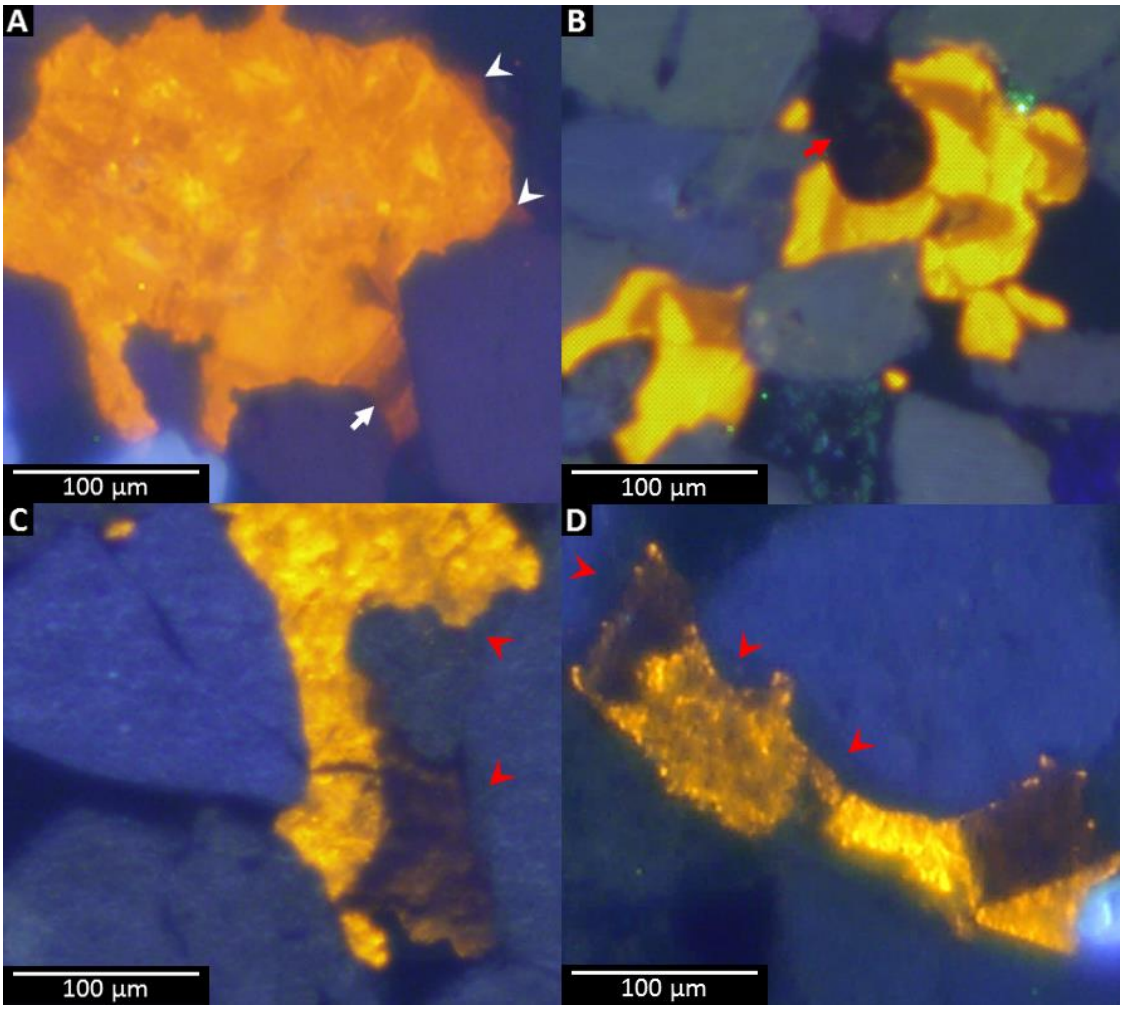

Figure 4.22. Variable luminescence and zonation in burial calcite cement from samples 107c1-b7, 106c1-b10, 109c1-b5, and 105c2-b5. Scale bar and visual indicators are the same for all CL photomicrographs although field of view differs for each. A) Concentric zoning with fine oscillatory zoning in burial calcite of sample 107c1-b7. Concentric zonation is visible in the quenched ~14-µm thick band (white arrow) which continues on the other side of the framework grain (white arrow-heads). Oscillatory zonation of <6-µm thick zones comprise several discrete lines which parallel the broader concentric quenched zone. B) Indeterminable overlapping zonation in calcite from sample 106c1-b10. Zonation is obscured by an air pocket in thin section (red arrow). Zonation appears to be initially concentric that became sectoral with unequal partitioning of activators and quenchers. C) Bright and quenched luminescent calcite in sample 109c1-b5. Quenched, nearly non-luminescent area is likely the first calcite to precipitate following quartz overgrowths (red arrowheads). D) Bright and quenched luminescent calcite from sample 105c2-b5. The quenched, nearly non-luminescent areas (far right and left) are likely the first calcite to precipitate following quartz overgrowths (red arrowheads) which are later embayed or blocked by luminescent calcite.

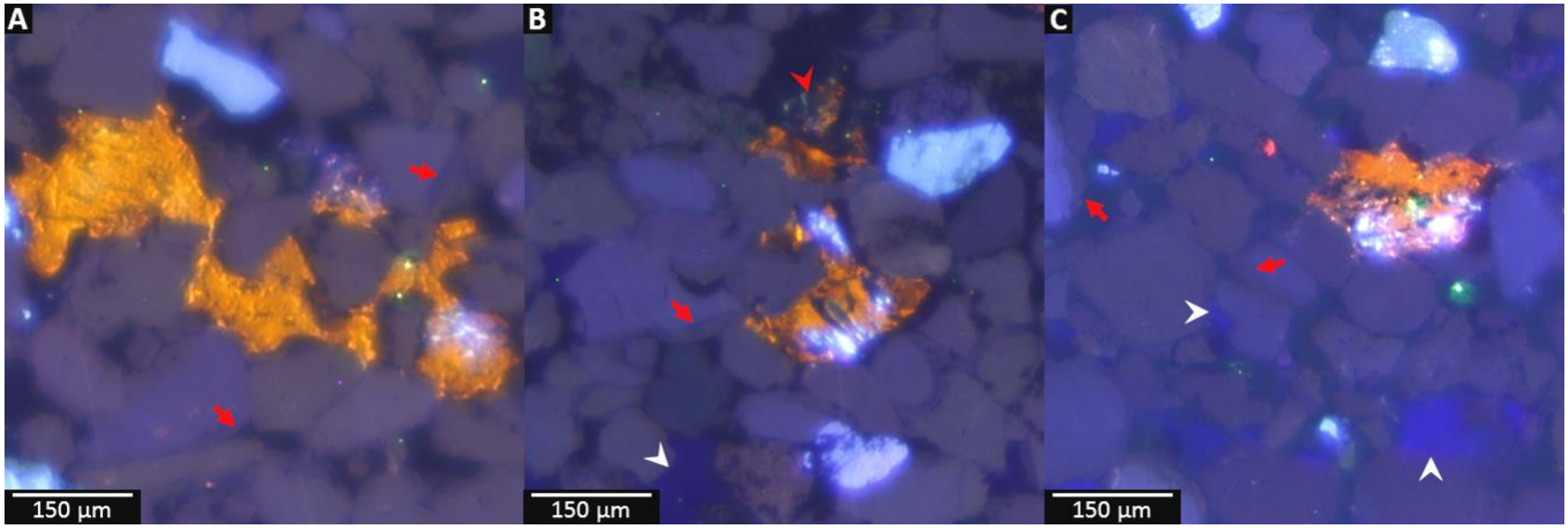

Figure 4.23. Luminescence of ferroan calcite stained purple from samples 106c1-b7, 106c1-b10, and 107c1-b7. Scale bar as well as visual indicators are the same for all CL photomicrographs although field of view differs for each. A) Burial calcite cement in sample 106c1-b7 appears orange with no zonation and relatively few inclusions. The most noticeable inclusions are fragments of brightly-luminescent feldspar that appear light blue within the calcite. Quartz overgrowths (red arrows) are poorly developed in this sample lacking thickness and euhedral terminations in pore throats. Grains are tightly packed around calcite cement, a potential indication of calcite resisting physical compaction. B) Burial calcite cement in sample 106c1-b10 appears dark orange and is mostly replacive and contains luminescent feldspar inclusions (light blue). The mineralogy of the other replaced grain (red arrowhead) is unknown and unrecognizable in PPL and XPL (not shown). Secondary porosity is noticeable in feldspars not replaced by calcite. Quartz overgrowths (red arrow) are moderately developed with many grains having discernable overgrowths on detrital grains that are not in contact with other grains or kaolinite (white arrowhead). C) Burial calcite in sample 107c1-b7 is almost exclusively replacive, and contains many fine and brightly-luminescent grain fragments. Quartz overgrowths (red arrows) as well as kaolinite (white arrowheads) cement grains and fill interstices. Quartz overgrowths are not common and few are well developed.

Despite the quenching effect the staining procedure has on calcite, luminescence of stained ferroan calcite nonetheless is still clearly visible. This quenching is caused by the additional iron from the precipitate of the potassium ferricyanide stain (Turnbull's blue), and the reduction in thickness of carbonate minerals thickness and, thus, interaction volume of the specimen and incident electrons (see Appendix C, section C.2, for details regarding electron beam and sample volume). Non-luminescent burial calcite exists in at least one location, sample 109c1-b5, although nowhere else is it observed (Figure 4.24). This non-luminescent patch of calcite contains quartz inclusions, as well as what appears to be points or 'pin-pricks' of yellowish orange luminescence. This calcite contains appreciable iron and magnesium concentrations above detectable limits (~2% by weight) with SEM-EDS. Burial calcite elsewhere within 109c1-b5 has dull to bright luminescence (Figures 4.21 and 4.22C); the dolomite, however, is non-luminescent (Figure 4.19). While observed dolomite is exclusively non-replacive, replacive textures with burial calcite are minimal in quartz and range from minor to moderate in labile minerals. These burial carbonates along with early and poikilotopic calcite will be discussed later in their paragenetic contexts in section 5.1.

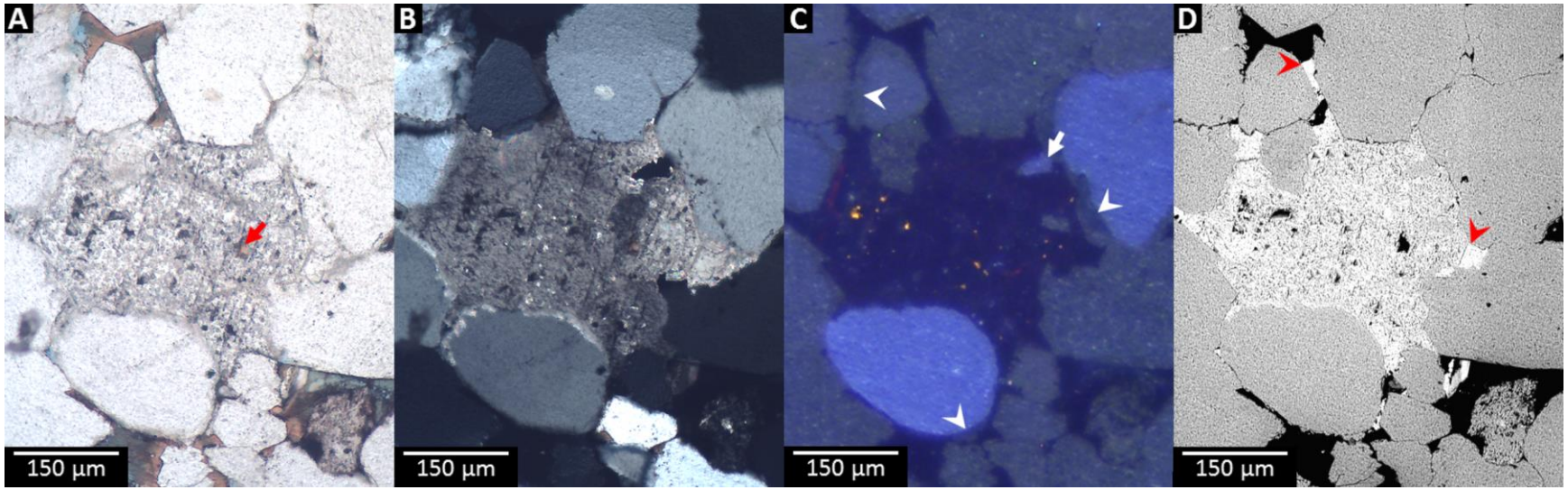

Figure 4.24. Magnesio-ferroan calcite in sample 109c1-b5. Scale bar and field of view is the same in all photomicrographs. A) Calcite contains inclusions and intercrystalline porosity (red arrow), PPL image. B) Calcite is a single crystal and extinction is not undulatory, XPL image. C) Calcite is non-luminescent but contains points of yellow-orange luminescence typical of calcite, CL image. A visible quartz grain-fragment suspended in calcite cement (white arrow). Development and distribution of quartz overgrowths (white arrowheads) are variable. D) Calcite cement is not uniformly white due to numerous inclusions and intercrystalline porosity, SEM-BSI. SEM-EDS analysis detected appreciable high iron and magnesium content within the white rhombs (red arrowheads).

4.3.4 Compaction

Compactional features are generally found along mud and very fine-grained laminae. Evidence for ductile as well as brittle deformation is observable in crushed and fractured framework grains as well as those with concavo-convex and sutured contacts (Figures 4.25 and 4.26). Quartz cementation occurring throughout compaction is evident in the contacts of quartz framework grains, especially those with contacts with particularly coarse grains (Figure 4.27), and in grains with fractures that have been subsequently healed (Figures 4.26).

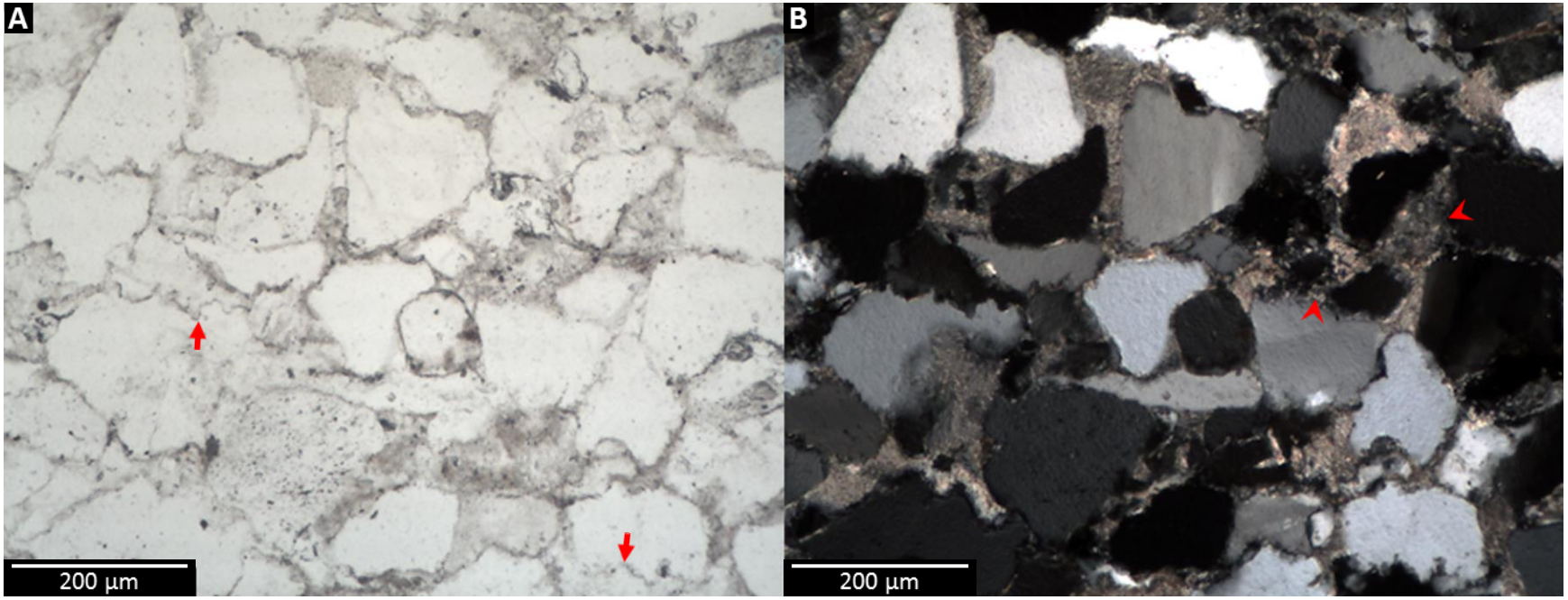

Figure 4.25. Compaction features visible in reservoir seal of sample 104c1-b10. Scale bar and field of view is the same in both photomicrographs. A) Sutured contacts visible on framework grain contacts (red arrows), PPL image. Hydrocarbon staining of framework grains appears light brown. B) Microstylolite crosscuts grains and chert cement (red arrowheads) but not calcite cement, XPL image. Fragments of crushed grains from compaction are visible between larger framework grains.

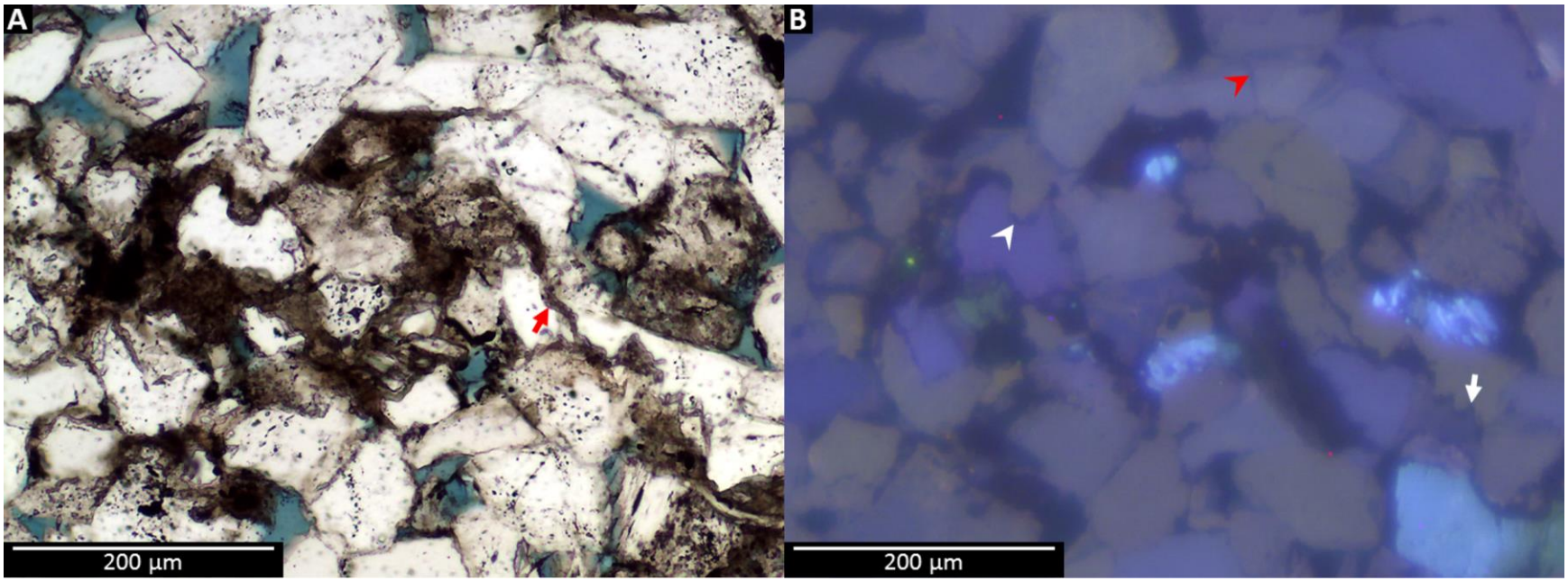

Figure 4.26. Compaction features from sample 106c1-b10. A) Microstylolite follows and crosscuts grain boundaries (red arrow), PPL image. B) Contrast in luminescence of framework grains elucidates sutured (white arrow) and concavo-convex contacts (white arrowhead), as well as healed fractures within grains (red arrowhead), CL image.

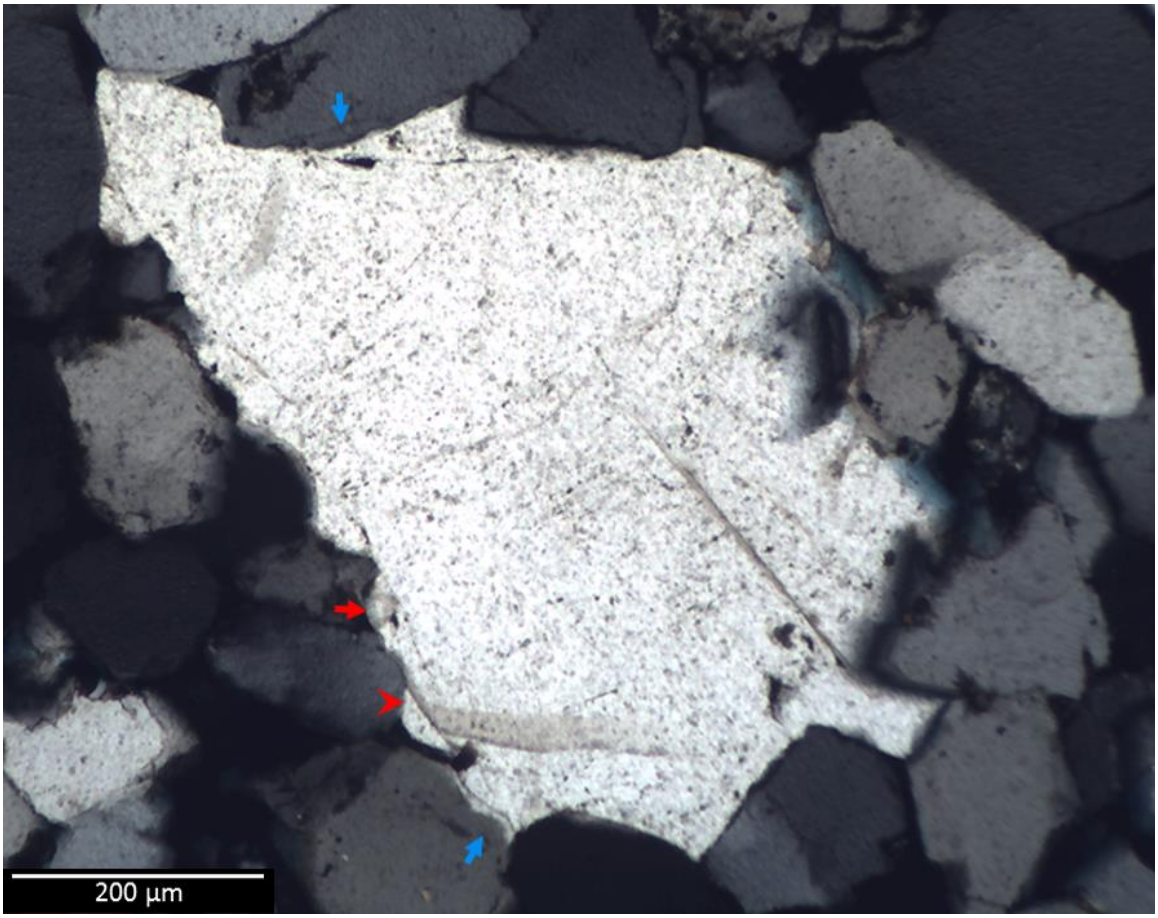

Figure 4.27. Compaction is visible in multiple, syntaxial, quartz overgrowths on coarse grain in sample 109c2-b4. Multiple generations (red arrow and arrowhead) of quartz cement are rarely this thick to be distinguishable with transmitted light. Other framework grains, some with visible overgrowths (blue arrows) interrupt the contiguity of both generations of quartz overgrowths on the coarse grain. Continued compaction during quartz cementation has limited the terminations of the latest overgrowth (red arrowhead) to be euhedral only locally.

4.3.5 Vugular Porosity

Vugular porosity persists in the section of core from which 107c2-b5 was sampled and at one point in time may also have also been present in the core from which 104c1-b10 was sampled. There are only two locations within sample 104c1-b10 where cement fills voids larger than grains that resemble vugs, one within the reservoir (Figure 4.28), the other the reservoir seal (Figure 4.29). In both locations of sample 104c1-b10, it appears in SEM-BSI that kaolinite has filled porosity that has been at least partially produced by the dissolution of framework grains the boundaries of which can be faintly discerned (Figure 4.29). It is unclear as to what mineral(s) the framework grains were composed of, although secondary porosity, and cementation thereof, by kaolinite occurred after compaction, as otherwise these obliquely horizontal vugs would be crushed with or without kaolinite cement. In sample 107c2-b5, porosity is relatively high and vugs are concentrated horizontally above and below low permeability (tight) sections of rock (Figure 4.30). Ferroan calcite and dolomite are present in sample 107c2-b5, as is kaolinite. None of these cements, however, are found in the vugs of this sample.

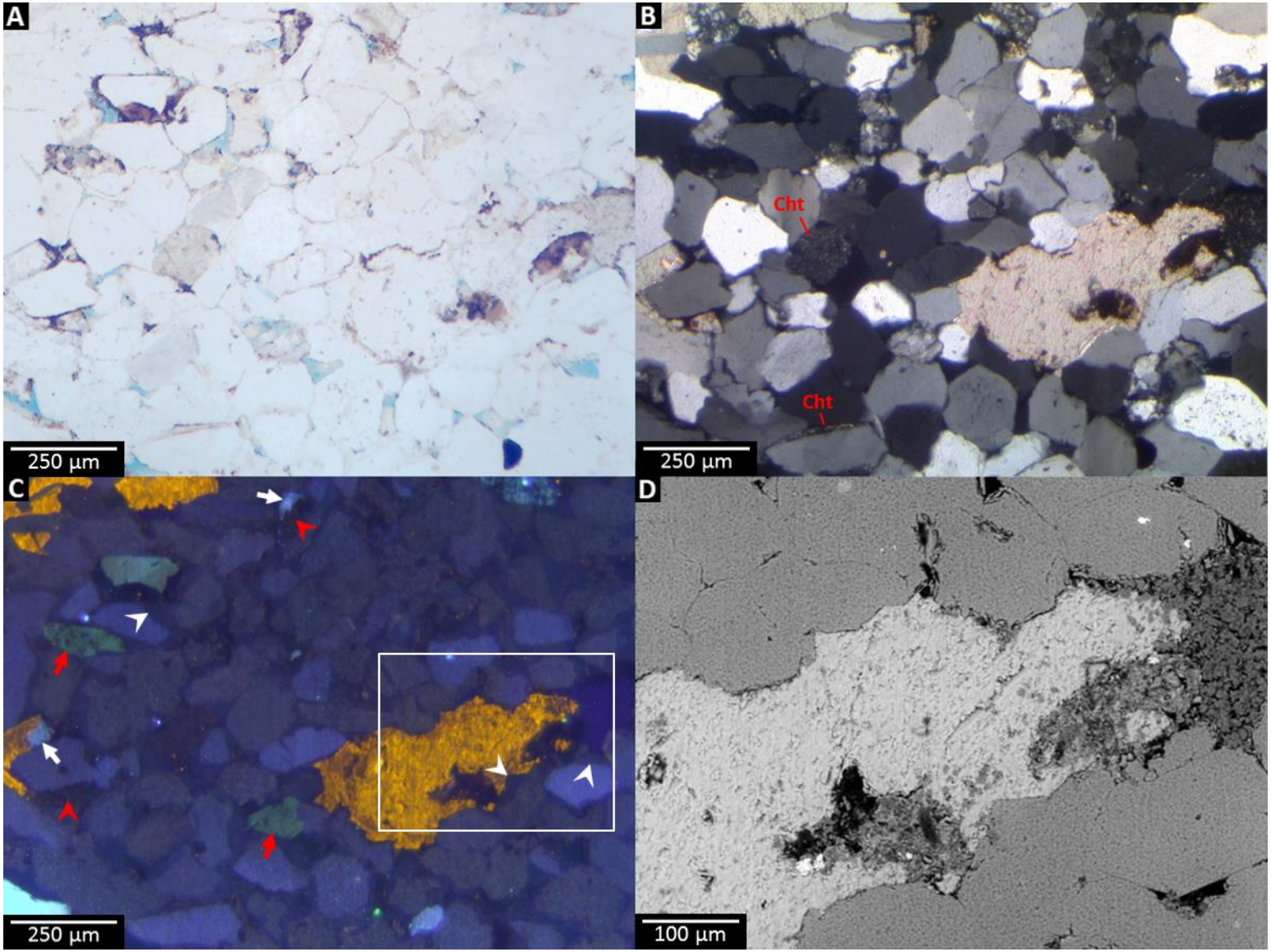
A
250 µm
B
Cht
Cht
250 µm
C
250 µm
D
100 µm

Figure 4.28 (from previous page). Calcite replacement of kaolinite filled vug proximal to reservoir-seal contact in sample 104c1-b10. Scale bar and field of view is the same for photomicrographs A, B, and C; D is the area inside rectangle in C. A) Porosity appears light blue and hydrocarbons coat grains and stain clays brown. B) Calcite cement in vug (lower right) is poikilotopic with that in seal (upper left), XPL image. Framework grains are predominantly quartz with a few feldspars and chert (Cht = chert) grain as well as cement. Grain contacts are predominantly long. C) Calcite is brightly luminescent appearing yellowish orange, except in two locations (red arrowheads) where it is non-luminescent, CL image. Differential luminescence of quartz grains from syntaxial overgrowths (white arrowheads) is common with possibly two separate cement generations based on different luminescence in overgrowths. Kaolinite (dark purple), weathered feldspars (green) (red arrows) as well as feldspars (light blue) replaced by calcite (white arrows) are apparent in CL. D) Calcite (light gray) replaces earlier kaolinite cement (dark gray) occludes porosity (black) in vug, SEM-BSI. Quartz (gray) overgrowth terminations are commonly euhedral but otherwise indistinguishable from quartz grains or other silica based on contrast in SEM-BSI.

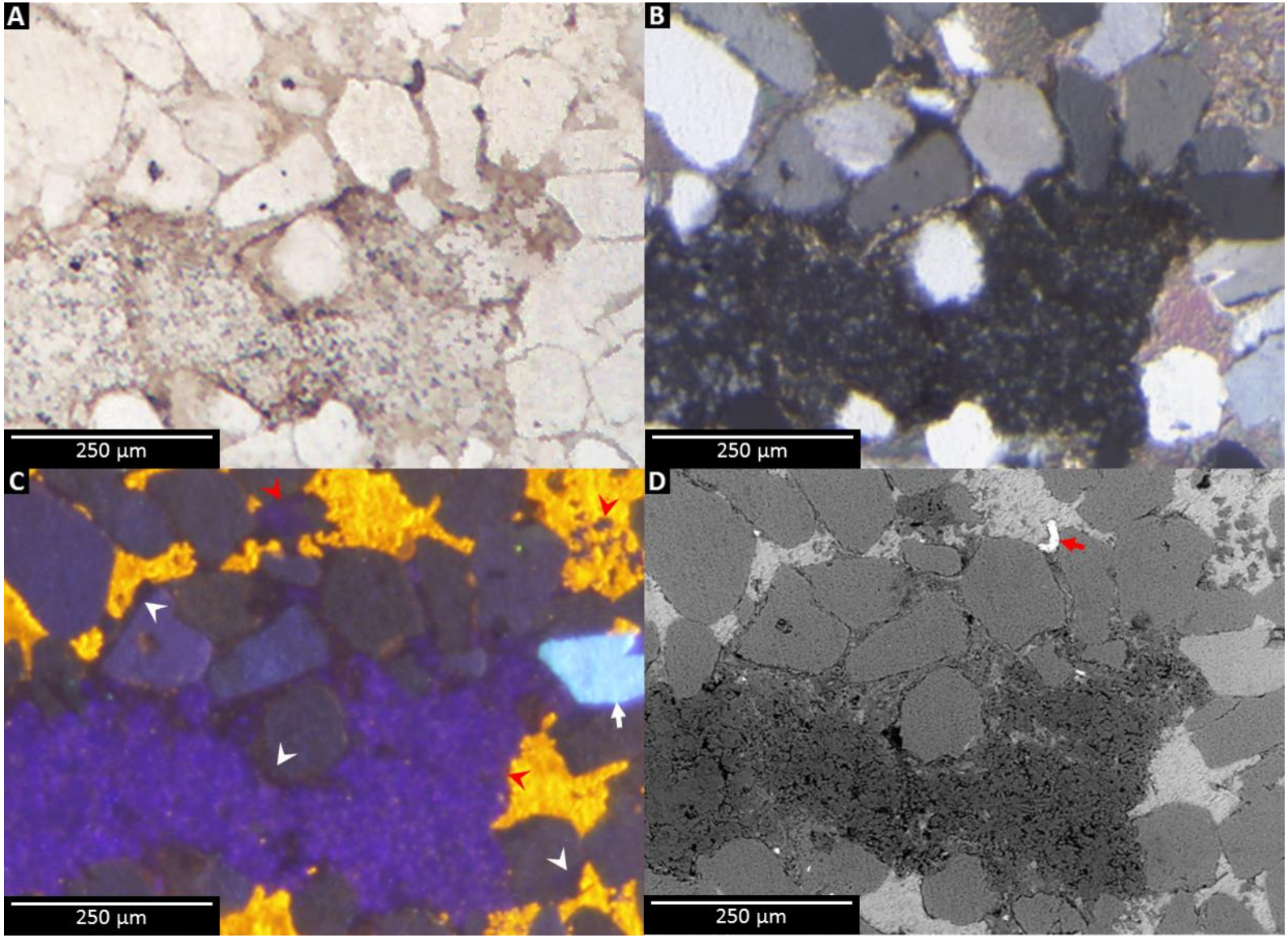
A
250 µm
B
250 µm
C
250 µm
D
250 µm

Figure 4.29 (from previous page). Calcite replaces framework grains and kaolinite in vug in sample 104c1-b10. Scale bars and field of view are the same in all photomicrographs. A) Hydrocarbons stain clays and grain surfaces brown, PPL image. B) Calcite cement is poikilotopic and the optic extinction of the cement in vug is similar to chert, XPL image. C) Differentiation of grains and cement is apparent under CL with calcite appearing yellowish orange and replacing kaolinite which appears purple (white arrowheads), CL image. Quartz grains and overgrowths (white arrowheads) appear dark blue and brown, and remain largely unembayed by calcite. Potassium feldspar (red arrow) appears bright light-blue under CL. D) Clay (dark gray), quartz (gray), and calcite (light gray) are distinguishable from each other in SEM-BSI. Feldspar however is a slightly darker shade of light gray than calcite and is less distinct. CL of the clay as well as first-order interference colors suggests kaolin mineralogy for the clay. SEM-EDS analysis of the white partial grain rim in D (red arrow) is a titanium-oxide cement possibly authigenic anatase or brookite. Note the quenching of the Ti-oxide under cathodoluminescence.

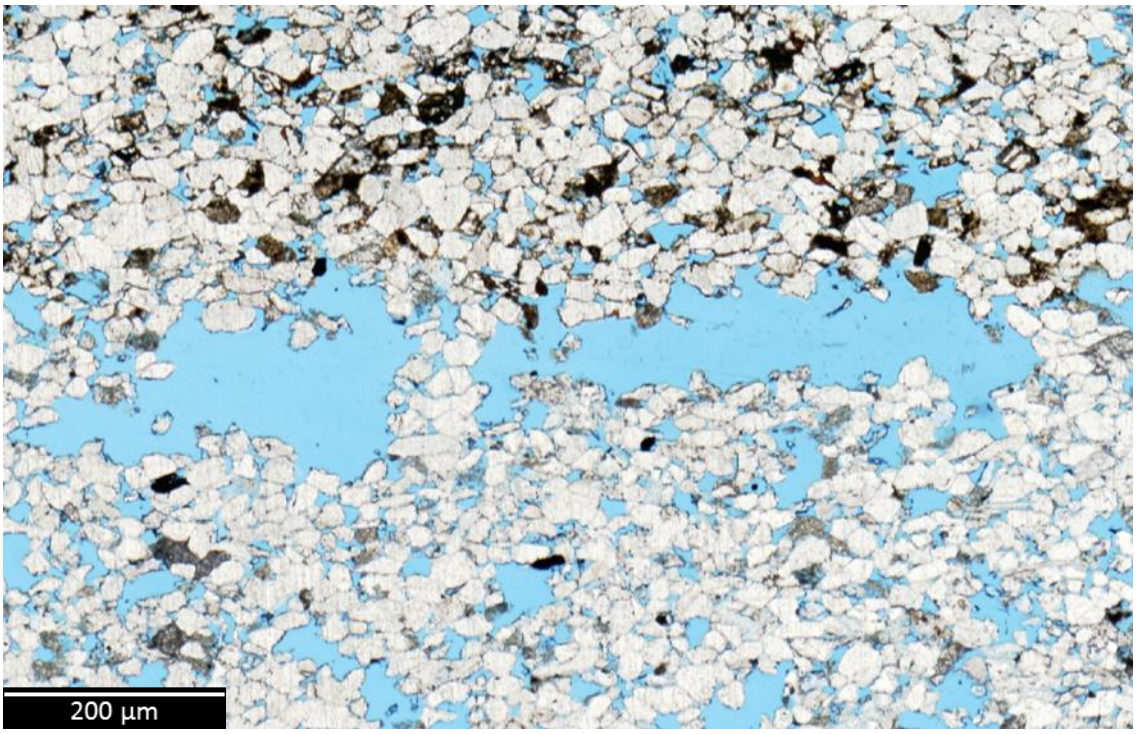

Figure 4.30. Horizon of vugular porosity in sample 107c2-b5, PPL scanned image. Porosity (blue) is greater in lower section than the upper where oil (black-red) persists between grains and stains weathered grains brown. Vugs are concentrated above and below tight zones in thin section and mimics laminated fenestral pores (vugs) in carbonates despite this rock being siliciclastic.

4.4 Reservoir Compartmentalization

4.4.1 Fabric-Selective Compartmentalization

Fabric selective compartmentalization is apparent in many intervals of MegaWest core sections taken from the reservoir. Compartmentalization concordant to fabric is fundamentally the result of sorting and subsequent diagenetic effects upon grains, cement, and matrix associated with sorting. The effects of grain sorting on oil saturation are most noticeable in samples retrieved from very-fine to fine-grained sandstone units containing cross- and ripple-laminated strata. Compaction is greatest along laminae where bedform stratification has concentrated very-fine grains and detrital matrix (Figure 4.31). Stylolitic features commonly parallel mud and clay-rich laminae. Expulsion of

fluids during compaction can concentrate insoluble material along stylolites creating an impermeable barrier. Porosity is furthered destroyed from authigenic pyrite and clay cement. The presence of pyrite is commonly associated with organics and phyllosilicates, namely kaolinite. Kaolinite is an alteration product of feldspars and other labile silicates that, along with pyrite, occludes interstitial and secondary porosity. The cumulative effect of porosity reduction along mud laminae is 1) decreased conductivity perpendicular to laminations and 2) smaller pore throats. Thus muddy laminae results in compartmentalization within beds.

A decreased winnowing of sediment possessing little detrital clay results in greater packing and, thus, less interparticle porosity, with little to no apparent change in associated mineral compositions. This is the case in sample 109c1-b3, where the bed in the upper portion of the sample is more poorly sorted than the bed comprising its lower portion of the sample (Figure 4.32). This sorting difference between the two beds is noticeable in hand sample with the upper section being noticeably less saturated than the lower (see Figure 3.1O and Appendix B for box-core images).

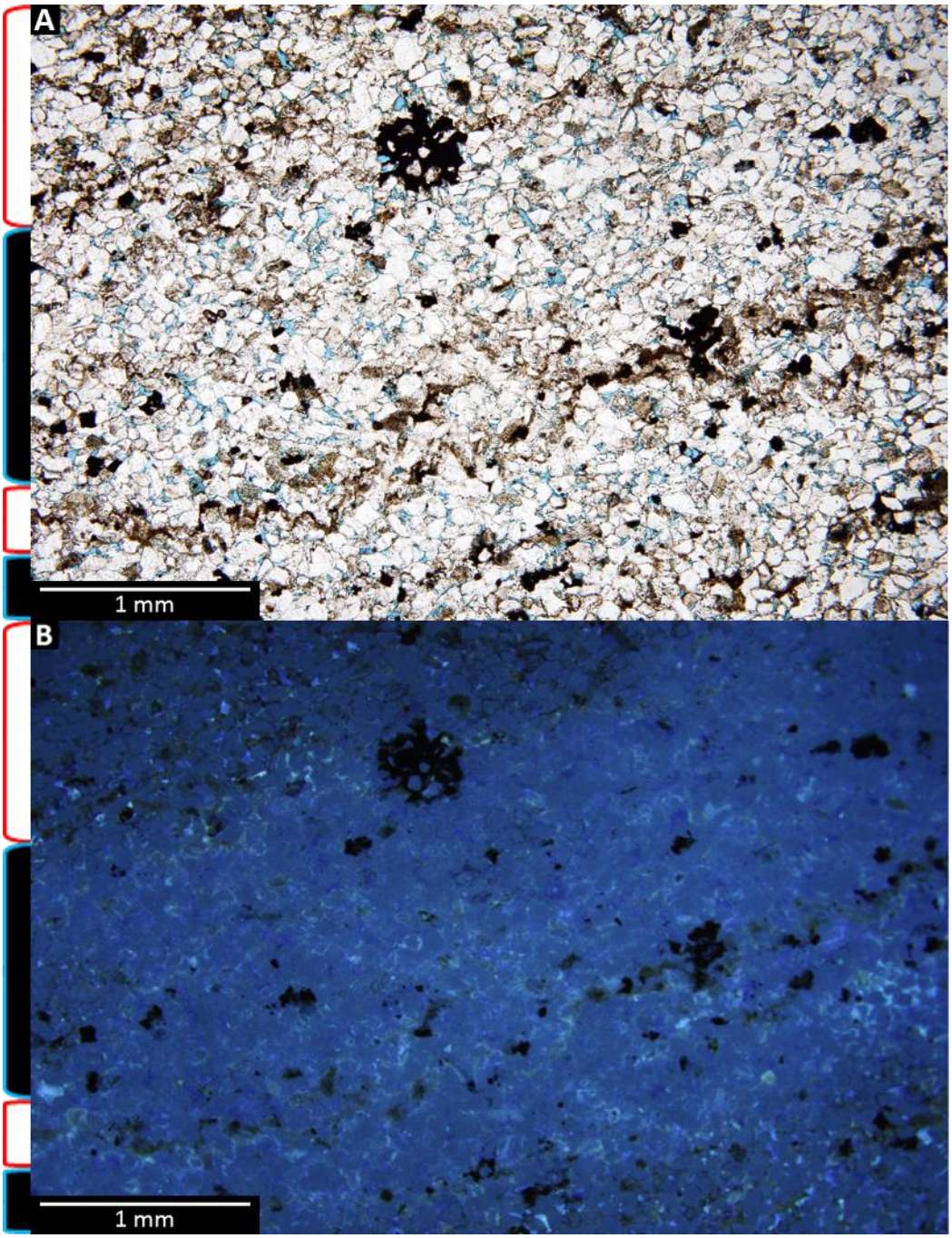

Figure 4.31. Graded cross laminae of sample 108c1-b2. A) Pore-throat diameters are greatest within the relatively thicker laminae (blue brackets with solid black fill) and least in the mud drapes and laminae comprised of fine clasts (red bracket with hollow fill), PPL image. B) Thick laminae are more fluorescent due to hydrocarbons' proclivity for more permeable strata although authigenic kaolinite commonly occludes pores, UV-epifluorescence image. Authigenic pyrite precipitates proximal to mud and clay-rich laminae both with and without microstylolites and commonly replaces phyllosilicates. Some authigenic pyrite nodules grow to macroscopic size.

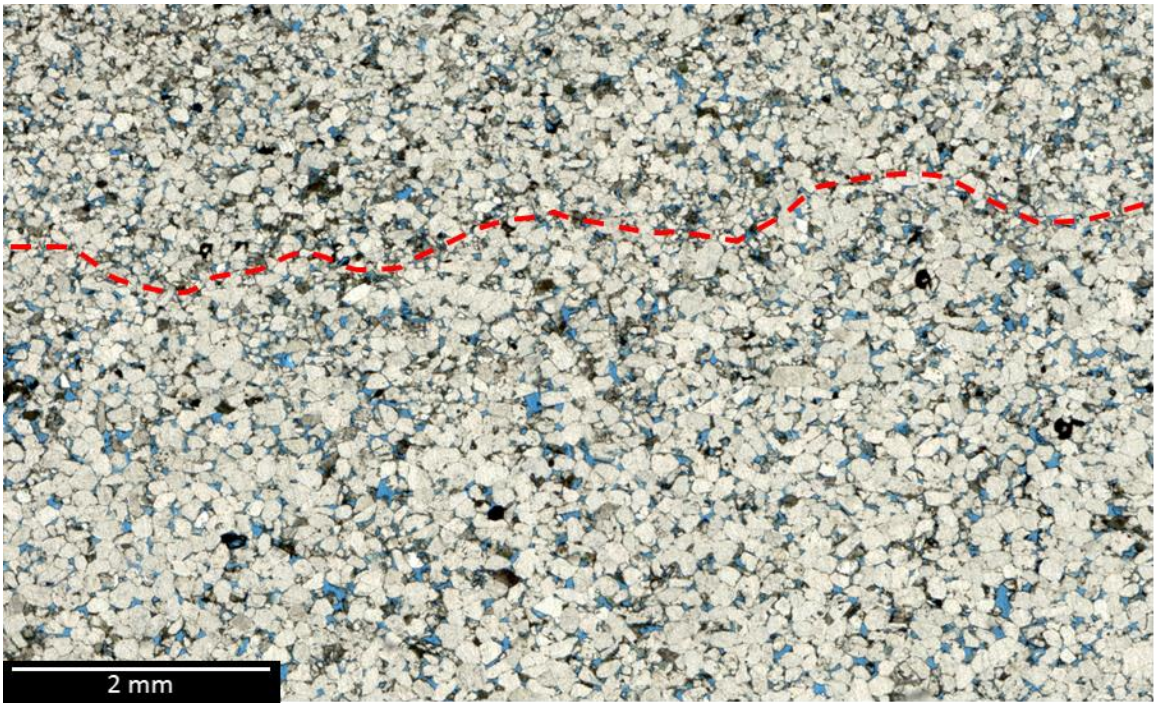

Figure 4.32. Winnowing difference between cross-strata bedding in reservoir of sample 109c1-b3, PPL scanned image. Greater grain packing in the upper bed (above dashed line) has decreased porosity and pore-throat diameter compared to the lower bed (below dashed line) (see Figure 3.1O and Appendix B).

Porous and permeable zones concordant to rock fabric may be exhibited as either preserved original depositional texture or the result of cement and grain dissolution. Sample 107c2-b5 was taken from a section of core initially thought, and incorrectly so, to be pervasively cemented by replacive carbonate given the white appearance of the core section, and the dark areas being the remaining porous laminae where oil persisted (see Figure 3.1L and see Appendix B for box-core images). This sample however is friable and the carbonate cement was not nearly as prevalent as was presumed. Unlike most other samples, sample 107c2-b5 contains vugular porosity with oil persisting in low porosity and permeability zones between fine grains (Figures 4.30 and 4.33). Calcite and

dolomite occur in tight zones where oil remains and in the more porous zones but does not fill vugs.

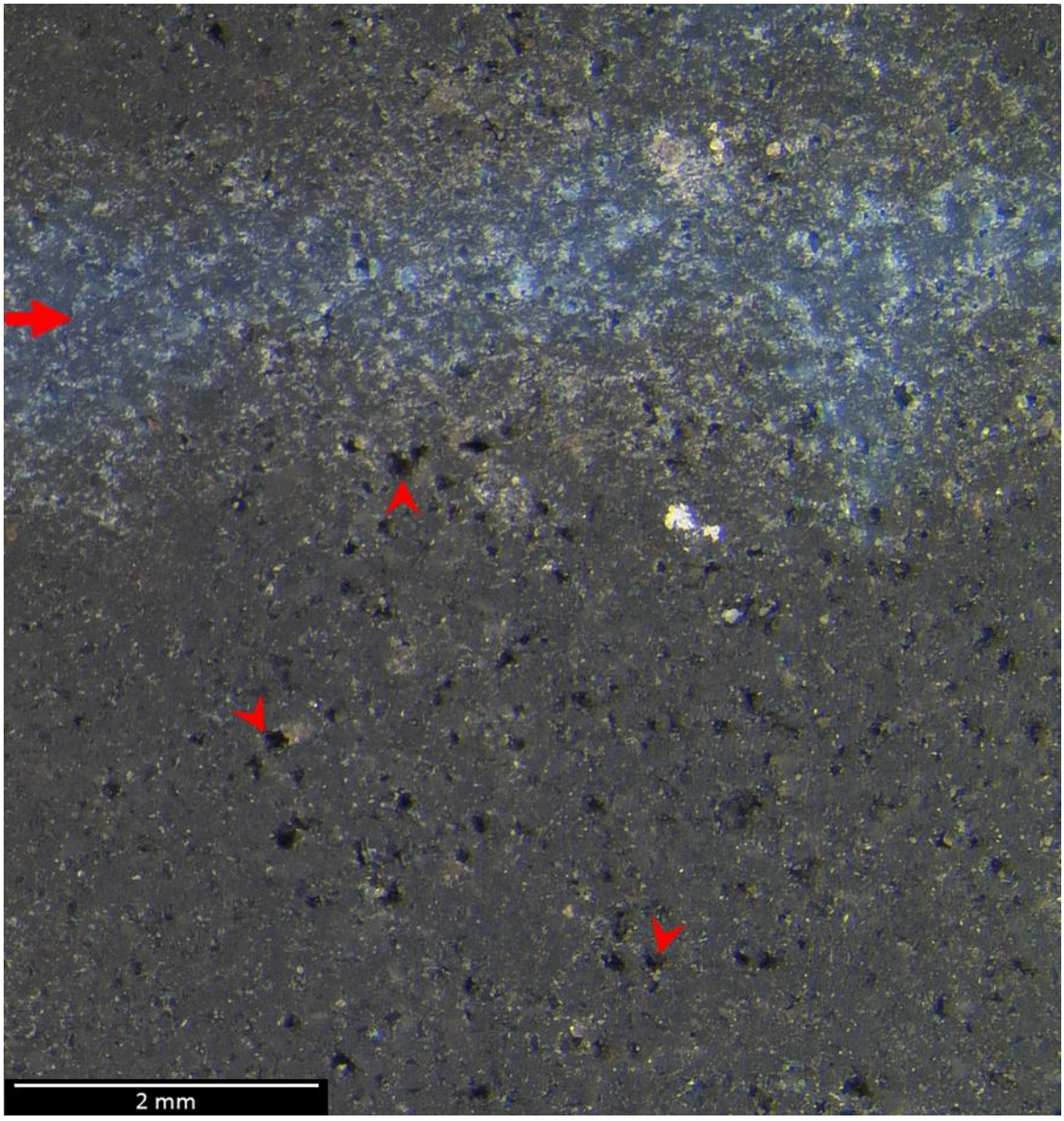

Figure 4.33. Vugular porosity visible in billet of sample 107c2-b5, orthoscopic view, RFL image. Epoxy (blue) is abundant along a porous horizontal zone (red arrow) in the upper portion of the photo. Epoxy is however absent in lower half of photo despite visible pore throats (red arrowheads).

The cause for this fabric selective vugular porosity is unknown. It is possible that current vugs represent pyrite cement that subsequently dissolved as there is very little pyrite observed in thin section or billet. Dissolution of depositional or diagenetic carbonate is also possible given the linear and horizontal arrangement of the vugs. Unfortunately, evidence of possible carbonate dissolution associated with vugs is abstruse as acid and stain solutions were poorly constrained to one side of the thin section. There is no apparent difference in distribution of carbonate cement around vugs or elsewhere in thin section between the left and right side of the 107c2-b5 thin section. The failure to constrain the acid and stain solution to one side precludes any direct comparison between the two. Calcite and dolomite are, however, the only minerals besides kaolinite that cement more than a few grains in any one location in sample 107c2-b5.

4.4.2 Non-Fabric Selective Compartmentalization

Nodular pyrite occurrences are only observed in reservoir sections of core. Incipient nodular pyrite is likely to be euhedral pyrite associated with phyllosilicate-rich mud laminae with compactional features. Expelled fluids from compaction may provide soluble iron as well as organics from oil brines that potentially allows for additional redox reactions with adsorped metals in clays. While small nodular pyrite (<5 mm in diameter) may begin as fabric selective growths, larger growths of nodular pyrite (≥5 mm) are not affected by grain size or grain sorting (e.g., the pyrite nodule in Figure 4.16 is ~8 mm in diameter). Sufficiently large nodules may displace oil and limit conductivity locally (see Figures 4.16 and 3.1F, and Appendix B); however, nodular pyrite never forms an effective seal in the absence of other porosity and permeability reducing factors.

Poikilotopic calcite is the most effective seal-forming phase observed in thin section. Poikilotopic calcite cement is not fabric selective in hand samples of 104c1-b10 and 105c3-b2, the latter of which calcite is not macroscopically observable (see Figures 3.1A&G and Appendix B). Additionally, replacive calcite from other unsampled intervals of cores 104 and 105 similarly does not appear to be related to the rock fabric (Figures 4.34 and 1.1). Calcite is more replacive in sample 104c1-b10 than 105c3-b2 with poikilotopic calcite replacing feldspar grains up to 240 μm in size (Figure 4.35) and deeply embaying quartz grains (Figure 4.36). Consequently, determination of primary rock fabric is somewhat conjectural in the case of such extensive overprinting. In the reservoir seal of sample 104c1-b10, poikilotopic calcite minimally embays grains with microcrystalline pyrite and opaque coatings (Figures 4.17 and 4.37). These coatings are observed in patches although the reason for their limited or selective distribution is ambiguous. The effect of diagenetic calcite on oil-saturation geometry in sample 104c1-b10 is striking, with a cuspate boundary visible in in both hand sample (see Figure 3.1A and Appendix B) and thin section (Figure 4.38). The cuspate boundary between the reservoir seal and reservoir is the result of two, large, poikilotopic, calcite crystals intersecting (Figure 4.39). Large masses of carbonate cement are not apparent in sandstone sections of core devoid of hydrocarbons. In addition, several sections that were suspected of similar calcite, such as the white core sections of 107c2-b5 (see Figures 1.1D and 3.1L, and Appendix B for box-core images), contained very little carbonate cement and were in fact porous. Porosity in reservoir of sample 104c1-b10 is low, although, evidence of vugs occurring within the reservoir as well as within the reservoir seal exists (Figures 4.28 and 4.29).

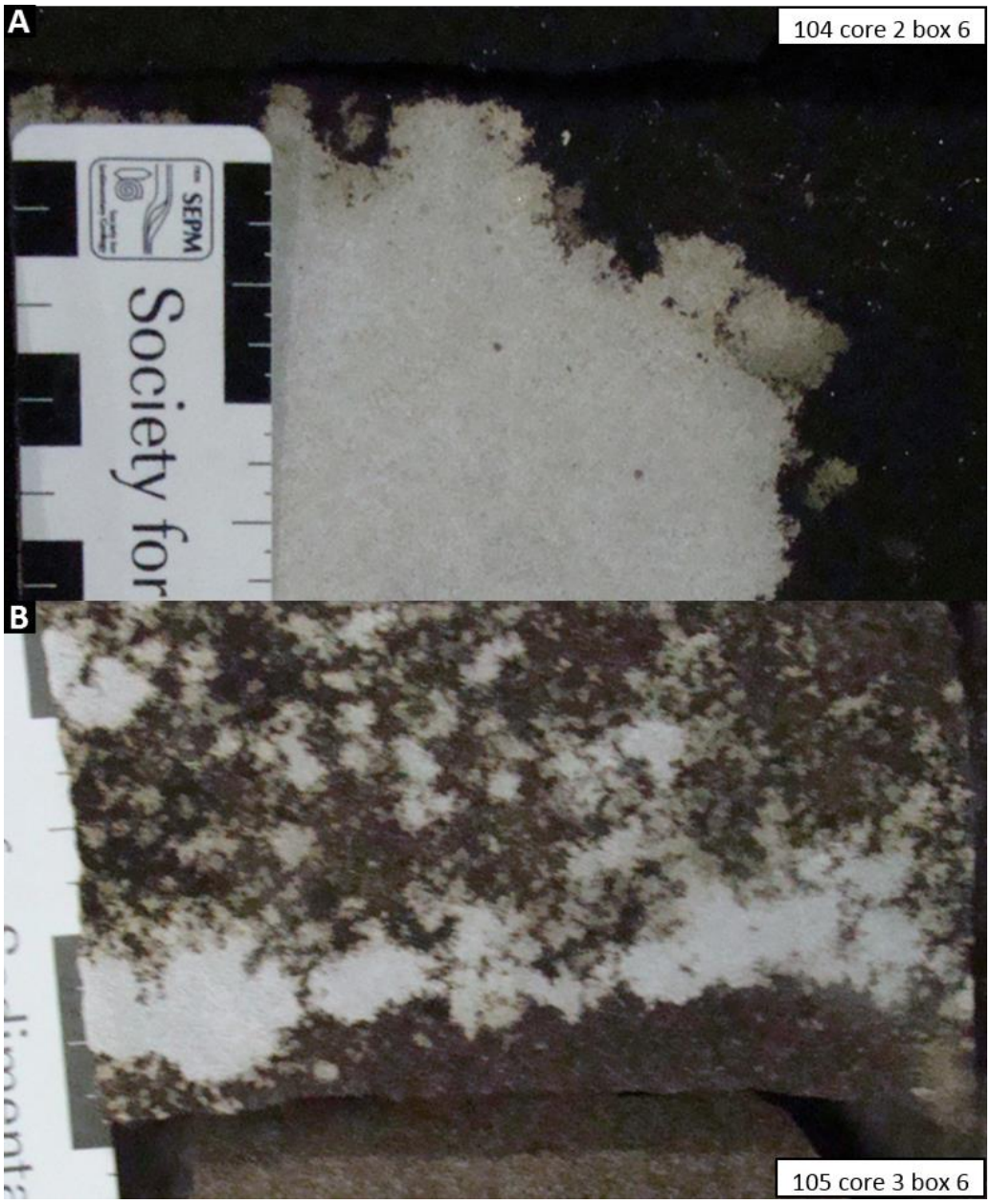

Figure 4.34. Replacive calcite in unsampled sections of cores 104 and 105. A) Calcite encroachment into reservoir of Core 104, core-section depth is ~502.9 ft. B) Incipient diagenetic calcite seal formation in reservoir of Core 105, core-section depth is ~480.4 ft.

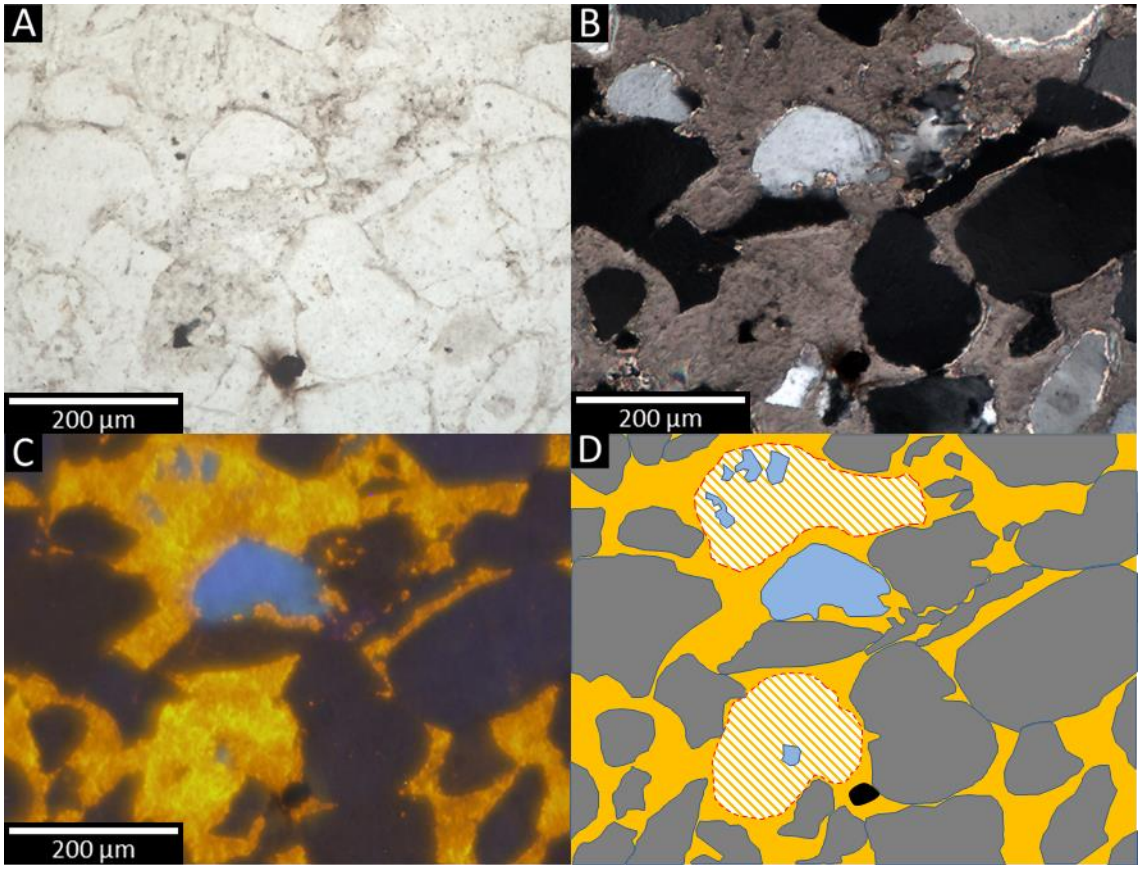

Figure 4.35. Near complete replacement of feldspar framework grains by calcite cement in the reservoir seal of sample 104c1-b10. Scale bar and field of view is same for photomicrographs A, B, and C; D is a view of grains outlined from C. A) Porosity is totally occluded and not visible, PPL image. B) Calcite is poikilotopic in replaced feldspars and surrounding cement, XPL image. C) Calcite cement is brightly-luminescent (yellowish orange) as are the feldspars (light blue), CL image. Former feldspar boundaries are discernable from relatively brighter luminescence of the replacive calcite than the surrounding calcite. D) Interpretation of replacive textures. Original grain boundaries (red dashed) of the feldspars (blue) have been significantly reduced to remnants by replacive calcite (white and orange striped). Black spot on photomicrographs and interpretation is where overexposure of electron irradiation burned a hole through thin section.

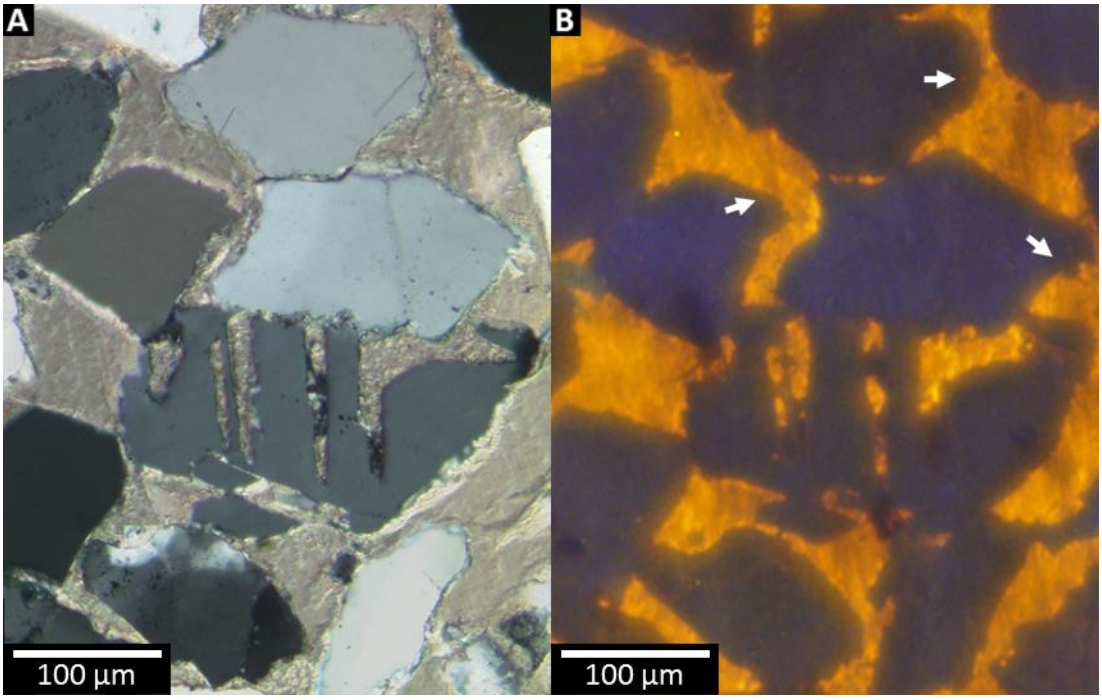

Figure 4.36. Severe embayment and replacement of quartz by calcite in seal of sample 104c1-b10. A) Embayed grain (center) was initially thought to be preferential replacement along albite twins in plagioclase, however grain was identified with Raman microscopy as quartz, XPL image. B) Lack of intense light-blue luminescence typical in feldspar supports Raman identification, CL image. Some quartz overgrowths (white arrows) remain.

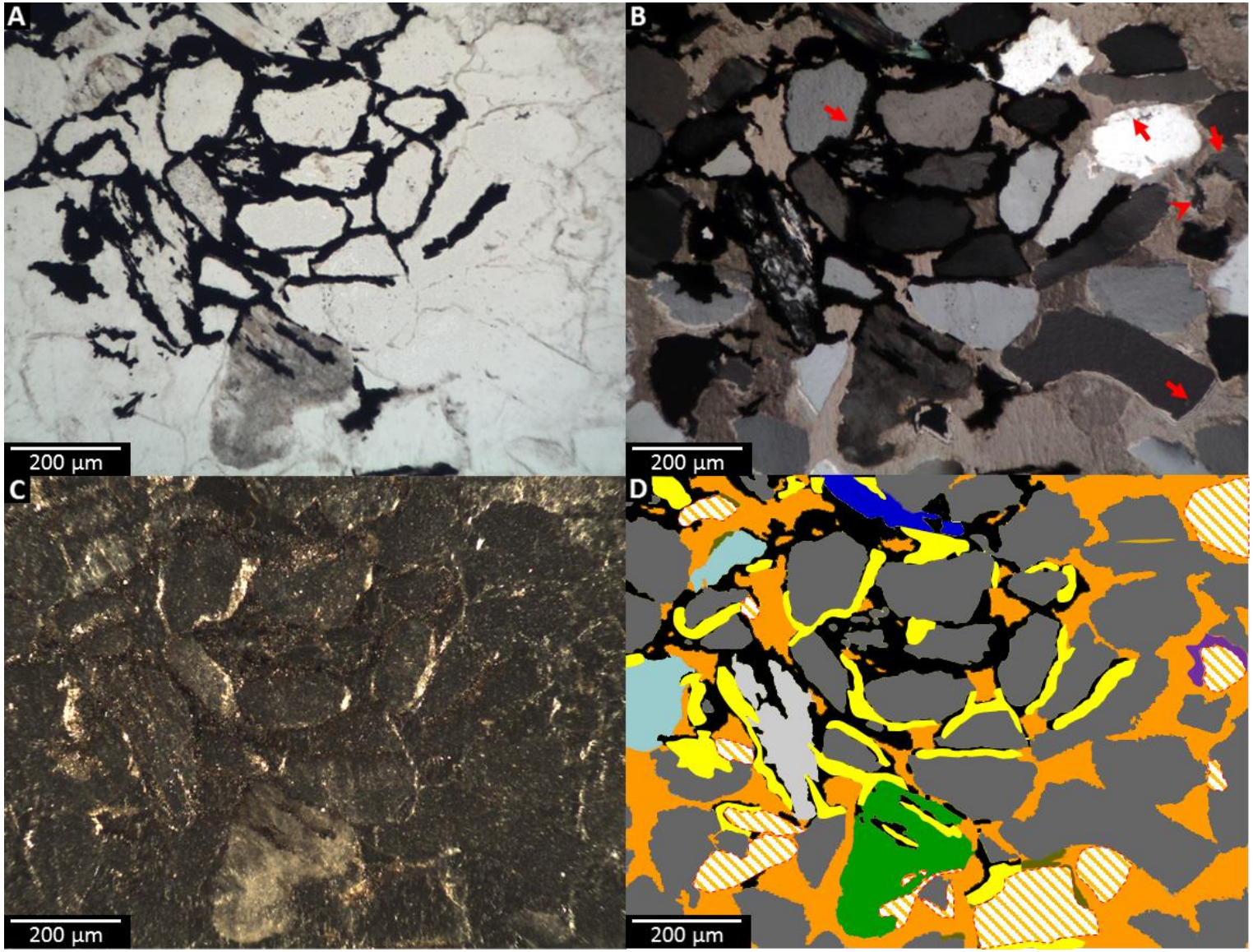
A
200 µm
B
200 µm
C
200 µm
D
200 µm

Figure 4.37 (from previous page). Microcrystalline pyrite and unidentified opaque coatings protect framework grains from replacive calcite in reservoir seal of sample 104c1-b10. Scale bar and field of view is same for photomicrographs A, B, and C; D represents outlines of features from A, B, and C. A) Opaque coatings and cement partially outline current and previous framework-grain boundaries as well as fill secondary porosity, PPL image. Hydrocarbons stain weathered grains and former grain-boundaries brown. B) Calcite cement is poikilotopic and replacive, XPL image. Biotite, feldspar, polycrystalline quartz grain, and chert cement (red arrowhead) are visible against calcite and opaque cement and coatings. Quartz overgrowths (red arrows) are rare. C) Pyrite appears gold and weathered feldspars appear cloudy, RFL image. Not all pyrite crystal surfaces are reflective and clearly visible at stage angle of photomicrograph. D) Interpretation of replacive textures based upon PPL, XPL, and RFL. Chert cement (purple) precedes quartz (dark gray) overgrowths. Pyrite (yellow) that is brightly reflective in reflected light at some stage angle is differentiated from unidentified opaques (black), which are not reflective at any stage angle. Weathered feldspars (green) and unweathered feldspars (light blue) are oil stained and is replaced (orange striped) by calcite (orange), and pyrite and opaques. Polycrystalline quartz grain (light gray) appears to be protected from calcite replacement by pyrite and opaques.

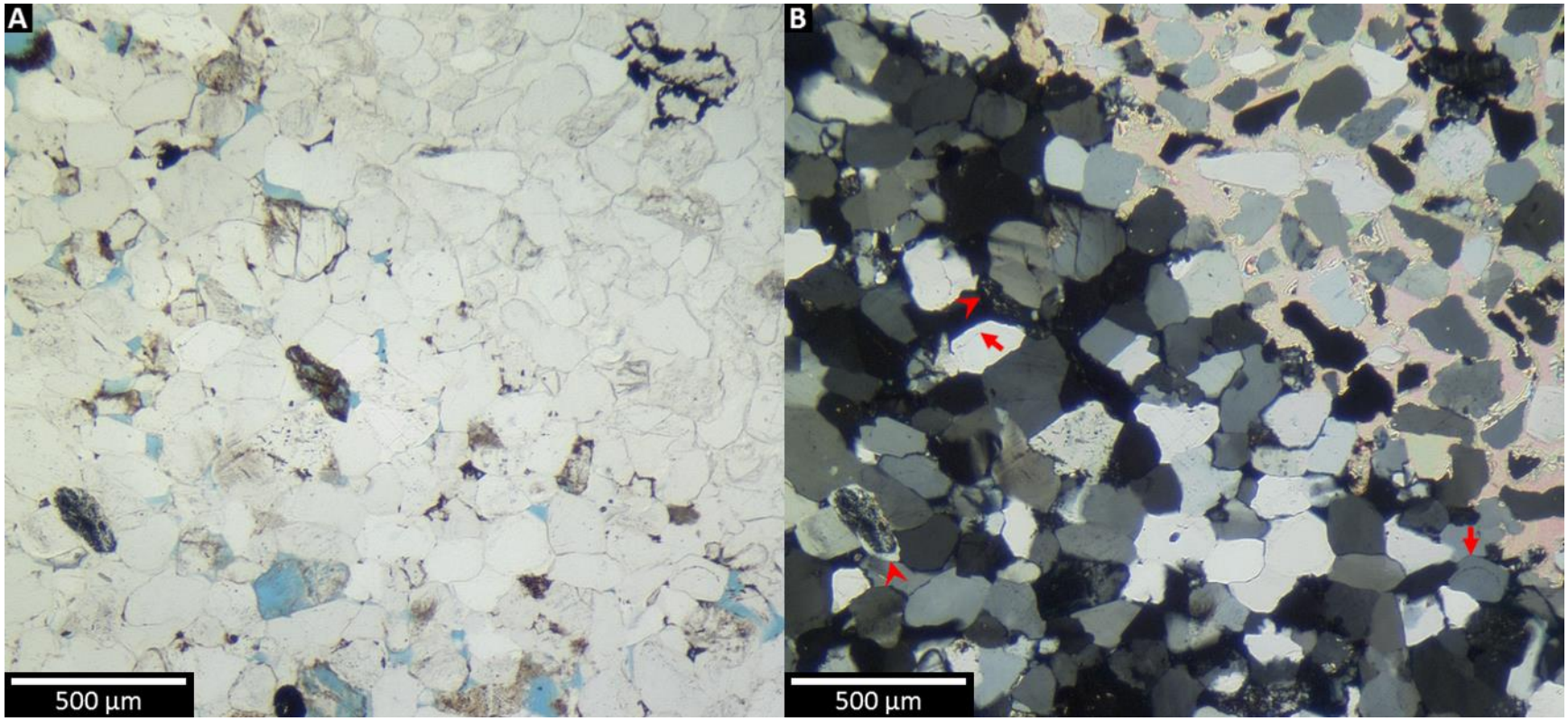

Figure 4.38. Cuspate reservoir-seal boundary of sample 104c1-b10. Scale bar and field of view is same for both A and B. A) Porosity (blue) is visible in the reservoir (lower left), PPL image. Opaque mineral (upper right) in reservoir seal is pyrite and coats a weathered plagioclase grain and a polycrystalline quartz grain. B) Poikilotopic calcite cement is apparent in XPL. Quartz cement is dominant in the reservoir with well-formed syntaxial (red arrows) and epitaxial (red arrowheads) overgrowths suggesting quartz cementation began early and was unimpeded by oil or other authigenic cements including alteration products of feldspar weathering. Framework grains in reservoir seal commonly have tangential contacts with each other and are smaller in size compared to those within the reservoir, see Appendix D.

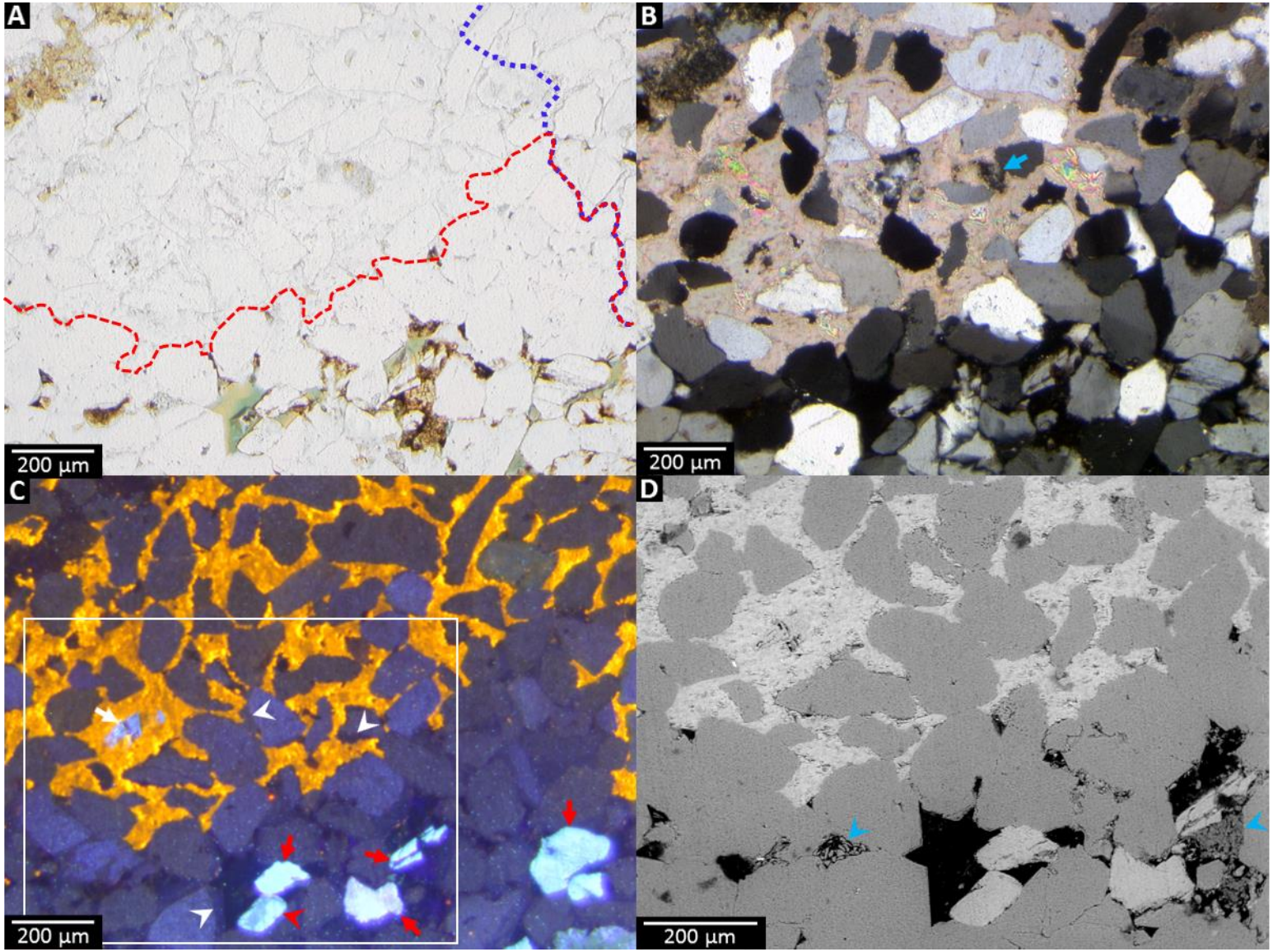
A
200 µm
B
200 µm
C
200 µm
D
200 µm

Figure 4.39 (from previous page). Cuspate tip of reservoir-seal boundary of sample 104c1-b10. Scale bar and field of view is the same for photomicrographs A, B, and C; D is the area inside the white rectangle of C. A) Blue-dyed epoxy was slightly browned from overexposure to electron beam and appears blue-green-yellow but otherwise shows porosity within the reservoir, PPL image. Dashed red line denotes reservoir-seal boundary. Dashed blue line denotes intersection of two large poikilotopic calcite crystals.
B) Framework grains appear suspended in poikilotopic calcite cement, XPL image. Partially-extinct poikilotopic calcite crystal (upper right) is visible right of the intersection of the two calcite crystals denoted by the dashed line in A. Chert (blue arrow) is more susceptible to replacement by calcite than is monocrystalline quartz. Microscope analyzer is purposefully non-perpendicular with the polarizer, albeit only slightly. This was done to better display both calcite crystals, although, as consequence the twinning in feldspar is obfuscated. C) Replacive textures and original grain boundaries are more apparent under CL as are feldspars appearing bright light-blue, CL image. Calcite is brightly-luminescent and appears yellowish orange. Quartz overgrowths (white arrowheads), are well developed and preserved in the reservoir and remnant in the seal where calcite has not replaced them. Microcline in reservoir seal (white arrow) has been nearly replaced by luminescent calcite. Carlsbad twinning is visible in sanidine, high-temperature alkali feldspar (red arrowhead). Albite twining of plagioclase (red arrows) is only apparent in CL where preferential dissolution along twins has occurred. D) Porosity (black), feldspars (light gray), quartz (gray), and authigenic clays (dark gray) filling (blue arrowheads) interparticle porosity are conspicuous within the reservoir while etched quartz grains in calcite cement is the most obvious textural relationship within the reservoir seal, SEM-BSI. Quartz and its polymorphs are indistinguishable in SEM-BSI based on contrast; however, the surface of chert commonly appears rougher toward edges than quartz and may be porous. Secondary porosity within microcline in reservoir seal is more conspicuous than the gray tonal differences between calcite and feldspar.

Chapter 5: Discussion

5.1 Paragenesis

5.1.1 Eogenesis

Iron oxides and glauconite are the earliest cements observed in the Big Clifty although unlike Pennsylvanian asphalt-rock deposits in the region hematite is more commonly manifested as occluding intraparticle porosity, or as “dust rims” under quartz overgrowths, than as interparticle cement. Glauconite is both cement as well as matrix where burial has packed it between grains (proto pseudomatrix). Following glauconite, chert is the next early authigenic cement that can be established from petrographic relationships (Figure 5.1). Chert precedes quartz overgrowths (Figure 4.37) and occurs in all cores, sans 106, albeit in trace amounts (Table 4.1). The source of silica is thought to be the result from early dissolution of labile silicate grains. Iron oxides/hydroxides and Ti-oxides could precede chert and possibly glauconite however, their extent is too limited to ascertain paragenesis prior to quartz overgrowths. It is possible these oxides in some sections of core precipitated later during eogenesis from meteoric waters when the Big Clifty parts of the basin were exposed or nearly exposed. This, and the evidence of exposure, are discussed later in subsection 5.1.3.

It is assumed that as pore waters became increasingly reduced with burial, pyrite likely began to precipitate in association with: 1) organics, 2) phyllosilicates along mud laminae, and 3) glauconite clasts and cement. Associations between pyrite and phyllosilicates are common and expected in pore waters of marine origin. Difficulty discriminating between early and later phases of pyrite is due to there being few conspicuous features with crosscutting relationships. With the exception of where pyrite

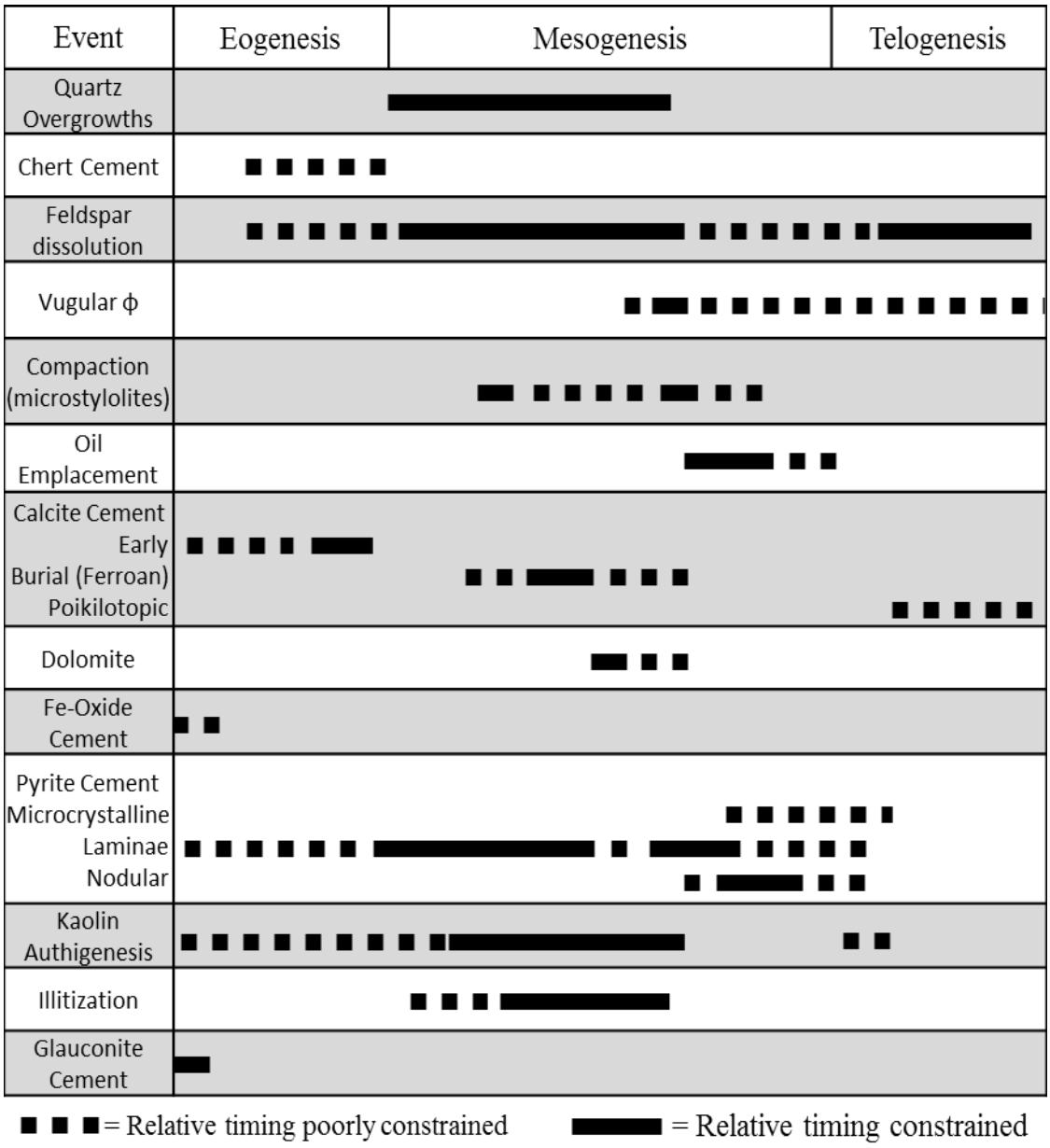

Figure 5.1. Paragenetic sequence of events based on petrographic observations. No scale implied. See text for constraining relative timing of compaction and development of vuggy porosity.

interrupts quartz overgrowths, the majority of pyrite precipitated after the development of quartz overgrowths. This later pyrite could have precipitated from burial brines with or without hydrocarbons, which all sampled core sections contained at one point in time. Early calcite that precipitated before quartz cementation was observed solely in sample 109c2-b4 where it exists within glauconite (Figure 4.12). Authigenic kaolinite also likely

began to form during eogenesis however, much of the observed kaolinite occluding interparticle porosity precipitated during mesogenesis.

5.1.2 Mesogenesis

Most of the diagenetic alterations observed in samples are mesogenetic. Quartz cementation (overgrowths) occurs early during mesogenesis. Quartz cementation is greater in samples from cores 104, 105, and 109 than those of 106, 107, and 108. Quartz overgrowths in these better cemented samples were thicker and euhedral terminations more distinct than those of cores 106, 107, and 108. Additionally but not surprisingly, these better cemented cores generally contained fewer mud laminae and microstylolites, but larger pore throats. The association of these last two features is at least partially attributable to the greater degree quartz of cementation in these cores. The source of silica in quartz overgrowths is likely similar to that of chert, produced from weathering of labile minerals both in situ as well as elsewhere that has been transported to the framework grain that it cements. Well-developed quartz overgrowths are visible within the reservoir of 104c1-b10 as are the remnants of such overgrowths in the reservoir seal (Figure 4.39).

Authigenic kaolinite and feldspar weathering are largely coeval with quartz cementation with some former framework grains possessing early epitaxial quartz overgrowths despite being weathered to kaolinite later (Figure 4.13D). The majority of observed primary and secondary pores filled with kaolinite and the associated weathered feldspars and ghost grains appear un-deformed by compaction. This generalization is less true in very-fine grained sandstone samples in which kaolinite cement and feldspar grains are easily be distinguished with OM-CL. Illitization of authigenic and detrital clays likely

occurred throughout burial but is best preserved in samples with little compaction. Vug development in samples 104c1-b10 and 107c2-b5 and kaolinite in 104c1-b10 occurred after major compaction in these samples. Evidence suggesting this is that these cavities and cement would have otherwise been destroyed. Compaction is poorly constrained relative to growth of ferroan burial dolomite and calcite as neither of these cements are crosscut by microstylolites nor grow from them.

Burial calcite and dolomite precipitated after initial development of quartz overgrowths and authigenic kaolinite, and occurring before the development of nodular pyrite. Stained carbonate from cores 106, 107, and 108 indicates a ferroan composition and all calcite and dolomite from these cores was burial and precipitated post-quartz overgrowths. There are potentially two generations of mesogenic carbonate with an early mesogenetic generation of calcite being dolomitized from brines which was later followed by a generation of ferroan calcite. Alternatively, all ferroan calcite could have precipitated in one generation with dolomitization or precipitation from brines. This would result in a few patches of dolomite. The magnesio-ferroan calcite in sample 109c1-b5 (Figure 4.24) with 'pin-pricks' of luminescence is the only evidence for potential alteration of pre-existing calcite. Clear, non-replacive, interparticle, baroque-dolomite crystals >100-μm diameter and with no visible inclusions is considered by some (Spötl and Pitman, 1998) to typify non-replacive brinal dolomite precipitated from warm brines. The presence of baroque or saddle dolomite cement is significant in that it is a reliable geothermometer. Such dolomite precipitates at minimum burial temperatures of 60°–80° C but more commonly forms at 90°–180° C. The latter of range of temperature coincides with the oil "window" of catagenesis (Spötl and Pitman, 1998; Machel, 2005). The brines

that precipitated ferroan dolomite and possibly burial calcite do not appear to have been accompanied by hydrocarbons as no oil inclusions were noticed within these cements nor were gangue minerals fluorite, barite, sphalerite, or galena observed which characterize hydrothermal source of brines.

Dissolved Fe^{2+} in the brines that produced dolomite and ferroan calcite may have contributed to euhedral authigenic pyrite along mud laminae and within primary and secondary pores. However, there is no textural relationship that suggests precipitation of pyrite was synchronous with dolomite, although there are a few occurrences of non-nodular euhedral pyrite interrupting quartz overgrowths. As stated earlier, non-nodular and non-microcrystalline pyrite cement phases are difficult to constrain in paragenesis. Pyrite cement associated with laminae as well as nodular forms of pyrite occur in oil-stained sections of core, although nodular pyrite is exclusively observed in oil-saturated reservoir sections of core. Nodular pyrite is believed to be nearly penecontemporaneous with oil emplacement with the accompanying brines providing dissolved Fe^{2+} and sulfides. Nodules of pyrite commonly occur near or along mud laminae. Some mud laminae also possess microstylolites and fractured grains within pyrite nodules. Oil staining and insoluble organics concentrated along microstylolites places the oil migration before some of the latest compactional events in paragenesis (Figure 5.1).

Later, secondary oil migration, or changes in the oil and water leg of the reservoir could preclude any relative timing between oil and compaction with other events such as the development of vugs in cores 104 and 107. Ostensibly, vugs and kaolinite within vugs of sample 104c1-b10 formed following the latest compaction, which would have destroyed the cavities. Vug development and authigenic kaolinite must also have

occurred prior to oil emplacement as oil would inhibit kaolinite precipitation within vugs if not arrest silicate diagenesis altogether (Figures 4.28 and 4.29). Vugs and authigenic kaolinite cement within them appear related in sample 104c1-b10, presumably the result of labile mineral dissolution and in situ precipitation of kaolinite as an alteration product. However, in the thin section of sample 104Bc1-b10 that was made from the same billet as 104c1-b10, a large lithic clast is visible within the reservoir of 104c1-b10 that contains large pores, possibly plucked during thin sectioning (see Appendix B for scanned images of thin sections). While the locations of both observed vugs in sample 104c1-b10 (Figures 4.28 and 4.29) do not coincide with this clast of 104Bc1-b10, it is possible that these vugs developed within similar but smaller lithic clasts. Compactional events following development of vuggy porosity (Figure 5.1) were not experienced by 104c1-b10.

The timing of vug development in 107c2-b5 is less well constrained than in 104c1-b10, although the vugs of 107c2-b5 similarly developed following compaction. Vug development in 107c2-b5 could have preceded or been coeval with oil emplacement with warm brines and/or organic acids dissolving preexisting carbonates and labile minerals to form the vugs. Alternatively, and somewhat less plausibly, is that vug formation in 107c2-b5 occurred after oil emplacement during telogenesis. This process would entail water flushing, thereby dissolving pyrite, carbonate, or other minerals unstable in the meteoric-phreatic realm. Dissolution of pyrite concentrated along lamina would also account for why the vugs in 107c2-b5 are horizontally orientated (Figure 4.30). Such vugs resemble laminar fenestral pores or “bird’s-eye vugs” typical of tidal carbonates despite the silica-rich composition and size of the framework grains. Pyrite,

however, is very scarce in both tight and porous zones of sample 107c2-b5. Thus, the relative timing of the precipitation and potential dissolution of pyrite is difficult to constrain. The core section from which 107c2-b5 was sampled appears white. Despite the white appearance, Dean Stark analysis conducted by Loring Tarcore Labs of an interval that corresponds to the core section from 107c2-b5 was sampled, calculated a greater saturation of pores by oil (0.519) than water (0.481) (see Appendix A, section A.1, for Loring Tarcore Labs analyses relevant to this study's samples).

Microcrystalline pyrite exists in the reservoir seal of 104c1-b10 and is associated with oil and opaque coatings, preceding seal forming poikilotopic calcite. Microcrystalline pyrite and opaque coatings appear to concentrate about chert and weathered feldspars, occluding secondary and microporosity therein, as well as coating nearby framework grains. There is selectivity exhibited by microcrystalline pyrite and unidentified opaques towards weathered grains. This selectivity suggests two possibilities: 1) Iron in the pyrite is locally sourced from precursor alterations; and 2) alteration products on weathered grains are preferential surfaces on which pyrite may precipitate and opaques adhere.

5.1.3 Telogenesis

Poikilotopic calcite is the last cement to precipitate, as is evident by it replacing and embaying earlier cements and framework grains. Poikilotopic calcite is inferred to have precipitated during telogenesis following oil emplacement, vug development, microcrystalline pyrite and opaque coatings. The large, poikilotopic, calcite crystals in sample 104c1-b10 cement oil-stained clays and grains placing this diagenetic phase post-oil in paragenesis. Development of vuggy porosity and microcrystalline pyrite and

opaque coatings in 104c1-b10 potentially may have formed during telogenesis but these events occurred prior to poikilotopic calcite cementation. Similarly, the nodular pyrite observed in the section of core from which 105c3-b1 was sampled (see Figure 3.1F), occurs less than 2 ft above 105c3-b2 (Table 3.1) and, potentially, also could have precipitated during telogenesis (see Appendices A for relative core intervals and sample position and B for images of sampled core sections). Nodular pyrite cannot be texturally constrained directly by poikilotopic calcite as neither cement is observed in the same thin section. In the seal of 104c1-b10 compaction is evident with sutured quartz grains and microstylolites that crosscut framework grains and earlier cements. These pressure dissolution features do not extend across poikilotopic calcite (Figure 4.25). This disparate textural context constrains precipitation of poikilotopic calcite, as well as the authigenic kaolinite it replaces within the vugs of the seal and reservoir. Such calcite, therefore, is discerned to be post-compaction.

The cuspate reservoir-seal boundary in 104c1-b10 suggests crystal growth was sufficiently slow to maintain the optic axis as the poikilotopic calcite destroyed primary porosity, and replaced earlier framework grains and cement, all while mobile hydro-carbons were expelled to the reservoir portion of core. The size of the poikilotopic calcite crystals in 104c1-b10 are considerably greater than those in 105c3-b2, having crystal diameters at minimum on the centimeter scale compared to the millimeter diameters at maximum in 105c3-b2. As stated before, poikilotopic calcite cement is less replacive around microcrystalline pyrite and opaque coatings in sample 104c1-b10.

There are a few locations in 104c1-b10 and 105c3-b2 where poikilotopic calcite is not brightly-luminescent but rather is non-luminescent (Figure 4.28C) or dully-

luminescent (Figure 4.11). Non-luminescent calcite in sample 104c1-b10 is in the reservoir's margins and is contiguous or separated by less than 100 μm, with the poikilotopic calcite of the reservoir seal with which it shares extinction angles under cross-nicols (Figure 4.28). Non-luminescent calcite is not observed outside of the reservoir in core 104c1-b10, and transition of the luminescence is coincident with the boundary between the reservoir and reservoir seal. This change, in calcite from brightly-luminescent to non-luminescent indicates a deficiency in Mn^{2+} content within the calcite of the reservoir to activate luminescence, much less overcome the quenching effects of Fe^{2+}. This lack of luminescence is likely due to immiscible oil within the reservoir hindering diffusion and advection of aqueous phases containing Mn^{2+} to the growth surface of the encroaching calcite.

Transitions are similarly abrupt in sample 105c3-b2 between areas of dully- and brightly-luminescent calcite (Figure 4.11). Not all instances of dully-luminescent calcite are contiguous with brightly-luminescent calcite, however (Figure 4.10). Neither the contiguous extensions (Figure 4.11) nor the separate patches (Figure 4.10) of dully-luminescent poikilotopic calcite in 105c3-b2 parallel any discernable oil saturation, diagenetic texture, or rock fabric. The difference in luminescence in 105c3-b2 does not resemble concentric zonation. Concentric zonation parallels the growth interfaces of crystals and can record changes in pore fluids with regard to the activities of Mn^{2+} and Fe^{2+} relative to Ca^{2+} (see Appendix C, subsection C.1.6, for more details regarding zonation). Dully-luminescent calcite from 105c3-b2 is unmistakably quenched and, thus, the Mn^{2+}:Fe^{2+} content is lower than in the brightly-luminescent calcite. Immiscible fluids limiting solute transport are believed to be a factor contributing to the deficiency of Mn^{2+}

content in dully-luminescent calcite of 105c3-b2. Poikilotopic calcite is less contiguous and patchier in sample 105c3-b2 than 104c1-b10 which, may be due to sample 105c3-b2 being relatively porous, 12.6% (Table 4.1). Greater porosity facilitates calcite precipitation in more places, despite some locations being further removed from the Mn^{2+} solute supply than others, resulting in some calcite patches that dully-luminescent and others that are not.

Concentric zonation was not observed in the luminescence of poikilotopic calcite from 105c3-b2 or 104c1-b10. The absence of concentric zonation in large poikilotopic crystals does not mean that pore-fluid chemistries remained constant during crystal growth. It does suggest, however, that the activity ratios of Mn^{2+} and Fe^{2+} to Ca^{2+} were sufficiently stable throughout the crystal's slow growth for the precipitated calcite to have consistent luminescence. Dull luminescence in calcite suggests available $Mn^{2+}_{(aq)}$ and $Fe^{2+}_{(aq)}$ during precipitation but with greater incorporation of Fe^{2+}. The bright and the dully-luminescent calcite within 105c3-b2 are both likely ferroan and would react to a potassium ferricyanide stain (Fe >1000 ppm). The calcite of 104c1-b10 may also react to a potassium ferricyanide stain, and possibly to a similar degree as that of 105c3-b2. Although sample 104c1-b10 contains little pyrite and no dully-luminescent calcite, the processes and pore fluids that precipitated in the poikilotopic calcite in Core 105 are likely similar to those responsible for the poikilotopic calcite in Core 104. Poikilotopic calcite cement is distinct from other burial carbonate phases. It is more abundant and more replacive than mesogenetic burial calcite. It also lacks any association or textural relationship with earlier phases of calcite or dolomite, baroque or otherwise. Despite the

differences in luminescence, poikilotopic calcite in both 105c3-b2 and 104c1-b10 share a common diagenetic origin post-oil emplacement.

It was once suggested to the author by another researcher that the poikilotopic calcite could be an early replacive cement. The consideration of poikilotopic calcite as an early cement is not meritless as evidence of exposure in the form of paleosols within the Big Clifty have been documented by earlier researchers (Treworgy, 1988; Horowitz and Kelly, 1997; Smith and Read, 2001; Nelson et al., 2002). Such an exposure surface is preserved roughly 16 ft above 104c1-b10 (Figure 5.2A). A similar feature is observed in Core 106 (Figure 5.2B) and is visible as a gamma spike at ~332-ft depth in a nearby well log (see Appendix A, section A.4, for subsurface correlation with this well). This exposure surface occurs elsewhere in the basin near the top of the Big Clifty, with the exception of Hardin and Hart counties in Kentucky. There are two textural features that best repudiate the possibility, as was suggested by this researcher, that poikilotopic calcite could have been an early replacive cement that preceded oil emplacement. First, microstylolites crosscut framework grains and earlier cements but not poikilotopic calcite (Figure 4.25). Second, the transition of calcite from brightly-luminescent to non-luminescent is coincident with the reservoir-seal contact (Figure 4.28). The only diagenetic phases or minerals that potentially are tied to early exposure and the development of paleosols are the few locations were iron oxides are visible in core.

Figure 5.2. Evidence of exposure prior to burial in unsampled core section from cores 104 and 106. Scale bar in both images is in centimeters. A) Pebble- to cobble-sized blocks of calcareous mudstone suspended in a green glauconitic cement crosscut by siderite veinlets in Core 104 core 1 box 4. Exposure surface is approximately 16 ±3 ft above sampled section of 104c1-b10 (466-ft elevation). B) Glauconitic shale and siltstone with calcareous cobbles in Core 106 core1 box 6.

5.2 Reservoir and Seal Evolution

The effects of diagenesis on the reservoir quality of the Big Clifty are mainly destructive. Few processes preserve or result in long-term enhancement of porosity and permeability (Table 5.1). The most recent diagenetic events of importance to reservoir quality are those that involve interactions between formation waters, meteoric water, and oil brines. The Big Clifty was likely a water-wet reservoir initially following oil emplacement with immiscible hydrocarbons occupying larger pore throats and displacing formation waters into nearby capillaries and pore fringes. Silicate diagenesis likely continued albeit very limited with the bulk of the oil phase occupying a majority of the pore network. Diagenesis and transport of aqueous phases continued to be retarded by oil until surfaces became oil-wet and interactions between crystals and aqueous phases were arrested (Bjørlykke and Jahren, 2015). Not all surfaces became oil wet or at least did not remain so as evidenced by the post-oil poikilotopic calcite in samples 104c1-b10 and 105c3-b2, and by the incomplete impregnation of epoxy of 107c2-b5 due to differential wettability between its porous and tight zones.

Sulfides (H_2S and HS^-) and dissolved iron (Fe^{2+}) within aqueous phases that accompanied oil migration preferentially precipitated pyrite on phyllosilicates and surfaces of weathered grains and others nearby. Desorption of iron and complexed Fe-oxide/hydroxides from authigenic clays as well as organics bound to clays are the most probable cause for the selectivity of pyrite crystallization and opaque coatings. The iron of these earlier weathering products are likely derived from labile Fe-bearing minerals such as biotite, ilmenite and any number of Fe-oxyhydroxides such as goethite. Organic acids associated within migrating petroleum and brines, such as carboxylic, naphthenic,

Event	Source	Effect on Reservoir Quality	Evidence in Cores
Quartz Overgrowths	SiO_2 from clays, labile silicates, and replaced SiO_2 grains	Initial $\downarrow\phi$, Long term ϕ preservation	All
Chert Cement	SiO_2 from clays, labile & replaced SiO_2 grains	Initial & Long term $\downarrow_{negligible}\ \phi$	104, 105, & 107–109
Feldspar Dissolution	Formation waters, possibly organic acids	$\uparrow_{minor}\ \phi^{2nd}$ & $\uparrow[H_4SiO_4]$	All
Vugular ϕ Development	Unknown, Pyrite or Carbonate dissolution?	Initial $\uparrow_{negligible\ -\ moderate}\ \phi^{2nd}$ & $K_{e,}$ Long term $\downarrow_{variable}\ \phi$ & $K_{e,}$	104 & 107
Compaction (microstylolites)	Burial, Compaction	$\downarrow_{variable}\ \phi$ & K_e	Minimal: 104, 105, & 109 Moderate: 106–108
Oil Emplacement	New Albany	Surface poisoning $\downarrow$cementation & $\downarrow$in diffusion and advection	All
Calcite Cement Early Burial (Ferroan) Poikilotopic	Initial pore fluids, brines, meteoric HCO_3^- loading	Early: Initial $\downarrow\phi$, Long term $\uparrow\phi$ Burial: $\downarrow_{minimal}\ \phi$ Poikilotopic: $\downarrow_{variable}\ \phi$ & K_e, $\downarrow_{severe}$ = Trap, $\downarrow_{moderate}$ = Reservoir	Early: 109 & possibly 105 Burial: 104–109 Poikilotopic: 104, 105
Dolomite	Brines	Initial $\downarrow$ & Long term $\uparrow_{negligible}\ \phi$	106, 107, & 109
Fe-Oxide Cement	Initial/early oxic cement	$\downarrow_{negligible}\ \phi$	Trace: 104, 105, 107, & 109
Pyrite Cement Microcrystalline Laminae Nodular	Anoxic pore fluids, Iron-oxide sulfate redox reactions w/ microbes, brines	Microcrystalline: $\downarrow_{minimal}\ \phi^{primary\ \&\ 2nd}$ Laminae/Nodular: $\downarrow_{minimal\ -\ moderate}\ \phi^{primary\ \&\ 2nd}$ & $\downarrow_{negligible\ -\ minimal}\ K_e$	Microcrystalline: 104 Laminae: 105–109 Nodular: 105 & 107–109
Kaolin Authigenesis	Feldspar hydrolysis	$\downarrow K_e$ & $\downarrow_{minor}\ \phi^{primary}$ & $\uparrow_{minor}\ \phi^{2nd}$	All
Illitization	Feldspar & kaolin alteration	$\downarrow_{negligible}\ \phi$	All
Glauconite Cement	Reduced marine fluids	$\downarrow_{negligible\ -\ minimal}\ \phi$ & K_e	104, 105, & 107–109

ϕ = porosity; $\phi^{primary}$ & ϕ^{2nd} (primary and secondary porosity respectively)

K_e = effective permeability

$\downarrow$ / $\uparrow$ = Decrease / Increase

Table 5.1. Effects of various diagenetic events and fluid migration events upon reservoir quality.

and acetic, can easily promote dissolution of labile minerals (Surdam et al., 1984; Stoessell and Pittman, 1990; Surdam et al., 1993; Lewan and Fisher, 1994; Ali et al., 2010). Organic acids may also be produced within formation waters which and along with sulfate (SO_4^{2-}) and sulfides be involved with redox reactions with earlier Fe-oxide/hydroxide cements to form pyrite (Machel, 2001). Additional reactions can possibly elevate concentrations of bicarbonate and thereby promote calcite precipitation (see Table 5.2) (Stoessell, 1992).

Numerous reactions are known to occur in sediments between sulfur and iron bearing compounds, many of which are microbially mediated and involve degradation of hydrocarbons (Schippers and Jørgensen, 2001). The presence of sulfate is especially important in sulfate-reduction reactions, by thermal or bacterial means. Such reactions degrade hydrocarbons as well as produce H_2S ($H^+ + HS^-$) and HCO_3^- ($H^+ + CO_{2(g)}$). The hydrogen sulfides "sour" the petroleum within the reservoir, as bacterial sulfate reduction (BSR) occurs at lower temperatures than does thermal sulfate reduction (TSR) processes (Figure 5.3) (Machel, 2001; 2005). BSR more readily occurs in shallow reservoirs where nutrients are more abundant and pressures and temperatures are not as prohibitive as deep burial environments (Machel, 2005). Gypsum or anhydrite were not observed in thin section although no steps were taken to prevent dissolution of sulfate these bearing minerals. The only known occurrences of these minerals proximal to Big Clifty is the gypsum in the upper levels of Mammoth Cave and (White and White, 2003). A recent study by Metzger et al. (2015) based on isotopic data of gypsum demonstrated that the $\delta^{34}S$ values of gypsum from cave passages are consistent with $\delta^{34}S$ of pyrite in immediately adjacent strata, which entails units other than the Big Clifty. They

Methane-Sulfate Redox: $CH_4 + SO_4^{2-} \rightarrow HCO_3^- + HS^- + H_2O$ (1)

Carbohydrate-Sulfate Redox: $2CH_2O + SO_4^{2-} \rightarrow 2HCO_3^- + HS^- + H^+$ (2)

Acetate-Sulfate Redox: $CH_3COO^- + SO_4^{2-} \rightarrow HS^- + 2HCO_3^-$ (3)

Acetate Methanogenesis: $CH_3COO^- + H_2O \rightarrow CH_4 + HCO_3^-$ (4)

Hydrogen Destruction and Iron-Hydroxide and Sulfide Redox:

$FeOOH + 1.125HS^- + 0.875H^+ \rightarrow FeS + 0.125SO_4^{2-} + 1.5H_2O$ (5a)

$FeO + HS^- + H^+ \rightarrow FeS + H_2O$ (5b)

$FeOOH + 1.875HS^- + 0.125SO_4^{2-} + 2.125H^+ \rightarrow FeS_2 + 2.5H_2O$ (5c)

$FeO + 1.75HS^- + 0.25SO_4^{2-} + 2.25H^+ \rightarrow FeS_2 + 2H_2O$ (5d)

General Carbohydrate-Sulfate-Goethite Redox:

$9CH_2O + 4SO_4^{2-} + 4FeOOH \rightarrow 4FeS + 9HCO_3^- + H^+ + 6H_2O$ (6)

Mobilization and Oxidation of Fe^{2+} from Biotite Weathering:

$2K(Mg_2Fe)(AlSi_3)O_{10}(OH)_2 + 10H^+ + 0.5O_2 + 6H_2O \rightarrow Al_2Si_2O_5(OH)_4 + 2K^+ + 4Mg^{2+} + 2Fe(OH)_3 + 4H_4SiO_4$ (7)

Pyrite Precipitation from Amorphous Solid Iron (II) Monosulfide (FeS):

$Fe^{2+} + 2HS^- \rightarrow FeS_{(amorph)} + H_2S$ (8a)

$FeS_{(amorph)} + H_2S \rightarrow FeS_2 + H_2$ (8b)

Pyrite Precipitation from Iron (II) Bisulfide (SH) complexes:

$Fe^{2+} + HS^- \rightarrow Fe(SH)_X + H_2S$ (9a)*

$Fe(SH)_X + H_2S \rightarrow FeS_2 + 1.5H_2$ (9b)*

Calcite Dissolution/Precipitation: $CaCO_3 \leftrightarrow Ca^{2+} + CO_3^{2-}$ (10)

Carbonic Acid: $CO_{2(g)} + H_2O \leftrightarrow H_2CO_3$ (11)

Bicarbonate: $HCO_3^- \leftrightarrow H^+ + CO_3^{2-}$ (12)

Chemical formula for Bisulfide is HS^-

* = Equation unbalanced with respect to H and S

Equations (1), (2), and (5) are from Stoessell (1992), (3) is from Bose et al. (2013), (4) is from Ngonadi (2013), (6) is from Morse et al. (1997), (7) and (10–12) are from Kehew (2001), and (8) and (9) are from Rickard (1994).

Table 5.2. Possible low P/T reactions involved in precipitation of observed pyrite and calcite. Equations are from above listed authors.

concluded that most, if not all, sulfate in gypsum observed in passages of Mammoth Cave is derived from oxidation of pyrite from adjacent, nearby strata and not from dissolution of sulfate from deeper units such as sedimentary anhydrite or gypsum within the St. Louis nor oxidation of pyrite within the Big Clifty.

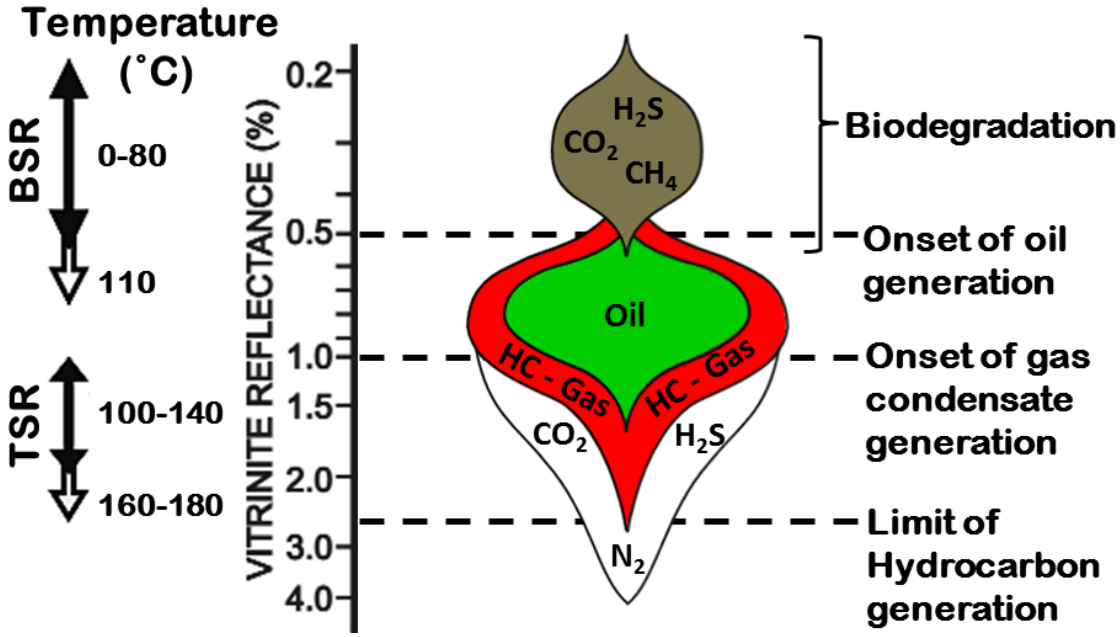

Figure 5.3. Generalized thermal ranges of catagenesis and bacterial and thermochemical sulfate reduction (BSR and TSR) and their expected products as well as expected vitrinite reflectance. Solid arrows denote normal ranges of BSR and TSR while hollow arrows denote anomalous conditions. Thermal gradients assumed are considered to be normal (25°–30° C/km). Modified by the author from Machel (2005), based on Machel (2001).

The absence of gypsum or anhydrite does not substantiate the precipitation of the observed pyrite as a byproduct of redox reactions involving in situ sulfate (SO_4^{2-}) and Fe^{3+} bearing minerals with hydrocarbons. Ferric (Fe^{3+}) iron could be reduced via redox reactions and precipitate in pyrite however the volumetrically limited quantities of minerals containing oxidized iron make them an unlikely source of iron. Redox of in situ ferric iron may contribute to some of the pyrite observed in thin sections (e. g., microcrystalline pyrite in 104c1-b10), but it cannot account for the iron where pyrite

cement is volumetrically significant. It is also dubious that redox of in situ oxides were a major reactant in biogeochemical pathways capable of producing high alkalinities and driving poikilotopic calcite cementation. Basinal brines either separate or accompanying oil are the probable source for a majority of the iron in pyrite observed in thin sections. Liesegang bands and iron staining are a common feature in tar seeps and asphaltic deposits of Chesterian and Pennsylvanian strata of western Kentucky where Fe^{2+} in minerals or aqueous phases that accompany hydrocarbons are oxidized (Figures 5.4 and 5.5) (May et al., 2007; May, 2013).

The presence of local surficial asphaltic deposits, the relatively shallow (<520 ft) depths of the sampled core intervals' (see Appendix A for more subsurface data of the cored wells), and the high viscosity oil are all reasons independent of petrographic observations to suspect meteoric fluids influenced reservoir quality. Biodegradation is most likely responsible for increasing the viscosity of the oil, and producing the bitumen and organic residuum that persisted in billets even after several treatments of organic solvents prior to those conducted by National Petrographic Inc. Various microbes were likely introduced from the mixing of freshwater with basinal brines and oil. Imbibed meteoric water may be responsible for the formation of the reservoir seal in 104c1-b10 as well as the luminescence of the calcite. Some Mn^{2+} activating luminescence in calcite is probably also locally sourced from replaced minerals such as feldspars (Figure 4.35). According to Gucsik et al. (2015) Mn^{2+} occurs in terrestrial feldspars in trace amounts. Plagioclase has higher concentrations of Mn^{2+} than alkali feldspars (<10 ppm) presumably because Mn^{2+} is more similar in ionic radius and valence to Ca^{2+} than Na^{+} or K^{+} (Götze et al., 2000; Gucsik et al., 2015). Reducing conditions allow for Mn^{2+}, Fe^{2+},

Figure 5.4. Liesegang banding in Caseyville Sandstone in Indian Creek Quarry in Sweeden, Kentucky. Quarry is located in northeastern Edmonson County, Kentucky, west of Mammoth Cave National Park, location not shown. Hammer-head length is 7 in. From May (2013).

Figure 5.5. Tar seep and oxidation of iron in the Big Clifty Sandstone, in Hardin County, Kentucky. Hammer length is 1 ft. Photographed section of the northern side of Wendell H. Ford (formerly Western Kentucky) Parkway, mile marker 120.0 (see section A.8 in Appendix A for location). From Butler and May (2013).

and Ni^{2+} to be incorporated into the crystal lattice of calcite. Nickel is known to occur with oil within the Big Clifty and may contribute to some of the quenching of luminescence in poikilotopic calcite within the reservoir (Reynolds et al., 1988; Lewan et al., 2002). Although currently the oil within the reservoir is viscous, it must still have been mobile during the precipitation of poikilotopic calcite in Core 104. Calcite precipitation, in addition to replacing preexisting minerals, displaced mobile oil from pores. There are only a few observed occurrences of hydrocarbon residue that have been enveloped by calcite (Figure 4.37). Porosity in what now comprises the reservoir seal of 104c1-b10 may have initially been slightly greater than in the current reservoir, and was subsequently invaded by aqueous phases until calcite precipitation eventually occluded these pores and sealed the reservoir. Conversely, cores with stark contrasts in oil-saturation geometries that are concordant with the rock fabric (Figure 1.D and Figures 3.1L&M) are due to the viscous-oil occupying the small pore throats, and the oil-wet surfaces of the finer grains resisting water flushing.

Replacement of framework grains and cements by poikilotopic calcite is believed to occur through force of crystallization. Supersaturation of pore fluids with respect to calcite and saturation or undersaturation of quartz, feldspar, and other replaced minerals can cause the precipitation of calcite to generate stresses normal to the crystal interface of the other minerals. The precipitation of calcite stress can induce dissolution of the undersaturated or saturated mineral (Fletcher and Merino, 2001; Machel, 2005). Supersaturation and saturation-undersaturation fluid mechanisms would explain why calcite is unable to replace grains coated with hydrocarbon residuum (i.e., hydrophobic crystal surface poisoning) (Drever, 1997). The extremely bright luminescence in Figure

4.35 is presumably due to additional Mn^{2+} liberated by and immediately incorporated into the crystal lattice of the replacing calcite creating locally a more luminescent zone that mimics the former grain boundaries.

While the mixing of two waters saturated with respect to calcite often leads to the dissolution of calcite, the mixing of basinal brines and meteoric water can potentially result in the supersaturation and precipitation of calcite (Morse et al., 1997). Either a decrease in pressure (pCO_2), or an increase in temperature can enhance calcite precipitation. In the shallow subsurface, calcite precipitation from brines is more likely to occur in response to a decrease in pressure; calcite precipitation from meteoric waters is more likely to occur in response to an increase in temperature. Dissolved carbonate in brines has numerous potential sources. These sources span diagenesis and include formation waters of carbonates, as well as dissolution of such formations from compaction, and faulting, or organic acids in migrating oil. Buoyant ascension along faults and carrier beds are the likely paths oil and brines migrated along and similarly, these paths are along which meteoric waters descended (Figure 5.6). Meteoric waters are rich in bicarbonate from the dissolution of Mississippian carbonates that comprise the karst regions in south-central Kentucky. Regional groundwater flow follows bedding dip basinward (Figure 2.4), although most groundwater flow is locally controlled by joints and dissolution enlarged cavities commonly affecting drainage. Both Core 104 and 105 were taken from wells near faults, and tributaries with karst drainages (Figure 2.10, and see Appendix A for local geologic maps of these cored wells).

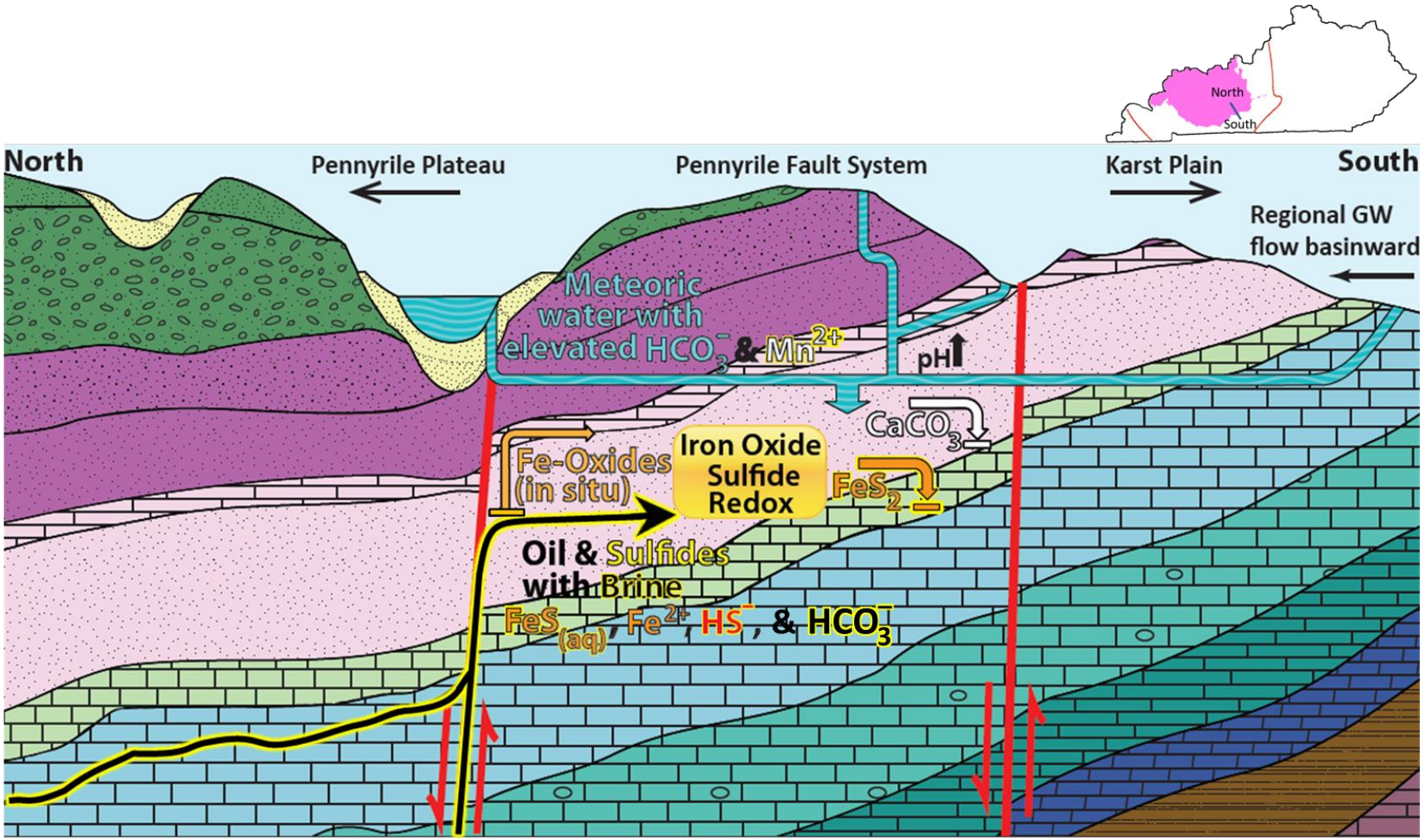

Figure 5.6. Diagrammatic cross section of study area with potential geochemical pathways. Water flushing and microbial activity has likely accompanied and compounded compartmentalization and thus degrading the quality of oil with consumption of shorter chain hydrocarbons (heavy-end concentration). Index map above shows transect and Chesterian rocks (pink) in Kentucky.

According to Lloyd and Lyke (1995), circulation of groundwater in Mississippian aquifers proximal to the Dripping Springs Escarpment (southern and western topographical expression of the Pennyrile Plateau) can occur at 500-ft depth, although most mixing occurs at <300 ft. Freshwater-saltwater interfaces are usually shallow in Pennsylvanian rocks at <500-ft depth, but may range from 100–1000-ft depth, with shallow fresh-saline interfaces commonly occurring beneath major stream valleys. Lloyd and Lyke (1995) reported that the iron content within these subsurface mixing zones is generally low, at >0.3 ppm. A review of the available water-quality data within the vicinity of the cored wells also showed elevated amounts of sodium and chlorine. The one water sample that did test for iron was corroborating mixing; however, only one well tested for iron reported 0.11 ppm (see Appendix A for water-quality data).

The relatively slow growth of calcite in 104c1-b10 led to larger crystals and resulted in the occlusion of pores and the displacement of oil along a contiguous front. Aqueous phases, likewise, would be limited to available porosity along poikilotopic crystal boundaries potentially concentrating dissolved Mn^{2+} and Fe^{2+}. This ionic concentration led to more homogenous and consistent luminescence throughout crystal growth. Impedance of solute transport, including Mn^{2+} and Fe^{2+} to the calcite crystal interface is the most probable cause for lack of luminescence in reservoir seal extensions in 104c1-b10 rather than quenching of luminescence from increased Fe^{2+} concentration. Loss of permeability due to calcite growth would more negatively affect a meteorically sourced aqueous phase of Mn^{2+} than an aqueous phase existing within the reservoir.

The transfer of heat from either oil or brines to infiltrating meteoric waters coupled with water flushing and secondary migration of petroleum out of the reservoir

would create favorable conditions for calcite precipitation and transport of aqueous phases. Advection and meteoritic water flushing could sustain calcite precipitation and is the more probable geochemical route responsible for the poikilotopic calcite. A decrease in pressure (pCO_2) would likely result in calcite precipitation within the water leg of the reservoir, which is clearly not the case (Figures 1.1A&B, 3.1A, and 3.34). The precipitation of calcite due to such conditions likely would not have resulted in continual crystal growth that displaced oil within the oil leg, nor maintained a similar optic axis. Additionally, if a preexisting aqueous phase within the reservoir did precipitate calcite in appreciable amounts, its distribution would be patchy, contain "snap-offs" of oil, and have variable luminescence, if at all. Such a calcite would likely have a ferroan content that exceeds ~1% Fe by weight, potentially concentrations detectable with SEM-EDS (>2% by weight) such as the calcite in Figure 4.24.

In any case both meteoric and brine waters are reduced; no oxidation fronts or gradients are suggested by mineral assemblages observed within core sections. It is possible that water flushing dissolved preexisting minerals to create the vugs observed in 107c2-b5, however, the iron-oxides of core section below where 107c2-b5 was sampled has only occurred post-drilling as such cements are easily brushed off (see Figure 3.1L, and Appendix B for box-core images). Both brine and freshwater were reported in driller notes from other local wells at shallow (<500 ft) depths (see Appendix A for formation waters encountered).

5.3 Basinal Context of Carbonate

The most immediate and obvious supply of bicarbonate would be that from the Green River, and its tributaries including the Barren River and associated aquifers. Cores 104 and 105 are located between the confluence of the Green and Barren Rivers (Figure 2.10). These rivers have well developed karst conduits, with the formation of Mammoth Cave occurring since the Late Pliocene (Granger et al., 2001). The fabric-discordant oil saturations and authigenic carbonate are not unique to cores 104 and 105, or other subsurface Big Clifty rocks proximal to the Green River and its tributaries. Fabric-discordant oil saturations due to authigenic carbonate are known to occur within Logan and Grayson counties (Figures 5.7, 5.8, and 2.4). The rocks in Figures 5.7 and 5.8 were retrieved from Chesterian units located proximal to fault systems in the southeastern margin of the Illinois Basin (Figure 2.4). These occurrences in Grayson and Logan counties are similar to cores 104 and 105 in that they are down dip from outcropping, older (pre-Chesterian), Mississippian carbonates.

Fabric-discordant oil-saturation geometries due to authigenic carbonate are not known to occur in deeper parts of the basin. Such features are only known to occur along the margin of the Chesterian outcrop and even within the outcrop belt examples of post-oil, authigenic, seal-forming calcite is rarely observed. Replacive authigenic calcite, of both sampled and unsampled sections of cores 104 and 105 (see Figures 3.1A&G, and Figures 4.34A&B, respectively) occur at different relative positions within the Big Clifty. The seal-forming calcite of sample 104c1-b10 (482.3-ft depth) and the unsampled authigenic calcite of Core 104 (~502.9-ft depth) occur in the upper portion of the main sandstone body in Core 104. The stratigraphic positions of 105c3-b2 (~470.8-ft depth)

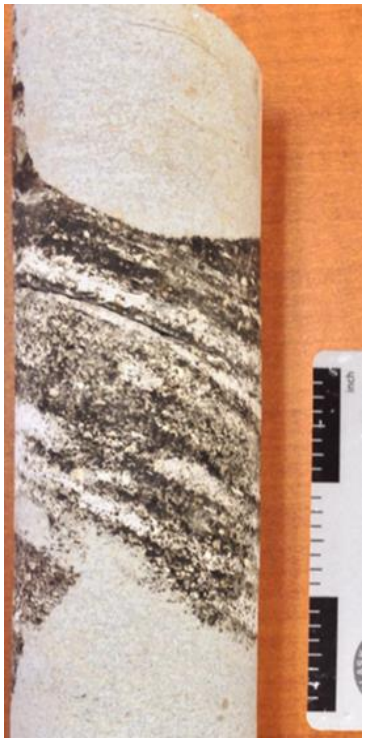

Figure 5.7. Fabric concordant and discordant oil-saturation geometries in core of Haney Limestone <50-ft depth taken from Stampede Asphalt Rock Mine in Logan County, Kentucky. Fabric discordant calcite is the latest calcite generation. For location see Figure 2.4.

Figure 5.8. Diagenetic calcite in asphalt rock sampled from section of Big Clifty exposed during road construction in Grayson County, Kentucky.

and the section containing the unsampled diagenetic calcite section of Core 105 (~480.4-ft depth), occur near the base of the Big Clifty and its contact with the Beech Creek (see Appendix A for sample positions relative to geophysical logs of proxy wells). The depths of the sampled and unsampled core sections are not correlative with one other on the geophysical logs from proxy wells. The only similarity between these sandstone sections is that the beds containing calcite appear to be relatively better sorted and more porous, than the beds which surround them (see Figures 1.1A&B for unsampled box-core images and see Appendix B for sampled box-core images).

The occurrence of authigenic calcite within permeable beds at variable stratigraphic positions suggests multiple carrier beds of aqueous phases similarly precipitating replacive calcite. Communication of waters between carrier beds is restricted by immiscible hydrocarbons, calcite, and strata of low permeability. This an important control regarding aqueous phases involved in the precipitation of reservoir-seal calcite. Waters supersaturated with respect to calcite are ostensibly from a disparate source(s) (i.e., meteoric, brines, regional groundwater) than the aqueous phase in the water leg of the reservoir, given that calcite cement is not pervasive. Capillary pore pressure and beds containing the immiscible phases limit diffusion and dilution of solutes during fluid migration. A similar mechanism was proposed by Meriño et al. (2015), to account for variation in vitrinite reflection of Pennsylvanian coals across depths from the southern to northern parts of the Illinois Basin. These variations are explained by permeability differences below the sub-Absaroka sequence boundary that restricted advection of warm fluids. The variations in coal rank are not only a function of depth but also communication and mixing with permeable carrier beds of warm fluids.

Chapter 6: Conclusions

6.1 Conclusions and Future Work

The cumulative effects of diagenesis on permeability and porosity within the hydrocarbon reservoir of the Big Clifty Sandstone along the Illinois Basin southeast periphery have been predominantly deleterious, yet they create trapping or sealing mechanisms. Oil saturation geometries in the Big Clifty are predominantly concordant with rock fabric. Compaction and precipitation of authigenic kaolinite and pyrite following deposition have further exacerbated permeability restrictions inherited from sedimentation. Quartz overgrowths are best developed in relatively coarse, and moderately- to well-sorted sandstone sections and in stratigraphic intervals typified as those resisting physical compaction. In contrast, there is a paucity of quartz overgrowths in very-fine to fine-grained sandstone with muddy components. Specifically, with regard to concordant and discordant oil-saturations and authigenic calcite, the conclusions of this study are:

- Oil-saturation geometries that are concordant to the observed rock fabric are due to grain size, degree of sorting, extent of quartz cementation, clay content (matrix and cement), presence or absence of stylolites, wettability of the rock, and the viscosity of the oil.
- Oil saturation geometries that are discordant to rock fabric are due to large crystal growths of authigenic calcite or pyrite, in addition to the wettability of the rock and the viscosity of the oil.
- The poikilotopic calcite that forms the interstratal seal and replaces framework grains and cement is the latest diagenetic cement and is not associated with greater calcareous lithic content or earlier carbonate cement generations.
- Optical cold-cathode cathodoluminescence microscopy is an effective tool for differentiating framework grains and authigenic cements particularly detrital quartz and overgrowths where embayment and overprinting of primary minerals is extensive by later authigenic mineral precipitation.

- Poikilotopic calcite is brightly luminescent except for a few locations where extensions of the cement precipitated in locally-restrictive pore networks limiting solute transport of Mn^{2+}.
- Interstratal seals formed by replacive calcite are unique to the southeastern Chesterian-outcrop belt and are only observed in localities that coincide with major karst drainage systems and near-vertical faults based on studied cores in outcrop belt of several counties.
- Multiple carrier beds with geochemically similar aqueous phases are responsible for the precipitation of replacive, post-oil-emplacement calcite observed at different stratigraphic positions within the reservoir of the Big Clifty in cores 104 and 105.
- Mixing of meteoric or phreatic freshwaters buffered in bicarbonate derived from dissolution of updip Mississippian carbonates with basinal brines also buffered in bicarbonate is the most probable explanation for the precipitation of the latest authigenic calcite within the reservoir. This accounts for the source(s) of bicarbonate and the favorable conditions created for calcite to precipitate at the expense of more resilient, both chemically and physically varieties of minerals such as quartz and chert.

Future work should include fluid inclusion and isotopic analysis of reservoir- and seal-rock cements better understand subsurface conditions in which different authigenic phases formed and constrain paragenesis. Fluid inclusions that could be particularly useful would be those containing oil and gas phases, as well as ones preceding oil migration and following poikilotopic calcite precipitation. Isotope data would also be of great benefit, particularly of pyrite and carbonate cements, as the precipitation or nodular and poikilotopic calcite potentially signified a regime change in formation water chemistry. Comparisons of $\delta^{34}S$ in sulfides and $\delta^{18}O$ in poikilotopic calcite, both luminescent and quenched or non-luminescent, with those of earlier phases and other Mississippian aged units would best assess fluid sources. Differences in luminescence in carbonates would be best resolved with chemical composition of fluid inclusions and bulk analysis of brightly luminescent, dully luminescent, and non-luminescent carbonate

zones sampled using micro drills. Isotopic analysis of $\delta^{13}C$ and $\delta^{34}S$ from calcite and sulfides as well as remaining hydrocarbons with complimentary gas chromatography should be able resolve to what degree microbial activities influence the production of these phases currently present within the reservoir.

References

Adams, A., and Mackenzie, I. R., 1998, A Colour Atlas of Carbonate Sediments and Rocks Under the Microscope, John Wiley & Sons, 184 p.

Adams, A., and Mackenzie, I. R., 1998, A Colour Atlas of Carbonate Sediments and Rocks Under the Microscope, John Wiley & Sons, 184 p.

Ali, S. A., Clark, W. J., and Dribus, J. R., 2010, "Diagenesis and Reservoir Quality", Oilfield Review 22, no. 2, p. 14–27.

Atherton, E., Emrich, G. H., Glass, H. D., Potter, P. E., and Swann, D. H., 1960, "Differentiation of Caseyville (Pennsylvanian) and Chester (Mississippian) sediments in the Illinois Basin", Illinois State Geological Survey, Circular 306, 36 p.

Ayan, T., 1965, "Chemical staining methods used in the identification of carbonate minerals", Bulletin Mineral Research Exploration Institute of Turkey, no. 65, p. 133–147.

Barnaby, R. J., and Rimstidt, J. D, 1989, "Redox Conditions of Calcite Cementation Interpreted from Mn and Fe Contents of Authigenic Calcites", GSA Bulletin, vol. 101, p. 795–804.

Barrows, M. H., and Cluff, R. M., 1984, "New Albany Shale Group (Devonian-Mississippian) Source Rocks and Hydrocarbon Generation in the Illinois Basin", *in* G. M. Demaison, R. J. Roelef, eds., M 35: Petroleum Geochemistry and Basin Evaluation, AAPG Special Publication, Memoir 35, p. 111–138.

Basu, A., Young, S. W., Suttner, L. J., James, W. C., and Mack, G. H., 1975, "Re-evaluation of the use of undulatory Extinction and polycrystallinity in detrital quartz for provenance interpretation", Journal of Sedimentary Petrology, vol. 45, no. 4, p. 873–882.

Bethke, C. M., Reed, J. D., and Oltz, D. F., 1990, "Long-Range Petroleum Migration in the Illinois Basin: Chapter 26: Part I. Illinois Basin: Oil and Gas Systems", *in* M. W. Leighton, D. R. Kolata, D. T. Oltz, J. J. Eidel, eds., M 51: Interior Cratonic Basins, AAPG Special Publication, Memoir 51, p. 455–472.

Biddle, K. T., and Wielchowsky, C. C., 1994, "Hydrocarbon Traps Perspective: Chapter 13: Part III. Processes", *in* L.B. Magoon, W. G. Dow, eds., M 60: The Petroleum System—from source to trap, AAPG Special Publication, Memoir 60, p. 219–235.

Bjørlykke, K., and Jahren, J., 2015, "Sandstone and Sandstone Reservoirs", *in* K. Bjørlykke, ed., Petroleum Geoscience - From Sedimentary Environments to Rock Physics, Second Edition, Springer-Verlag, p. 113–140.

Boggs, S. Jr., 2005, Principles of Sedimentology and Stratigraphy, Fourth edition, Pearson Prentice Hall, 662 p.

Boggs, S., Jr., and Kinsley, D., 2006, Application of Cathodoluminescence Imaging to the Study of Sedimentary Rocks, Cambridge University Press, 165 p.

Bose, A., Rogers, D. R., Adams, M. M., Joye, S. B., and Girguis, P. R., 2013, "Geomicrobiological linkages between short-chain alkane consumption and sulfate reduction rates in seep sediments", Frontiers in Microbiology, vol. 4, article 386, p. 1–13.

Bristol, H. M., 1968, "Structure of the Base of the Mississippian Beech Creek (Barlow Limestone in Illinois", Illinois State Geological Survey, Illinois Petroleum 88, 12 p.

Budd, D. A., Hammes, U., and Ward, W. B., 2000, "Cathodoluminescence in Calcite Cements: New Insights on Pb and Zn sensitizing, Mn Activation, and Fe Quenching at Low Trace-Element Concentrations", Journal of Sedimentary Research, vol. 70, no. 1, p. 217–226.

Buschbach, T. C., and Kolata, D. R., 1990, "Regional Setting of Illinois Basin: Chapter 1: Part I. Illinois Basin: Regional Setting", *in* M. W. Leighton, D. R. Kolata, D. T. Oltz, J. J. Eidel, eds., M 51: Interior Cratonic Basins, AAPG Special Publication, Memoir 51, p. 29–55.

Butler, K. H., and May, M. T., 2013, "Diagenetic Compartmentalization of a Late Mississippian Reservoir in Warren and Butler Counties, KY", GSA Annual Meeting, Denver, Colorado, October 27–30, 2013, Abstracts with Programs, vol. 45, no. 7, p.174.

Cant, D. J., 1986, "Diagenetic Traps in Sandstones", AAPG Bulletin, vol. 70, no. 2, p. 155–160.

Catacosinos, P. A., Harrison, W. B. III, and Daniels, P. A. Jr., 1990, "Structure, Stratigraphy, and Petroleum Geology of the Michigan Basin: Chapter 30: Part II. Selected Analog Interior Cratonic Basins: Analog Basin", *in* M. W. Leighton, D. R. Kolata, D. T. Oltz, J. J. Eidel, eds., M 51: Interior Cratonic Basins, AAPG Special Publication, Memoir 51, p. 561–601.

Chayes, F., 1956, Petrographic Modal Analysis, John Wiley & Sons, 113 p.

Choquette, P. W., and James, N. P., 1987, “Diagenesis in Limestones – The Deep Burial Environment”, Geoscience Canada, vol. 14, p. 3–35.

Cluff, R. M., and Byrnes, A. P., 1990, “Lopatin Analysis of Maturation and Petroleum Generation in the Illinois Basin: Chapter 25: Part I. Illinois Basin: Oil and Gas Systems”, *in* M. W. Leighton, D. R. Kolata, D. T. Oltz, J. J. Eidel, eds., M 51: Interior Cratonic Basins, AAPG Special Publication, Memoir 51, p. 425–454.

Davidson, S. T., 2002, “Spatial database of the Bowling Green North quadrangle, Kentucky”, Kentucky Geological Survey, Series 12, Digitally Vectorized Geologic Quadrangle Data DVGQ-234 (Adapted from Shawe, F. R., 1963, “Geology of the Bowling Green North quadrangle, Kentucky”, U.S. Geological Survey Geologic Quadrangle Map GQ-234, scale 1:24,000).

Devera J. A., and Hasenmueller, N. R., 1990, “Kaskaskia Sequence: Middle and Upper Devonian Series through Mississippian Kinderhookian Series: Chapter 8: Part 1. Illinois Basin Stratigraphy”, *in* M. W. Leighton, D. R. Kolata, D. T. Oltz, J. J. Eidel, eds., M 51: Interior Cratonic Basins, AAPG Special Publication, Memoir 51, p. 113–123.

Dickinson, W. R., and Suczek, C. A., 1979, “Plate Tectonics and Sandstone Compositions”, AAPG Bulletin, vol. 63, p. 2164–2182.

Dickson, J. A. D., 1966, “Carbonate Identification and Genesis as Revealed by Staining”, Journal of Sedimentary Petrology, vol., 36, no. 2, p. 491–505.

Dott, R. H. Jr., 1964, “Wacke, greywacke and matrix; what approach to immature sandstone classification?”, SEPM, Journal of Sedimentary Research, vol. 34, no. 3, p. 625–632.

Drever, J. I., 1997, The Geochemistry of Natural Waters Surface and Groundwater Environments, Third edition, Prentice-Hall, 436 p.

Droste, J. B., Furer, L. C., and Horowitz, A. S., 2000, “Patterns of Deposition during the Early Pennsylvanian (Morrowan) in the Illinois Basin”, Indiana Geological Survey, Special Report 62, 16 p.

Dusausoy, Y., and Weil, J. A., 1994, “Point Defects as Precursors for Electron-Hole Centers: Systematics and Theories of Radiation Centers in Minerals”, *in* A. S. Marfunin, Advanced Mineralogy: Volume 1 Composition Structure and Properties of Matter: Concepts, Results, and Problems, Springer-Verlag, p.180–196.

England, W. A., Mann, A. L., and Mann, D. M., 1991,"Migration from Source to Trap: Chapter 3: Petroleum Generation and Migration", *in* R. K. Merrill, ed., Source and Migration Processes and Evaluation Techniques, AAPG Special Publication, Treatise Handbook of Petroleum Geology, p. 23–46.

Ervin, C. P., and McGinnis, L. D., 1975, "Reelfoot Rift; reactivated precursor to the Mississippi Embayment", GSA Bulletin, vol. 86, no. 9, p. 1287–1295.

Fetter, C. W., 2000, Applied Hydrogeology, Fourth Edition, Pearson Prentice Hall, 598 p.

Fisher Ponce, A. M., 2009, "Optical Properties of Wide Gap Semiconductors Studied by Means of Cathodoluminescence", Ph.D. Dissertation, University of Arizona, 146 p.

Flegler, S. L., Heckman, J. W. Jr., and Klomparens, K. L., 1993, Scanning and Transmission Electron Microscopy, An Introduction, Oxford University Press Inc., 225 p.

Fletcher, R. C. and Merino, E., 2001, "Mineral growth in rocks: kinetic-rheological models of replacement, vein formation, and syntectonic crystallization", Geochimica et Cosmochimica Acta, vol. 65, p. 3733–3748.

Folk, R. L., 1980, Petrology of Sedimentary Rocks, Hemphill Publishing Company, 182 p.

Fox, M., 2001, Optical Properties of Solids, Oxford University Press, 305 p.

Gaft, M., Reisfeld, R., and Panczer, G., 2005, Modern Luminescence Spectroscopy of Minerals and Materials, Springer-Verlag, 356 p.

Garrison, E. G., 2003, Techniques in Archaeological Geology, Springer, 304 p.

Gilkes, R. J., and McKenzie, R. M., 1988, "Geochemistry of Manganese in Soil", *in* R. D. Graham, R. J. Hannam, and N. C. Uren, eds., Manganese in Soils and Plants, Kluwer Academic Publishers, p. 23–34.

Götze, J., 2002, "Potential of cathodoluminescence (CL) Microscopy and Spectroscopy for the Analysis of Minerals and Materials", Analytical and Bioanalytical Chemistry, vol. 374, no. 4, p. 703–708.

Götze, J., 2012, "Application of Cathodoluminescence Microscopy and Spectroscopy in Geosciences", Microscopy and Microanalysis, vol. 18, no. 6, p. 1270–1284.

Götze, J., and Kempe, U., 2008, "A Comparison of Optical Microscope- and Scanning Electron Microscope-based Cathodoluminescence (CL) Imaging and Spectroscopy Applied to Geosciences", Mineralogical Magazine, vol. 72, no. 4, p. 909–924.

Götze, J., Plötze, M., and Habermann, D., 2001, "Origin, spectral characteristics and practical applications of the cathodoluminescence (CL) of quartz – a review", Mineralogy and Petrology, vol. 71, p. 225–250.

Götze, J., Krbetschek, D., Habermann, D., and Wolf, D., 2000, "High-Resolution Cathodoluminescence Studies of Feldspar Minerals", *in* M. Pagel, V. Barbin, P. Blanc, and D. Ohnenstetter, eds., Cathodoluminescence in Geosciences, Springer, p. 245–270.

Götze, J., Plötze, M., Götte, T., Neuser, R. D., and Richter, D. K., 2002, "Cathodoluminescence (CL) and electron paramagnetic resonance (EPR) studies of clay minerals", Mineralogy and Petrology, vol. 76, p. 195–212.

Granger, D. E., Fabel, E. D., and Palmer, A. N., 2001, "Plio-Pliestocene incision of the Green River, Kentucky from radioactive decay of cosmogenic 26Al and 10Be in Mammoth Cave sediments", GSA Bulletin, vol. 113, no. 7, p. 825–836.

Gucsik, A., Nishido, H., Ninagawa, K., Kereszturi, A., Nakamura, T., Tsuchiyama, A., Jäger, C., Ott, U., and Kayama, M., 2015, "Luminescence Spectroscopical Properties of Plagioclase Particles from Hayabusa Sample Return Mission", 46th Lunar and Planetary Science Conference 2015, Lunar and Planetary Institute Contribution, no. 1832, p. 2931–2932.

Hatert, F., and Burke, A. J., 2008, "The IMA-CNMNC Dominant-Constituent Rule Revisted and Extended", Canadian Mineralogist, vol. 46, p. 717–728.

Heigold, P. C., 1990, "Crustal Character of the Illinois Basin: Chapter 17: Part I. Illinois Basin: Evolution", *in* M. W. Leighton, D. R. Kolata, D. T. Oltz, J. J. Eidel, eds., M 51: Interior Cratonic Basins, AAPG Special Publication, Memoir 51, p. 247–261.

Hem, J. D., 1963, "Chemical Equilibria and Rates of Manganese Oxidation", U.S. Geological Survey, Geological Water-Supply Paper, no. 1667-A, 64 p.

Hemming, G. H., Meyers, W. J., and Grams, J. C., 1989, "Cathodoluminescence in Diagenetic Calcites: the Roles of Fe and Mn as Deduced from Electron Probe and Spectrophotometric Measurements", Journal of Sedimentary Petrology, vol. 59, no. 3, p. 404–411.

Hiatt, E. E., and Pufahl, P. K., 2014, "Cathodoluminescence Petrography of Carbonate Rocks: A Review of Applications for Understanding Diagenesis, Reservoir Quality, and Pore System Evolution", *in* I. M. Coulson, ed., Cathodoluminescence and its Application to Geoscience, Mineralogical Association of Canada, Short Course Series, vol. 45, p. 75–96.

Horowitz, A. S., and Kelly, S. M., 1987, "The Chesterian section near Sulphur, Indiana", GSA Centennial Field Guide – North-Central Section, Boulder, Colorado, p. 387–390.

Howard, R. H., 1990, "Hydrocarbon Reservoir Distribution in the Illinois Basin: Chapter 21", *in* M. W. Leighton, D. R. Kolata, D. T. Oltz, J. J. Eidel, eds., M 51: Interior Cratonic Basins, AAPG Special Publication, Memoir 51, p. 299–327.

Howard, R. H., and Whitaker, S. T., 1988, "Hydrocarbon accumulation in a paleovalley at Mississippian-Pennsylvanian unconformity near Hardinville, Crawford County, Illinois: A model paleogeomophic trap", Department of Energy and Natural Resources, Illinois State Geological Survey, Illinois Petroleum 129, 26 p.

Houseknecht, D. W., 1992, "Part 5, Laboratory Methods, Thin Section Analysis", *in* D. Morton-Thompson, and A. M. Woods, eds., Development Geology Reference Manual, AAPG Special Publication, Methods 10, p. 233–236.

Hunt, J. M., 1987, "Primary and Secondary Migration of Oil: Section III. Geological Environments and Migrations", *in* T. L. Bear, ed., SG25: Exploration for Heavy Crude Oil and Natural Bitumen, AAPG Special Publications, Studies in Geology 25, p. 345–349.

Ibach, H., and Lüth, H., 2003, Solid-State Physics, Third edition, Springer-Verlag, 501 p.

Jobe, H., and Saller, A., 1995, "Oil Reservoirs in Grainstone Aprons around Bryozoan Mounds, Upper Harrodsburg Limestone, Mississippian, Illinois Basin", AAPG Bulletin, vol. 79, no. 6, p. 783–800.

Kaxiras, E., 2003, Atomic and Electronic Structure of Solids, Cambridge University Press, 676 p.

KDGI (Kentucky Division of Geographic Information), 2015, "Ky_DEM_USGS_10M", Kentucky Digital Elevation Model (DEM), KDGI, http://kyraster.ky.gov/arcgis/rest/services/ElevationServices/Ky_DEM_USGS_10M/ImageServer (accessed February, 2015).

Kehew, A. E., 2001, Applied Chemical Hydrogeology, Prentice Hall, 368 p.

Kehn, T. M., Beard, J. G., and Williamson, A. D., 1982, “Mauzy Formation, a new stratigraphic unit of Permian age in western Kentucky”, U.S. Geological Survey Bulletin, vol. 1529-H, p. 73–86.

Kellerhals, R., Shaw, J., and Arora, V. K., 1975, “On Grain Size from Thin Sections”, Journal of Geology, vol. 83, no. 1, p. 79–96.

KGS (Kentucky Geological Survey), 2015a, Kentucky Geologic Map Information Service, KGS, http://kgs.uky.edu/kgsmap/kgsgeoserver/viewer.asp (accessed February, 2015).

KGS (Kentucky Geological Survey), 2015b, Oil and Gas Records Database, KGS, http://kgs.uky.edu/kgsweb/DataSearching/OilGas/OGSearch.asp (accessed February, 2015).

KGS (Kentucky Geological Survey), 2015c, Water Well and Spring Records Database, KGS, http://kgs.uky.edu/kgsweb/DataSearching/Water/WaterWellSearch.asp (accessed February, 2015).

Kolata, D. R., 1990, “Overview of Sequences: Chapter 2: Part I. Illinois Basin: Stratigraphy”, *in* M. W. Leighton, D. R. Kolata, D. T. Oltz, J. J. Eidel, eds., M 51: Interior Cratonic Basins, AAPG Special Publication, Memoir 51, p. 59–73.

Kolata, D. R., and Nelson, J. W., 1990a, “Tectonic History of the Illinois Basin: Chapter 18: Part I. Illinois Basin: Evolution”, *in* M. W. Leighton, D. R. Kolata, D. T. Oltz, J. J. Eidel, eds., M 51: Interior Cratonic Basins, AAPG Special Publication, Memoir 51, p. 263–285.

Kolata, D. R., and Nelson, J. W., 1990b, “Basin-forming Mechanisms of the Illinois Basin: Chapter 19: Part I. Illinois Basin: Evolution”, *in* M. W. Leighton, D. R. Kolata, D. T. Oltz, J. J. Eidel, eds., M 51: Interior Cratonic Basins, AAPG Special Publication, Memoir 51, p. 287–292.

Kolata, D. R., and Olive, W. W., 1990, “Zuni and Tejas Sequences: Late Cretaceous through Holocene Series: Chapter 11: Part I. Illinois Basin: Stratigraphy”, *in* M. W. Leighton, D. R. Kolata, D. T. Oltz, J. J. Eidel, eds., M 51: Interior Cratonic Basins, AAPG Special Publication, Memoir 51, p. 165–168.

Leighton, M. W., and Kolata, D. R., 1990, “Selected Interior Cratonic Basins and Their Place in the Scheme of Global Tectonics: A Synthesis: Chapter 35: Part III. Synthesis and Analysis of Interior Cratonic Basins: Synthesis”, *in* M. W. Leighton, D. R. Kolata, D. T. Oltz, J. J. Eidel, eds., M 51: Interior Cratonic Basins, AAPG Special Publication, Memoir 51, p. 729–797.

Lewan, M. D., and Fisher, J. B., 1994, "Organic Acids from Petroleum Source Rocks" *in* E. D. Pittman, and M. D. Lewan, eds., Organic Acids in Geological Processes, Springer-Verlag, p. 70–114.

Lewan, M. D., Henry, M. E., Higley, D. K., and Pitman, J. K., 2002, "Material-balance assessment of the New Albany-Chesterian Petroleum System of the Illinois Basin", AAPG Bulletin, vol. 86, no. 5, p. 745–778.

Lindholm, R. C., and Finkelman, R. B., 1972, "Calcite Staining: Semi-Quantitative Determination of Ferrous Iron", Journal of Sedimentary Petrology, vol. 42, p. 239–242.

Lloyd, O. B., Jr., and Lyke, W. L., 1995, "Interior Low Plateaus Aquifers: Segment 10, Illinois, Indiana, Kentucky, Ohio, Tennessee", *in* J. A. Miller, ed., Ground Water Atlas of the United States, U.S. Geological Survey, Hydrologic Atlas 730-K, 30 p.

London, J. T., 2014, "Geologic Factors Affecting Hydrocarbon Occurrence in Paleovalleys of the Mississippian-Pennsylvanian Unconformity in the Illinois Basin", M.S. Thesis, Western Kentucky University, 88 p., http://digitalcommons.wku.edu/theses/1355 (accessed September, 2015).

Long, A. D., 1977, Raman Spectroscopy, McGraw-Hill, 276 p.

Machel, H. G., 1985, "Cathodoluminescence in Calcite and Dolomite and Its Chemical Interpretation", Geoscience Canada, vol. 12, no. 4, p. 139–147.

Machel, H. G., 2000, "Application of Cathodoluminescence to Carbonate Diagenesis", *in* M. Pagel, V. Barbin, P. Blanc, and D. Ohnenstetter, eds., Cathodoluminescence in Geosciences, Springer, p. 271–302.

Machel, H. G., 2001, "Bacterial and Thermochemical Sulfate Reduction in Diagenetic Settings – Old and New Insights", Sedimentary Geology, vol. 140, p. 143–175.

Machel, H. G., 2005, "Investigations of Burial Diagenesis in Carbonate Hydrocarbon Reservoir Rocks", Geoscience Canada, vol. 32, no. 3, p. 103–128.

Machel, H. G., and Burton, E. A., 1991, "Factors Governing Cathodoluminescence in Calcite and Dolomite, and their Implications for Studies of Carbonate Diagenesis", *in* C. E. Barker and O. C. Kopp, eds., Luminescence Microscopy and Spectroscopy: Qualitative and Quantitative Applications, SEPM Short Course, vol. 25, p. 37–58.

Machel, H. G., Mason, R. A., Mariano, A. N., and Mucci, A., 1991, "Causes and Emission of Luminescence in Calcite and Dolomite", *in* C. E. Barker and O. C. Kopp, eds., Luminescence Microscopy and Spectroscopy: Qualitative and Quantitative Applications, SEPM Short Course, vol. 25, p. 9–26.

Mack, G. H., James, W. C., and Thomas, W. A., 1981, "Orogenic Provenance of Mississippian Sandstones Associated with Southern Appalachian-Ouachita Orogen", AAPG Bulletin, vol. 65, no. 8, p. 1444–1456.

Macke, D. L., 1996, "Illinois Basin Province (064)", *in* Gautier, D. L., Dolton, G. L., Takahasi, K. I., eds., 1995 National Assessment of United Sates Oil and Gas Resources – Results, Methodology, and supporting data, U.S. Geological Survey, Digital Data Series 30, 35 p.

Marfunin, A. S., 1979, Spectroscopy, Luminescence and Radiation Centers in Minerals, Springer-Verlag, 356 p.

Mason, R. A., 1987, "Ion Microprobe analysis of Trace Elements in Calcite with an Application to the Cathodoluminescence Zonation of Limestone Cements from the Lower Carboniferous of South Wales, U.K.", Chemical Geology, vol. 64, p. 209–224.

Maxwell, B. W., and Devaul, R. W., 1961, "Reconnaissance of Ground-Water Resources in the Western Coal Field Region, Kentucky", U.S. Geological Survey, Geological Survey Water-Supply Paper, no. 1599, 34 p.

May, M. T., Kuehn, K. W., and Schoefernacker, S., 2007, "Geology of the Mammoth Cave and Nolin River Gorge Region with Emphasis on Hydrocarbon and Karst Resources. Part II: Rock Asphalt Redux and Paleovalleys Anew", Kentucky Society of Professional Geologists, Guidebook Series, 33 p.

May, M. T., 2013, "Oil-saturated Mississippian-Pennsylvanian sandstones of south-central Kentucky", *in* F. J. Hein, D. Leckie, S. Larter, and J. R. Suter, eds., Heavy Oil and Oil Sand Petroleum Systems in Alberta and Beyond, AAPG, Studies in Geology 64, p. 373–405.

McBride, E. F., 1963, "A Classification of Common Sandstones", Journal of Sedimentary Petrology, vol. 33, p. 664–669.

McFarlan, A. C., 1943, "Rock asphalt: Chapter 24", *in* Geology of Kentucky, University of Kentucky Press, Lexington, Kentucky (reprinted by the Kentucky Geological Survey 1961), 531 p., http://www.uky.edu/OtherOrgs/KPS/goky/pages/gokych24.htm (accessed November, 2014).

McGrain, P., and Sutton, D. G., 1973, “Economic geology of Warren County, Kentucky”, Kentucky Geological Survey, Series 10, County Report no. 7, 28 p.

McLemore, V. T., and Barker, J. M., 1987, “Some Geological Applications of Cathodoluminescence Examples from the Lemitar Mountains and Riley Travertine, Socorro County, New Mexico”, New Mexico Geology, vol. 9, p. 37–40.

Meriño, J., Marshak, S., and Mastalerz, M., 2015, “Evidence for stratigraphically controlled paleogeotherms in the Illinois Basin based on vitrinite-reflectance analysis: Implications for interpreting coal-rank anomalies”, AAPG Bulletin, vol. 99, no. 10, p. 1803–1825.

Metzger, J. G., Fike, D. A., Osborn, G. R., Guo, C. J., and Addison, A. N., 2015, “The source of gypsum in Mammoth Cave, Kentucky”, Geology, vol., 43, no. 62, p. 187–190.

Meyers, W. J., 1991, “Calcite Cement Stratigraphy: An Overview”, *in* C. E. Barker and O. C. Kopp, eds., Luminescence Microscopy and Spectroscopy: Qualitative and Quantitative Applications, SEPM Short Course, vol. 25, p. 133–148.

Mikulic, D. G., 1990, “Tippecanoe II Subsequence: Silurian System through Lower Devonian Series: Chapter 6: Part: Part I. Illinois Basin: Stratigraphy”, *in* M. W. Leighton, D. R. Kolata, D. T. Oltz, J. J. Eidel, eds., M 51: Interior Cratonic Basins, AAPG Special Publication, Memoir 51, p. 101–107.

Montañez, I. P., 1997, “Secondary Porosity and Late Diagenetic Cements of the Upper Knox Group, Central Tennessee Region: A Temporal and Spatial History of Fluid Flow Conduit Development within the Knox Regional Aquifer” *in* I. P. Montañez, J. M. Gregg, and K. L. Shelton, eds., Basin-wide Diagenetic Patterns: Integrated Petrologic and Geochemical, and Hydrological Considerations, SEPM Special Publication, no. 57, p. 101–117.

Morris, M. D., 1992, “Modern Techniques in Raman Spectroscopy”, *in* D. L. Andrews, ed., Applied Laser Spectroscopy: Techniques, Instrumentation, and Applications, VCH Publishers, p. 227–265.

Morse, J. W., Hanor, J. S., and He, S., 1997, “The Role of Mixing and Migration of Basinal Waters in Carbonate Mineral Mass Transport”, *in* I. P. Montañez, J. M. Gregg, and K. L. Shelton, eds., Basin-wide Diagenetic Patterns: Integrated Petrologic and Geochemical, and Hydrological Considerations, SEPM Special Publication, no. 57, p. 41–50.

Mullins, J. E., 2002a, “Spatial database of the Brownsville quadrangle, Kentucky”, Kentucky Geological Survey, Series 12, Digitally Vectorized Geologic Quadrangle Data DVGQ-411 (Adapted from Gildersleeve, B., 1965, Geology of the Brownsville quadrangle, Kentucky”, U.S. Geological Survey Geologic Quadrangle Map GQ-411, scale 1:24,000).

Mullins, J. E., 2002b, “Spatial database of the Hadley quadrangle, Kentucky”, Kentucky Geological Survey, Series 12, Digitally Vectorized Geologic Quadrangle Data DVGQ-237 (Adapted from Rainey, H. C., III, 1963, “Geology of the Hadley quadrangle, Kentucky”, U.S. Geological Survey Geologic Quadrangle Map GQ-237, scale 1:24,000).

Mullins, J. E., 2002c, “Spatial database of the Morgantown quadrangle, Butler and Warren Counties, Kentucky”, Kentucky Geological Survey, Series 12, Digitally Vectorized Geologic Quadrangle Data DVGQ-1040 (Adapted from Gildersleeve, B., 1972, “Geologic map of the Morgantown quadrangle, Butler and Warren Counties, Kentucky”, U.S. Geological Survey Geologic Quadrangle Map GQ-1040, scale 1:24,000).

Mullins, J. E., 2002d, “Spatial database of the Sugar Grove quadrangle, Kentucky”, Kentucky Geological Survey, Series 12, Digitally Vectorized Geologic Quadrangle Data DVGQ-225 (Adapted from Miller, T. P., 1963, “Geology of the Sugar Grove quadrangle, Kentucky”, U.S. Geological Survey Geologic Quadrangle Map GQ-225, scale 1:24,000).

Mullins, J. E., 2006, “Spatial database of the South Hill quadrangle, Butler and Ohio Counties, Kentucky”, Kentucky Geological Survey, Series 12, Digitally Vectorized Geologic Quadrangle Data DVGQ-1180 (Adapted from Moore, S. L., 1974, “Geologic map of the South Hill quadrangle, Butler and Ohio Counties, Kentucky”, U.S. Geological Survey Geologic Quadrangle Map GQ-1180, scale 1:24,000).

Nasdala, L., Götze, J., Hanchar, J. M., Gaft, M., and Krbetschek, M. R., 2004, “Luminescence techniques in Earth Sciences”, *in* A. Beran and E. Libowitzky, eds., Spectroscopic Methods in Mineralogy, EMU notes in Mineralogy, vol. 6, p. 43–91.

Nelson, J. W., 1990, “Structural Styles of the Illinois Basin: Chapter 16: Part I. Illinois Basin: Structural Geology”, *in* M. W. Leighton, D. R. Kolata, D. T. Oltz, J. J. Eidel, eds., M 51: Interior Cratonic Basins, AAPG Special Publication, Memoir 51, p. 209–243.

Nelson, W. A., and Read, J. F., 1990, "Updip to Downdip Cementation and Dolomitization Patterns in a Mississippian Aquifer, Appalachians", Journal of Sedimentary Petrology, vol. 60, no. 3, p. 379–396.

Nelson, J. W., Damberger, H. H., Trask, C. B., Williamson, A. D., Jacobson, R. J., and Williams, D. A., 1990, "Absaroka Sequence Pennsylvanian and Permian Systems: Chapter 10", *in* M. W. Leighton, D. R. Kolata, D. T. Oltz, J. J. Eidel, eds., M 51: Interior Cratonic Basins, AAPG Special Publication, Memoir 51, p. 143–164.

Nelson, J. W., Smith, L. B., and Treworgy, J. D., 2002, "Sequence Stratigraphy of the Lower Chesterian (Mississippian) Strata of the Illinois Basin", Illinois State Geological Survey, Bulletin 107, 70 p.

Ngonadi, N., 2013, "Using PLFA to Constrain Microbial Distribution Related to S-cycling in Oil-sands Composite Tailings during Reclamation", Open Access Dissertations and Theses, Paper 7660, 60 p.

Nilges, M. J., Pan, Y., and Mashkovtsev, R. I., 2008, "Radiation-damage-induced defects in quartz. I. Single-crystal W-band EPR study of hole centers in an electron-irradiated quartz", Physics and Chemistry of Minerals, vol. 35, no. 2, p. 103–115.

Noger, M. C., 1984, "Tar-Sand Resources of Western Kentucky", Reprint 45, Series XI, 1999, Kentucky Geological Survey, 27 p.

Noger, M. C., 1987, "Tar-Sand Exploration in Kentucky: Section V. Exploration Histories", *in* R. F. Meyer, ed., SG25: Exploration for Heavy Crude Oil and Natural Bitumen, AAPG Special Publication, Studies in Geology 25, p. 521–536.

Owen, M. R., 1991, "Application of Cathodoluminescence to Sandstone Provenance", *in* C. E. Barker and O. C. Kopp, eds., Luminescence Microscopy and Spectroscopy: Qualitative and Quantitative Applications, SEPM Short Course, vol. 25, p. 67–75.

Pagel, M., Barbin, V., Blanc, P., and Ohnenstetter, D., 2000, "Cathodoluminescence in Geosciences: An Introduction", *in* M. Pagel, V. Barbin, P. Blanc, and D. Ohnenstetter, eds., Cathodoluminescence in Geosciences, Springer, p. 1–22.

Palenik, C. S., and Buscagalia, J., 2007, "Applications of Cathodoluminescence in Forensic Science", *in* R. D. Blackledge, ed., Forensic Analysis on the Cutting Edge New Methods for Trace Evidence Analysis, John Wiley & Sons, p. 141–174.

Parsons, I., Steele, D. A., Lee, M. R., and Magee, C. W., 2008, "Titanium as a cathodoluminescence activator in alkali feldspars", American Mineralogist, vol. 93, p. 875–879.

Pitman, J. K., Henry, M. E., and Leetaru, H. E., 1999, “Diagenesis and reservoir quality of the Upper Mississippian Aux Vases Sandstone, Illinois Basin”, U.S. Geological Survey, Professional Paper 1609, 19 p.

Plas, L., and Tobi, A. C., 1965, “A Chart for Judging the Reliability of Point Counting Results”, American Journal of Science, vol. 263, no. 1, p. 87–90.

Poppe, L. J., Paskevich, V. F., Hathaway, J. C., and Blackwood, D. S., 2001, “A Laboratory Manual for X-Ray Powder Diffraction”, U.S. Geological Survey, Open-File Report 1-41, 88 p.

Portnov, A., Gorobets, B., Rogozhin, A., Bushev, A., and Kvitko, T., 2001. “Luminescent geochemical anomalies in lithosphere and haloes of ore bodies”, Periodico di Mineralogia, vol. 70, no. 3, p. 85–100.

Potter, P. E., 1962, “Late Mississippian Sandstones of Illinois”, Illinois Geological Survey, Survey Circular 340, p. 1–36.

Powers, M. C., 1953, “A New Roundness Scale for Sedimentary Particles”, Journal of Sedimentary Petrology, vol. 23, no. 2, p. 117–119.

Pownceby, M. I., and MacRae, C. M., 2011, “Electron microbeam analysis techniques”, *in* G. E. Christidis, ed., Advances in the Characterization of Industrial Minerals, European Mineralogical Union, Mineralogical Society of Great Britain and Ireland, vol. 9, p. 227–286.

Pryor, W. A., Lamborg, A., D., Roberts, M. J., Tharp, T. C., and Wilsey, W. L. M., 1990, “Geologic Controls on Porosity in Mississippian Limestone and Sandstone Reservoirs in the Illinois Basin: Chapter 22: Part I. Illinois Basin: Oil and Gas Systems”, *in* M. W. Leighton, D. R. Kolata, D. T. Oltz, J. J. Eidel, eds., M 51: Interior Cratonic Basins, AAPG Special Publication, Memoir 51, p. 329–359.

Pye, K., 2007, Geological and Soil Evidence: Forensic Applications, CRC Press, 356 p.

Qin, C., and Ortoleva, P. J., 1994, “Banded Diagenetic Pressure Seals: Types, Mechanisms, and Homogenized Basin Dynamics”, *in* P. J. Ortoleva, ed., M 61: Basin Compartments and Seals, AAPG Special Publication, Memoir 61, p. 385–400.

Rakovan, J., and Waychunas, G., 1996, “Luminescence in Minerals”, Mineralogical Record, vol. 27, p. 7–19.

Ramseyer, K., Baumann, J., Matter, A., and Mullis, J., 1988, “Cathodoluminescence colours of α-quartz”, Mineralogical Magazine, vol. 52, p. 669–677.

Ramseyer, K., and Mullis, J., 2000, "Geologic Application of Cathodoluminescence of Silicates", *in* M. Pagel, V. Barbin, P. Blanc, and D. Ohnenstetter, eds., Cathodoluminescence in Geosciences, Springer, p. 177–192.

Ray, J. A., and Currens, J. C., 1998, "Mapped karst groundwater basins in the Beaver Dam 30 x 60 minute quadrangle", Kentucky Geological Survey, Series 11, Map and Chart 17, scale 1:100,000.

Reed, R. M., and Milliken, K. L., 2003, "How to Overcome Imaging Problems associated with Carbonate Minerals on SEM-Based Cathodoluminescence Systems", Journal of Sedimentary Research, vol. 73, no. 2, p. 328–332.

Reeder, R. J., 1991, "An Overview of Zoning in Carbonate Minerals", *in* C. E. Barker and O. C. Kopp, eds., Luminescence Microscopy and Spectroscopy: Qualitative and Quantitative Applications, SEPM Short Course, vol. 25, p. 77–82.

Reynolds, J. G., Jones, E. L., Bennett, J., and Biggs, W. R., 1988, "Characterization of Nickel and Vanadium Compounds in Tar Sands Bitumen by Petroporphyrin Coupled with Element Specific Detection", Lawerence Livermore National Laboratory, Preprint, 18 p.

Richter, D. K., Götte, T., Götze, J., and Neuser, R. D., 2003, "Progress in Application of Cathodoluminescence in Sedimentary Petrology", Mineralogy and Petrology, vol. 79, p. 127–166.

Rickard, D., 1994, "A New Sedimentary Pyrite Formation Model", Mineralogical Magazine, vol. 58A, p. 772–773.

Roduit, N., 2014, "JMicroVision: Image analysis toolbox for measuring and quantifying components of high-definition images", Version 1.2.7, http://www.jmicrovision.com (accessed January, 2014).

Rowan E. L., Goldhaber, M. B., and Hatch, J.R., 2002, "Regional fluid flow as a factor in the thermal history of the Illinois basin: Constraints from fluid inclusions and the maturity of Pennsylvanian coals", AAPG Bulletin, vol. 86, no. 2, p. 257–277.

Russell, W. L., 1933, The Origin of the asphalt deposits of western Kentucky", Society of Economic Geologists", Economic Geology, vol. 28, no. 6, p. 571–586.

Sable, E. G., 1979, "Eastern Interior Basin Region" *in* L. C. Craig, and C. W. Conner, eds., Paleotectonic investigations of the Mississippian system in the United States, Part I. Introduction and Regional Analyses of the Mississippian System, U.S. Geological Survey, Professional Paper 1010-E, p. 57–106.

Salh, R., 2011a, “Defect Related Luminescence in Silicon Dioxide Network: A Review”, *in* S. Basu, ed., Crystalline Silicon - Properties and Uses, InTech, p.135–172.

Salh, R., 2011b, “Silicon Nanocluster in Silicon Dioxide: Cathodoluminescence, Energy Dispersive X-Ray Analysis and Infrared Spectroscopy Studies”, *in* S. Basu, ed., Crystalline Silicon - Properties and Uses, InTech, p.173–218.

Schippers, A., and Jørgensen, B. B., 2001, “Biogeochemistry of Pyrite and Iron Sulfide Oxidation in Marine Sediments”, Geochimica et Cosmochimica Acta, vol. 66, no. 1, p. 85–92.

Schmidt, V., and McDonald, D. A., 1979, “The Role of Secondary Porosity in the Course of Sandstone Diagenesis”, Society of Economic Paleontologists and Mineralogists Special Publication 26, p. 175–207.

Schwalb, H. R., 1975, “Oil and Gas in Butler County Kentucky”, Kentucky Geological Survey, Report of Investigation 16, Series 10, 65 p.

Sedimentation Seminar, 1978, “Sedimentology of the Kyrock and (Pennsylvanian in the Brownsville Paleovalley, Edmonson and Hart Counties, Kentucky”, Kentucky Geological Survey, Report of Investigations no. 21, 24 p.

Seyler, B., and Cluff, R. M., 1990, “Petroleum Traps in the Illinois Basin: Chapter 23”, *in* M. W. Leighton, D. R. Kolata, D. T. Oltz, J. J. Eidel, eds., M 51: Interior Cratonic Basins, AAPG Special Publication, Memoir 51, p. 361–401.

Smith, L. B. Jr., and Read, F. J., 2001, “Discrimination of Local and Global Effects of Upper Mississippian Stratigraphy, Illinois Basin, U.S.A.”, SEPM, Journal of Sedimentary Research, vol. 71, no. 6, p. 985–1002.

Spötl, C., and Pitman, J. K., 1998, “Saddle (baroque) dolomite in carbonates and sandstones: a reappraisal of the burial-diagenetic concept”, *in* S. Morad, ed., Carbonate Cementation in Sandstones: Distribution Patterns and Geochemical Evolution, International Association of Sedimentologists, Special Publication 26, p. 437–460.

Stevens-Kalceff, M. A., Phillips, M. R., Moon, A. R., and Kalceff, W., 2000, “Cathodoluminescence Microcharacterization of Silicon Dioxide Polymorphs”, *in* M. Pagel, V. Barbin, P. Blanc, and D. Ohnenstetter, eds., Cathodoluminescence in Geosciences, Springer, p. 193–224.

Stoessell, R. K., 1992, “Effects of sulfate Reduction on $CaCO_3$ Dissolution and Precipitation in Mixing-zone Fluids”, Journal of Sedimentary Petrology, vol. 62, no. 5, p. 873–880.

Stoessell, R. K., and Pittman, E. D., 1990, "Secondary Porosity Revisited: The Chemistry of Feldspar Dissolution by Carboxylic Acids and Anions", AAPG Bulletin, vol. 74, p. 1795–1805.

Strąpoć, D., Mastalerz, M., Schimmelmann, A., Drobniak, A., and Hasenmueller, N. R., 2010, "Geochemical Constraints on the Origin and Volume of gas in the New Albany Shale (Devonian-Mississippian), Eastern Illinois Basin, AAPG Bulletin, vol. 94, no. 11, p. 1713–1740.

Struve, W. S., 1989, Fundamentals of Molecular Spectroscopy, John Wiley & Sons, 379 p.

Surdam, R. C., Boese, S. W., and Crossey, L. J., 1984, "The Chemistry of Secondary Porosity: Part 2. Aspects of Porosity Modification", *in* D. A. McDonald and R. C. Surdam, eds., M 37 Clastic Diagenesis, AAPG Special Publications, Memoir 37, p. 127–149.

Surdam, R. C., Jiao, Z. S., and MacGowan, D. B, 1993, "Redox Reactions Involving Hydrocarbons and Mineral Oxidants: A Mechanism for Significant Porosity Enhancement in Sandstones", AAPG Bulletin, vol. 77, no. 9, p. 1509–1518.

Suryanarayana, C., and Norton, M. G., 1998, X-Ray Diffraction a Practical Approach, Plenum Press, 273 p.

Swann, D. H., 1963, "Classification of Genevievian and Chesterian (Late Mississippian) rocks in Illinois", Illinois Geological Survey, Report of Investigations no. 216, 91 p.

Swann, D. H., 1964, "Late Mississippian Rhythmic Sediments of Mississippi Valley", AAPG Bulletin, vol. 48, no. 5, p. 637–658.

Swanson, R. G., 1981, "Hydrocarbons: Chapter 6", *in* Sample Examination Manual, AAPG Special Publication, Methods 1, p. 19–24.

Thompson, M. F., 2002, "Spatial database of the Reedyville quadrangle, western Kentucky", Kentucky Geological Survey, Series 12, Digitally Vectorized Geologic Quadrangle Data DVGQ-520 (Adapted from Shawe, F. R., 1966, "Geologic map of the Reedyville quadrangle, western Kentucky", U.S. Geological Survey Geologic Quadrangle Map GQ-520, scale 1:24,000).

Tianrui, S., 1991, "Textural Maturity of arenaceous rocks derived by microscopic grain size analysis in thin section", *in* J. P. M. Syvitski, ed., Principles, Methods and Application of Particle Size Analysis, Cambridge University Press, p. 163–173.

Toth, K. S., 2006a, “Spatial database of the Bristow quadrangle, Kentucky”, Kentucky Geological Survey, Series 12, Digitally Vectorized Geologic Quadrangle Data DVGQ-216 (Adapted from Gildersleeve, B., 1963, “Geology of the Bristow quadrangle, Kentucky”, U.S. Geological Survey Geologic Quadrangle Map GQ-216, scale 1:24,000).

Toth, K. S., 2006b, “Spatial database of the Quality quadrangle, Butler and Logan Counties, Kentucky”, Kentucky Geological Survey, Series 12, Digitally Vectorized Geologic Quadrangle Data DVGQ-673 (Adapted from Gildersleeve, B., 1968, “Geologic map of the Quality quadrangle, Butler and Logan Counties, Kentucky”, U.S. Geological Survey Geologic Quadrangle Map GQ-673, scale 1:24,000).

Toth, K. S., 2006c, “Spatial database of the Riverside quadrangle, Butler and Warren Counties, Kentucky”, Kentucky Geological Survey, Series 12, Digitally Vectorized Geologic Quadrangle Data DVGQ-736 (Adapted from Shawe, F. R., 1968, Geologic map of the Riverside quadrangle, Butler and Warren Counties, Kentucky: U.S. Geological Survey Geologic Quadrangle Map GQ-736, scale 1:24,000).

Treworgy, J. D., 1988, “The Illinois Basin – a tidally and tectonically influenced ramp during mid-Chesterian time”, Illinois State Geological Survey, Circular 544, 20 p.

Treworgy, J. D., 1990, “Kaskaskia Sequence: Valmeyeran and Chesterian Series: Chapter 9: Part I. Illinois Basin: Stratigraphy”, *in* M. W. Leighton, D. R. Kolata, D. T. Oltz, J. J. Eidel, eds., M 51: Interior Cratonic Basins, AAPG Special Publication, Memoir 51, p. 125–142.

Treworgy, J. D., and Devera, J. A., 1990, “Kaskaskia Sequence Overview: Middle Devonian Series Through Chesterian Series: Chapter 7: Part I. Illinois Basin: Stratigraphy”, *in* M. W. Leighton, D. R. Kolata, D. T. Oltz, J. J. Eidel, eds. M 51: Interior Cratonic Basins, AAPG Special Publication, Memoir 51, p. 109–112.

Udden, J. A., 1914, “Mechanical Composition of Clastic Sediments”, GSA Bulletin, vol. 25, p. 655–744.

University of Leuven, 2010, “X-ray diffraction – Bruker D8 Discover – Nuclear and Radiation Physics”, https://fys.kuleuven.be/iks/nvsf/images/xrd_figure_1.jpg (accessed August, 2015).

Walcott, C. D., 1901, “Director’s Report and a Paper on Asphalt and Bituminous Rock Deposits Part I” *in* Twenty-Second Annual Report of the United States Geological Survey to the Secretary of the Interior, U.S. Geological Survey, p. 256–258.

Waychunas, G. A., 2014, “Luminescence Spectroscopy”, Reviews in Mineralogy & Chemistry, vol. 78, p. 175–217.

Weller, J. M., 1927, “The Geology of Edmonson County, Kentucky”, Kentucky Geological Survey, Series 6, vol. 28, 248 p.

Wentworth, C. A., 1922, “A Scale of Grade and Class Terms for Clastic Sediments”, Journal of Geology, vol. 30, no. 5, p. 377–392.

White, B. W., and White, E. L., 2003, “Gypsum wedging and cavern breakdown: Studies in the Mammoth Cave System Kentucky”, Journal of Cave and Karst Studies, vol. 65, no. 1, p. 43–52.

Williams, D. A., 2013, Personal Communication, Bowling Green, KY

Wilson, M. D., and Stanton, P. T., 1994, Diagenetic Mechanisms of Porosity and Permeability Reduction and Enhancement, *in* Wilson, M. D., ed., Reservoir Quality Assessment and Prediction in Clastic Rocks, SEPM Short Course, vol. 30, p. 23–41.

Zeng, E. F., 2013, “The study of physical property in GdN films”, M.S. Thesis, National Sun Yat-Sen University, 53 p., http://etd.lib.nsysu.edu.tw/ETD-db/ETD-search-c/view_etd?URN=etd-0812113-133225 (accessed October, 2015).

Zinkernagel, U., 1978, “Cathodoluminescence of quartz and its application to sandstone petrology”, *in* H. Füchtbauer, A. P. Lisitzyn, J. D. Milliman, and E. Seibold, eds., Contributions to Sedimentology, vol. 8, Balogh Scientific Books, 69 p.

Appendix A: Local Geologic Setting

A.1 Overview of Data

This section contains numerous geologic maps of the seven sample locations in addition to well and stratigraphic logs corresponding to the six sampled cores. Locations and elevations of the seven sample locations are shown in Table A.1 along with corresponding sample codes from this study. Table A.2 also shows reported Dean Stark analysis results of certain sampled intervals of core by Loring Tarcore Labs Ltd., available on the KGS (2015b) website. All elevation data, both surficial and subsurface, is in feet relative to mean sea level. Core footage was not labeled on each box by the operators but instead was given over a cored interval. Consequently, the author measured and summed the footage of core barrel in each box and core interval. Understandably the amount of core barrel measured by the author differs from the footage of core Loring Tarcore Labs reported having received. Measured footage of core barrel from this study is designated as "Measured", whereas "Received" is the reported boxed footage by Loring Tarcore Labs that excludes lost core portions (labeled "LC" on "oil sands" analysis available on the KGS (2015b) website), and "Cut" is the designated cored

Sample Locations	Sample #'s	KGS Oil & Gas Record #	Latitude (NAD1983)	Longitude (NAD1983)	Total Depth (ft)	Surface Elev. (ft)
Core 104	1,1B	133678	37.168209	-86.56375	n/a	488
Core 105	8–13	136343	37.149166	-86.576666	660	571.5
Core 106	14, 15(A&B)	133621	37.140052	-86.775573	460	464
Core 107	16, 17(A&B), 18	133622	37.129945	-86.678079	450	428
Core 108	19	133623	37.162777	-86.414999	449	513
Core 109	2–7	136344	37.159833	-86.406918	485	482
Roadcut	RC	N/A	37.552351	-86.093116	-	819.3

Table A.1. Sample location with elevation and total subsurface depth. For Sample #'s See Table 3.1 for matching 'Sample #'. Core elevation values are from the KGS (2015b) Oil and Gas Records Database (accessed February, 2015) except for 105 and 109, which use values from a 10-meter DEM of Kentucky (KDGI, 2015) (accessed February, 2015), in place of erroneous database elevations reported for these wells. Roadcut elevation is also from the 10-meter DEM.

interval. The "Approximate Difference" listed below each core section is the footage discrepancy between the "Received" and "Measured" values and is applicable to any listed depth value within that cored interval. Unless noted, lost sections of core are included for intervals' approximate footage for the boxes.

Down-borehole geophysical logs from wells near the cores were used to correlate formation tops and relative positions of cored intervals and samples. Formation tops picked from publicly available geophysical logs of nearby wells were corroborated in cores 104, 105, and 109 with proprietary well logs. Proprietary well logs were briefly shared by an industry contact for the purpose of validating publicly available geophysical

Oil Sand Sample	Interval (depth ft)		Rep Thick (ft)	Dean Stark Analysis					Sample Codes of interval or nearest representative interval
	Top	Bottom		Bulk Mass Fraction		Calc. Porosity	Saturation Pore Volume		
				Oil	Water		Oil	Water	
OB0-1	481.46	482.48	1.02	0.011	0.028	0.098	0.291	0.709	104c1-b10
OB9-1	450.20	452.10	1.9	0.007	0.042	0.121	0.141	0.859	105c2-b5
OB9-2*	452.10	452.92	0.82	0.020	0.027	0.115	0.428	0.572	105c2-b6
OB10-4	454.43	455.81	1.38	0.026	0.020	0.115	0.563	0.437	105c2-b7
OB15-9	461.94	463.45	1.51	0.020	0.026	0.113	0.431	0.569	105c2-b9
OB18-14	468.60	469.85	1.25	0.013	0.025	0.094	0.339	0.661	105c3-b1
OB20-15*	471.00	472.28	1.28	0.015	0.030	0.110	0.326	0.674	105c3-b2
OB2-1	338.06	339.14	1.08	0.002	0.044	0.114	0.052	0.948	106c1-b7
OB5-8	346.88	347.83	0.95	0.017	0.027	0.109	0.387	0.613	106c1-b10
OB6-9†	179.33	180.71	1.38	0.005	0.034	0.090	0.128	0.872	107c1-b6
OB7-10	181.07	182.12	1.05	0.008	0.032	0.100	0.196	0.804	107c1-b7
OB15-29	210.01	211.68	1.67	0.022	0.020	0.105	0.519	0.481	107c2-b5
OB1-2	254.69	255.74	1.05	0.013	0.023	0.089	0.356	0.634	108c1-2
OB2-3	279.43	281.10	1.67	0.004	0.035	0.098	0.192	0.898	109c1-b2
OB2-5	282.91	284.09	1.18	0.011	0.032	0.108	0.258	0.742	109c1-b3
OB3-7	285.30	286.52	1.22	0.008	0.034	0.106	0.198	0.802	109c1-b4
OB3-9	289.79	290.62	0.89	0.018	0.034	0.128	0.350	0.650	109c1-b5
OB8-18	301.90	303.41	1.51	0.020	0.032	0.126	0.309	0.611	109c1-b10
OB15-26*	316.17	317.19	1.02	0.014	0.023	0.092	0.374	0.626	109c2-b4

* Oil core sand interval is nearest representative of sample studied

† Oil core sand interval is not representative of studied sample (shale chips) despite being in the interval

Table A.2. Oil sands analysis conducted by Loring Tarcore Labs Ltd. Data are available from the KGS (2015b) database with corresponding studied core sample from approximated depth.

logs and correlations with other logs in areas where there was a paucity of quality geophysical logs. This information was immensely useful as correlations between wells would have been tenuous, if not erroneous, as it was with the cored sandstone from 108 initially not being recognized as Hardinsburg. As per request of the contact, confidentiality will be maintained although this data may become publicly available at a future time. With the exception of springs and water wells, all unique record numbers listed on maps and text in this section refer to the unique KGS oil and gas well Record numbers. Springs and water wells are denoted with "AKGWA" (Assembled Kentucky Ground Water Database) before their record numbers.

A.2 Core 104 (KGS Record #133678)

Core Hole 104		Warren County		Permanent Datum: GL			Elevation	488	ft
Core 1 11 Boxes		Interval:	457.45 – 488.55 ft			Cut/Received/Measured:		31.1/30.3/27.1 ft	
Box #	Measured Thickness (ft)	Approximate Interval (ft)		Sample Code & (Sample #)		Sample location in box	Approximate Sample Depth		Elevation
1	2.9	457.5	460.4						
2	1.1	460.4	461.5						
3	3.1	461.5	464.6						
4	2.9	464.6	467.5						
5	2.7	467.5	470.2						
6	2.9	470.2	473.1						
7	3.3	473.1	476.4						
8	2.8	476.4	479.2						
9	2.8	479.2	482.0						
10	2.3	482.0	484.3	104c1-b10	1, 1B	0.3’ below top	482.3’		5.7’
11	0.3 +0.8 lost	484.3	485.4						
	Approximate Difference ±3.2								
Core 2 11 Boxes		Interval:	488.55 – 518.54 ft			Cut/Received/Measured:		29.9/29.9/28.6 ft	
Box #	Measured Thickness (ft)	Approximate Interval (ft)		Sample Code & (Sample #)		Sample location in box	Approximate Sample Depth		Elevation
1	2.9	488.6	491.5						
2	1.1	491.5	492.6						
3	2.8	492.6	495.4						
4	3.0	495.4	498.4						
5	2.9	498.4	501.3						
6	3.1	501.3	504.4						
7	3.0	504.4	507.4						
8	3.2	507.4	510.6						
9	2.9	510.6	513.5						
10	2.8	513.5	516.3						
11	0.9	516.3	517.2						
	Approximate Difference ±1.3								

Table A.3. Core 104 (KGS Record #133678) boxes and corresponding depth intervals and samples.

Core 104 is situated between two normal faults with the downthrown side toward the northwest within the Pennyrile Fault System in northern Warren County at 488-ft elevation according to the KGS website (Figure A.1). The well was drilled through surficial Tradewater-Caseyville (undifferentiated). All faults are normal faults with the downthrown side to the north. There is no available down-borehole geophysical log for Core 104 on the KGS (2015b) website (as of February 2015). The closest well to 104 with a geophysical that includes the Big Clifty is Record #17692; however, this well’s geophysical log does not contain data for the entirety of the Golconda Formation and has

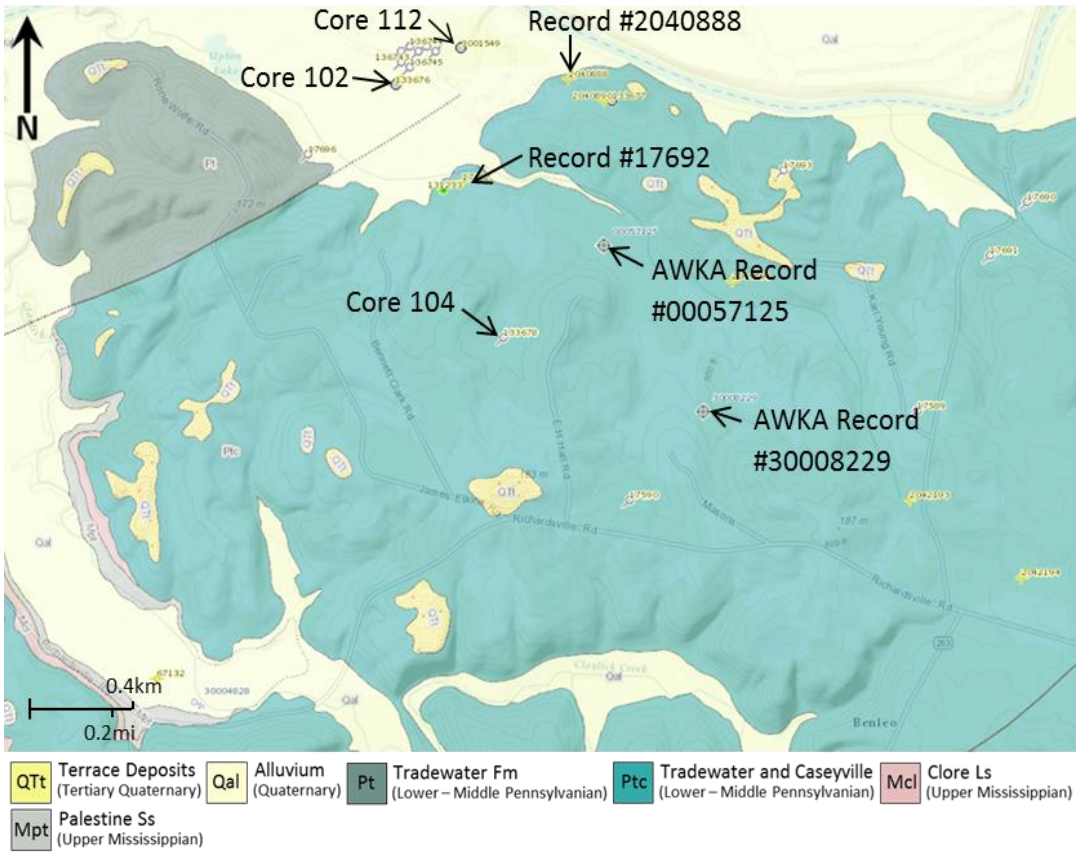

Figure A.1. Core 104 location and nearby well locations. Modified from Kentucky Geologic Map Information Service website (KGS, 2015a).

insufficient geophysical tool-data (gamma and neutron porosity) to confidently infer lithology in all sections. MegaWest cores 102 and 112 are nearby across the concealed fault north of 104, however, these cores were in somewhat disarray at the KGS and thus not included in the study. The geophysical type log used for this study (Figure A.2), from Record #2040888, is approximately 3,350 f. northeast of Core 104 and was correlated with a proprietary type log of Core 104 for the purpose of placing sampled positions and cored intervals' depths (Table A.3). Formation tops picked from publicly-available geophysical logs were corroborated in cores 104, 105, 106, and 109 with proprietary well logs.

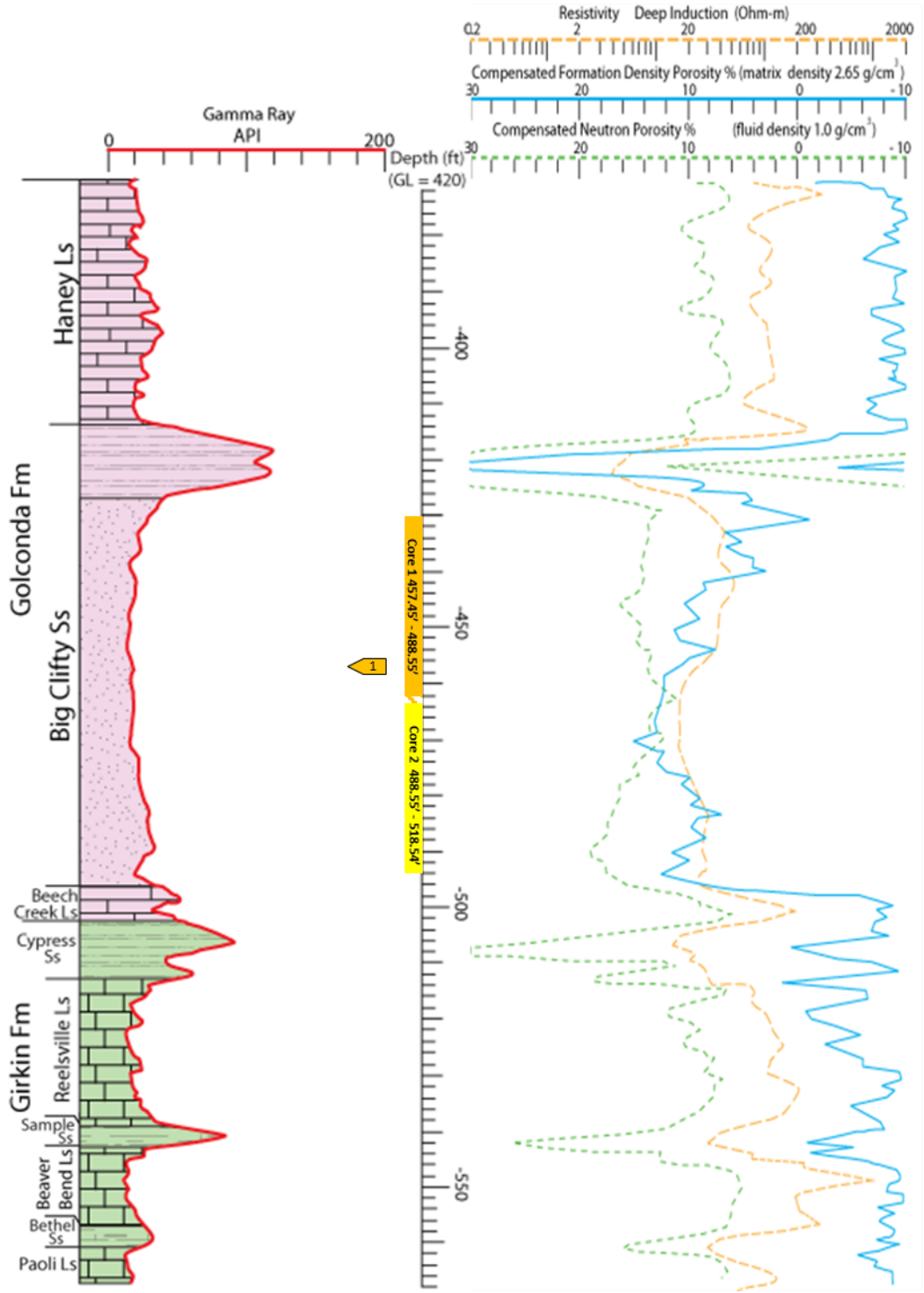

Figure A.2. Geophysical well log of KGS Record #2040888 with superimposed core intervals and sample position from Core 104. Sample (tag), and depths of cored sections of 104 (colored depth track, solid = received, striped = lost) were located on proprietary geophysical well log then correlated with Record #2040888. Tag numbers are ordinal within the cored interval and irrespective of sample code. Thus 1 within the core 1 interval is sample 104c1-b10. The shaley, heterolithic facies in the upper portion of the Big Clifty extends through all but the bottom 8 ft of core 1 of 104 which is not similarly as thick in Record #2040888. Modified from KGS (2015b), accessed October, 2014.

Within 1780 ft of Core 104 there was a water well, AKWA Record #00057125, drilled at 445-ft elevation on the Tradewater-Caseyville (undifferentiated) to a depth of 200 ft (245-ft elevation). The well did not reach the water table and the well was plugged. During drilling coal was encountered at a depth of 39 ft (406-ft elevation), and from 104–200 ft (341–245-ft elevation) only "soft spot" is recorded in the lithologic log. The closest water data to Core 104 (2,770 ft), is from AKWA Record #30008229, and it only contains water-analysis data and no information on elevation or static-water level. Results from the water-quality sampling are included in Table A.4.

Analyte Name	Analyte Group	Number of Analyses	First Date	Last Date	Max Result
Dysprosium		1	2/9/1979	2/9/1979	-0.001 ppb
Fluorine		1	2/9/1979	2/9/1979	45 ppb
Aluminum	Metals	1	2/9/1979	2/9/1979	55 ppb
Magnesium	Metals	1	2/9/1979	2/9/1979	2650 ppb
Manganese	Metals	1	2/9/1979	2/9/1979	122 ppb
Sodium	Metals	1	2/9/1979	2/9/1979	11680 ppb
Vanadium	Metals	1	2/9/1979	2/9/1979	-0.1 ppb
Uranium	Radionuclides	1	2/9/1979	2/9/1979	0.03 ppb
Chlorine, free (Field)	VOCs	1	2/9/1979	2/9/1979	3600 ppb
Field Conductivity	Field	1	2/9/1979	2/9/1979	130 mmohs

Table A.4. Water-quality data from spring, AKWA Record #30008229. Values from KGS (2015c).

A.3 Core 105 (KGS Record #136343)

Core Hole 105		Warren County		Permanent Datum: GL		Elevation	571.5 ft
Core 2 11 Boxes		Interval:	437.89 – 467.59 ft	Cut/Received/Measured:		29.7/29.7/29.0 ft	
Box #	Measured Thickness (ft)	Approximate Interval (ft)		Sample Code & (Sample #)		Sample location in box	Approximate Sample Depth	Elevation
1	2.6	437.9	440.5					
2	1.8	440.5	442.3					
3	2.6	442.3	444.9					
4	3.0	444.9	447.9					
5	2.9	447.9	450.8	105c2-b5	8	0.1’ above bot	450.7’	120.8’
6	3.0	450.8	453.8	105c2-b6	9	0.8’ below top	451.6’	119.9’
7	3.0	453.8	456.8	105c2-b7	10	1.5’ below top	455.3’	116.2’
8	2.9	456.8	459.7					
9	3.1	459.7	462.8	105c2-b9	11	0.2’ above bot	462.6’	108.9’
10	3.0	462.8	465.8					
11	1.1	465.8	466.9					
	Approximate Difference ±0.7							
Core 3 7 Boxes		Interval:	467.59 – 551.87 ft	Cut/Received/Measured:		84.2/18.2/18.1 ft	
Box #	Measured Thickness (ft)	Approximate Interval (ft)		Sample Code & (Sample #)		Sample location in box	Approximate Sample Depth	Elevation
1	2.9	467.6	470.5	105c3-b1	12	1.4’ below top	469.0’	102.5’
2	2.8	470.5	473.3	105c3-b2	13	0.3’ below top	470.8’	100.7’
3	2.9	473.3	476.2					
4	3.1	476.2	479.3					
5	1.1	479.3	480.4					
6	2.3	480.4	482.7					
7	3.0 +66.0lost*	482.7	485.7					
	Approximate Difference ±0.1							
	* Footage was not included in box interval							

Table A.5. Core 105 (KGS Record #136343) boxes and corresponding depth intervals and samples. Surface elevation taken from 10-meter DEM from the KDGI (2015).

Core 105 was retrieved from near the top of a ridge (Pisgah Ridge) east of the terminus of a normal fault (downthrown side to the north) (Figure A.3). The well itself is in a fault block between two normal faults with the throw direction of both being down to the northwest. The surficial geology is undifferentiated Tradewater-Caseyville with some Tertiary-Quaternary terrace deposits nearby at a similar elevation (550–560 ft) and Quaternary alluvium surrounding the hill. Core 105 has no borehole geophysical log, or well-completion notes associated with the core data available on the KGS (2015b) website (as of February 2015). The KGS incorrectly lists the elevation of this well at

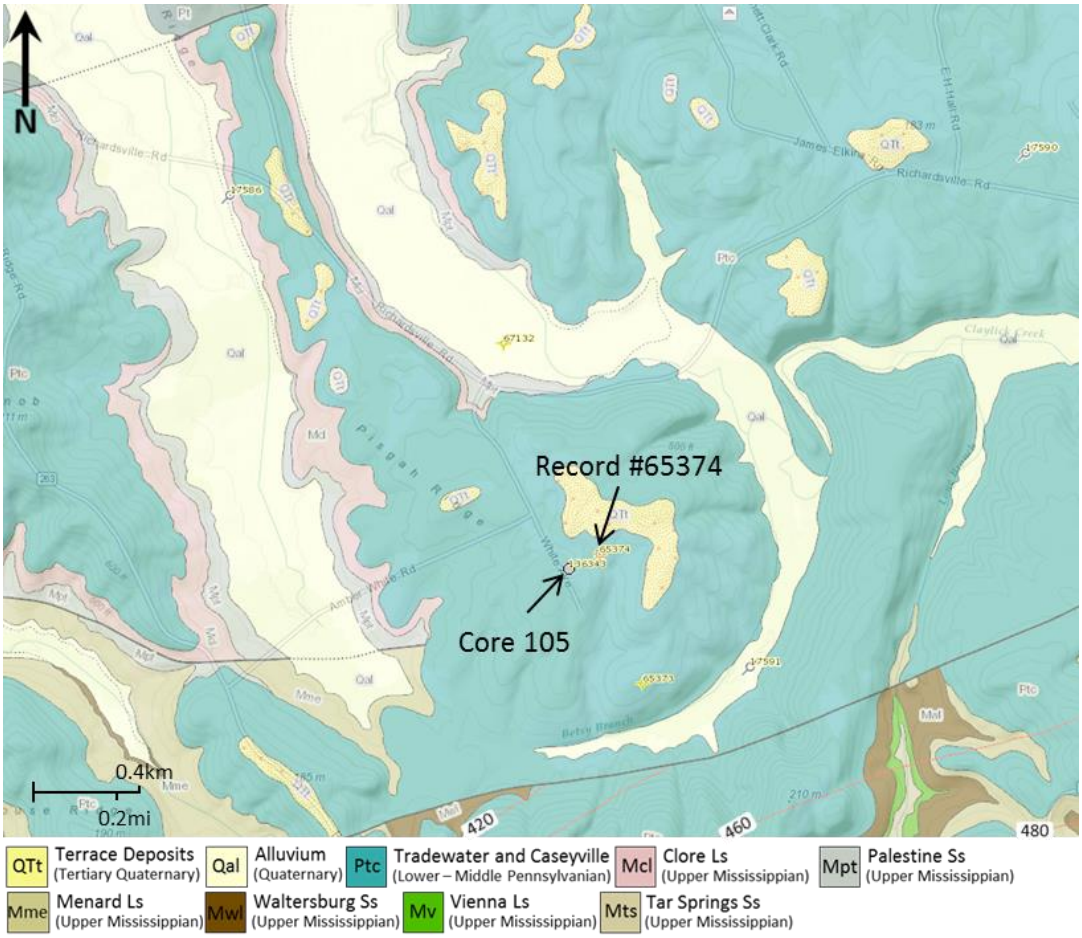

Figure A.3. Core 105 and nearby well locations. Modified from KGS (2015a).

775-ft elevation. This elevation is obviously incorrect, as Pisgah Ridge does not exceed 600-ft elevation (KGS, 2015a). Surface elevation at well 105 is 571.5 ft according to DEM data from the KDGI (2015) accessed in February, 2015.

Approximately 440 ft east-northeast of Core 105 is another oil and gas well, Record #65374, with a geophysical log as well as pertinent driller notes regarding formation waters. The driller reported encountering brine and sulfur water in siliciclastic Chesterian units, although the names of these units were misidentified which is quite common in driller's notes of wells drilled within Chesterian units in Kentucky (Schwalb, 1975).

Sample depths and cored intervals from Core 105 were located on a proprietary geophysical log from Core 105 and were then correlated with the geophysical log from Record #65374 and superimposed. There appears to be a 10–12-ft difference in depths associated with Core 105 and Record #65374, with the interval of clean sandstone within the Big Clifty being similar in thickness, 46 and 42 ft, respectively (Figure A.4). This difference, in addition to being attributed to regional structure, may also be due to DEM data used for ground elevation for Core 105 (Table A.5).

Surface elevation of well Record #65374 is 550 ft with fresh water encountered at a depth of 61 ft (489-ft elevation) according to the driller's log and completion report (Figure A.5) (KGS, 2015b). Brine waters are reported to have been encountered at a depth of 440 ft (110-ft elevation) (Figure A.5), which corresponds to the Big Clifty and not the Hardinsburg as misidentified by the driller. The Hardinsburg which, along with other units, is consistently misidentified in the well completion report, formation record (not shown), and other documents tied to this well (KGS, 2015b). This brine was described by the driller as "Brine H_2O very little salt mixed color" which may explain why the resistivity of the deep-induction wireline log (not shown) from 440–444-ft depth (110–106-ft elevation) does correspond with a decrease in resistivity. The driller noted on the resistivity log "Salt water in hole caused medium induction to have false data", and the lack of shallow induction-data precludes any comparison. The interval of 424–436-ft depth (126–114-ft elevation) within the Big Clifty had gas reported and from 440–460-ft depth (110–90-ft elevation), and pyrite described for the first time in the driller's log.

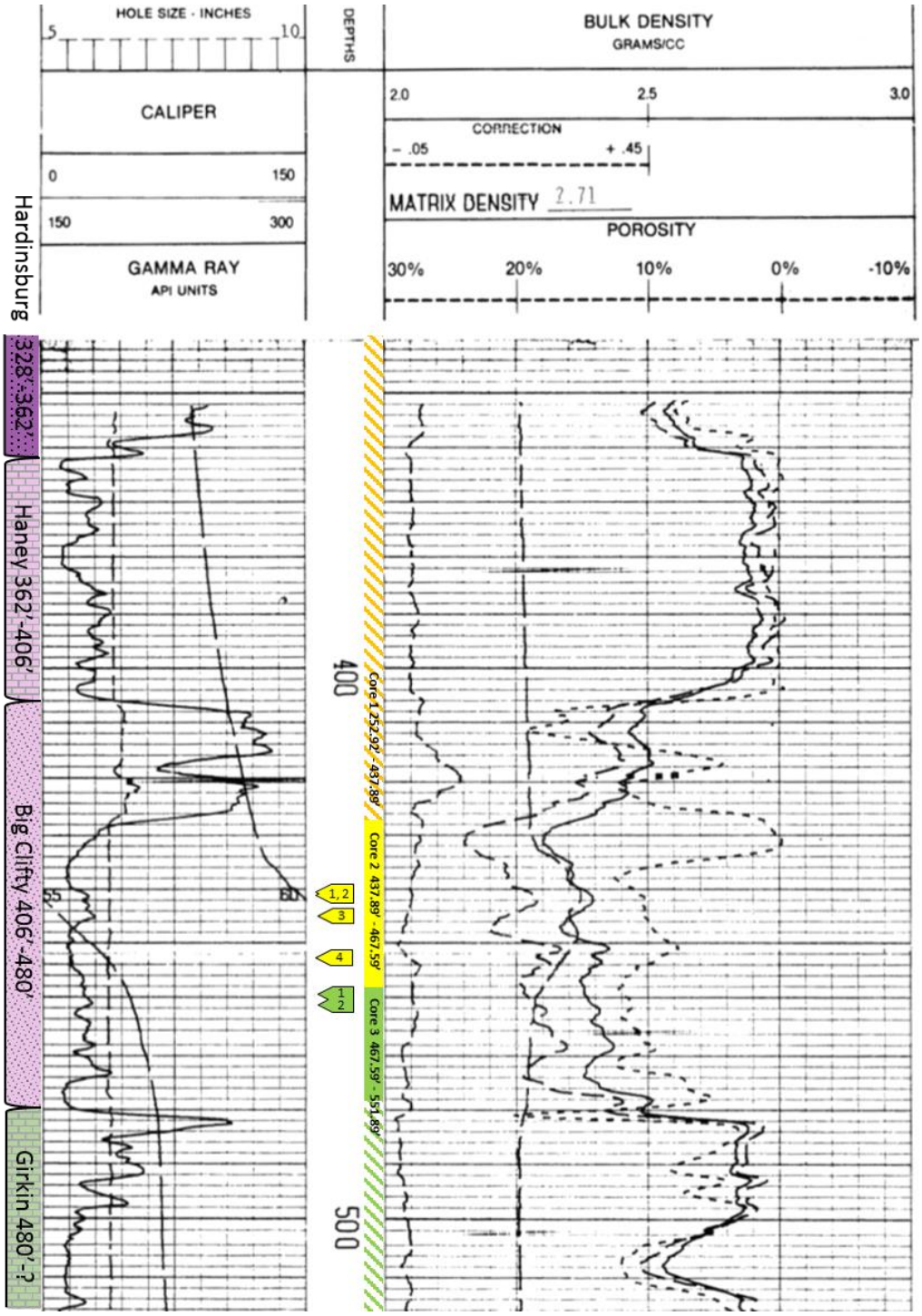

Figure A.4. Geophysical well log of KGS Record #65374 with superimposed core intervals and sample position from Core 105. Sample (tags) depths from cored sections of 105 (colored depth track, solid = received, striped = lost) were located on proprietary geophysical well log then correlated with KGS Record #65374. Tag numbers are ordinal to within the cored interval and irrespective of sample code. Thus 1, 2, 3, and 4 within the core 2 interval are samples 105c2-b5, 105c2-b6, 105c2-b7, and 105c2-b9, respectively. Modified from KGS (2015b), accessed October, 2014.

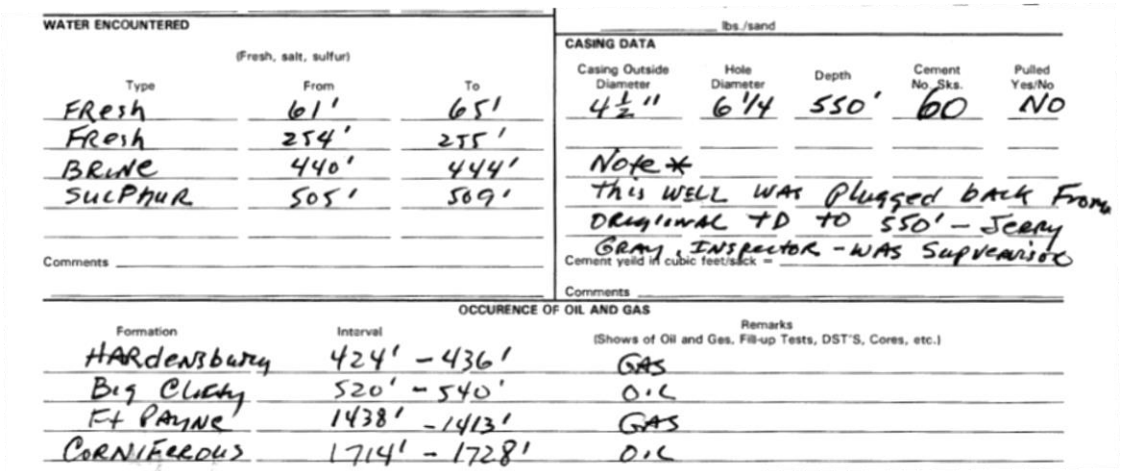

WATER ENCOUNTERED

(Fresh, salt, sulfur)

Type	From	To
FRESH	61'	65'
FRESH	254'	255'
BRINE	440'	444'
SULPHUR	505'	509'

Comments

lbs./sand

CASING DATA

Casing Outside Diameter	Hole Diameter	Depth	Cement No. Sks.	Pulled Yes/No
4½"	6¼	550'	60	NO

Note *
THIS WELL WAS Plugged BACK From ORIGINAL TD TO 550' – JERRY GRAY, INSPECTOR – WAS SUPERVISOR

Cement yeild in cubic feet/sack =

Comments

OCCURENCE OF OIL AND GAS

Formation	Interval	Remarks (Shows of Oil and Gas, Fill-up Tests, DST'S, Cores, etc.)
HARDENSBURG	424' – 436'	GAS
Big Clifty	520' – 540'	O.C
Ft PAYNE	1438' – 1413'	GAS
CORNIFEROUS	1714' – 1728'	O.C

Figure A.5. Driller's log of well KGS Record #65374. Formation names are incorrect, although the informal "Corniferous" is correctly named. From KGS (2015b).

At a depth of 505 ft (45-ft elevation), the top of the Girkin, "sulfur" is noted under the "Water Encountered" section of the driller's log, and extends to a depth of 509 ft (Figure A.5). There are no well-water data in the vicinity within the fault block and the only water data, besides that found in the driller's log of Record #65374 are the hydrological features visible on the geologic maps. Claylick Creek, the creek just north of Pisgah Ridge where Core 105 was drilled, is at ~430-ft elevation (Figure A.3).

A.4 Core 106 (KGS Record #133621)

Core Hole 106		Butler County		Permanent Datum: GL			Elevation	464	ft
Core 1 10 Boxes		Interval:	319.09 – 350.98 ft			Cut/Received/Measured:	31.8/28.8/26.8ft		
Box #	Measured Thickness (ft)	Approximate Interval (ft)		Sample Code & (Sample #)		Sample location in box	Approximate Sample Depth		Elevation
1	2.8	319.1	321.9						
2	2.7	321.9	324.6						
3	2.7	324.6	327.3						
4	2.6	327.3	329.9						
5	2.8	329.9	332.7						
6	2.8 +1.3lost	332.7	336.8						
7	2.8	336.8	339.6	106c1-b7	14	1.1’ above bot	338.5’		125.7’
8	3.0	339.6	342.6						
9	3.0	342.6	345.6						
10	1.6 +1.7lost	345.6	348.5	106c1-b10	15	0.7’ below top	347.2’		116.8’
Approximate Difference ±2.0									
Core 2 9 Boxes		Interval:	350.98 – 376.67 ft			Cut/Received/Measured:	25.6/25.6/24.5ft		
Box #	Measured Thickness (ft)	Approximate Interval (ft)		Sample Code & (Sample #)		Sample location in box	Approximate Sample Depth		Elevation
1	2.9	351.0	353.9						
2	2.9	353.9	356.8						
3	3.0	356.8	359.8						
4	3.0	359.8	362.8						
5	2.8	362.8	365.6						
6	3.1	365.6	368.7						
7	2.9	368.7	371.6						
8	2.9	371.6	374.5						
9	1.0	374.5	375.5						
Approximate Difference ±1.1									

Table A.6. Core 106 (KGS Record #133621) boxes and corresponding depth intervals and samples.

Core 106 was drilled through the surficial Menard Limestone at a surface elevation of 464-ft elevation (Figure A.6) (according to KGS website) to a depth of 460 ft. The section of interest is a relatively “clean” sandstone section of the Big Clifty. The cored interval is 319–377-ft depth (145–87-ft elevation). The first cored interval of 106 includes approximately 2.5 ft of shale at the very top before predominantly clean-sandstone body (321.6-ft depth, 142.1-ft elevation) (Table A.6). The second core includes the lower sandstone portion of the Big Clifty which is contains 11-ft thick bed of calcareous shale at 357.5–366.5-ft depth. Neither geophysical logs nor formation tops data exist, nor are they included with the online KGS data (as of February 2015). Lack of

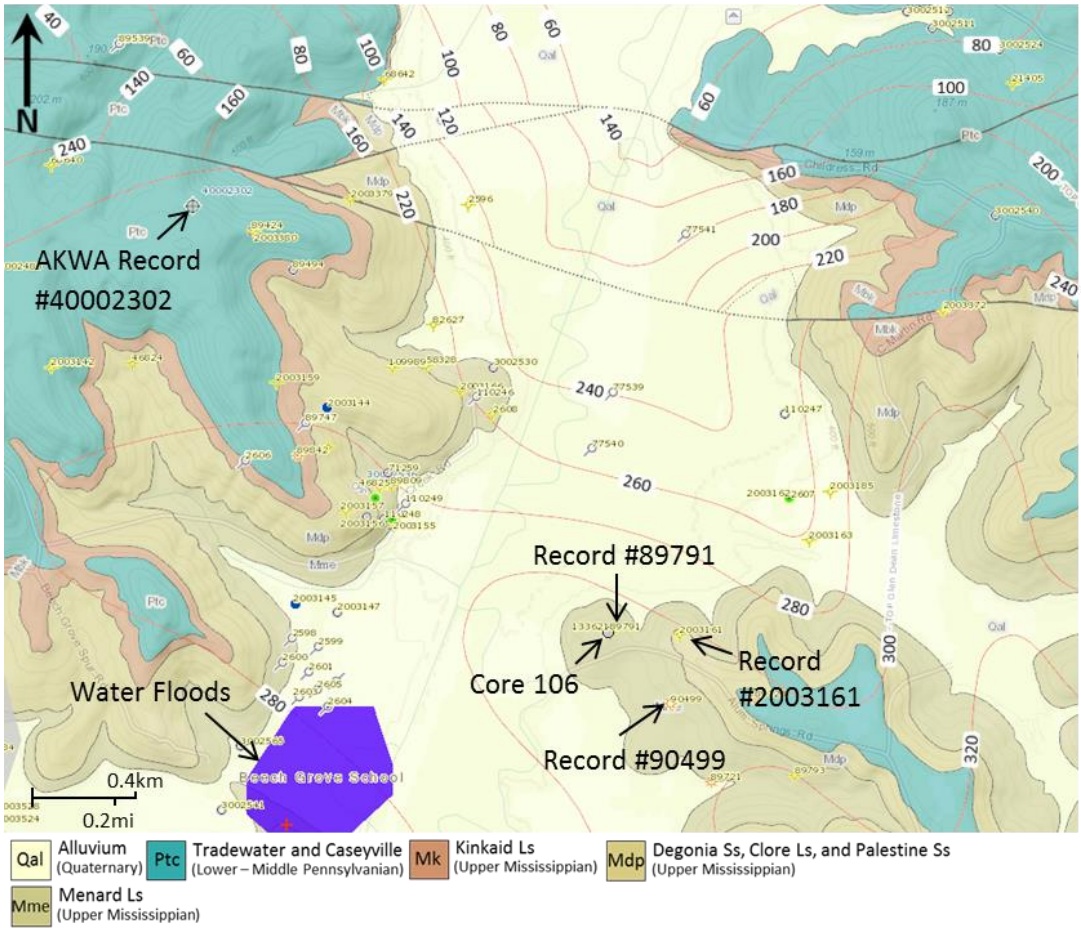

Figure A.6. Core 106 and nearby well locations. Red contour lines are the top of the Glen Dean Limestone according to the KGS. Purple area denotes a waterflood. Modified from KGS (2015a).

tops data or geophysical logs precludes correlation of Big Clifty from Core 106 with other sampled locations, and thus limiting the utility of examination of the samples in any broader geological context beyond Core 106's interval and immediate vicinity. Therefore, relative positioning of core intervals and samples' depths from Core 106 within the local Big Clifty unit as a whole required additional stratigraphic/lithologic and depth data above and below the cored interval that could be confidently tied to core lithology. This was accomplished by correlating the upper shale-sandstone (clean) contact observed in 106 (Figure A.7) with a gamma reading at 320-ft depth, 145-ft elevation (Figure A.8).

Figure A.7. Upper shale and sandstone contact in Core 106. Transition from shale to clean sandstone denoted with arrow. Core top is in the upper left. Sample was wetted with water prior to photographing.

This nearby dry gas well is only 20 ft from Core 106 and was drilled from a similar elevation, 465 ft. The 2.9-ft discrepancy between Record #89791 well and Core 106 for the shale-sandstone contact is negligible, considering the ±2 ft approximate difference measured in core from 106 (Table A.6). Although the driller's log does not identify units or include detailed lithologic information, it does note freshwater was encountered from 130–140-ft depth (335–325-ft elevation).

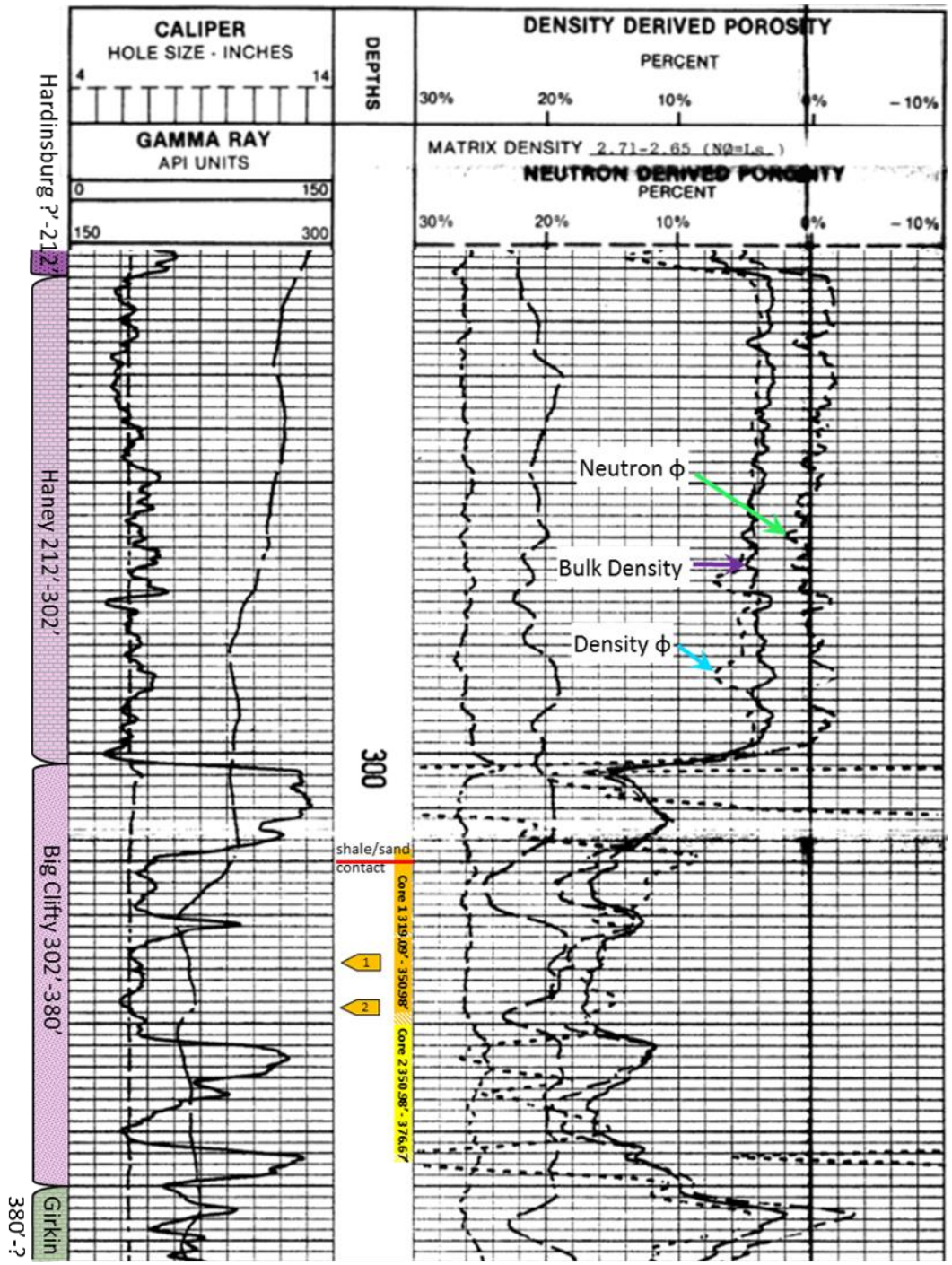

Figure A.8. Geophysical well log of KGS Record #89791 with superimposed cored and sampled intervals from Core 106. Sample (tags) depths from cored sections of 106 (colored depth track, solid = received, striped = lost) were positioned on the log relative to the correlative upper shale-sandstone contact (red line). Tag numbers are ordinal to within the cored interval and irrespective of sample code. Thus 1 and 2 within core 1 interval are samples 106c1-b7, and 106c1-b10, respectively. The Haney is unusually thick at this well. Modified from KGS (2015b).

A nearby gas well that penetrates the Big Clifty, Record #2003161, has formation picks recorded on the driller's log. This well was drilled approximately 860 ft east of Core 106, with shows of gas, oil, and dead oil occurring in siliciclastic units above the Big Clifty as well as shows of gas at the top of the Big Clifty, and dead oil within the middle portion of the member. Record #2003161 was vertically drilled at 482-ft elevation to a depth of 795 ft, with the top and base of the Big Clifty at 320 and 400 ft-depth, respectively (162–82-ft elevation). There is only 2-ft difference between the Big Clfity interval in the driller's notes of Record #2003161 and the picked intervals from the geophysical log of Record #89791 (Figure A.8).

Approximately 1,120 ft to the southeast of Core 106 is a gas well (Record #90499), which was drilled at 450-ft elevation. The well record notes freshwater from a 110–116-ft depth interval (340–334-ft elevation), roughly 200 ft above the top of the Big Clifty. There are no other water well data within a one-mile radius of Core 106 that have water-quality data from a known depth. There is one well that contains water-quality data (AWKA Record #40002302) (Table A.7); however, it is 7,040 ft to the northwest of Core 106, across the valley and at a higher elevation (Figure A.6). AWKA Record #40002302 provides no information as to the depth of the well or the static water level. Its water-quality data do show high total dissolved solids and high concentrations of Na and Cl for a domestic usage well. Although the depth of this well is unknown, the elevated levels of sodium and chloride are not surprising given the well's proximity to a fault and the presence of oil and gas in the area (Figure A.6).

Analyte Name	Analyte Group	Number of Analyses	First Date	Last Date	Max Result
Density		1	5/29/1973	5/29/1973	1.02 g/mL
Bicarbonate		1	5/29/1973	5/29/1973	492 mg/L
Silica		1	5/29/1973	5/29/1973	3.6 mg/L
Alkalinity	Bulk	1	5/29/1973	5/29/1973	600 mg/L
Hardness, total	Bulk	2	5/29/1973	5/29/1973	750 mg/L
Chloride	Inorganics	1	5/29/1973	5/29/1973	10999.97 mg/L
Fluoride	Inorganics	1	5/29/1973	5/29/1973	0.4 mg/L
Sulfate	Inorganics	1	5/29/1973	5/29/1973	1.6 mg/L
Calcium	Metals	1	5/29/1973	5/29/1973	13 mg/L
Iron	Metals	1	5/29/1973	5/29/1973	0.11 mg/L
Magnesium	Metals	1	5/29/1973	5/29/1973	170 mg/L
Manganese	Metals	1	5/29/1973	5/29/1973	0.026 mg/L
Potassium	Metals	1	5/29/1973	5/29/1973	40 mg/L
Sodium	Metals	1	5/29/1973	5/29/1973	7199.99 mg/L
Solids, Total Dissolved	Residues	1	5/29/1973	5/29/1973	19100 mg/L
Field Conductivity	Field	1	5/29/1973	5/29/1973	29400 µS/m

Table A.7. Water-quality data from domestic well, AKWA Record #40002302. Values from KGS (2015c).

A.5 Core 107 (KGS Record #133622)

Core Hole 107		Butler County		Permanent Datum: GL		Elevation	428	ft
Core 1 12 Boxes		Interval:	167.39 – 197.97 ft	Cut/Received/Measured:		30.5/29.6/25.9 ft		
Box #	Measured Thickness (ft)	Approximate Interval (ft)		Sample Code & (Sample #)		Sample location in box	Approximate Sample Depth	Elevation
1	0.8	167.4	168.2					
2	2.1	168.2	170.3					
3	2.1	170.3	172.4					
4	2.8	172.4	175.2					
5	2.9	175.2	178.1					
6	2.8	178.1	180.9	107c1-b6	16	0.6’ above bot	180.3’	247.7’
7	2.8	180.9	183.7	107c1-b7	17	1.4 below top	182.3’	245.7’
8	2.1	183.7	185.8					
9	2.7	185.8	188.5					
10	2.8	188.5	191.3					
11	1.4	191.3	192.7					
12	0.6 +0.8 lost	192.7	194.1					
	Approximate Difference ±3.7							
Core 2 6 Boxes		Interval:	197.93 – 213.91 ft	Cut/Received/Measured:		15.9/15.9/14.6 ft		
Box #	Measured Thickness (ft)	Approximate Interval (ft)		Sample Code & (Sample #)		Sample location in box	Approximate Sample Depth	Elevation
1	2.4	197.9	200.3					
2	2.7	200.3	203.0					
3	2.9	203.0	205.9					
4	2.8	205.9	208.7					
5	2.9	208.7	211.6	107c2-b5	18	0.9’ above bot	210.7’	217.3’
6	0.9	211.6	212.5					
	Approximate Difference ±1.3							

Table A.8. Core 107 (KGS Record #133622) boxes and corresponding depth intervals and samples. The oil sands analysis document available from the KGS (2015c) website lists three cored intervals however the 1st and 2nd cores with 8 and 4 boxes, respectively, were combined into single core interval of 12 boxes which is how it is designated in this document and figures.

Core 107 was drilled from 428-ft elevation to a depth of 450 ft through Quaternary alluvium. Core 107 lies upon the downthrown fault block of the normal fault to the northwest as well as the concealed fault to the northeast (Figure A.9). The Big Clifty top elevation is unknown, although it is assumed that the cored interval by MegaWest (Table A.8), which included the top of the clean sandstone section but not the upper shale-sandstone contact, is of the Big Clifty. There are no known geophysical logs of wells within the same fault block proximal to Core 107 to correlate with lithology. The driller’s log from a nearby well (Record #2003182) drilled from a similar elevation (435

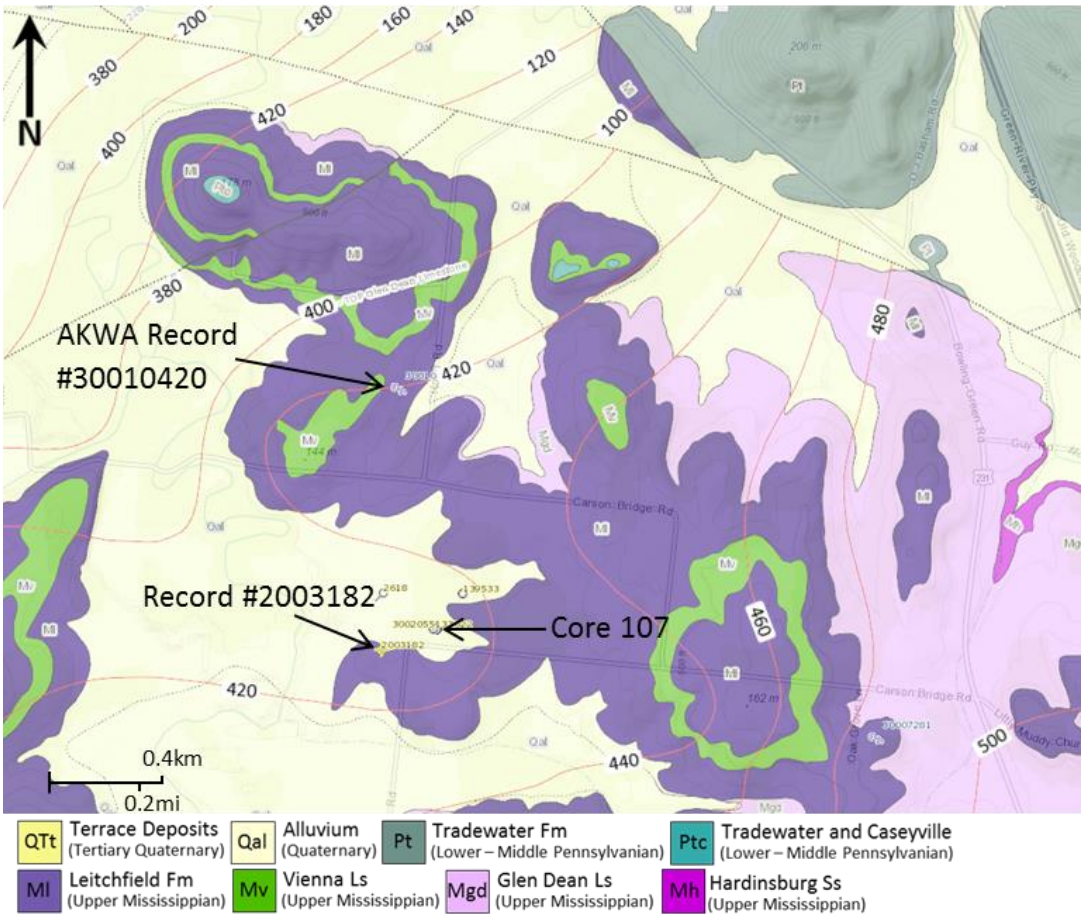

Figure A.9. Core 107 and nearby well locations. Red contour lines are the top of the Glen Dean Limestone. Modified from KGS (2015a).

ft) and to a similar depth, 220 ft (255-ft elevation), mentions a 15-ft interval of "sandy lime" following a 40-ft interval of "lime (hard)", and preceding a 40-ft section of "sand" and "sand white" before the well terminates (Figure A.10). This well is approximately 660 ft southwest of Core 107, and the 45-ft interval the driller's log notes as "lime (hard)" is likely the lower portion of the Haney Limestone, with the 15 ft of "sandy lime" being the heterolithic calcareous shale and silt in the upper portion of the Big Clifty above the main body of a clean sandstone "sand" and "sand white". Placement of the top of the Big Clifty cannot be confirmed without the contact of Haney in the cored interval

or a geophysical log to accompany the core. Therefore, it is assumed that the 10–16 ft of calcareous shale overlies the sandstone portion of the Big Clifty (Figure A.11).

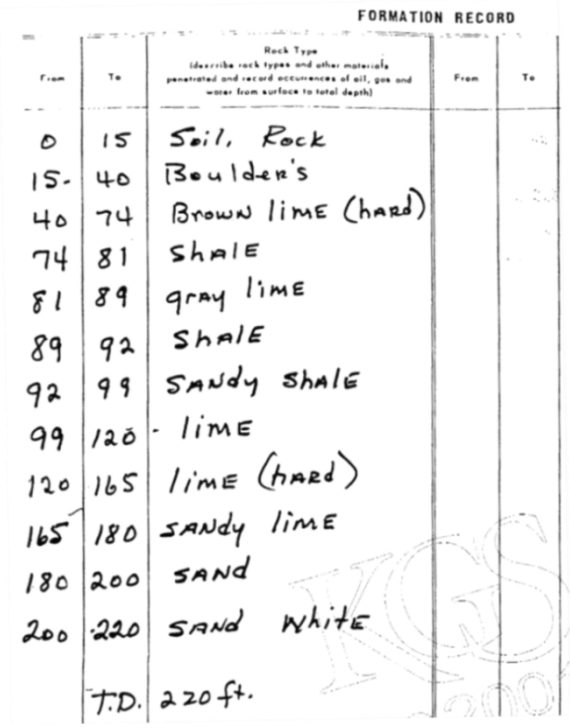

FORMATION RECORD

From	To	Rock Type (describe rock types and other materials penetrated and record occurrences of oil, gas and water from surface to total depth)	From	To
0	15	Soil, Rock		
15	40	Boulders		
40	74	Brown lime (hard)		
74	81	shale		
81	89	gray lime		
89	92	shale		
92	99	sandy shale		
99	120	lime		
120	165	lime (hard)		
165	180	sandy lime		
180	200	sand		
200	220	sand white		
	T.D.	220 ft.		

Figure A.10. Driller's log of well KGS Record #2003182. No formation names are given but depths and recorded lithologies from 120-220 ft roughly correspond to the upper units of the Golconda Formation. From KGS (2015b).

Despite the location of well Record #2003182, in the vicinity of Core 107, the information from this well remains problematic for the correlation and the placement of the Big Clifty top in Core 107 with the start of "sand" at 180-ft depth in the drillers' log (Figure A.10). It is probable that a similarly thick interval of a calcareous siliciclastic lithology to "sandy lime" lies above the cored interval of clean sandstone taken from Core 107. Correlation of wells based on lithologies, formation names, and depth measurements recorded by drillers without corresponding geophysical logs is quixotically optimistic.

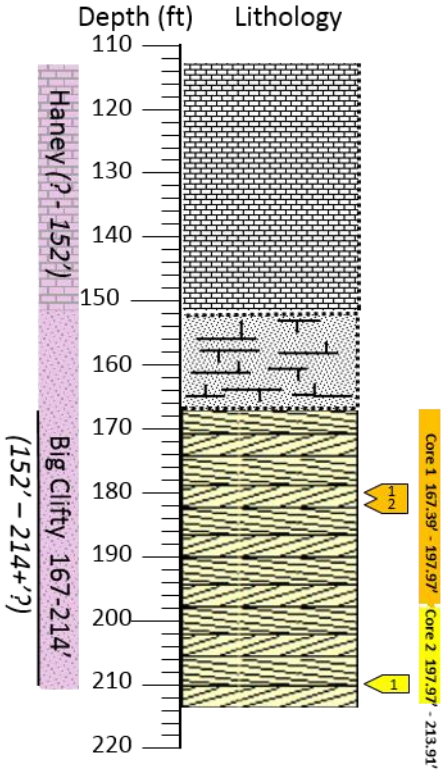

Figure A.11. Stratigraphic column of Core 107, KGS Record #133622, with core and sample intervals. The observed lithology from Core 107 is cross-bedded sandstone approximately 167–214-ft depth. The calcareous shale (152–167-ft depth) and limestone (113–152-ft depth) were not observed in core. The thicknesses and lithologies of these unobserved intervals are based off on the reported lithologies in the driller's notes from nearby well, KGS Record #2003182. The thicknesses, subsurface elevations, and lithologies in the driller's notes of Record #2003182 were sufficiently similar to the expected typical values of the Haney Limestone, the upper shaley section of the Big Clifty and the main sandstone-body of the Big Clifty to extrapolate similar values at Core 107. The parenthesized number ranges left of the depth track are the estimated depth intervals of the Haney and the Big Clifty. The non-parenthesized number range is the interval of observed Big Clifty core. Sample (tags) depths from cored sections of 107 (colored sections, solid = received, striped = lost) are to the right of the stratigraphic column. Tag numbers are ordinal to within the core intervals and irrespective of sample code. Thus 1 and 2 within the core 1 interval are samples 107c1-b6, and 107c1-b7, respectively.

There exists no depth-to-water table or formation waters data with Core 107 or any other wells in the nearby vicinity. A perennial stream, Richland Creek, flows to the north 1,660 ft west of Core 107 at a slightly lower elevation (419 ft approximately).

Approximately 2,920 ft north of Core 107 is a ‘spring’, AKWA Record #30010420, from which there is water-quality data (Table A.9). No additional information associated with this spring exists beyond analyte concentrations tested. It should be noted that the longitude and latitude of this spring places its location within a field, according to aerial photos viewed in google maps.

Analyte Name	Analyte Group	Number of Analyses	First Date	Last Date	Max Result
Dysprosium		1	2/10/1979	2/10/1979	-0.001 ppb
Bromide	Inorganics	1	2/10/1979	2/10/1979	10 ppb
Aluminum	Metals	1	2/10/1979	2/10/1979	95 ppb
Magnesium	Metals	1	2/10/1979	2/10/1979	2310 ppb
Manganese	Metals	1	2/10/1979	2/10/1979	100 ppb
Sodium	Metals	1	2/10/1979	2/10/1979	5410 ppb
Vanadium	Metals	1	2/10/1979	2/10/1979	0.3 ppb
Uranium	Radionuclides	1	2/10/1979	2/10/1979	0.166 ppb
Chlorine, free (Field)	VOCs	1	2/10/1979	2/10/1979	4400 ppb
Field Conductivity	Field	1	2/10/1979	2/10/1979	170 mmohs

Table A.9. Water-quality data from spring, AKWA Record #300010420. Values From KGS (2015c).

A.6 Core 109 (KGS Record #136344)

Core Hole 109		Warren County		Permanent Datum: GL			Elevation	482	ft
Core 1 10 Boxes		Interval:	276.84 – 306.07 ft			Cut/Received/Measured:		29.2/28.0/26.5 ft	
Box #	Measured Thickness (ft)	Approximate Interval (ft)		Sample Code & (Sample #)		Sample location in box	Approximate Sample Depth		Elevation
1	3.1	276.8	279.9						
2	2.8	279.9	282.7	109c1-b2	2	1.2’ below top	281.1’		200.9’
3	2.8	282.7	285.5	109c1-b3	3	0.8’ below top	283.5’		198.5’
4	2.8	285.5	288.3	109c1-b4	4	0.4’ below top	285.9’		196.1’
5	2.8	288.3	291.1	109c1-b5	5	0.7’ below top	289.0’		193.0’
6	2.9	291.1	294.0						
7	2.8	294.0	296.8						
8	2.8	296.8	299.6						
9	3.0	299.6	302.6						
10	0.7 +1.2lost	302.6	304.5	109c1-b10	6	0.1’ below top	302.7’		179.3’
	Approximate Difference ±1.5								
Core 2 11 Boxes		Interval:	306.07 – 335.99 ft			Cut/Received/Measured:		29.9/29.9/27.3 ft	
Box #	Measured Thickness (ft)	Approximate Interval (ft)		Sample Code & (Sample #)		Sample location in box	Approximate Sample Depth		Elevation
1	1.0	306.1	307.1						
2	3.1	307.1	310.2						
3	3.2	310.2	313.4						
4	2.9	313.4	316.3	109c2-b4	7	0.5’ above bot	315.8’		166.2’
5	2.8	316.3	319.1						
6	2.7	319.1	321.8						
7	2.7	321.8	324.5						
8	2.8	324.5	327.3						
9	2.7	327.3	330.0						
10	2.5	330.0	332.5						
11	0.9	332.5	333.4						
	Approximate Difference ±2.6								

Table A.10. Core 109 (KGS Record #136344) boxes and corresponding depth intervals and samples. Source: Surface elevation taken from 10-meter DEM from the KDGI (2015).

Core 109 was drilled near the top of a ridge on the southern side of the Green River in northeastern Warren County. According to the Kentucky Geologic Map Information Service website, the locations of mapped faults suggest that Core 109 is similar to Core 108 in that it is located on a fault block within a discontinuous section of the Pennyrile Fault System (Figure A.12). The nearest faults are: 1) a northwest-southeast trending concealed normal fault to the west (downthrown side to the southwest), and 2) an east-west trending normal fault (downthrown side to the south) to the east. Core 109

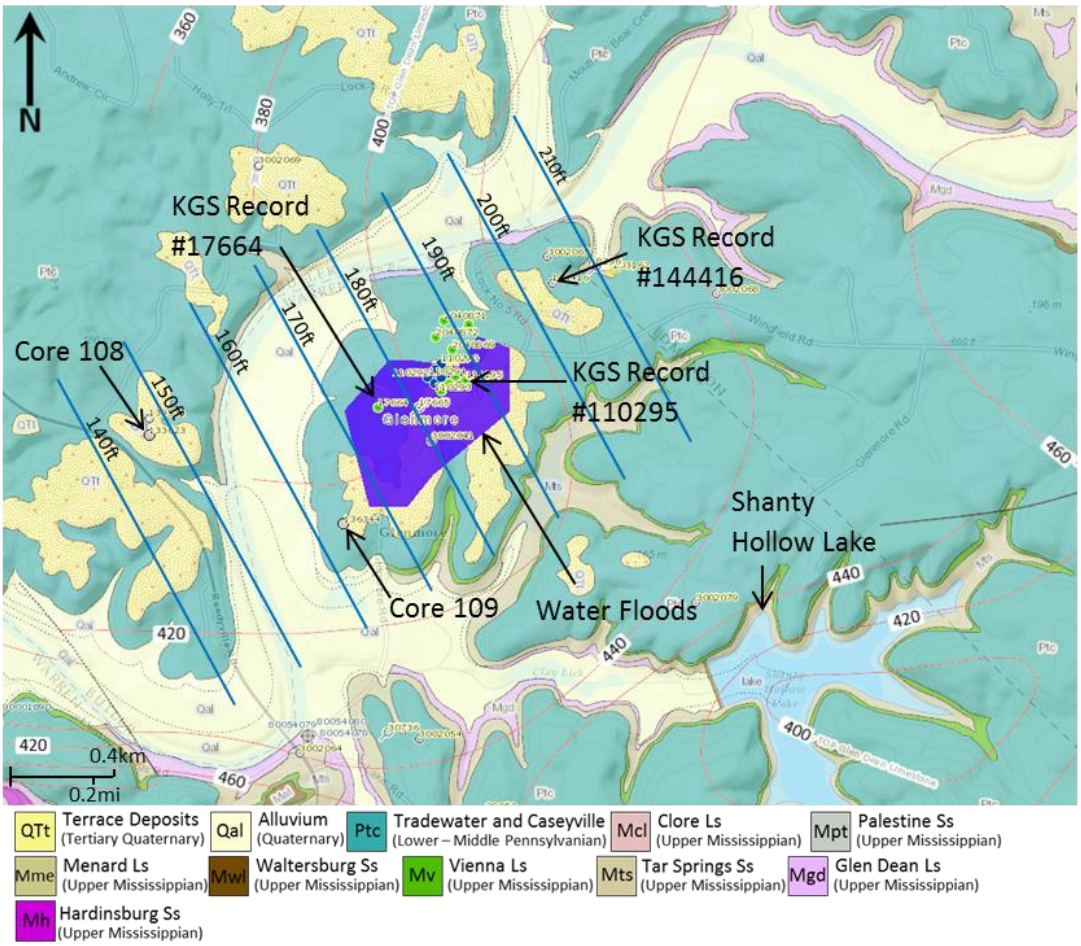

Figure A.12. Cores 108 and 109 and nearby well locations. Red contour lines are the top of the Glen Dean Limestone according to the KGS, however these are erroneous across the wells as shown here. Dark-blue lines are redrawn structure contours of the top of the Beech Creek (Barlow) Limestone, redrawn by author. The purple area denotes a water flood. Modified from KGS (2015a).

(Record #136344) was drilled through undifferentiated Pennsylvanian Tradewater and Caseyville Formations from an elevation of 482 ft to a depth of 485 ft (3-ft elevation). The section of interest is a relatively clean sandstone section of the Big Clifty from 280–316-ft depth (208–166-ft elevation) (Table A.10). The cored intervals include the sandstone body of Big Clifty, and 21 ft of carbonate and shale of the Beech Creek and the Cypress of the Girkin in the lower portion of the cored section.

Core 109 has no geophysical log, well completion notes, or core data available on the KGS (2015b) website (as of February 2015). The database does list the surface elevation of the well at 775 ft, although neither the geologic map nor the DEM indicate an elevation at that well's reported location above 500 ft Core 109 was drilled near many other oil and gas wells. These nearby oil and gas wells as well as the water injection wells for secondary recovery northeast of Core 109 in the Glenmore Oil and Gas Field, were drilled to similar depths. The most proximal well to Core 109 with usable borehole geophysical data is KGS Record #110295 (Figure A.13), which is approximately 2,290 ft away. This well, (Record #110295), was drilled at 499-ft elevation in Tertiary-Quaternary terrace deposits to a depth of 325 ft (174-ft elevation) into the Girkin Formation. Freshwater was reported in the top 50 ft of the hole within Caseyville, with heavy oil encountered at a 200–210-ft depth in the Hardinsburg Formation (299–289-ft elevation) and again from 248–313-ft depth in the Big Clifty Member interval (251–186-ft elevation).

The logged geophysical data of Record #110295, however, did not include resistivity data and the gamma-ray data quality was suspect. For this reason, a well with higher quality geophysical logs, although from a more distant location, was used. The well with geophysical logs used to correlate the sample positions and cored intervals of Core 109. The well with the higher quality geophysical logs was Record #144416 (Figure A.14). It is located approximately 3,870 ft northeast of Core 109. This well was drilled on undifferentiated Pennsylvanian Tradewater-Caseyville at 492-ft elevation to a depth of 350 ft (142-ft elevation). Despite a similar thickness of the interval of clean sandstone in Core 109, Record #110295, and #144416, (42, 42, and 46 ft, respectively), neither the

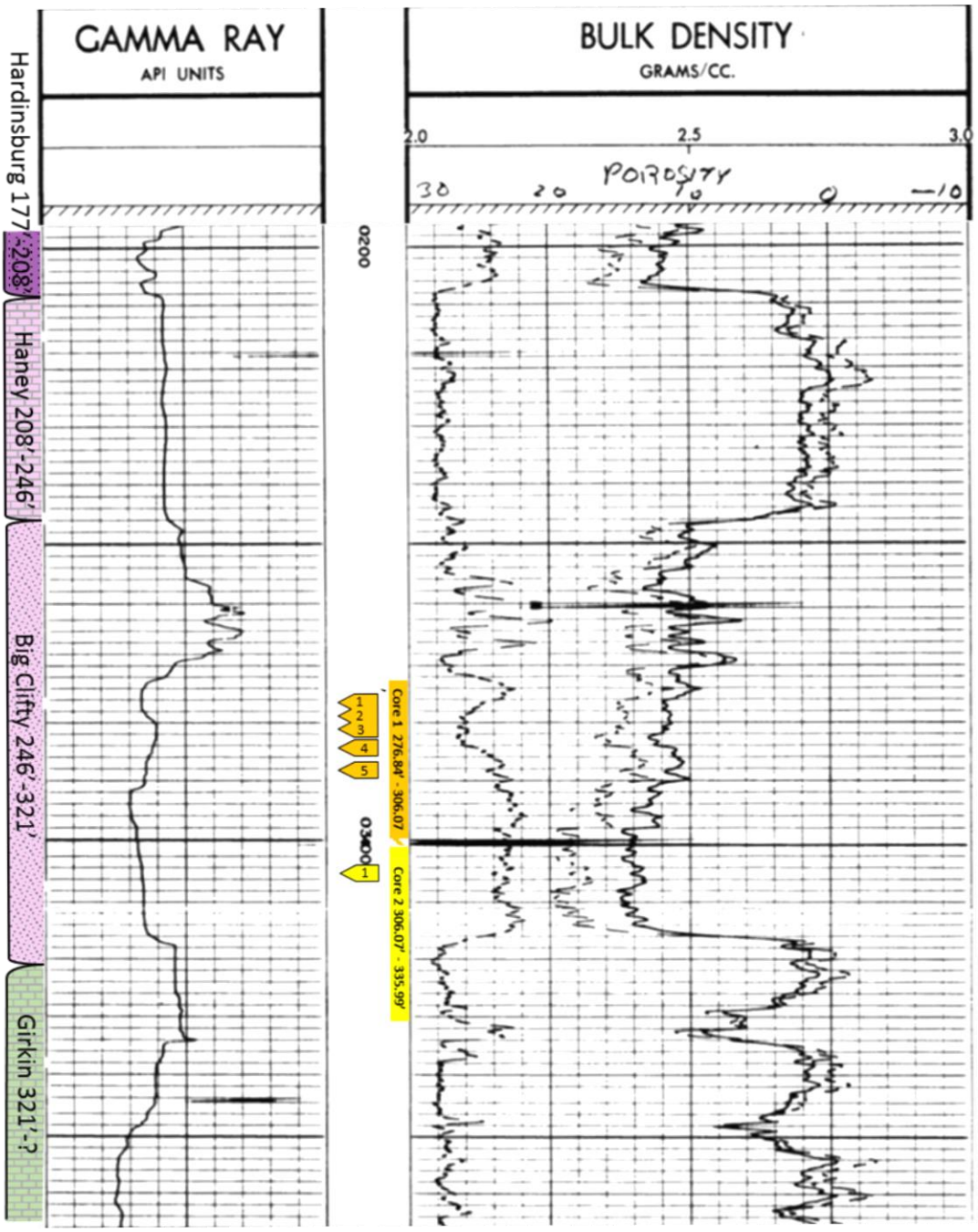

Figure A.13. Geophysical well log of KGS Record #110295 with superimposed core and sample intervals from Core 109. Sample (tags) depths from cored sections of 109 (colored depth track, solid = received, striped = lost) were positioned on the log relative to the correlative upper shale-sandstone contact (red line). Tag numbers are ordinal to within the core interval and irrespective of sample code. Thus 1, 2, 3, 4, and 5 within the core 1 interval are samples 109c1-b2, 109c1-b3, 109c1-b4, 109c1-b5, and 109c1-b10, respectively. Modified from KGS (2015b).

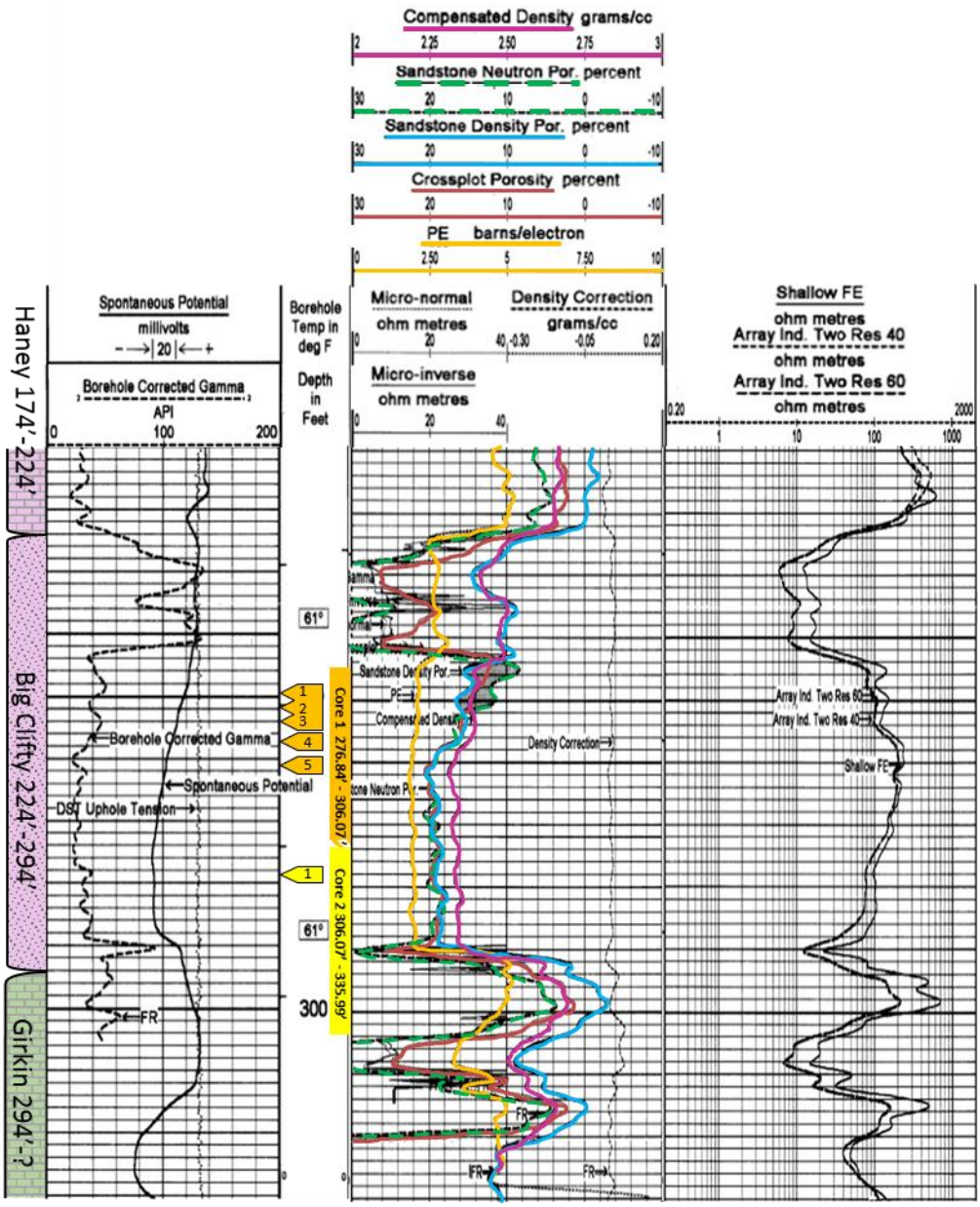

Figure A.14. Geophysical well log of KGS Record #144416 with superimposed core intervals and sample position from Core 109. Sample (tags) depths from cored sections of 109 (colored depth track, solid = received, striped = lost) were located on proprietary geophysical well log then correlated with KGS Record #144416. Tag numbers are ordinal to within the core interval and irrespective of sample code. Thus 1, 2, 3, 4, and 5 within the core 1 interval are samples 109c1-b2, 109c1-b3, 109c1-b4, 109c1-b5, and 109c1-b10, respectively. Modified from KGS (2015b).

structural tops nor bases (253 and 268 ft, and 178 and 198 ft for Record #110295 and #144416, respectively) of the Big Clifty Sandstone Member agree with the structural dip inferred from the Glen Dean Limestone structure contours of the Kentucky Geologic Map Information Service (Figure A.12). It is likely that the lack of data points south and west of the Glenmore Oil and Gas Field detract from a tenable structure map within this locality, and the curve in the Glen Dean contour (at least the 400-ft line) should continue more or less straight towards the south-southeast beyond the Glenmore Oil and Gas Field and Core 109 (Figure A.12). Despite the incongruity between the Big Clifty tops of said wells and the Glen Dean structure tops generated from limited data by the KGS, the well 3,870 ft to the northeast of Core 109, Record #144416, was sufficiently similar to Core 109 to confidently correlate and place sample positions and intervals of cored section.

A.7 Core 108 (KGS Record #133623)

Core Hole 108		Butler County		Permanent Datum: GL			Elevation	513	ft
Core 1 12 Boxes		Interval:	253.22 – 283.17 ft			Cut/Received/Measured:		29.9/29.9/28.1 ft	
Box #	Measured Thickness (ft)	Approximate Interval (ft)		Sample Code & (Sample #)		Sample location in box	Approximate Sample Depth		Elevation
1	0.8	253.2	254.0						
2	2.3	254.0	256.3	108c1-b2	19	0.9’ above bot	255.4’		257.6’
3	2.7	256.3	259.0						
4	2.9	259.0	261.9						
5	2.9	261.9	264.8						
6	2.8	264.8	267.6						
7	2.9	267.6	270.5						
8	2.7	270.5	273.2						
9	2.9	273.2	276.1						
10	2.9	276.1	279.0						
11	1.2	279.0	280.2						
12	1.1	280.2	281.3						
	Approximate Difference ±1.8								

Table A.11. Core 108 (KGS Record #133623) boxes and corresponding depth intervals and sample position. The Hardinsburg-Haney contact is at 262.2-ft depth (250.8-ft elevation).

Core 108 was drilled at 513-ft elevation on Tertiary-Quaternary terrace deposits to a depth of 449 ft (64-ft elevation). As with other MegaWest cores, there is a lack of data regarding formation tops and no borehole geophysics associated with this well available on the KGS (2015b) website (as of February 2015). There are several oil and gas wells of the Glenmore Consolidated Oil and Gas Field near Core 108, however, these wells are on the southern side of the Green River in Warren County (Figure A.12). An oil well in this field, Record #110295, located approximately 3,610 ft east of Core 108 and 2,130 ft northeast of Core 109, has a geophysical log with accurately identified tops of subsurface units (the authors of other drillers’ logs from other wells in the vicinity mistakenly identified the Big Clifty Member of the Golconda as the Cypress Sandstone. This well (Record #110295), as described earlier, was drilled on surficial Tertiary-Quaternary terrace deposits at 499-ft elevation to a depth of 325 ft (174-ft elevation) into the Girkin Formation. Fresh water was encountered in the Caseyville within the first 50 ft

of the hole and heavy oil was encountered at 200–210-ft depth (299–289-ft elevation) in the Hardinsburg Formation and at 248–313-ft depth (251–186-ft elevation) in the Big Clifty Sandstone Member.

The cored interval from 108 was the shortest of all six MegaWest wells examined with a reported 29.9 ft of core (28.1 ft measured) in box (Table A.11). The cored interval consists of approximately 9 ft of sandstone overlying 19.1 ft of crinoidal grainstone. The nearest well to 108 was 109 and correlation was done based on the sandstone-limestone contact. The sandstone-limestone contact observed in core from 108 was distinctly sharp with no transition, unlike that observed in core from 109 that had shale in the lower Big Clifty and wackestone-shale interbeds in the upper Beech Creek (Figure A.15). While initially thought to be Big Clifty and the upper Beech Creek, the core from 108 contains the Hardinsburg Sandstone and Haney Limestone. This well never reached the Big Clifty presumably because the drillers were under the impression that the basal Chesterian sandstone unit had been penetrated. This is understandable if the top of the Glen Dean structure contour lines from the KGS interactive map were used (Figure A.12), as these contours do not agree with well-log signatures from any of the wells labeled in Figure A.12. The top and base of the Beech Creek (Barlow) Limestone have each been used successfully for many years as subsurface datum in structure maps in the Illinois Basin (Bristol, 1968; Nelson et al., 2002). The tops of the Beech Creek picked from well logs of Record #144416 and #17664 were used along with the contact from Core 109, to solve the dip graphically and extrapolate the top of the Beech Creek towards Core 108. This estimate puts the top of the Beech Creek at 147-ft elevation (366-ft depth) at the location of Core 108, which is 103.8 ft below the sandstone-limestone

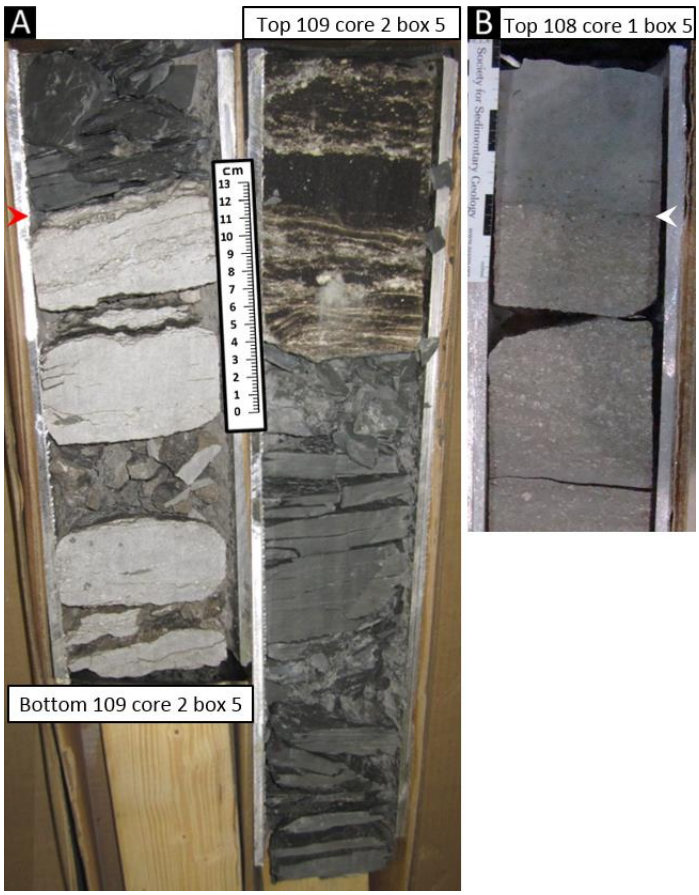

Figure A.15. Difference in sandstone contacts. A) Big Clifty and Beech Creek (Barlow) Limestone contact (red arrowhead) from Core 109, scale along box divider is in centimeters. Lithology transitions from sandstone to shale to wackestone down hole. B) Hardinsburg and Haney contact (white arrowhead) from Core 108, scale left of core is in inches. The Hardinsburg (above the white arrowhead) is a clean sandstone while the Haney (below the white arrowhead), is a crinoidal grainstone. The core was wetted with water prior to photographing.

contact observed in core at 250.8-ft elevation (262.2-ft depth) (Figure A.16). This 103.8-ft difference is ~12 ft shy of the approximate thickness of the combined Haney Limestone (58 and 50 ft) and Big Clifty Sandstone (61 and 70 ft) of wells Record #144416 and #17664 (119 and 120 ft, respectively). The approximate 12 ft of difference is reasonable, considering the extrapolation and variations in depositional environments. As Core 109 is closest to 108, the geophysical well log of Record #144416 was also used to place the sample position

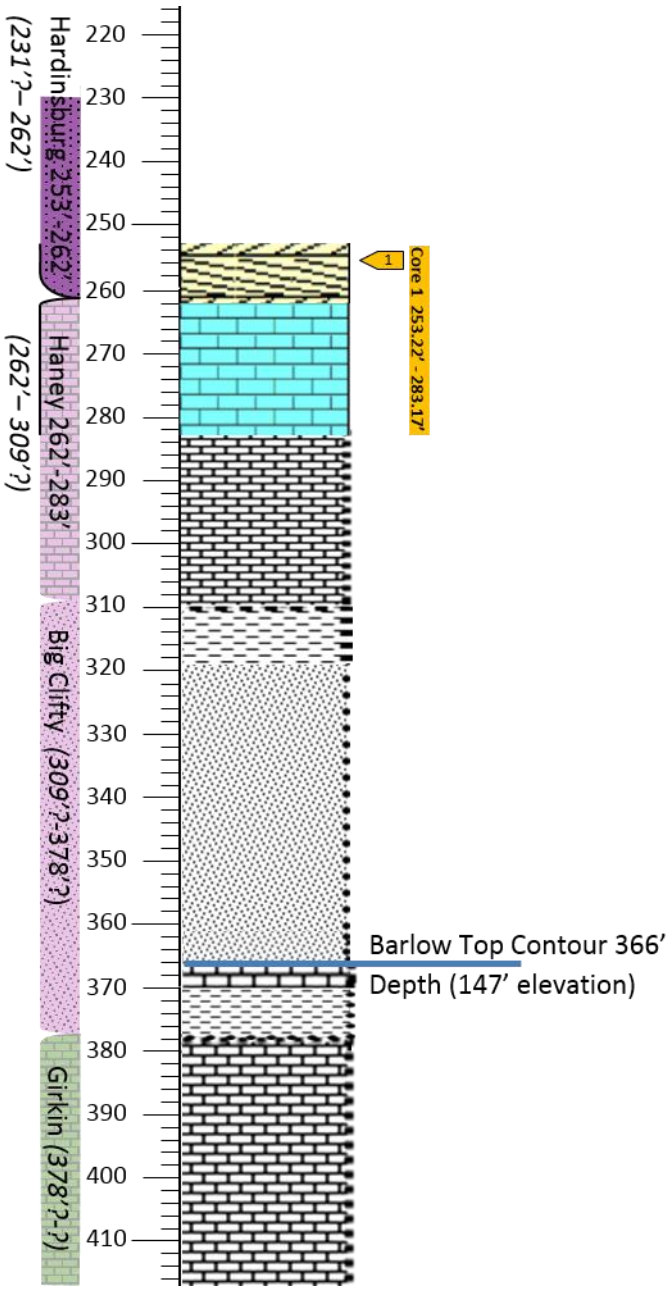

Figure A.16. Stratigraphic column of Core 108, KGS Record #133623, with core and sample intervals. Sample (tag) depth from cored section (colored, solid = received) is to the right of lithology. The observed lithology (colored) from Core 108 is approximately 9 ft of cross-bedded sandstone overlying 21 ft (19 ft measured) of crinoidal packstone and grainstone limestone, is colored approximately 253–283-ft depth. Lithology, thickness, and position of the limestone, shale, sandstone, shale, then limestone lithology sequence (283–416-ft depth) below the observed lithology (253–283-ft depth) was inferred from nearby well logs and the structure of the Beech Creek (Barlow) Limestone as are the parenthesized depths associated with these geologic units.

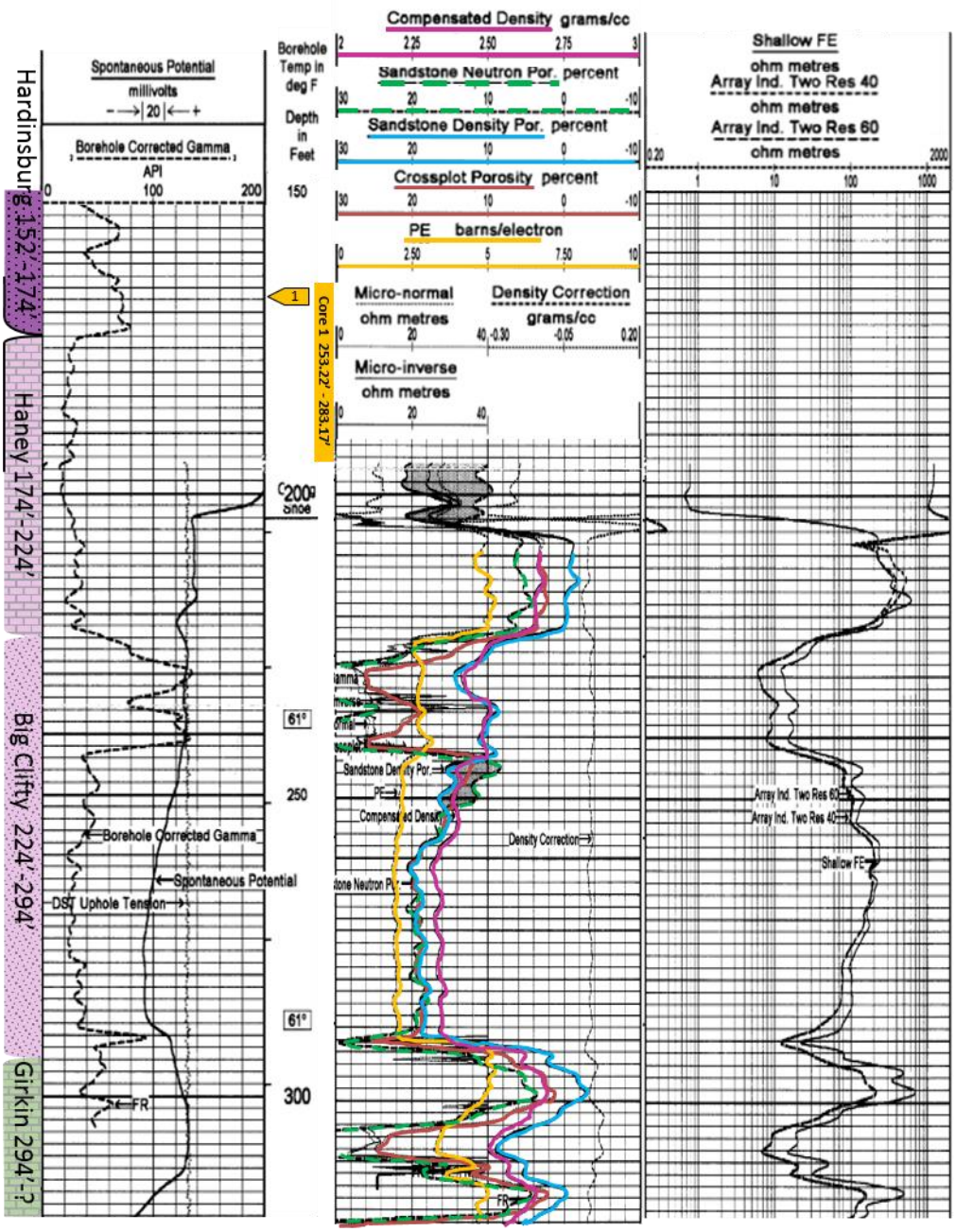

Figure A.17. Geophysical well log of KGS Record #144416 with superimposed cored interval and sample position from Core 108. Sample (tag) depth from cored section of 108 (colored depth track, solid = received, striped = lost) were located relative to the Hardinsburg and Haney contact on the geophysical well log of KGS Record #144416. Tag numbers are ordinal to within the core interval and irrespective of sample code. Thus 1, within the core 1 interval is sample 108c1-b2. Modified from KGS (2015b).

and cored interval (Figure A.17). Despite the late realization of the inclusion of sandstone other than Big Clifty in the study, the sample from Core 108 was allowed to remain as it, too, contained heavy-end hydrocarbons and potentially shared paragenetic histories with the Big Clifty samples.

A.8 Roadcut, Hardin County

A sample of Big Clifty was collected from a roadcut exposure on the southern side of the Wendell H. Ford (formerly Western Kentucky) Parkway, mile marker 120.1, in southeastern Hardin County (Figure A.18). This sample was retrieved five miles east-northeast of the type section outcrop of the Big Clifty Sandstone Member of the Golconda Formation in Kentucky (Figure 2.2). The type section is just south of the town of Big Clifty on Highway 62 mile marker 28.8 on the banks of Clifty Creek in Grayson County (not shown). The Roadcut sample was taken at approximately 819.3-ft elevation from the upper section of Big Clifty near the contact with the Haney that contained heavy oil. The type section and the Roadcut sample are on fault blocks within normal, north-northeastern trending faults that intersect with the Rough Creek Shawneetown Fault System "dogleg" to the south. The downthrown side of the normal fault east of the Roadcut sample in Figure A.18, Summit Fault, is to the northwest, and the downthrown side of the unnamed normal fault northeast of the sample is towards the northeast.

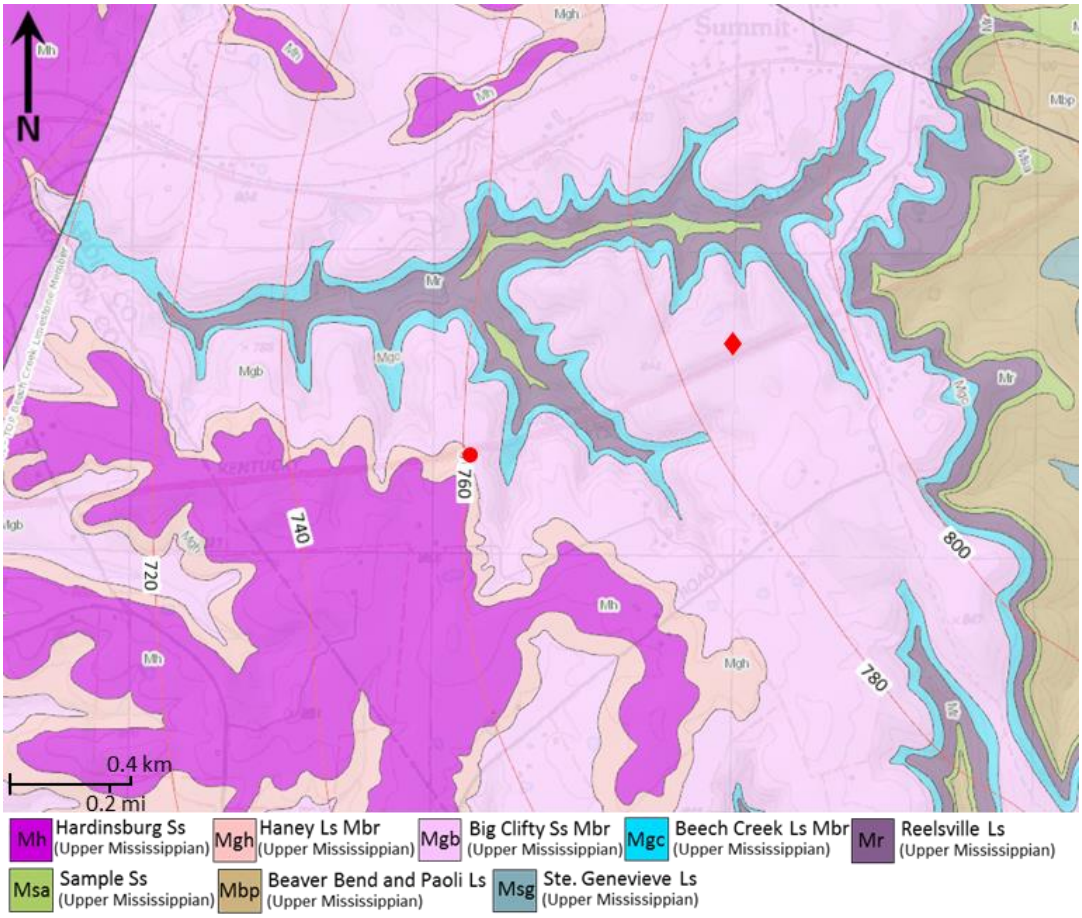

Figure A.18. Roadcut sample location. Sample (red circle) was taken from southern side of Wendell H. Ford (formerly Western Kentucky) Parkway mile marker 120.1. Red diamond denotes location of Figure 5.5. Red contour lines are the top of the Beech Creek (Barlow) Limestone. For location in larger geological context see Figure 2.2. Modified from KGS (2015a).

APPENDIX B: Sample Inventory

The following is the complete inventory of samples studied including a sample not taken from core. Images of thin sections and cores in this section are orientated correctly (e.g., up being the upwards direction). Notches and arrows on the thin sections and billets themselves do not consistently indicate the up orientation across all samples. Thin sections and billets that depart from conventional orientation indicators are 105c3-b2, 106Bc1-b10, 109c1-b2, and 109c1-b3. The red bracket to the side of core boxes indicates the section of core sampled. The dashed red boxes in the figures indicate the exact location from which the billet or sample was taken. The black and white scale bar in core box images has one side in inches and the other centimeters. Two of core box images do not contain this scale bar but have scale indicated in either inches or centimeters. Core diameters are all four inches across. Thin sections were scanned in a specialized scanner with polarizing films. In some samples epoxy began to discolor brown due to prolonged exposure to high-voltage electrons used in cathodoluminescence and, as a result, some of these thin sections' current appearance differs slightly from those in the following images. Scanned 60-µm thick thin sections, intended for fluid inclusions are included, despite the fact that the quality of the thin sections was poor. Sample peeling and poor polish inhibited these samples from being efficiently utilized in this study. For the most part standard 30-µm thick thin sections were utilized for this study.

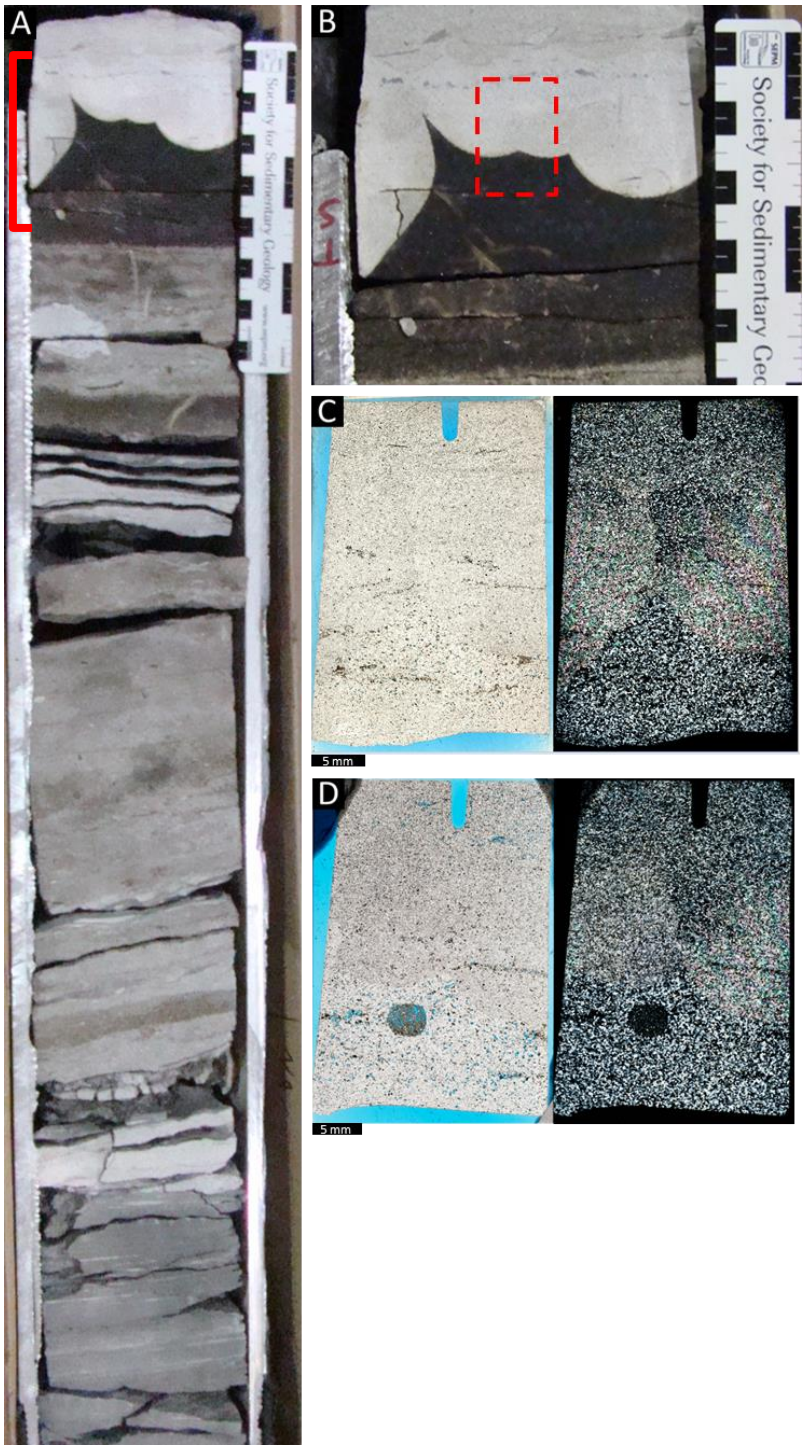

Figure B.1. MegaWest Core 104 core 1 box 10. A) Box of core. B) Sampled location in core. C & D) Scanned thin sections under plane-polarized and cross-polarized light (left to right). Standard thin section (C) 30-µm thick, of sample 104c1-b10; and 60-µm thick thin section of 104Bc1-b10, (D), intended for fluid inclusion study.

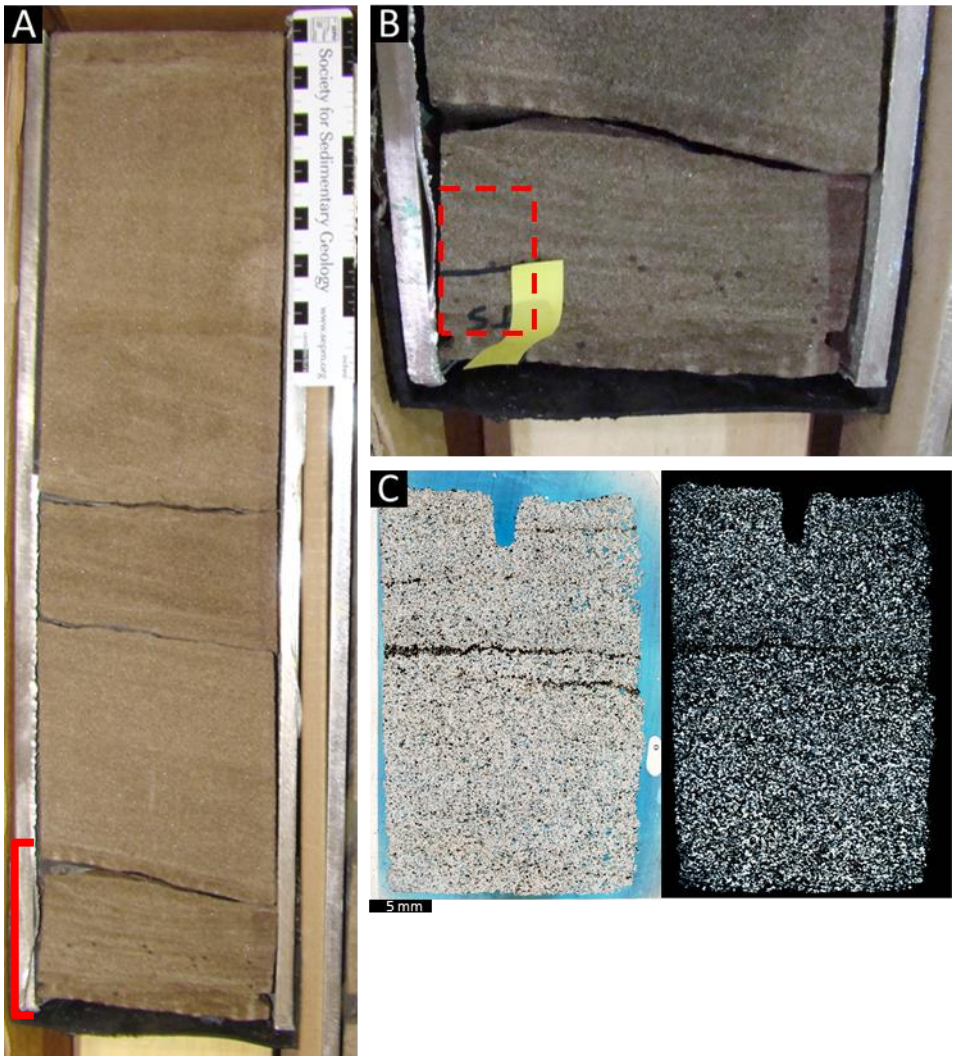

Figure B.2. MegaWest Core 105 core 2 box 5. A) Box of core. B) Sampled location in core. C) Scanned thin section under plane-polarized (left) and cross-polarized light (right). Thin section of sample 105c2-b5 is of standard 30 µm thickness.

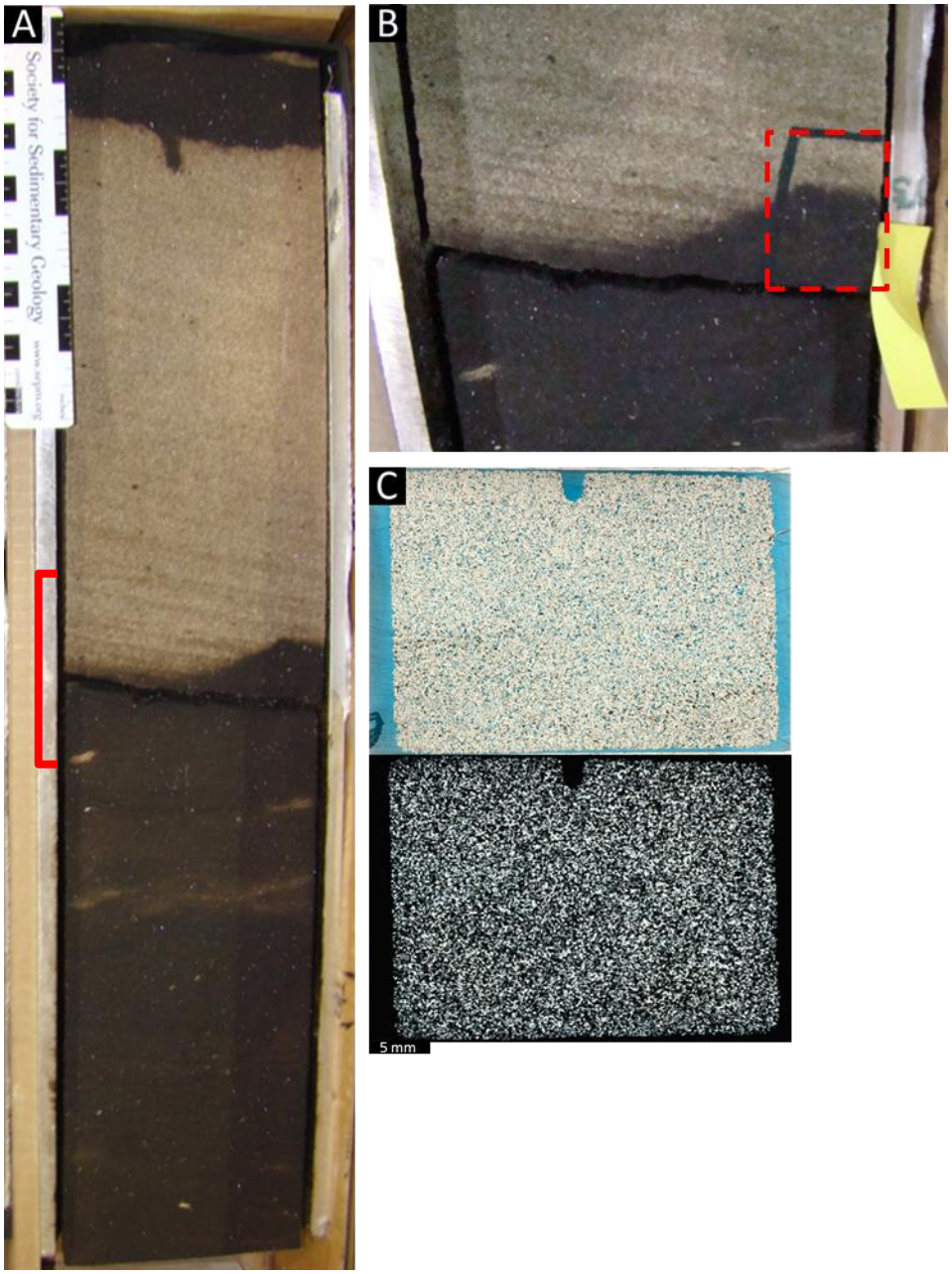

Figure B.3. MegaWest Core 105 core 2 box 6. A) Box of core. B) Sampled location in core. C) Scanned thin section under plane-polarized (upper) and cross-polarized light (lower). Thin section of sample 105c2-b6 is of standard 30 µm thickness.

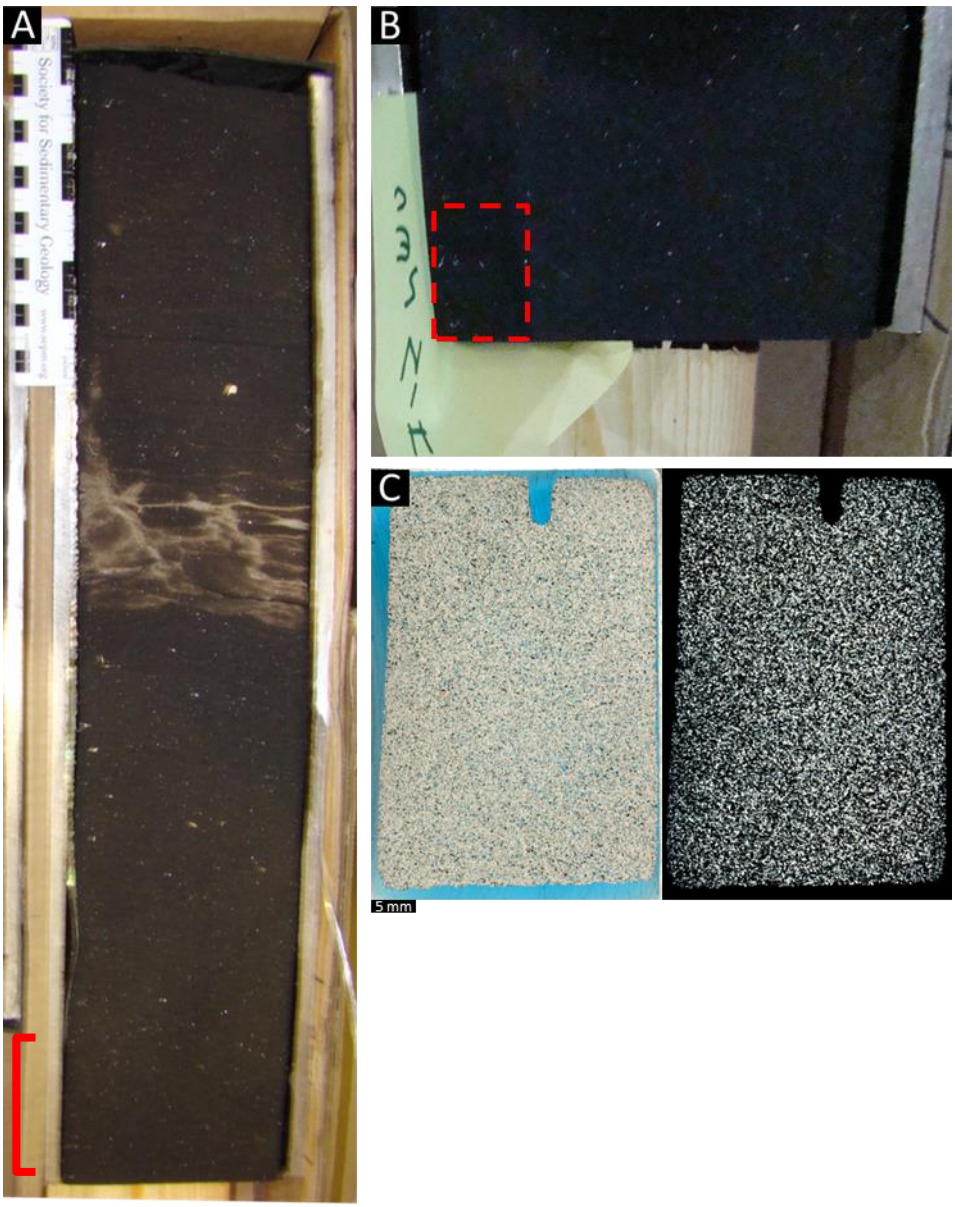

Figure B.4. MegaWest Core 105 core 2 box 7. A) Box of core. B) Sampled location in core. C) Scanned thin section under plane-polarized (left) and cross-polarized light (right). Thin section of sample 105c2-b7 is of standard 30 µm thickness.

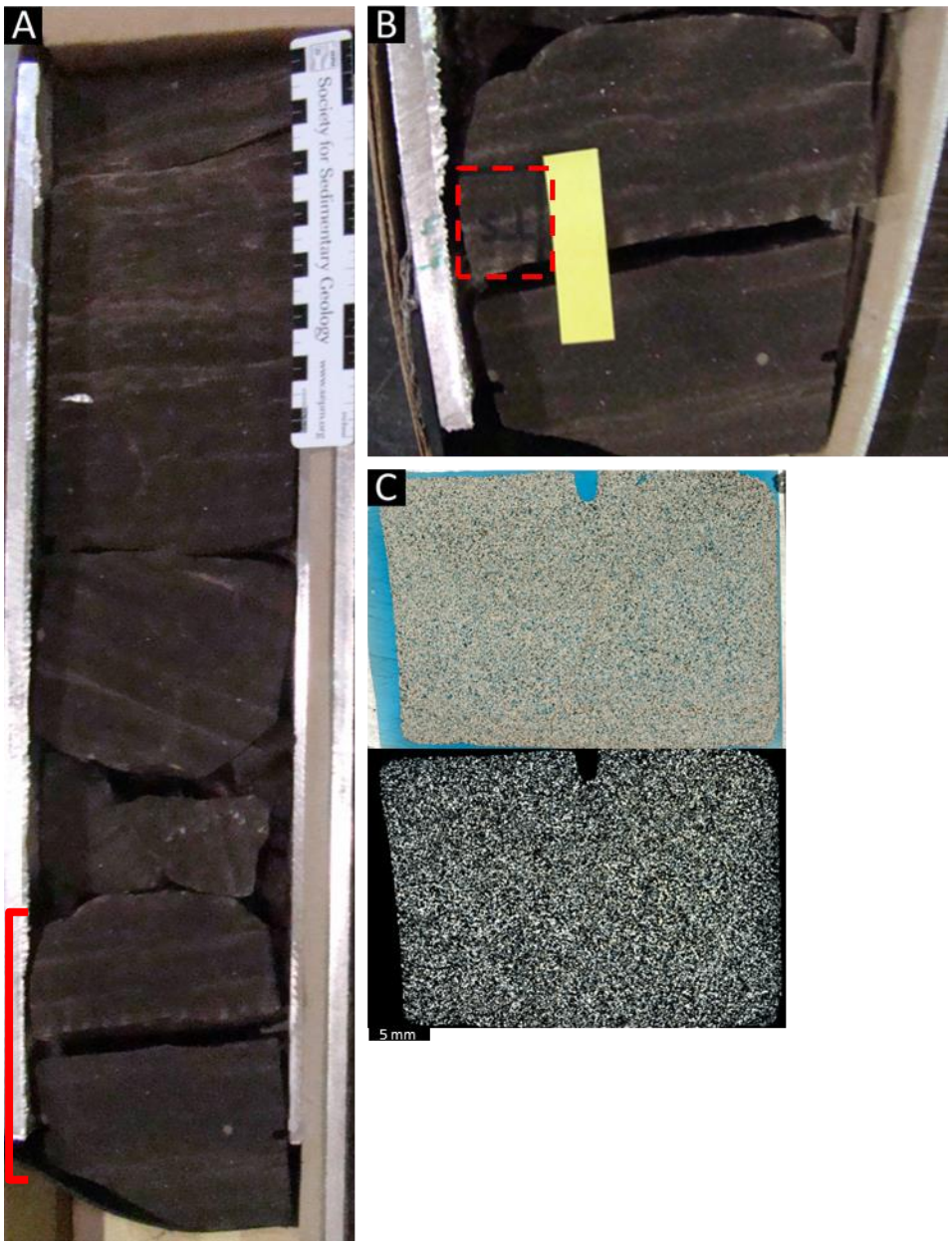

Figure B.5. MegaWest Core 105 core 2 box 9. A) Box of core. B) Sampled location in core. C) Scanned thin section under plane-polarized (left) and cross-polarized light (right). Thin section of sample 105c2-b9 is of standard 30 µm thickness.

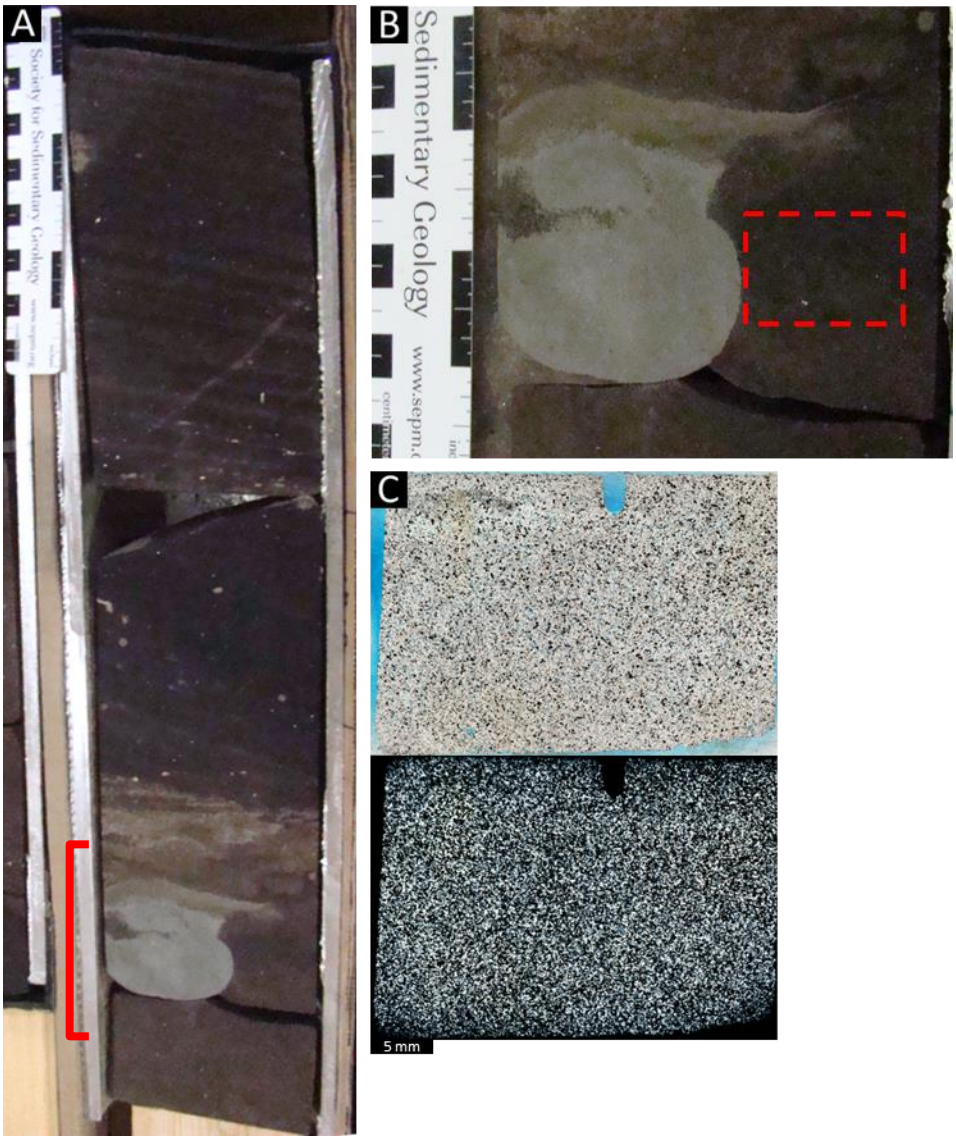

Figure B.6. MegaWest Core 105 core 3 box 1. A) Box of core. B) Sampled location in core. C) Scanned thin section under plane-polarized (left) and cross-polarized light (right). Thin section of sample 105c3-b1 is of standard 30 µm thickness.

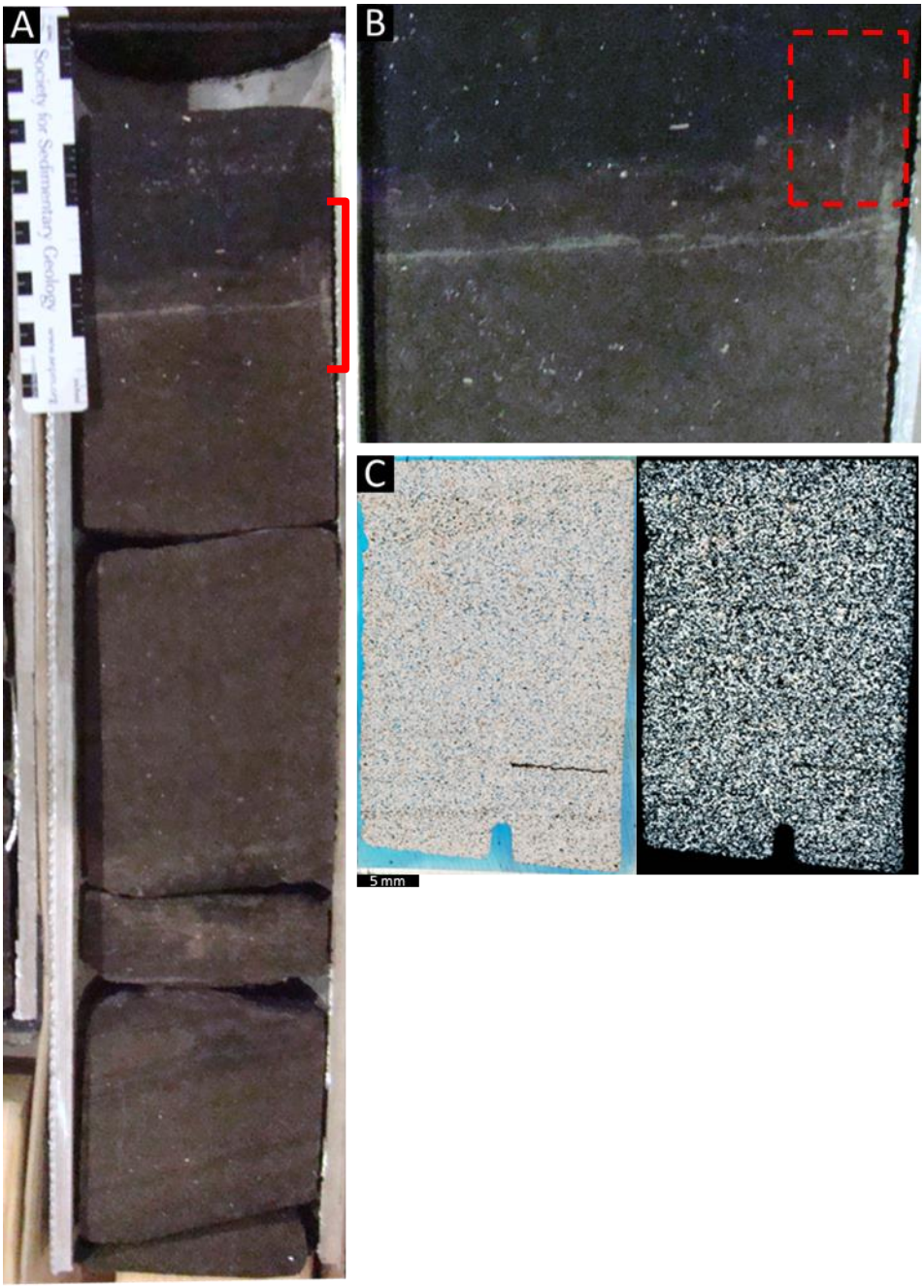

Figure B.7. MegaWest Core 105 core 3 box 2. A) Box of core. B) Sampled location in core. C) Scanned thin section under plane-polarized (left) and cross-polarized light (right). Thin section of sample 105c3-b2 is of standard 30 µm thickness. Orientation indicated with notch in thin section and billet (not shown) indicates downward direction for sample 105c3-b2.

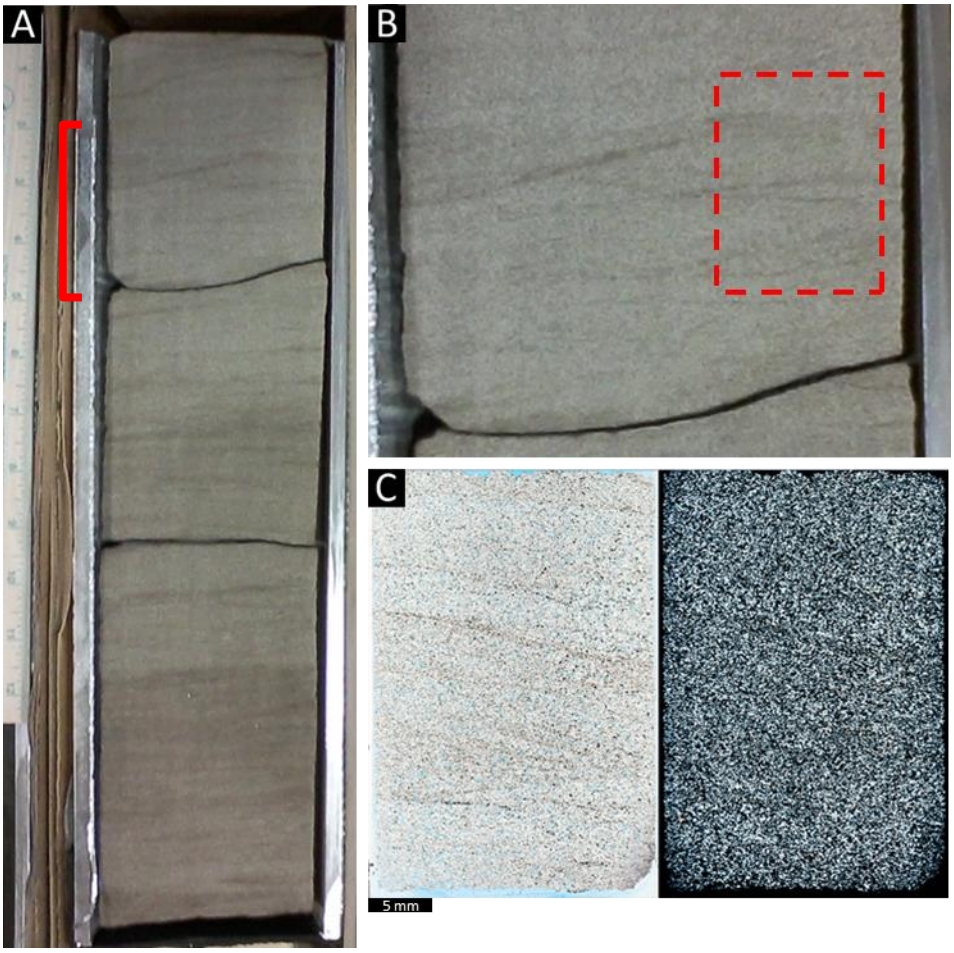

Figure B.8. MegaWest Core 106 core 1 box 7. A) Box of core, scale left of box is in inches (12 in). B) Sampled location in core. C) Scanned thin section under plane-polarized (left) and cross-polarized light (right). Thin section of sample 106c1-b7 is of standard 30 µm thickness.

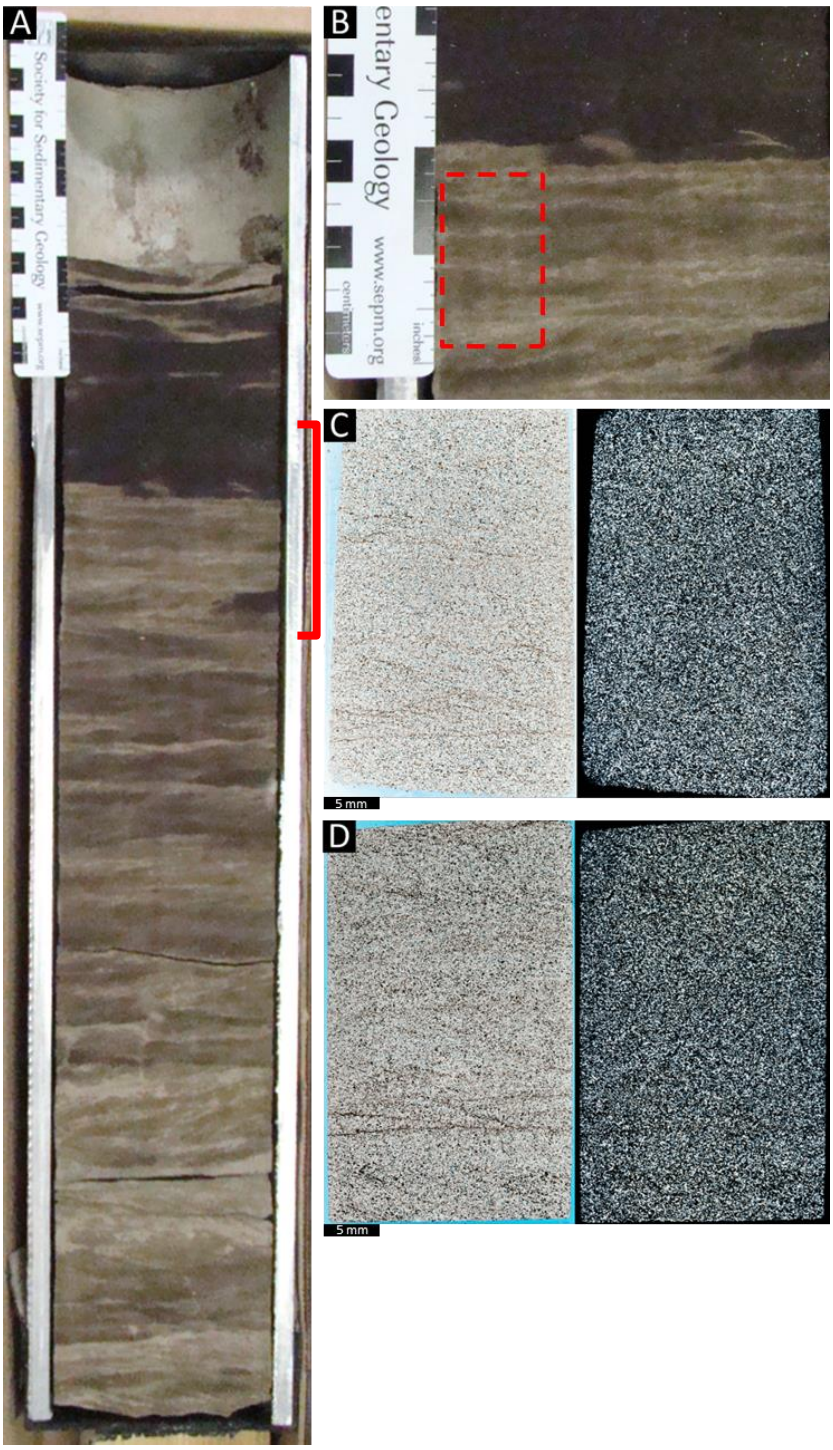

Figure B.9. MegaWest Core 106 core 1 box 10. A) Box of core. B) Sampled location in core. C & D) Scanned thin sections under plane-polarized and cross-polarized light (left to right). Standard thin section (C) 30-µm thick, of sample 106c1-b10; and 60-µm thick thin section of 106Bc1-b10, (D), intended for fluid inclusion study. D) Arrow on thin section and billet of 106Bc1-b10 indicates downward orientation.

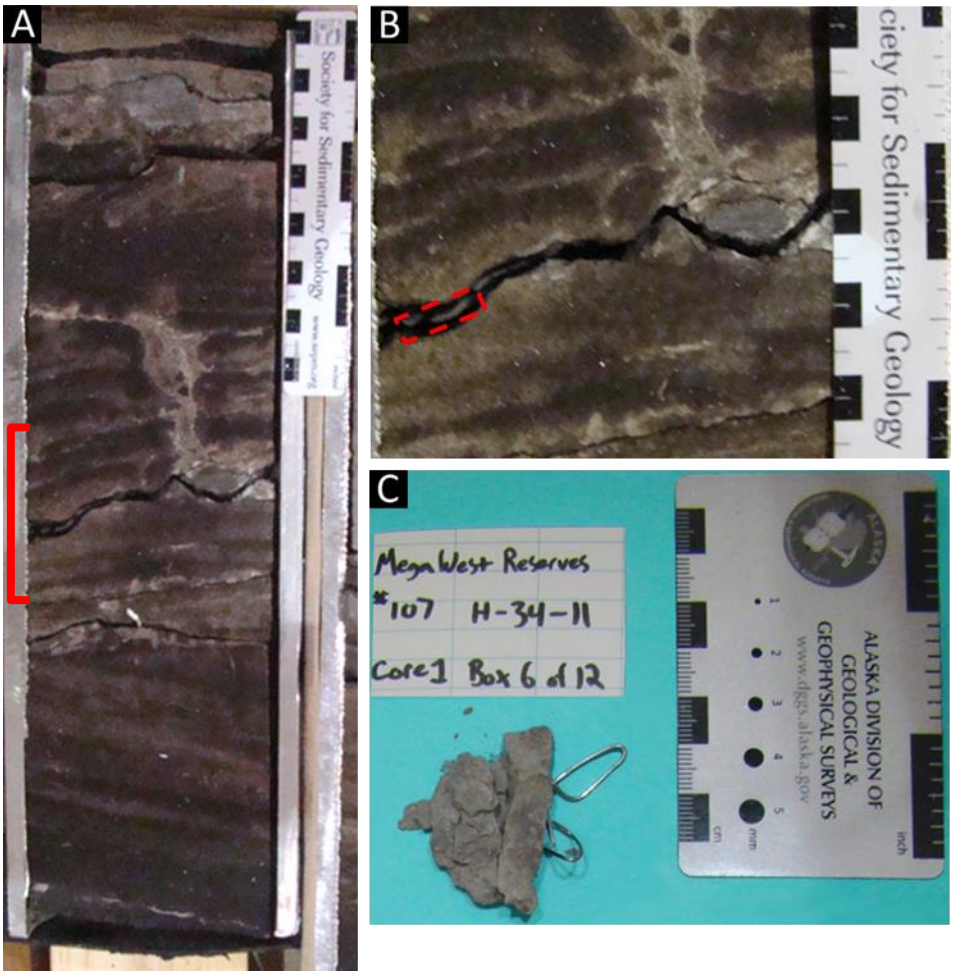

Figure B.10. MegaWest Core 107 core 1 box 6. A) Box of core. B) Sampled location in core. C) 107c1-b6 shale chips used in XRD analysis of clays.

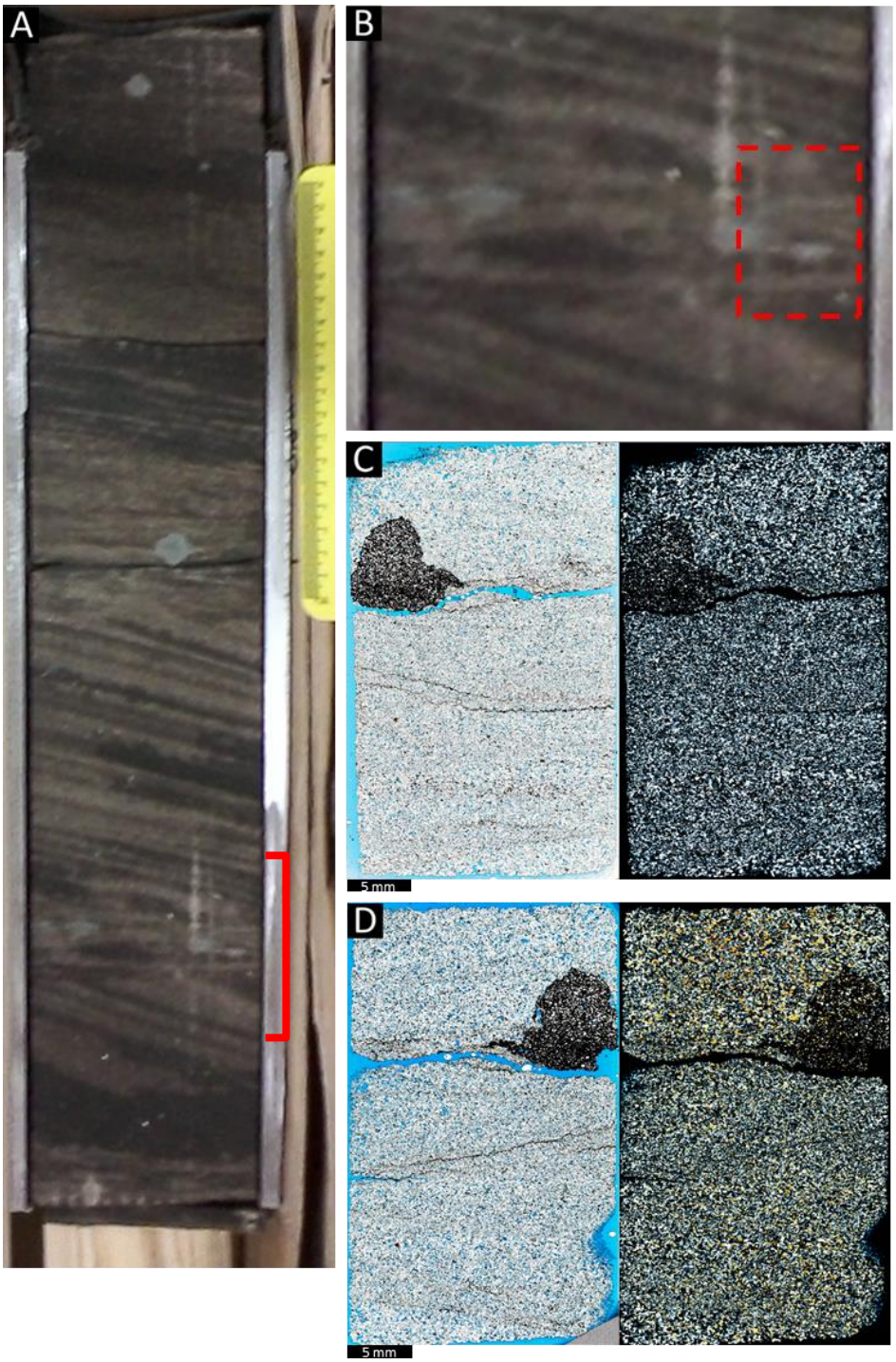

Figure B.11. MegaWest Core 107 core 1 box 7. A) Box of core, yellow scale right of box is in centimeters (18 cm). B) Sampled location in core. C & D) Scanned thin sections under plane-polarized and cross-polarized light (left to right). Standard thin section (C), 30-µm thick of sample 107c1-b7; and 60-µm thick thin section of 107Bc1-b7, (D), intended for fluid inclusion study.

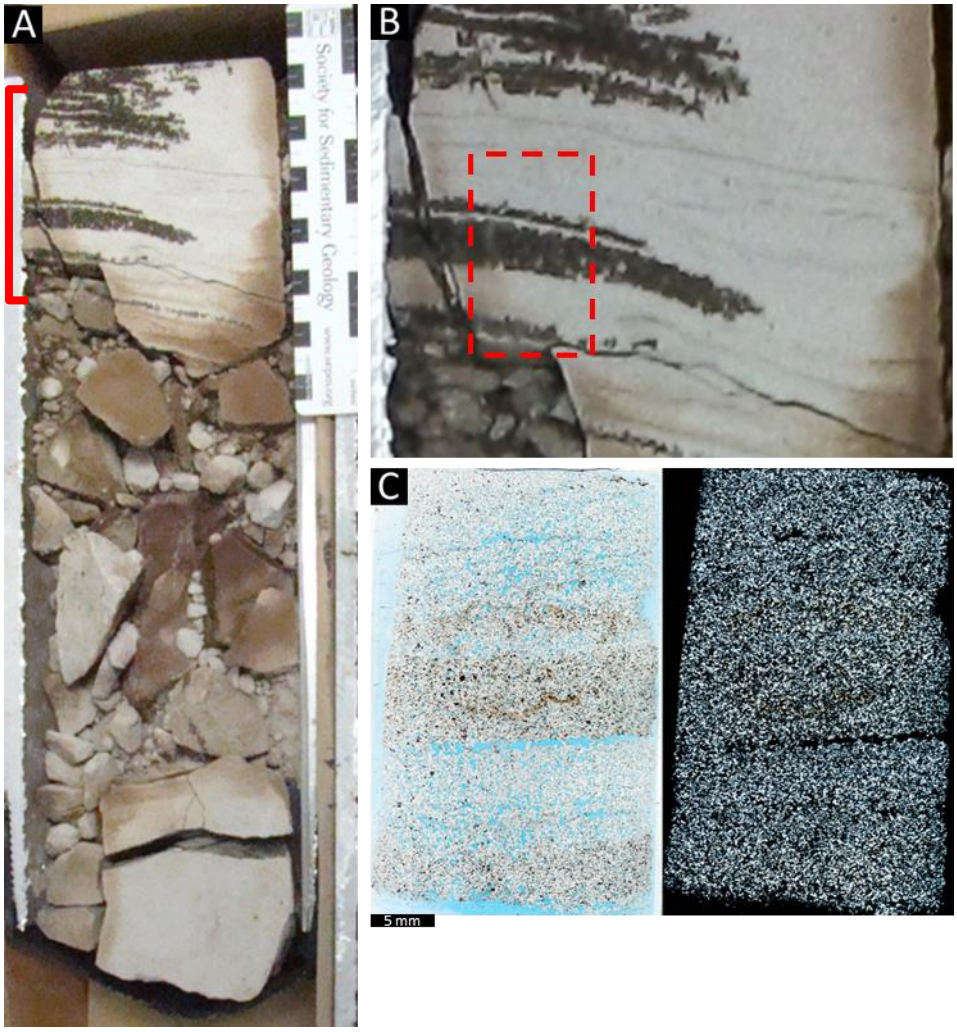

Figure B.12. MegaWest Core 107 core 2 box 5. A) Box of core. B) Sampled location in core. C) Scanned thin section under plane-polarized (left) and cross-polarized light (right). Thin section of sample 107c2-b5 is of standard, 30 µm thickness.

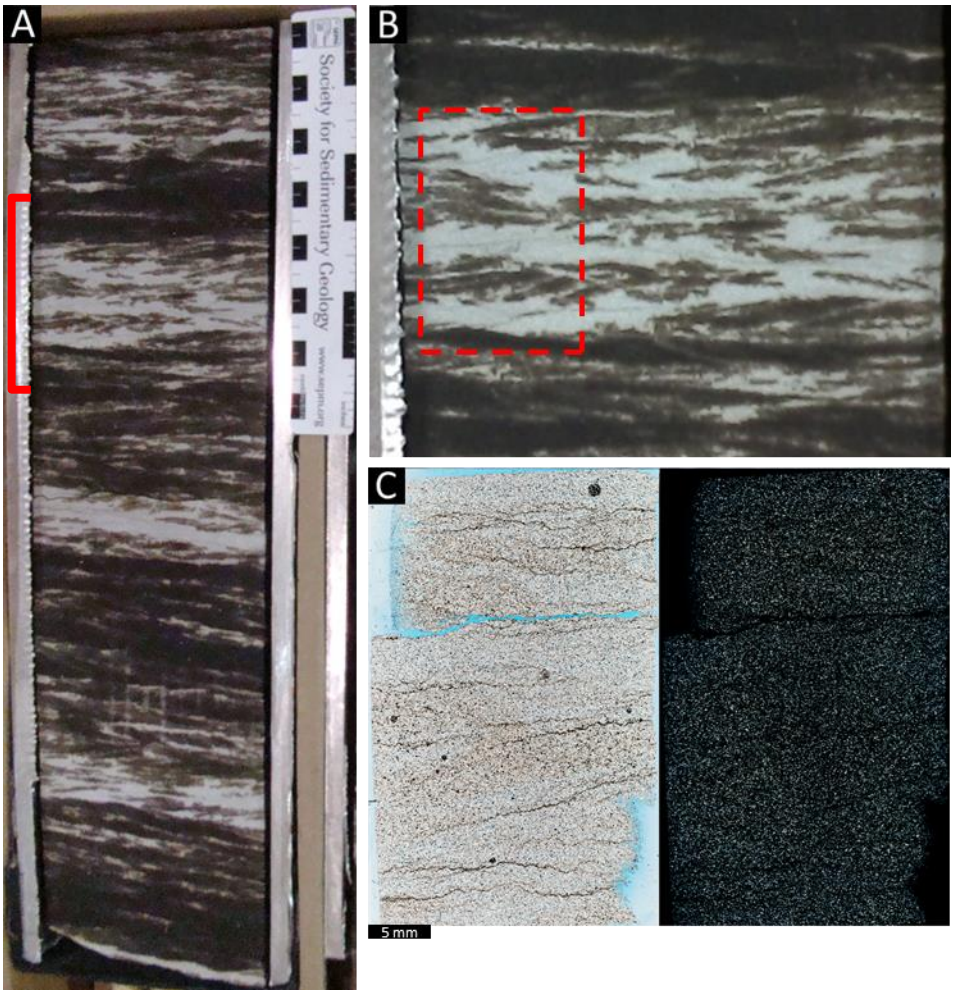

Figure B.13. MegaWest Core 108 core 1 box 2. A) Box of core. B) Sampled location in core. C) Scanned thin section under plane-polarized (left) and cross-polarized light (right). Thin section of sample 108c1-b2 is of standard, 30 µm thickness.

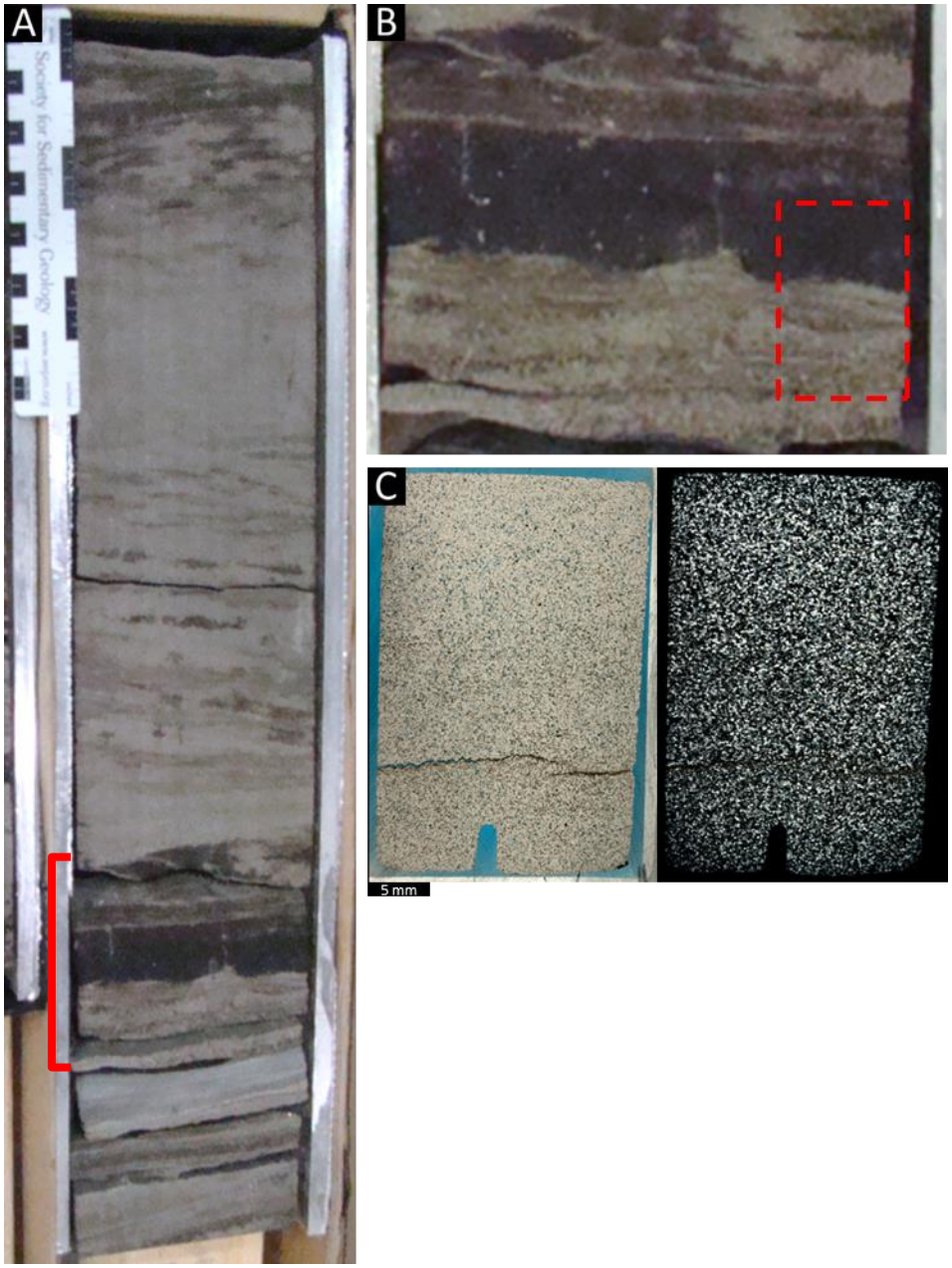

Figure B.14. MegaWest Core 109 core 1 box 2. A) Box of core. B) Sampled location in core. C) Scanned thin section under plane-polarized (left) and cross-polarized light (right). Thin section of sample 109c1-b2 is of standard, 30 µm thickness. Orientation indicated with notch in thin section and billet (not shown) indicates downward direction for sample 109c1-b2.

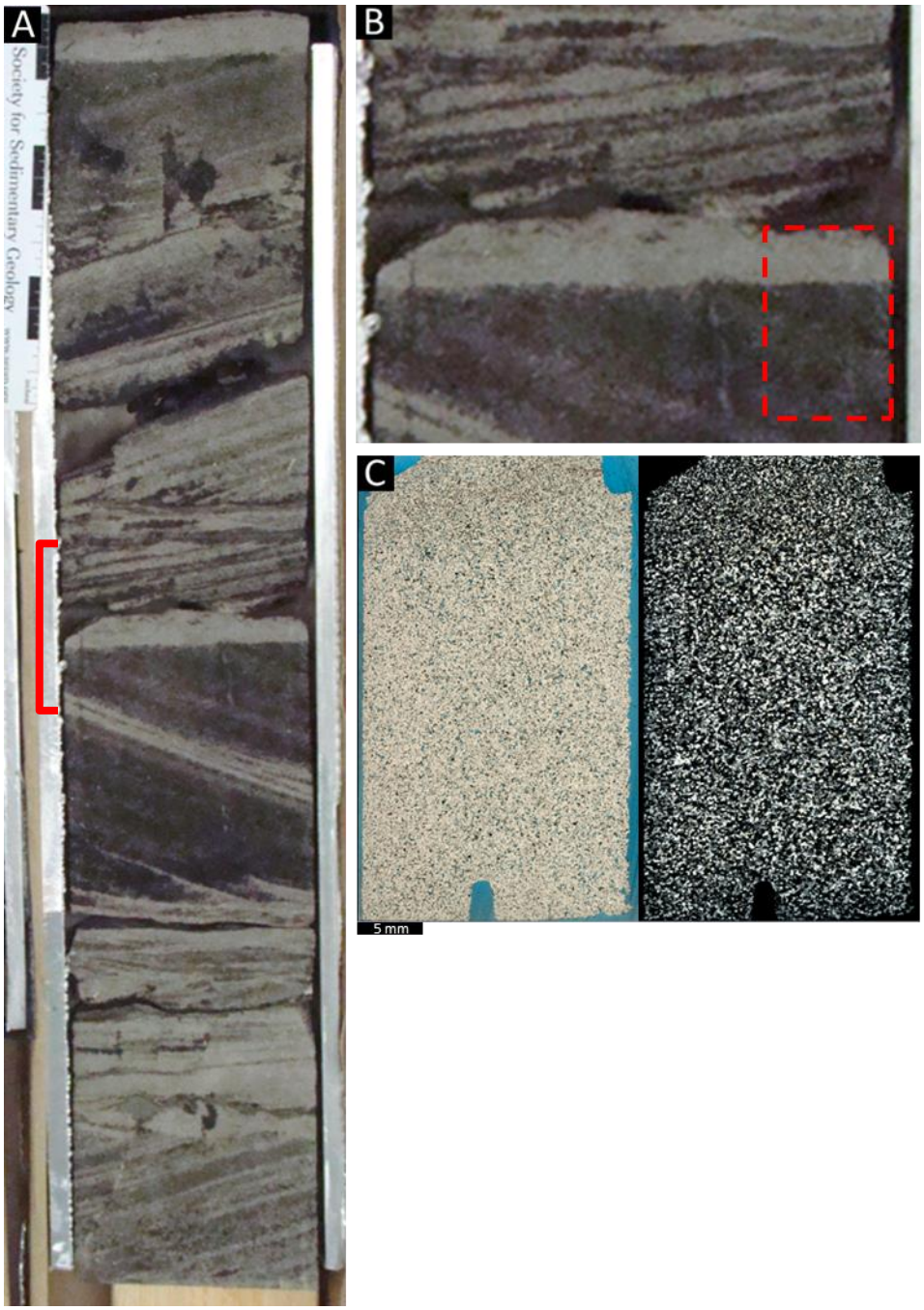

Figure B.15. MegaWest Core 109 core 1 box 3. A) Box of core. B) Sampled location in core. C) Scanned thin section under plane-polarized (left) and cross-polarized light (right). Thin section of sample 109c1-b3 is of standard, 30 µm thickness. Orientation indicated with notch in thin section and billet (not shown) indicates downward direction for sample 109c1-b3.

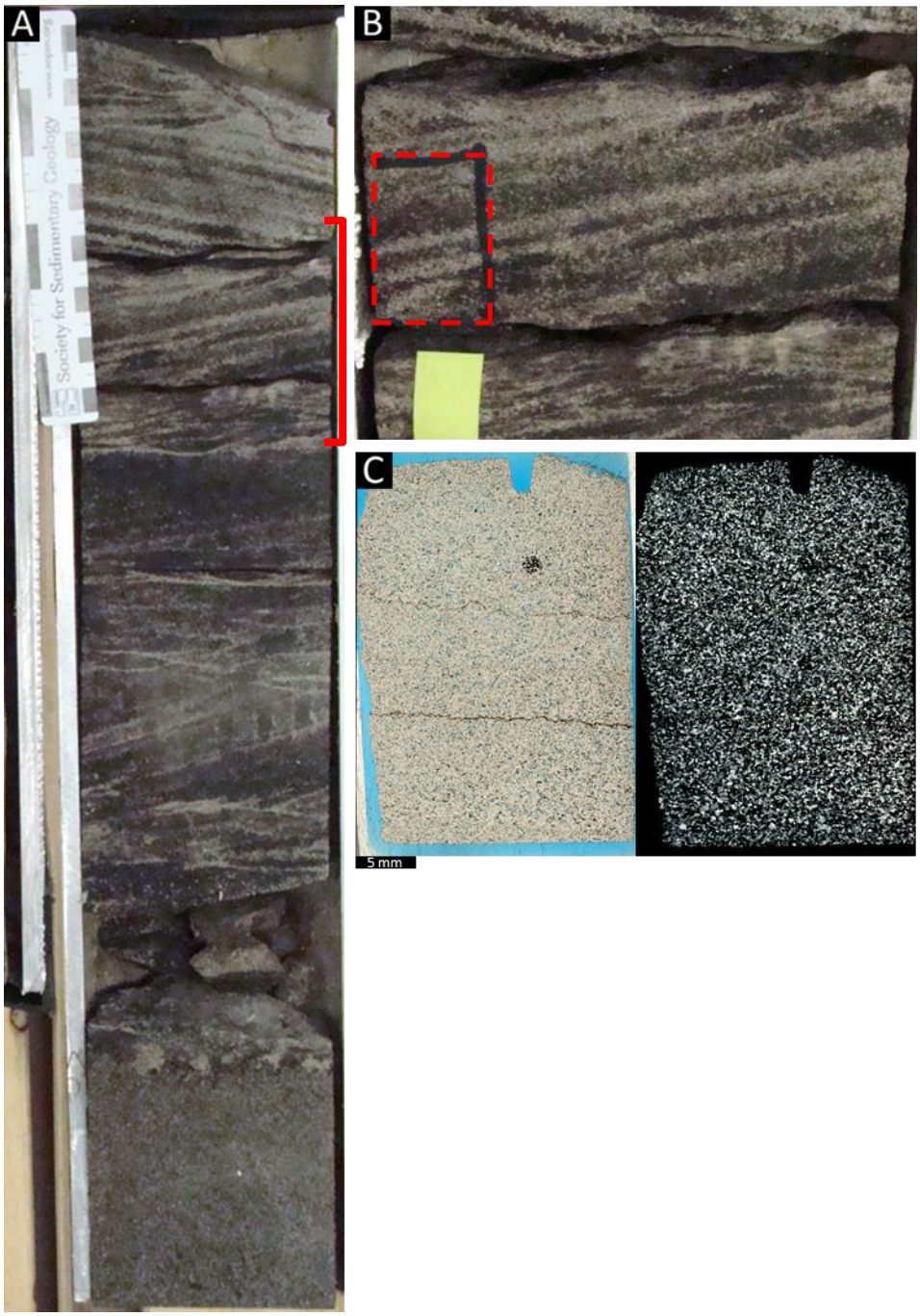

Figure B.16. MegaWest Core 109 core 1 box 4. A) Box of core. B) Sampled location in core. C) Scanned thin section under plane-polarized (left) and cross-polarized light (right). Thin section of sample 109c1-b4 is of standard, 30 µm thickness.

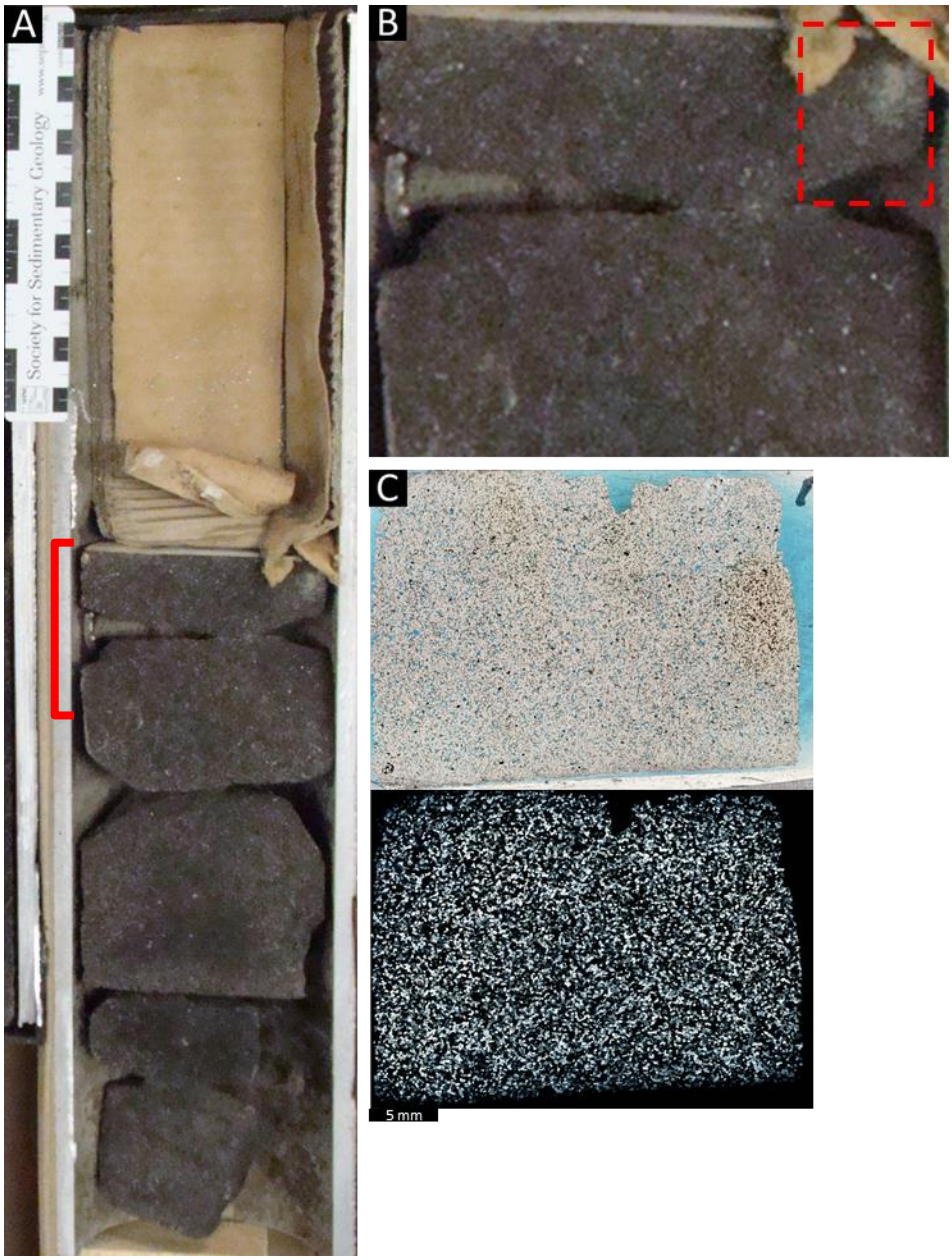

Figure B.17. MegaWest Core 109 core 1 box 5. A) Box of core. B) Sampled location in core. C) Scanned thin section under plane-polarized (upper) and cross-polarized light (lower). Thin section of sample 109c1-b5 is of standard, 30 µm thickness.

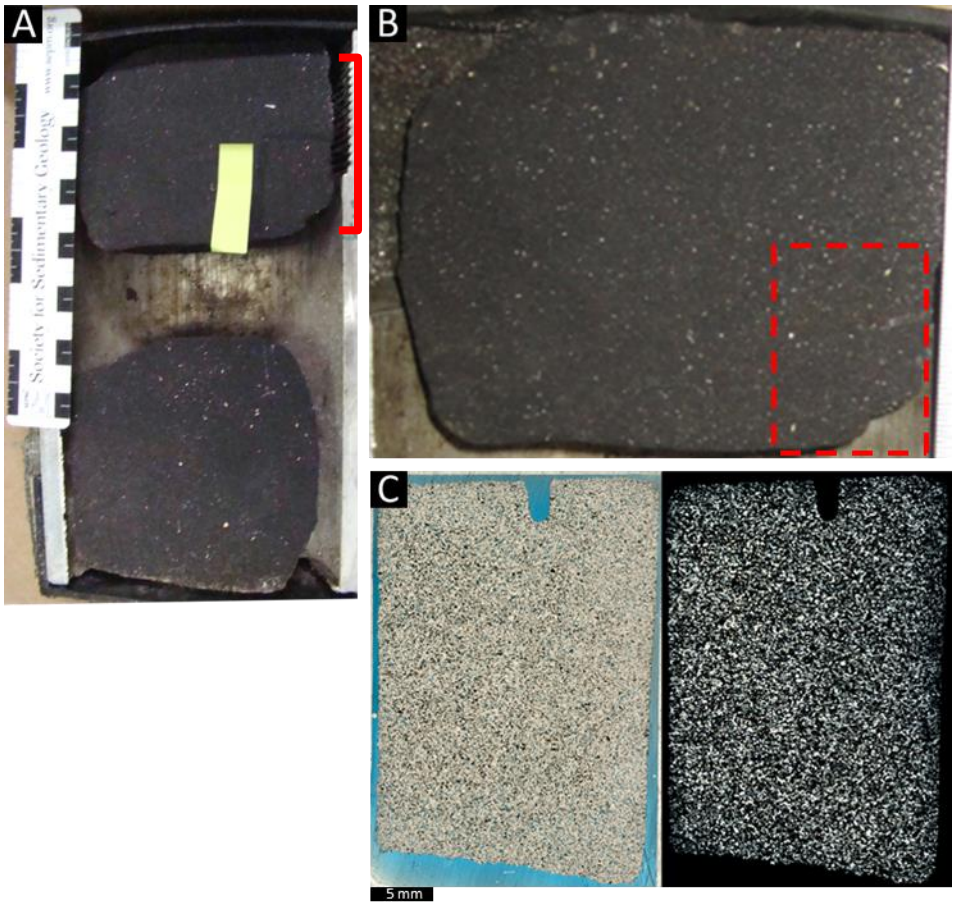

Figure B.18. MegaWest Core 109 core 1 box 10. A) Box of core. B) Sampled location in core. C) Scanned thin section under plane-polarized (left) and cross-polarized light (right). Thin section of sample 109c1-b10 is of standard, 30 µm thickness.

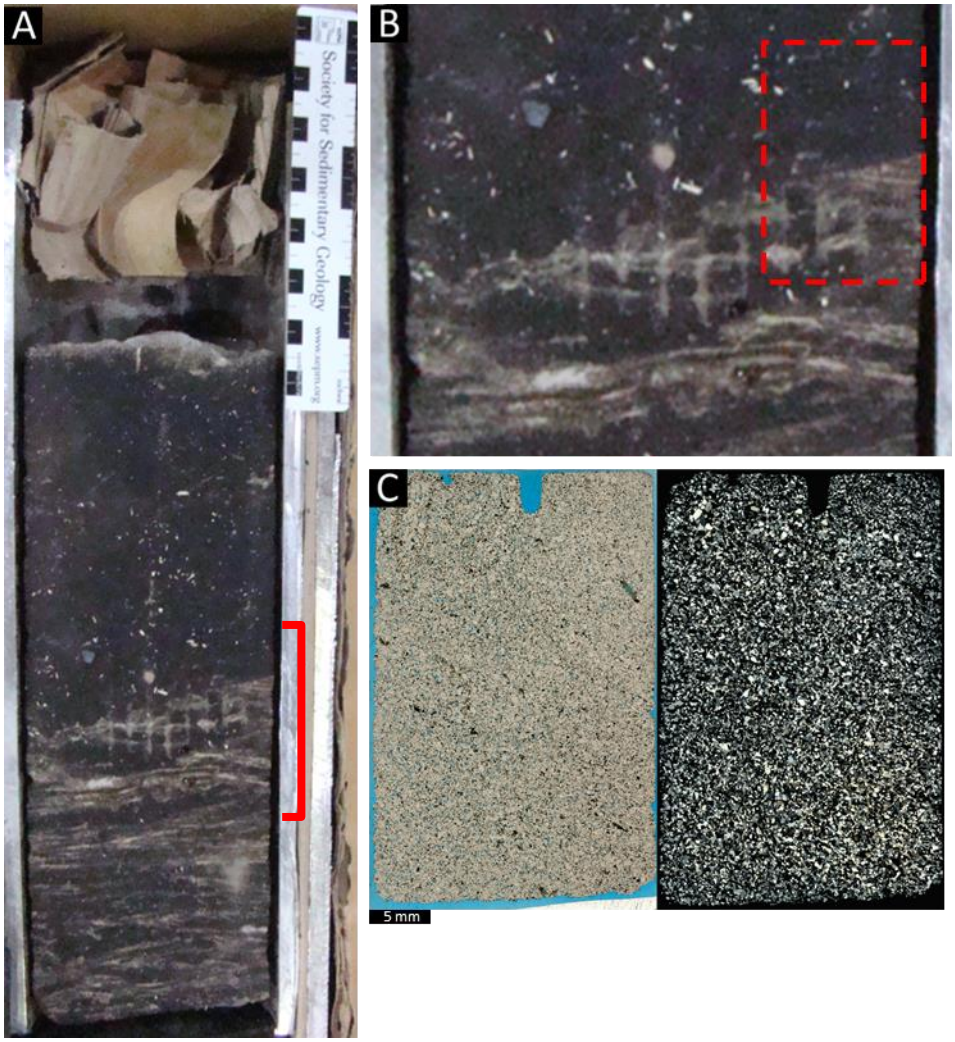

Figure B.19. MegaWest Core 109 core 2 box 4. A) Box of core. B) Sampled location in core. C) Scanned thin section under plane-polarized (left) and cross-polarized light (right). Thin section of sample 109c2-b4 is of standard, 30 µm thickness.

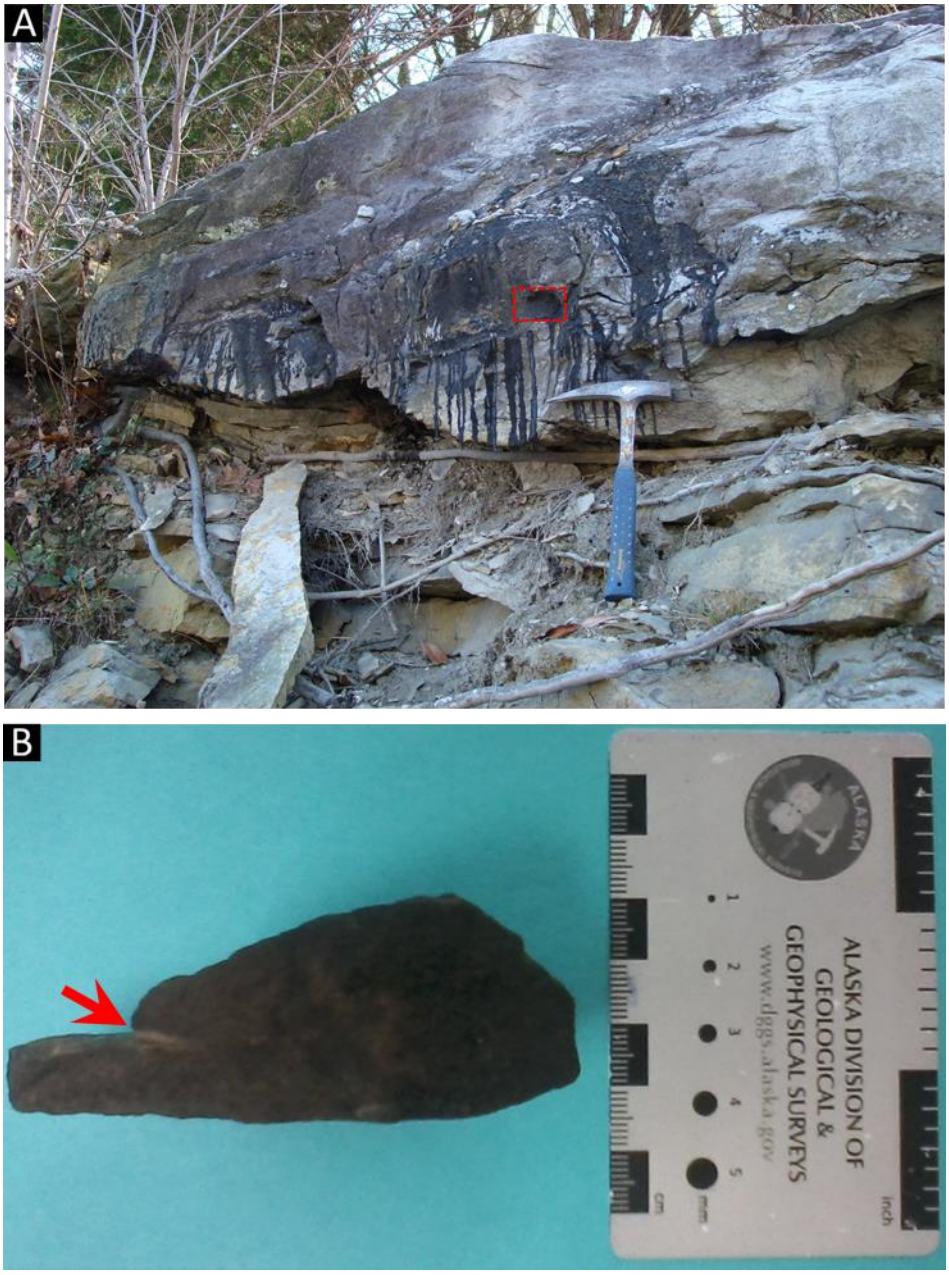

Figure B.20. Roadcut sampled in Hardin County on southern side of Wendell H. Ford (formerly Western Kentucky) Parkway mile marker 120.1. A) Red box denotes where hand sample was taken from outcrop. Hammer length is 1 ft. B) Roadcut hand sample taken. Red arrow denotes clay drape from which clay was sampled and isolated for TEM analysis and finely ground for XRD.

APPENDIX C: Theoretical Background of Analytical Techniques

C.1 Cathodoluminescence

C.1.1 Physical Basis Background

Luminescence is the emission or re-emission of electromagnetic radiation concomitant with a decrease in the energy state of a material (Fox, 2001). The emission of energy in the form of light as the result of excited electrons transitioning to lower energy states is the basis for numerous standard analytical methods used to investigate the composition and structure of materials. Types of luminescence and associated techniques are referred to by the respective energy source used to produce luminescence from a material (Götze, 2002; Boggs and Kinsley, 2006). Cathodoluminescence (CL) is produced from a solid under the bombardment of high-energy electrons with an emission spectra characteristic, but not limited to, visible and ultraviolet (UV) wavelengths (Götze, 2002; Boggs and Kinsley, 2006). Other forms of electromagnetic radiation may result from the electron bombardment but only spectra within the near-UV to near-infrared (IR) wavelength range are used in CL investigations.

The molecular electronic structure of a solid consists of multiple energy bands where electrons of similar energy can exist separated by exclusion zones, or band gaps, where electrons cannot exist (Fox, 2001; Ibach and Lüth, 2003; Kaxiras, 2003). As atoms become more closely spaced, electron orbitals begin to interact with each other and overlap. This overlapping forces the electron orbitals of one atom to differ slightly in energy relative to the overlapping orbital of another. No two electrons can occupy exactly the same quantum state (Fox, 2001; Ibach and Lüth, 2003). The cumulative result of overlapping orbitals of very similar, but discrete, energy levels is the formation of energy

bands (Figure C.1). These bands are more distinct in crystalline solids because of the periodicity of the lattice structure (Fox, 2001; Kaxiras, 2003; Ibach and Lüth, 2003).

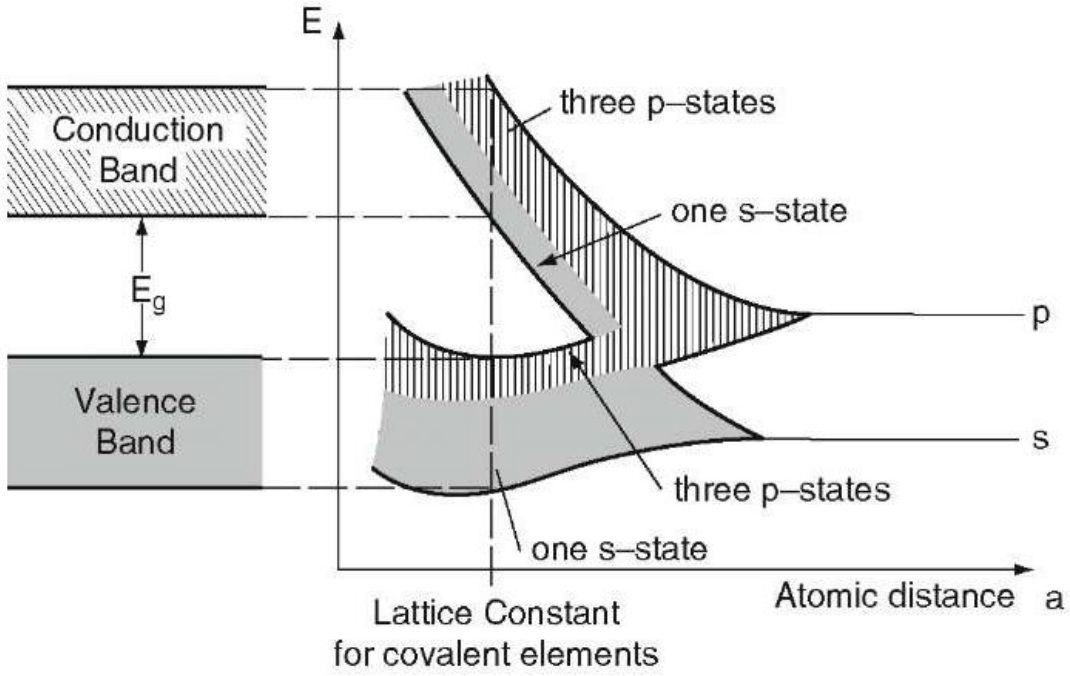

Figure C.1. Schematic of energy band structure in solids. As distance between atoms decreases, overlap between electron orbitals' of atoms increases, which raises the orbitals energy levels. Interactions between overlapping orbitals force electrons to differ slightly in energy to occupy the same space. Electron interference creates the band gap, splitting the energy levels where electrons can exist into the valence band (lower energy) and the conduction band (higher energy). P and S states are electron subshells. From Zeng (2013).

The energy difference between the electrons of the two highest energy bands, the valence and conduction, is important in cathodoluminescence studies as it affects the luminescence or non-luminescence of a material. This difference in energy is represented schematically by the width of the energy gap = E_g in Figure C.1. The conduction band is composed of energy levels in which electrons may "flow" and become delocalized from the molecular bonds which form the valence band (Boggs and Kinsley, 2006). Cathodoluminescence microscopy uses electron irradiation to excite electrons from the valence band to the conduction band of a compound. This creates an "electron hole" (a

positive charge within the valence band) which is negated following electron recombination (Figure C.2) (Boggs and Kinsley, 2006). The negation of the electron hole need not be from recombination of the same electron that made it. Energy can be emitted radiatively during electron recombination, and the wavelengths of the emitted photons are indicative of the energy difference between the conduction and valence bands. This energy difference can be calculated using the following equation: $E_{\Delta} = (hc) / \lambda$ where h = Planck constant, c = speed of light, and λ = photon wavelength (Boggs and Kinsley, 2006; Salh, 2011a, b). The greater the energy difference between excited and ground states (the larger the band gap), the shorter the wavelength is of the radiation emitted (Boggs and Kinsley, 2006; Götze, 2002). Electrons may also transition to lower-energy states through non-radiative emission of phonons. Phonons are a discrete quantum of vibrational energy that are imparted to the crystal lattice resulting in a slight heating of the crystal (Boggs and Kinsley, 2006; Salh, 2011b; Götze, 2012).

Conduction and valence bands either overlap or are one-and-the-same in conductive solids and, as a result, no cathodoluminescence is produced from electron transitions in these materials (Boggs and Kinsley, 2006; Flegler et al., 1993; Götze, 2012). The energy gap between a molecule's valence and its conduction band is narrow in semi-conductive solids and the wavelengths of photons produced during electron recombination of these materials are generally within the infrared (IR) (Gaft et al., 2005). Some human-made and some natural semi-conductors, such as sphalerite, produce visible luminescence from direct band-to-band transitions (Marfunin, 1979; Gaft et al., 2005; Boggs and Kinsley, 2006; Fisher Ponce, 2009; Salh, 2011b; Götze, 2012). Insulators have the largest energy gap between conduction and valence bands making them the most

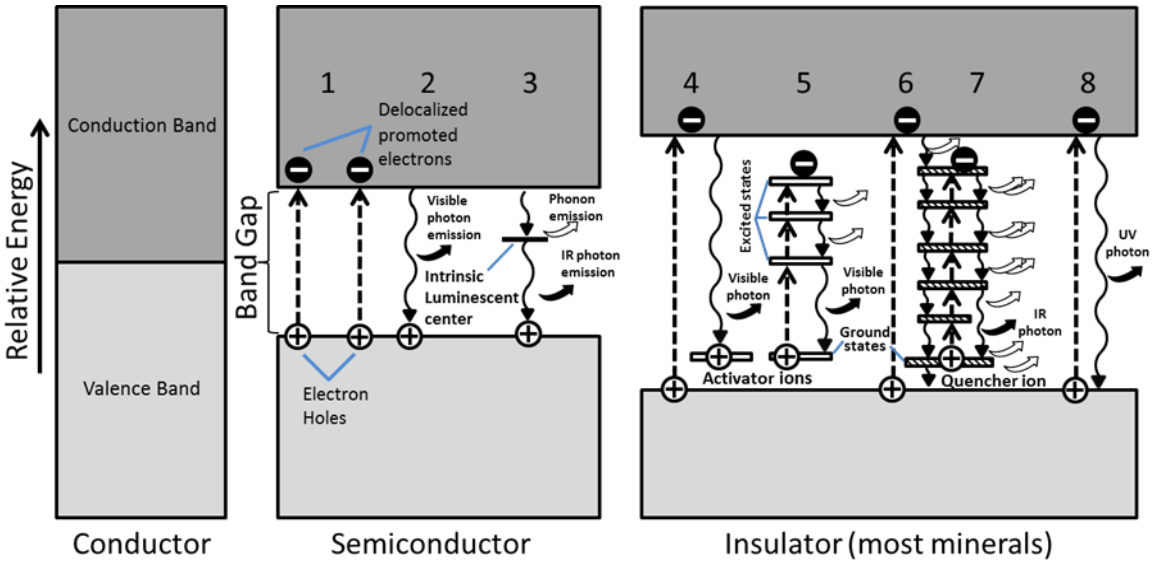

Figure C.2. Schematic of CL processes and effects of activators and quenchers. Intrinsic luminescence centers are not exclusive to semi-conductors nor are extrinsic luminescence centers exclusive to insulators. Solid and dotted lines represent emissive and non-emissive electron transitions, respectively. Solid and hollow "swept" arrows indicate radiative and non-radiative emissions, respectively. Process 1: electrons are promoted to an excited state within the conduction band from the valence band. Processes 2 & 3: intrinsic luminescence can result from delocalized electrons transitioning directly from the conduction band to the valence band filling electron holes and emitting photons (2), or from electrons becoming briefly trapped in an energy state within the band gap due to crystal defects and lattice distortions resulting in the emission of photons and potentially phonons. Process 4: extrinsic luminescence occurs when electrons from the conduction band transition to a lower-energy state and recombine with an activator ion at an energy level that exists locally within the band gap. Process 5: electron transitions (promotion and recombination) occur locally within the band gap among activator ions. Process 6: extrinsic non-luminescence centers suppress luminescence by permitting multiple non-radiative transitions through which promoted electrons can cascade and recombine with electron holes in activator ground states or the valence band. Process 7: extrinsic non-luminescence centers suppress luminescence by competing directly with activators, absorbing energy and either emitting phonons or long wavelength IR photons. Process 8: cathodoluminescence from direct band-to-band electron transitions in insulators generally produce UV photons requiring specialized detectors. Based on Boggs and Kinsley (2006), Salh (2011a), Götze (2002, 2012), and Machel et al. (1991).

suitable for study using cathodoluminescence (Boggs and Kinsley, 2006). Larger band gaps allow for crystal defects and impurities to occupy discrete energy levels between bands from which radiative emissions in the visible to near-visible spectrum are produced (Boggs and Kinsley, 2006). A few minerals, such as scheelite, powellite, cassiterite, chlorargyrite, and uranyl minerals, may display cathodoluminescence because the minerals' metal groups are host activators of luminescence but not as a result of direct band-to-band transitions (Portnov et al., 2001; Gaft et al., 2005).

C.1.2 Luminescence Centers

Crystal imperfections may momentarily trap a de-excited electron within the band gap before the electron recombines within the valence band or a similar lower-energy band with an electron hole (Boggs and Kinsley, 2006; Götze, 2002). These electron traps are normally unoccupied. If their momentary interceptions of de-excited electrons affect luminescence, they are also known as luminescence centers, which may be intrinsic or extrinsic (Boggs and Kinsley, 2006). Intrinsic centers are caused by crystal lattice defects and extrinsic centers are due to 'impurities', both of which will be subsequently explained in detail.

Intrinsic luminescence centers are crystal lattice defects that result in the momentary trapping of electrons within the band gap prior to their recombination with electron holes in the valence band or a similarly lower-energy level (Nasdala et al., 2004). Such defects may be distortions from vacancies, incorporated substitutional foreign ions, damaged/broken bonds that either have unpaired electron configurations (aka radicals and electron holes) or bonds from which an electron-hole pair might be induced or trapped (Marfunin, 1979; Dusausoy and Weil, 1994; Machel, 2000; Ramseyer

and Mullis; 2000; Götze et al., 2001; Götze, 2002; Boggs and Kinsley, 2006; Salh, 2011a; Pownceby and MacRae, 2011). Electron-hole defects are ubiquitous in all minerals. Many minerals exhibit weak cathodoluminescence in the absence of extrinsic luminescence centers or host luminescence resulting from the recombination from the conduction band to the valence band (Dusausoy and Weil, 1994; Nasdala et al., 2004).

Foreign ions may be of equal or different valences than the crystal's substituted ions. Any charge difference arising from the incorporation of a foreign ion into the crystal must be balanced by an electron hole or interstitial ion (Boggs and Kinsley, 2006). Foreign ions may potentially have different coordination than the substituted ions which may create other luminescence or recombination centers by bond strain and crystal lattice distortions (Marfunin, 1979; Götze et al., 2001; Götze, 2002; Boggs and Kinsley, 2006; Salh, 2011a; Pownceby and MacRae, 2011). Intrinsic luminescence centers from distortion of the crystal lattice may also be produced by temperature, ionizing radiation, and mechanical stress (Salh, 2011a; Pownceby and MacRae, 2011).

Extrinsic or impurity luminescence centers in a crystal lattice are foreign ions that have unfilled or partially-filled electron orbitals with energy levels between the valence and conduction band of the crystal (Marfunin, 1979; Götze, 2002; Boggs and Kinsley, 2006; Pownceby and MacRae, 2011; Waychunas, 2014). These discrete energy levels, from which electrons can transition to and from and, in some cases, within (as in rare earth elements or REEs) before returning to a ground state, are the basis of cathodoluminescence in insulators (Salh, 2011b; Pownceby and MacRae, 2011). Extrinsic luminescence centers are the most common cause of bright cathodoluminescence, according to Pownceby and MacRae (2011).

Trace impurities that directly result in the emission of visible photons are known as activators (Götze, 2002; Boggs and Kinsley, 2006; Waychunas, 2014). Activators are primarily transition metal ions and REEs that act as electron traps within the band gap (Machel and Burton, 1991; Götze, 2002; Boggs and Kinsley, 2006; Waychunas, 2014). Sensitizers are ions that do not have electrons directly promoted, that is, have electrons excited from the valence to conduction band, but rather transfer absorbed energy to activator ions contributing to the promotion of the activator ion's electron. Ions that act similarly to activators, but suppress luminescence are known as quenchers (Götze, 2002; Boggs and Kinsley, 2006). Unlike activators, the energy difference between the electron trap(s) and/or valence band of quenchers is insufficient to emit photons and the energy transition is accomplished radiatively with the emission of IR photons, or non-radiatively with the emission of phonons (Götze, 2002; Boggs and Kinsley, 2006). In addition to high concentrations of quenchers relative to activators, an excess of activators may induce a self-quenching phenomenon. This occurs when activators reach a concentration where energy can transfer between proximate ions with electrons of similar energy levels (Marfunin, 1979; Boggs and Kinsley, 2006; Waychunas, 2014).

Extrinsic and intrinsic luminescence centers are not mutually exclusive and an under-coordinated foreign ion (an ion with less ligand bonds than expected of its valency) may create an intrinsic luminescence center defect, which may also be an extrinsic luminescence center (Ramseyer and Mullis, 2000; Götze et al., 2001; Götze, 2002; Salh, 2011b). A compiled list of reported extrinsic and intrinsic luminescence centers in silicates and carbonates is posted below (Table C.1).

Luminescent and non-Luminescent Center Types		Effect on Luminescence	Examples in Silicates (Quartz and Feldspars mainly)	Examples in Carbonates
Extrinsic Centers "Impurity Centers"	Activator Ions	Allow electrons to occupy energy levels within the band gap emitting photons when electrons return to their ground state.	Mn^{2+}, $Ti^{3,4+}$, Fe^{3+} and Cr^{3+} substitution for Al^{3+}, REE: Ce^{3+}, Pr^{3+}, Nd^{3+}, $Sm^{2,3+}$, $Eu^{2,3+}$, Gd^{3+}, Tb^{3+}, $Dy^{2,3+}$, Ho^{3+}, Er^{3+}, $Yb^{2,3+}$	Mn^{2+} substitution for Ca^{2+} and Mg^{2+}, U^{6+}, REE: Tb^{3+}, $Sm^{2,3+}$, Pr^{3+}, Nd^{3+}, $Dy^{2,3+}$, $Eu^{2,3+}$, Er^{3+}, Ho^{3+}, Gd^{3+}
	Sensitizer Ions	Transfer energy to activators for electron excitation.	Pb^{2+}, Ce^{3+} Zn^{2+}, with Mn^{2+} Trivalent REEs with Divalent REEs, and Nd^{3+} for Sm^{3+}, Eu^{3+}, Tb^{3+}, and Dy^{3+}	Pb^{2+}, Ce^{3+}, Tl^{+}, Cu^{+}, Zn^{2+}, with Mn^{2+} although Pb^{2+} only sensitizes in UV emission and Zn^{2+} perhaps not at all, see text for details.
	Quencher Ions	Have orbitals that have energy levels within band gap emitting phonons or long IR photons as electrons pass through them to their ground state.	$Fe^{2,3+}$, Ni^{2+}, Co^{2+}, and Trivalent REEs activators especially Pr^{3+} by concentration	$Fe^{2,3+}$, Ni^{2+}, and Co^{2+}, as well as Mn^{2+} in excess concentrations
Intrinsic Centers	Foreign Ion Lattice Defect Centers (substitutional and interstitial)	Have electron holes, or strain bonds from which an electron-hole pairs can be induced or an electron trapped, at energy levels within the band gap.	$[AO_4/M^{+}]^0$, where A = Al^{3+}, Ti^{3+}, Fe^{3+}, Ge^{3+}, and M = H^{+}, Li^{+}, Na^{+}	Nonstoichiometric CO_3^{2-} replacement by OH^{-}, Cl^{-}, SO_4^{2-}, PO_4^{3-}, and Ca^{2+} by H^{+}, K^{+}, and Na^{+} not known to cause luminescence.
	Electron Hole Centers and Radicals	Have unpaired electrons from atomic vacancies, excesses (homobonds of interstitials), or under-coordinated ions at energy levels within the band gap.	*E'* and O^{-} centers and associated NBOHC: SiO_4^{3-}, SiO_3^{2-}	CO_3^{3-}, CO_3^{-}, CO_2^{-}

For a more complete list of extrinsic and intrinsic defects and their typical emission bands, see Marfunin (1979), Machel et al. (1991), Machel and Burton (1991), Budd et al. (2000), Machel (2000), Pagel et al. (2000), Ramseyer and Mullis (2000), Stevens-Kalceff et al. (2000), Götze et al. (2000, 2001, 2002), Götze (2002, 2012), Boggs and Kinsley (2006), Götze and Kempe (2008), and Salh (2011a, b).

Table C.1. Extrinsic and Intrinsic Luminescence centers in CL of Quartz and Feldspar Silicates and Carbonates.

C.1.3 Luminescence Centers in Silicates

While common in minerals, intrinsic luminescence centers are weak in intensity when compared to most extrinsic centers which dominate luminescence in many minerals (Dusausoy and Weil, 1994; Palenik and Buscagalia, 2007; Pownceby and MacRae, 2011). In silicates, electron-hole defects associated with atomic vacancies of O and Si positions are known as *E*' and O^- centers, respectively (Boggs and Kinsley, 2006). *E*' centers, also known as oxygen vacancy centers, are comparably better understood than vacancies ascribed to silicon (O^- centers) or other vacancies similar to silicon (Marfunin 1979; Nilges et al., 2008). Non-bridging oxygen hole centers (NBOHC) separating silica tetrahedra are also common centers in silicates although such defects are not exclusively due to *E*' centers (Götze et al., 2001). Peroxy linkages (≡Si–O–O–Si≡) and peroxy radicals, bound to the atypical lattice O^{2-} ions linking silica tetrahedrons, are precursors to NBOHC defects (Götze et al., 2001; Nilges, et al., 2008). Substitution of Si^{4+} with Al^{3+} is often associated with *E*' defects and is common in quartz and feldspars (Ramseyer and Mullis, 2000; Götze et al., 2000; Boggs and Kinsley, 2006). For in-depth explanations of such defects, refer to the research of Götze et al. (2001), Nilges et al. (2008), and Salh (2011a).

Visible cathodoluminescence of α-quartz can exhibit blue, violet, or brown colors (Zinkernagel, 1978; Ramseyer et al., 1988; Owens, 1991; Götze et al., 2001; Götze, 2002; Boggs and Kinsley, 2006). According to research by Zinkernagel (1978), the lumen-escence exhibited by α-quartz is due to disorder of the crystal lattice. This is observed in plutonic and hydrothermal quartz while diagenetic quartz is non-luminescent. Attempts have been made to ascribe provenance and genetic information (igneous, metamorphic,

and hydrothermal) to detrital quartz from observed spectra, however, the reliability of such a method is questionable due to mutual or overlapping colors (Owens, 1991; Richter et al., 2003). Authigenic quartz overgrowths, however, are non-luminescent, and are conspicuous against grains which were typically dark blue in this study. This apparent difference in mineral phases was less-apparent to indistinguishable under conventional optical microscopy methods and absent under SEM (Scanning electron microscopy).

Cathodoluminescence in feldspars is commonly caused by Mn^{2+}, Fe^{3+}, and peroxy radicals bound to the atypical lattice O^{2-} ion (Götze et al., 2001; Götze, 2012). Feldspars may exhibit a range of luminescence including peaks in the blue spectrum similar to quartz. These peaks are also believed to be produced from traps associated with defects in oxygen bonding and with Al and Ti substitutions for Si (Marfunin, 1979; Nasdala et al., 2004; Parsons et al., 2008; Götze, 2012). In the cathodoluminescence analysis of this study, I observed that feldspars typically exhibited bright light-blue luminescence in thin section, except for weathered feldspars that appeared dark green.

Cathodoluminescence of phyllosilicates have been little studied, although Götze et al. (2002) compared the emitted visible spectra of minerals from several clay groups including kaolinite (kaolin) and illite (micas). They found that illite and trioctohedral clays do not exhibit luminescence while dioctrahedral clays, including kaolinite, do (Götze et al., 2002; Boggs and Kinsley, 2006; Götze 2012). According to Götze (2012) and Götze et al. (2002), there exists a transient nature of cathodoluminescence intensity around 400 nm (blue) in many silicates, declining over time, which is suspected to be due to electron irradiation effect on other defects and electron holes. The intensity of luminescence from kaolinite and halloysite decreases with prolonged electron irradiation

presumably with the incident electrons saturating and filling electron holes (Götze et al., 2002; Götze and Kempe, 2008; Götze, 2012). Dickite, nacrite, and pyrophyllite minerals exhibit an increase in emission intensity with prolonged electron irradiation. This is possibly due to electron bombardment creating holes and traps that produce the emissions (Götze et al., 2002; Götze and Kempe, 2008; Götze, 2012). The observed emitted light from kaolinite in the Big Clifty samples was a deep purple while illite, glauconite, and muscovite were non-luminescent. Götze et al. (2002) reported a deep blue color in kaolinite and attributed it to radiation-induced defects associated with electron holes and traps associated with Si–O^- and Al–O^-–Al crystal defects common in silicates. OM-CL is very useful in identifying kaolinite, as the mineral can easily be distinguished from cryptocrystalline quartz or chert which is non-luminescent, as well as from dickite that displays more intense cathodoluminescence over time in thin section.

C.1.4 Applications of Cathodoluminescence Petrography to Silicates

Application of cathodoluminescence in diagenetic investigations of silicates is especially valuable for discriminating boundaries between detrital grains and authigenic overgrowths as well as distinguishing between minerals with similar optical features (Owen, 1991; Hiatt and Pufahl, 2014). Cathodoluminescence petrography may eventually be successfully utilized in provenance studies. However, the variety of luminescence colors and the factors governing them are not completely understood. In detrital quartz it is not possible to reliably infer provenance from differences in luminescence color or intensity (Owen, 1991; Götze, 2002; Richter et al., 2003; Boggs and Kinsley, 2006). Similarly, the reported cathodoluminescence of feldspars is more varied in terms of identified emission spectra and their defect-related causes than is quartz, yet there

remains a paucity of empirical studies that can definitively relate the cathodoluminescence of detrital feldspars with provenance (Owen, 1991; Richter et al., 2003; Boggs and Kinsley, 2006). Cathodoluminescence of phyllosilicates is less understood or studied than of quartz or feldspars; however, OM-CL is very useful in distinguishing kaolinite from chert as well as the rest of the kaolin mineral group. One of the primary applications of cathodoluminescence in the study of siliciclastics is to distinguish boundaries between detrital grains and authigenic cement(s) (Owens, 1991). Differences in concentrations of luminescence centers potentially enable framework grains and multiple generations of authigenic cements to be distinguished, permitting a more robust construction of paragenesis.

C.1.5 Luminescence Centers in Carbonates

Cathodoluminescence in carbonates is primarily affected by the relative abundances of extrinsic luminescence centers of activators such as Mn^{2+}, U^{6+}, and REE^{3+}, and quenchers $Fe^{2,3+}$, Ni^{2+}, and Co^{2+} (Machel, 1985; Machel et al., 1991, Machel and Burton, 1991; Reeder, 1991; Budd et al., 2000; Machel, 2000; Götze, 2002; Hiatt and Pufahl, 2014). The activator Mn^{2+} and quencher Fe^{2+} are ubiquitous in many minerals and are the dominant activator and quencher, respectively, in carbonates (Machel and Burton, 1991; Budd et al., 2000; Götze, 2012; Hiatt and Pufahl, 2014). Small concentrations of Mn^{2+}, minimally ~25 ppm by weight, can create visible luminescence in calcite that would otherwise only have host cathodoluminescence in the UV (Budd et al., 2000; Reed and Milliken, 2003; Boggs and Kinsley, 2006). Naturally occurring luminescence in calcite and dolomite is most intense in the yellow to red wavelengths due to Mn^{2+} substituting for Ca^{2+} (as well as Mg^{2+} in dolomite) with possible contributions from REEs

(Machel et al., 1991; Boggs and Kinsley, 2006; Hiatt and Pufahl, 2014). Naturally occurring luminescent calcite colors range from yellowish orange to orange (Figure C.3) and naturally-occurring luminescent dolomite may produce reddish orange to deep red and, in some cases, maroon (Machel et al., 1991; Boggs and Kinsley, 2006). The interaction of the impurity centers of transition metals with the local crystal field broadens the emission peak into a band in calcite. In the case of dolomite, two overlapping bands are associated with Mn^{2+} substituting for both Ca^{2+} and Mg^{2+} with a preference for Mg^{2+} sites in sedimentary dolomite and Ca^{2+} sites in high pressure dolomite (Machel et al., 1991; Götze, 2012; Hiatt and Pufahl, 2014).

An increase in Fe concentration in luminescent carbonates is associated with a decrease in emission intensity and a color shift towards longer wavelengths. This yellow CL in calcite becomes orange to deep orange and dark brown. Colors range for dolomite from red, to deep red or maroon, to dark brown (Machel et al., 1991). This shift in color is accompanied by a decrease in emission intensity. In minerals possessing sufficiently high quencher concentrations there may be an extinguishment of all extrinsic luminescence of a mineral (Machel et al., 1991). The ratio of quenchers to activator ions needed to totally suppress or extinguish luminescence is not entirely understood although several studies have shown that far greater quantity of quenchers than activators is required (Figure C.4) (Hemming et al., 1989; Machel et al., 1991; Machel and Burton, 1991; Boggs and Kinsley, 2006). The general influences of activators and quenchers on the color of carbonates is different for each type of carbonate mineral but the perceived effects are generally the same, with luminescence being qualitatively classified as: 1) bright luminescence from activators, 2) dull luminescence due to quenchers and/or self-

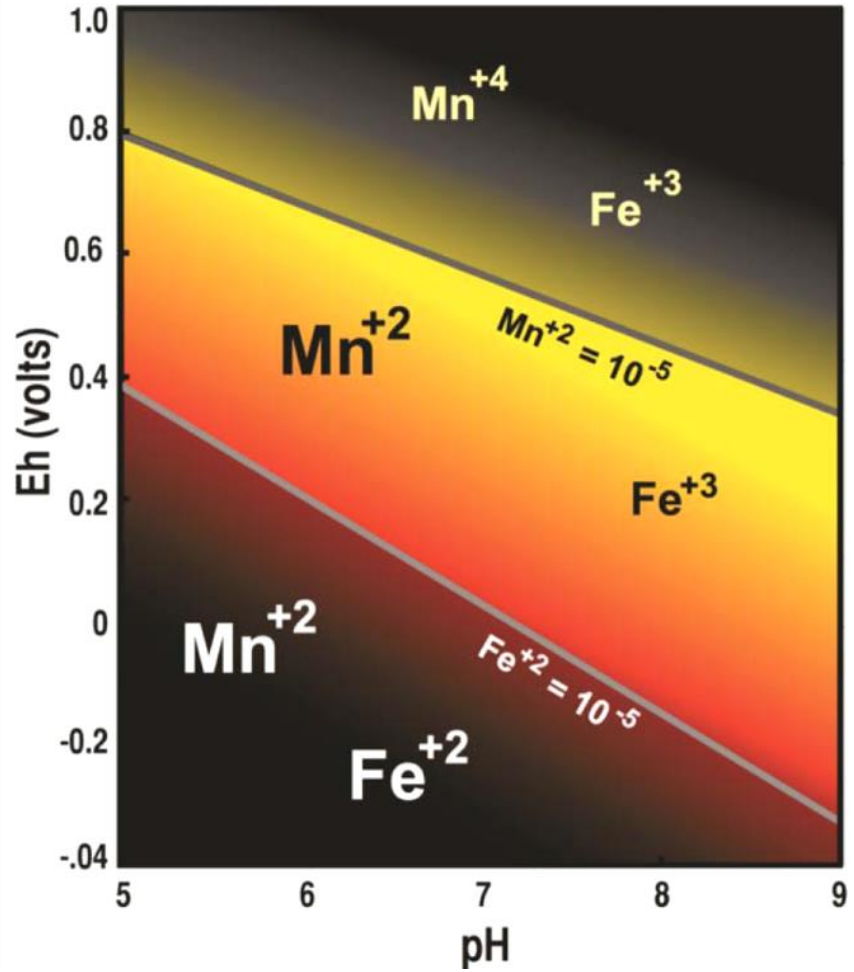

Figure C.3. Idealized diagram of cathodoluminescent colors due to Mn and Fe species in calcite formed under different Eh-pH conditions. From Hiatt and Pufahl (2014), after Mason (1987), and Barnaby and Rimstidt (1989).

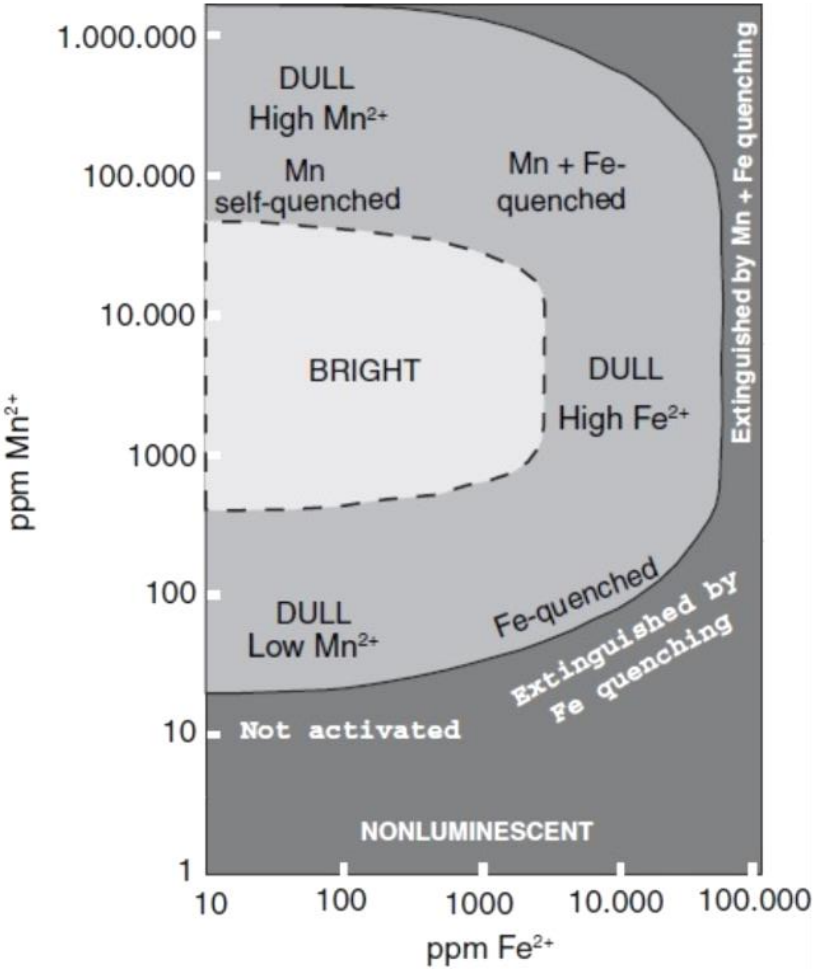

Figure C.4. Interpretive schematic of relative cathodo-luminescence intensity from calcite and dolomite as a function of Fe^{2+} and Mn^{2+} concentrations. Modified (scale) from Boggs and Kinsley (2006), after Machel et al. (1991).

quenching by a high activator concentration, or 3) non-luminescent due to luminescence being extinguished by quenchers or a lack of activators (Machel et al., 1991; Budd et al., 2000).

The ions Pb^{2+} and Zn^{2+} have been previously thought to sensitize Mn^{2+} (Machel et al., 1991). However, according to research by Budd et al. (2000), there is no relationship between Pb^{2+} and Zn^{2+} concentrations and Mn^{2+}-activated CL intensity in the visible spectra of carbonates. Trivalent REEs are known to act as sensitizers with divalent REEs in silicates. This may also be the case for carbonates. However, the broadening of emission bands due to the impurity centers with 3d orbital electron transitions such as Mn^{2+} and $Fe^{2,3+}$ strongly interact with the local crystal field emission peaks from divalent REEs. As a result discrete peaks, such as those from trace amounts of REEs, are unidentifiable in spectra where broad emission bands such as those of Mn^{2+} and $Fe^{2,3+}$ coincide or overlap (Rakovan and Waychunas, 1996; Machel et al., 1991; Nasdala et al., 2004; Götze, 2012).

C.1.6 Carbonate-Cement Stratigraphy

Differences in the activities and redox potential of Mn and Fe in carbonates may lead to differences in the intensity and color of cathodoluminescence. Within a given crystal, regions of different CL are known as zones (Machel and Burton, 1991; Hiatt and Pufahl, 2014). Cathodoluminescence has been used in the past to infer the paleogeochemical conditions under which authigenic carbonates precipitated. This is done by interpreting carbonate zonation with other textural features in the context of cement stratigraphy (Barnaby and Rimstidt, 1989; Machel and Burton, 1991; Hiatt and Pufahl, 2014). The basis of cement stratigraphy relies on the correlation of similar

compositional zones in different crystals. OM-CL is uniquely useful with zoned carbonates because it allows visualization of spatial distributions of quenchers and activators and, thus, areas of different composition in a crystal structure (Reeder, 1991).

The CL of authigenic calcite and dolomite is, in part, due to the valences and activities of Mn and Fe species in pore waters during carbonate precipitation (Barnaby and Rimstidt, 1989). Manganese and iron mineral phases with Eh/pH-dependent solubilities can affect the activities of Mn^{2+} and Fe^{2+} in pore fluids, particularly in near-subsurface sedimentary environments where Fe and Mn oxyhydroxides are ubiquitous and redox reactions involving Fe and Mn equilibria are rapid (Barnaby and Rimstidt, 1989; Machel and Burton, 1991). Cation activities of Mn^{2+} and Fe^{2+} are generally low in shallow, oxygenated groundwater where manganese and iron either remain in primary minerals or are found in secondary, more-or-less stable oxyhydroxides minerals in $Mn^{2,3,4+}$ and $Fe^{2,3+}$ valences (Gilkes and McKenzie, 1988; Barnby and Rimstidt, 1989; Machel and Burton, 1991).

Carbonate cement precipitated in waters with low Mn^{2+} activity lacks sufficient numbers of Mn^{2+} ions to activate luminescence (Figure C.3) (Hiatt and Pufahl, 2014). As the Eh potential decreases, the activities of Mn^{2+} and Fe^{2+} in pore fluids increase. This is generally associated with insoluble Mn^{4+} and Fe^{3+} phases being reduced to soluble divalent phases allowing for more Mn^{2+} and Fe^{2+} to be incorporated into carbonate cement (Barnaby and Rimstidt, 1989; Machel and Burton, 1991; Hiatt and Pufahl, 2014). If sufficient Mn^{2+} is incorporated into the crystal lattice to activate luminescence, and there is insufficient $Fe^{2,3+}$ to quench, a bright zone (yellowish orange for calcite) would follow the initial non-luminescent zone. As pore waters become increasingly reduced,

Fe^{2+} becomes more available in the pore fluids and competes with Mn^{2+} for Ca^{2+} and/or Mg^{2+} sites in carbonates (Hiatt and Pufhal, 2014). If sufficient Fe^{2+} is incorporated into carbonates to quench the Mn^{2+}-activated luminescence, then the precipitated cement zone will appear dull under CL as compared to bright zones (Machel and Burton, 1991; Hiatt and Pufhal, 2014).

Extinguishing Mn^{2+}-activated CL of calcite by Fe^{2+} requires concentrations upwards of tens of thousands ppm by weight of Fe^{2+} for low (<100 ppm) Mn^{2+} concentrations (Figure C.4) (Machel et al., 1991; Boggs and Kinsley, 2006). CL may also be extinguished in calcite with excessive Mn^{2+}content, ostensibly hundreds of thousands of ppm, with similarly high Fe^{2+} content, for the combined self-quenching and quenching to effectively suppress cathodoluminescence (Figure C.4) (Machel et al., 1991). Calcite or dolomite with such a high Fe concentration would be considered ferroan (Machel, 1985; Hiatt and Pufahl, 2014). Competition for aqueous Fe^{2+} in the precipitation of pyrite, driven by sulfate-organic redox, may decrease the incorporation of Fe^{2+} into calcite and, thus, lessen its quenching effect (Hiatt and Pufhal, 2014). High concentrations of Mn^{2+} alone in carbonates can lead to self-quenching, but this is not common unless natural groundwaters are in contact with Mn^{2+}-enriched supergene or hypogene deposits (Hem, 1963; Machel and Burton, 1991; Machel et al., 1991).

The general trend of carbonate cements, non-luminescent followed by brightly-luminescent then dully-luminescent (Figure C.5), has been observed in carbonate precipitated in meteoric-influenced aquifers, as well as in phreatic marine settings, and is not indicative of either environment (Machel and Burton, 1991). Although Mn phases are more readily reduced than are Fe phases, interdependent redox reactions exist between

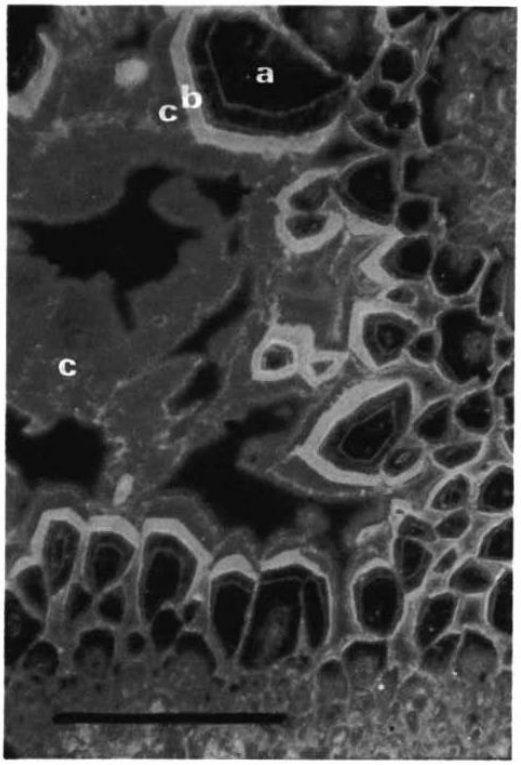

Figure C.5. Distinct, idealized sequence of luminescence zonation in carbonate with drop in Eh. Earliest cement is non-luminescent calcite core "**a**", followed by a rim of bright orange luminescent cement "**b**" and "**c**" a dull red luminescent ferroan calcite. Scale bar is 1 mm. From Machel (1985).

the two metals at appreciable rates in natural waters. This suggests that the stability boundaries constructed from separate redox pair-reactions from phases of these two cations (Figure C.3), are erroneous and an oversimplification (Machel and Burton, 1991; Drever, 1997). According to Machel and Burton (1991), electrochemical disequilibrium is ubiquitous in natural waters and, therefore, Eh-pH diagrams that assume equilibrium cannot be used to estimate activities of Mn^{2+} and Fe^{2+} from concentrations measured in calcite. Thus, one cannot use diagrams such as Figure C.3 to infer pore-fluid chemistry from observed CL. Redox-state is not the sole factor affecting Mn^{2+} and Fe^{2+} content and, thus, cannot be inferred only from the cathodoluminescence of carbonates. Figure C.3 is a qualitative generalization of Mn and Fe redox states at Eh-pH conditions typical of

natural waters in a carbonate-buffered aquifer with the associated, but highly idealized, cathodoluminescence expected of calcite precipitated under such conditions.

While redox does play an important part in the activities and availability of Mn^{2+} and Fe^{2+}, the incorporation of these impurity ions into calcite is better modeled by the activity ratios of Mn^{2+}:Ca^{2+} and Fe^{2+}:Ca^{2+}, and the precipitation rate of carbonate. This means that processes independent of the activities of Mn^{2+} and Fe^{2+} can also affect the incorporation of these cations into calcite by changing the activity of Ca^{2+} in solution or the growth rate of the crystal (Machel and Burton, 1991). Similarly, cathodoluminescent calcites can precipitate from waters with vastly different bulk chemistries but with similar Mn^{2+}:Ca^{2+} and Fe^{2+}:Ca^{2+} activity ratios. Precipitation, dissolution, evaporation, dilution, salinity, and temperature all affect the activity of Ca^{2+} (Machel and Burton, 1991). Interactions between hydrocarbons and brines with freshwaters are of particular interest as thermal, redox, and salinity gradients may arise in addition to microbially-mediated redox reactions and the complexation of metals and organics with clays (Barnaby and Rimstidt, 1989; Machel and Burton, 1991; Reeder, 1991). Salinity and temperature directly affect the activities and distribution of aqueous species, along with crystal growth rates, which may be reflected in gradual cathodoluminescence zonation of carbonate precipitated along a mixing gradient (Machel and Burton, 1991).

C.1.7 Zonation Types in Carbonates

Utilization of CL for carbonate-cement stratigraphy, can reveal pertinent information regarding the subsurface environment and placement in the paragenetic sequence in which a given carbonate phase formed (Boggs and Kinsley, 2006; Reeder, 1991; Meyers, 1991; Hiatt and Pufahl, 2014). CL zonation may further be classified by

the textural relationship between zones and the crystal growth interface (surface) or by a preexisting surface (Reeder, 1991). Partitioning of trace activators and quenchers within the crystal is not uncommon in carbonate cements potentially resulting in three types of zones: concentric, oscillatory, and sectoral (Figure C.6) (Machel and Burton, 1991; Reeder, 1991). Concentric zones parallel the crystal growth interface during precipitation and, consequently, are the most useful zonation type. This is because any changes in cathodoluminescence (and, thus, bulk fluids) are recorded in the cement and can potentially be correlated with other, similarly zoned, crystals (Reeder, 1991).

Non-concentric zones do not record temporal changes in the bulk chemistry of the formation waters and, thereby, cannot be used to estimate changes in fluid properties such as quencher and activator activities (Reeder, 1991). Sectoral zonation is oblique to the crystal growth interface and arises due to a difference in the growth rates between crystal sectors. Intrasectoral zonation can occur within sectoral zonation due to similar growth rate differences. Partitioning of trace elements during coeval growth results in different spatial activator and quencher concentrations. These different concentrations become apparent where sectors meet. Oscillatory zonation parallels the crystal growth interface and resembles concentric zoning although on a scale of microns to nanometers (Reeder, 1991). The process responsible for oscillatory zoning in carbonates is not fully understood but it is believed to be similar to the process creating oscillatory zonation in some igneous plagioclase. Oscillatory zonation in plagioclase is a result of periodic fluctuation of growth rate and solute transport to the crystal growth interface (Reeder, 1991).

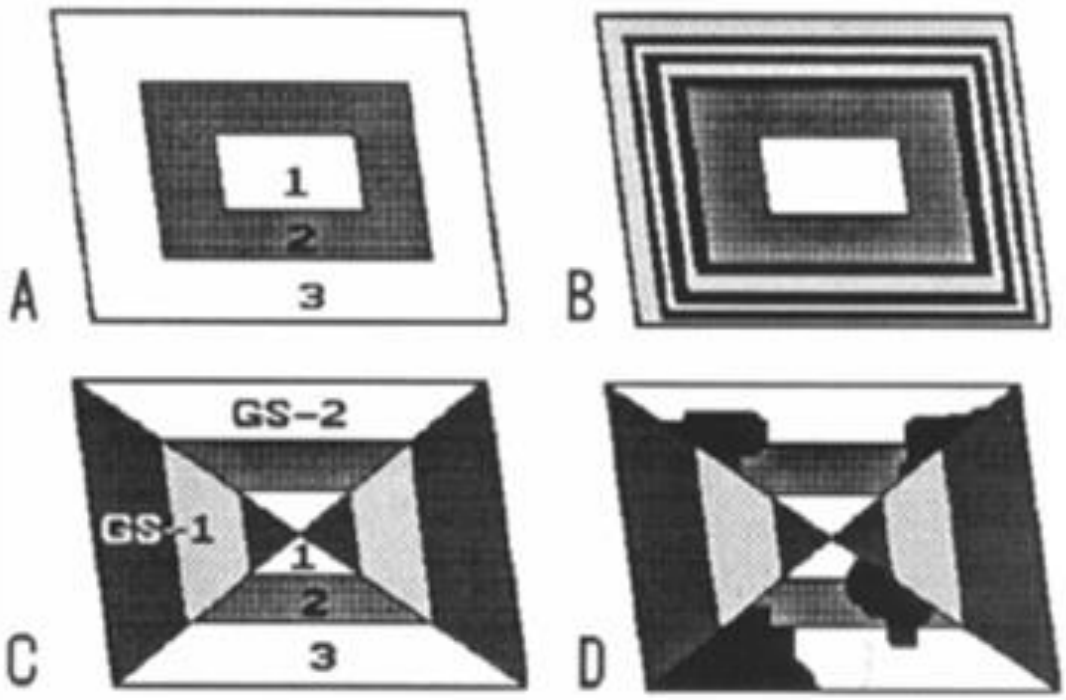

Figure C.6. Potential types of zonation found in carbonates. Shading does not imply the presence or absence of luminescence but distinction. A) Simple concentric zonation with different compositions in zones 1, 2, and 3. B) Concentric oscillatory zoning in zone 3 of crystal A. C) Concentric zoning similar to crystal (A) but with two non-equivalent crystallographic growth sectors with trace element partitioning within (GS-1 and GS-2). D) Zonation similar to crystal (C) with intrasectoral zonation occurring in GS-2. From Machel and Burton (1991).

Oscillatory zones similar, to those found in nature, have been observed in synthetic calcite precipitated under supersaturated conditions with high concentrations of Mn^{2+}. Fluctuation in the growth rate of calcite apparently partitions the Mn^{2+} within the crystal as incorporation of Mn^{2+} into calcite is partially growth dependent (Reeder, 1991). Concentric, sectoral, and oscillatory zonations are not mutually exclusive within the same carbonate crystal and partial dissolution between precipitation events, leading to complicated patterns, can make interpretations more challenging (Reeder, 1991). Only a few crystals with carbonate zonation were observed in the sampled core. The majority

was concentrically zoned and all but one instance were from samples with minor carbonate cement content.

C.1.8 Applications of Cathodoluminescence Petrography to Carbonates

The cathodoluminescence of carbonate cements cannot be used by itself to infer the redox potential of the waters that formed them (Machel and Burton, 1991). Interpretations of cathodoluminescent carbonate cements should be supported by textural relationships of reduced and oxidized cements and/or auxiliary investigative techniques such as fluid inclusions, isotopes, and microthermometry (Machel and Burton, 1991; Machel, 2005). Interplay between the activities of Ca^{2+}, Mn^{2+}, and Fe^{2+} and various geochemical processes, particularly in areas with basinal brine and meteoric influences, makes correlation of cathodoluminescent cement zones over distances greater than tens of kilometers ill-advised (Machel and Burton, 1991). The cathodoluminescence of diagenetic carbonate can be affected by the following: (1) crystal surface kinetics, (2) distribution and solubility coefficients of and between aqueous species and their solid phases (aqueous phases of crystal constituents including activators and quenchers in addition to constituents of competing minerals that share reactants), (3) microbial metabolic processes (specifically dissimilatory, $Fe^{3+}$and Mn^{4+} oxyhydroxides redox effect on chemical equilibrium of minerals and species in solution), (4) organic and inorganic complexation with clay adsorption, mixing of formation waters with meteoric and/or basinal brines, and (5) changes in temperature (Machel and Burton, 1989; Barnaby and Rimstidt, 1989; Reeder, 1991). Despite the difficulties that may arise when interpreting CL of carbonates, cathodoluminescence is still a powerful tool that allows visualization of activators' and quenchers' spatial distributions. Inferences to the general chemistry of

pore fluids from which carbonate precipitated based on CL cement-stratigraphy should also be supported by textural features and cements that constrain the carbonate in paragenesis, and corroborate, or, at minimum, be consistent with the interpreted aqueous geochemical conditions.

C.1.9 Common CL Petrographic Instrumentation and Limitations

Cathodoluminescence in materials is observed either via optical or scanning electron microscopy (SEM). Instrumentation in optical cathodoluminescent microscopy (OM-CL) usually utilizes a cathode tube which ionizes gas (cold-cathode) to produce an electron beam (Flegler et al., 1993; Boggs and Kinsley, 2006; Götze and Kemp, 2008; Götze, 2012). An optical microscope adapted for cathodoluminescence is fitted with a cold-cathode source in a windowed vacuum chamber compact enough to fit as a stage attachment. The electron beam produced by the cathode tube lamp is defocused, stationary, and centered on the sample (Figure C.7) (Götze and Kemp, 2008; Götze, 2012). The relatively poor vacuum in the vacuum chamber helps prevent the buildup of charge on a non-conductive sample.

SEM cathodoluminescence microscopy (SEM-CL) uses a heated tungsten filament (hot-cathode) as an electron source. The electrons are focused to a fine spot that scans across the sample collecting the image one pixel at a time. It uses a higher vacuum such that non-conductive mineral samples may require a carbon coating to prevent charging of the sample during electron bombardment (Boggs and Kinsley, 2006; Götze, 2012). SEMs provide greater magnification and higher resolution, albeit grayscale, photomicrographs than all OM-CL microscopes, in addition to other analysis capabilities (Reed and Milliken, 2003; Boggs and Kinsley, 2006; Götze and Kemp, 2008).

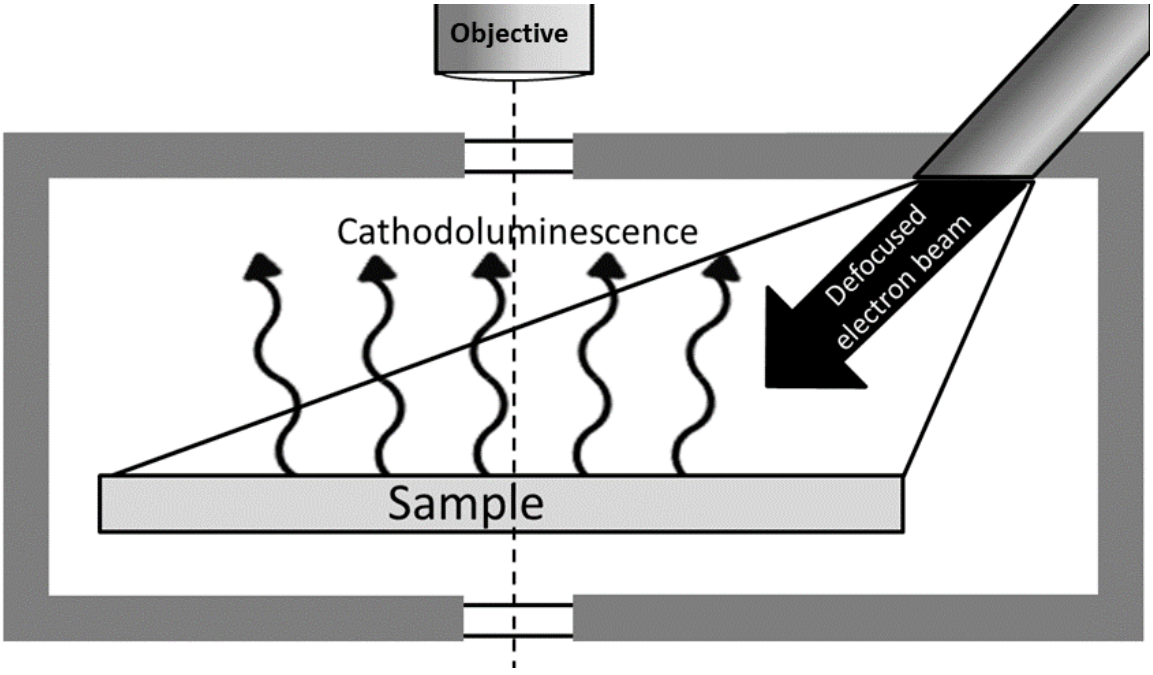

Figure C.7. Cross-sectional view of cold-cathode stage attachment used for optical cathodoluminescence microscopy. After Götze and Kempe (2008), and Boggs and Kinsley (2006).

Unfortunately, SEM-CL photomicrographs, particularly those of luminescent carbonates and apatite, are susceptible to phosphorescence (latent photon emission $>10^{-8}$ seconds with cessation of exciting energy). This latent emission creates streaking and blurring in images as luminescence occurs in multiple locations as the beam rasters across the sample (Pagel et al., 2000; Reed and Milliken, 2003; Boggs and Kinsley, 2006; Götze and Kemp, 2008). Phosphorescence-related artifacts can be negated with changes in scanning beam dwell times or the addition of a monochromator or filters to exclude the problematic wavelengths (Reed and Milliken, 2003). The contributions of photons from the near-UV and IR wavelengths are included with the visible spectra in panchromatic SEM-CL photomicrographs, which vary only by intensity as the number of photons detected. Differentiation of photon contributions by wavelength requires a CL-spectrophotometer with a monochromator for selective ranges or filters (Reed and

Milliken, 2003; Boggs and Kinsley, 2006). SEM-CL systems are more suitable for spectral analysis than OM-CL. OM-CL is limited by the resolving power of the microscope as well as the glass in the optics that absorbs wavelengths <380 nm inhibits signal acquisition and differentiation in the UV. Polished samples are prefer-able for cathodoluminescence imaging but necessary for spectral analysis in both optical and scanning electron microscopy (McLemore and Barker, 1987; Götze and Kemp, 2008).

In cold-cathode OM-CL, fluctuations in the pressure difference between the cathode tube lamp and the chamber can produce variable luminescence in both intensity and color (wavelength) in the sample (Boggs and Kinsley, 2006; Götze and Kempe, 2008). Such fluctuations are noticeable in their effect on photomicrographs of areas with weak luminescence that require long exposure times to capture sufficient light for textural details to be distinguishable. Changes in luminescence due to vacuum and current fluctuations, as well as transient luminescence in silicates from electron irradiation, may result in slight blurring and loss of detail in images taken with longer exposures.

Epoxy, underlying glass, as well as any staining can affect the cathodoluminescence of thin section samples. These materials, if luminescent, potentially contribute or detract from the visible luminescent spectra being transmitted through the sample (Götze and Kemp, 2008). On OM-CL systems the chamber window can affect the observed luminescence by introducing outside light, or absorbing visible sample luminescence if the window and chamber are coated with oil back-streamed from the vacuum pump. Alizarin red S and potassium ferricyanide-combined staining of carbonates can introduce Fe ions that quench CL, and the acid etching can reduce sample

thickness, particularly of calcite, potentially reducing the beam-specimen interaction volume (Dickson, 1966; Adams and MacKenzie, 1998).

C.2 Electron Microscopy

Scanning electron microscopy scans a surface with an electron beam which produces backscattered electrons that are subsequently detected to produce an image (SEM-BSI). Backscattered electrons are electrons produced from the elastic interaction of incident electrons with the specimen that are scattered out of the sample from the same side they entered at a slightly lower energy than the incident electrons (Figure C.8) (Flegler et al., 1993). The yield of backscattered electrons is very dependent upon the average atomic number of the specimen as well as the accelerating voltage of the electron beam (Figure C.9). Specimens with larger atomic numbers result in greater interaction frequency between the incident electrons of the beam and those of the nuclei of the

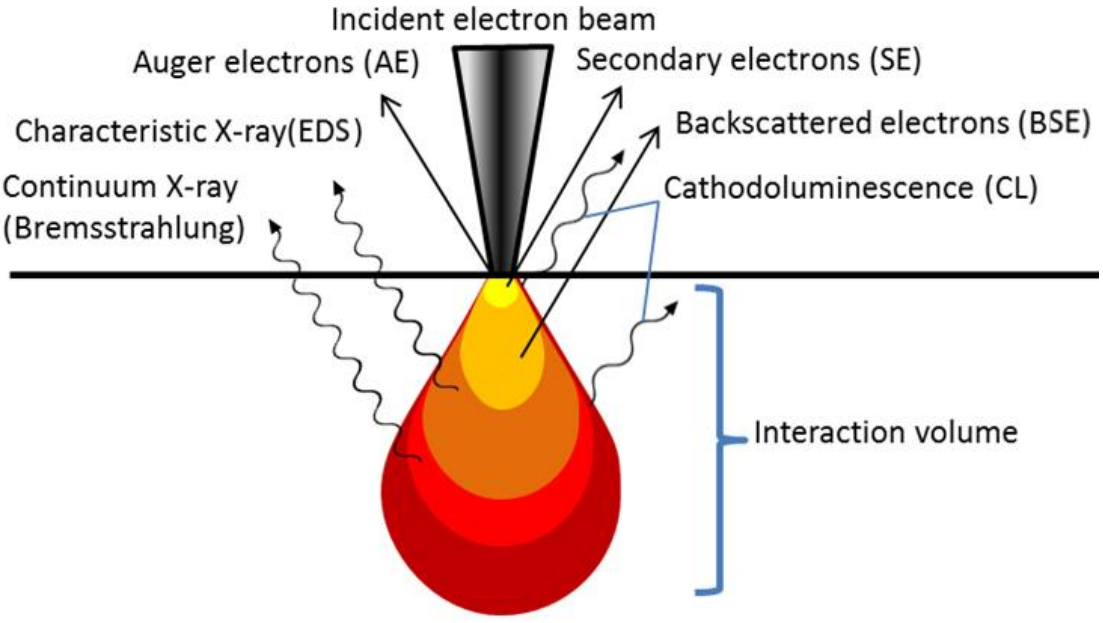

Figure C.8. Electron-matter interactions of an incident electron beam. Photons as well as other energetic particles resulting from the incident electron interaction deep within the sample are not detected if absorbed by the sample material or fail to reach the detector/objective. Based on Salh (2011a) and Flegler et al., (1993).

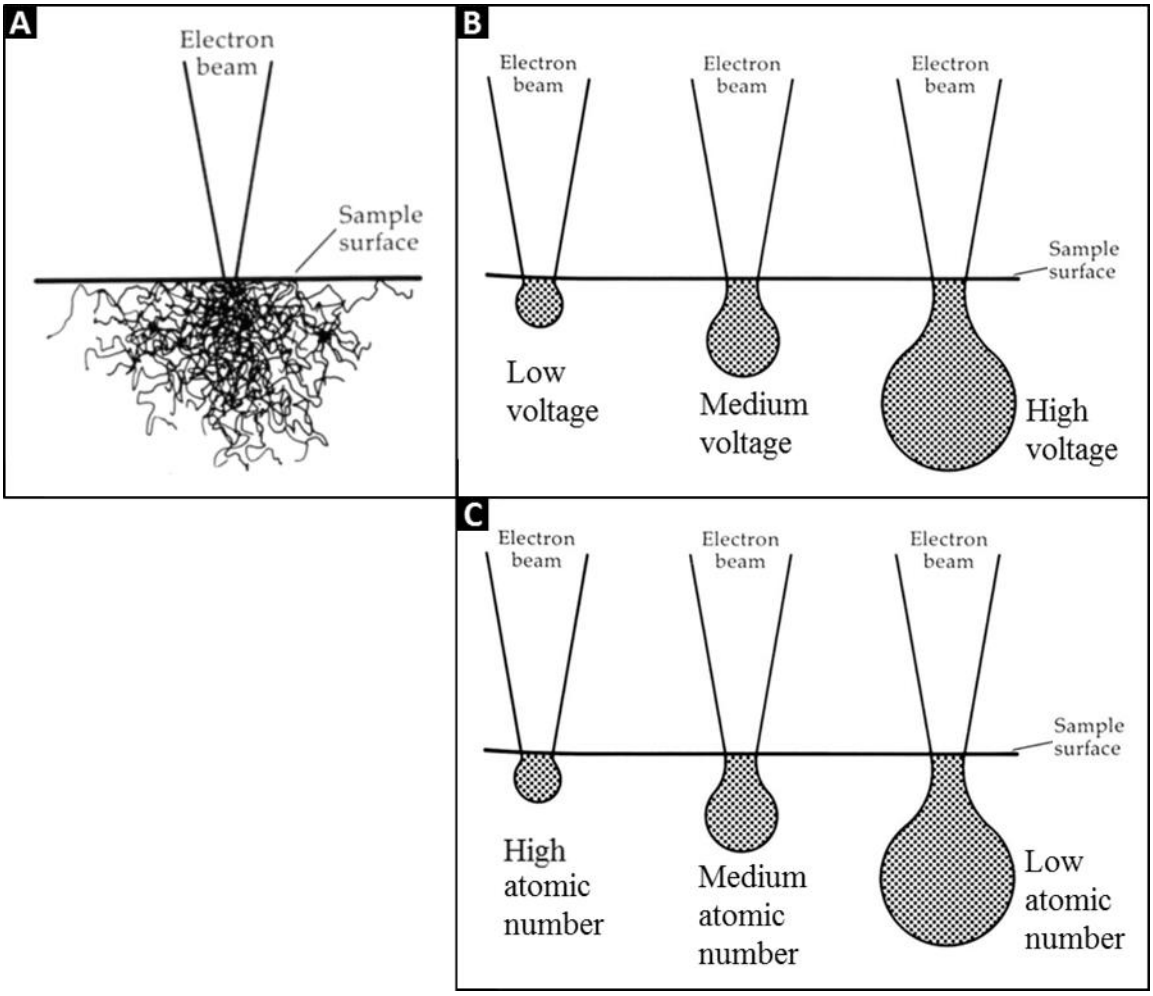

Figure C.9. Specimen-beam electron interactions. A) Pathways of beam electrons in sample interior as they interact with the sample's atoms. B) Effect of varying accelerating voltages of beam on the specimen interaction volume of the scattered electrons. C) Effect of average atomic number of specimen on interaction volume of scattered electrons. From Flegler et al., (1993).

specimen (Flegler et al., 1993). If the accelerating voltage of the electron beam is kept constant for all samples, it follows that apparent contrast differences in SEM-BSI photomicrographs are due to differences in the average atomic number of the interaction volumes (Flegler et al., 1993). Dark regions on SEM-BSI photomicrographs correspond to material with a smaller average atomic number, and lighter regions correspond to material of higher average atomic number. There is one photomicrograph (Figure 4.16C),

where a light region does not correspond to higher average atomic number, but is, instead, due to charge buildup on residual hydrocarbons repelling the electron beam.

Spectral data for energy dispersive spectroscopy (EDS) are constructed from the measured energy of X-rays emitted, when an outer-shell electron fills a vacancy of an inner-shell electron that was displaced by an inelastic collision with an electron (Flegler et al., 1993). Similar to cathodoluminescence photons produced by emissive radiation, the outer-shell electron emits energy in the form of a photon, in this case an X-ray, as the electron transitions to a lower shell and thus lower energy. Although possible electron transitions between shells are limited, multiple transitions within an element are possible. This particularly is the case in higher atomic elements resulting in multiple X-ray lines, each possessing characteristic energy and wavelength (Flegler et al., 1993). It is from groups (families) of these lines of characteristic X-rays that correspond to known atomic-energy transitions from which identification of elemental composition and interpretation of abundance from peak area can be discerned. EDS is, however, limited by: 1) the incident electron energy (greater energy allows for displacement of more inner shell electrons and production of higher energy X-rays), 2) specimen interaction volume (greater interaction volume produces more X-rays but decreases analytical spatial resolution unless the sample is thin), and 3) atomic number (lower atomic number elements have fewer filled inner shells and thus fewer characteristic X-rays that have sufficient energy to penetrate the membrane "window" that protects the X-ray detector from contaminants in the specimen chamber) (Flegler et al., 1993).

The SEM-EDS spectral analyses consistently included peaks of Si and O. These peaks were present even in selected areas within pyrite crystals with no observable silica

nearby. The inclusion of the glass slide within the interaction volume is assumed to be responsible for the contribution of Si and O peaks to the various EDS spectra. Due to the presence of epoxy mounting resins, as well as the underlying glass slide, consistent elemental detection was restricted to atomic numbers $\geq$8 (oxygen and above), and the resulting EDS spectra are, at best, semi-quantitative of the mineral within the investigated area. Interpretation of EDS spectra are, at best, from clays is more problematic. Potentially polymineralic clay clasts and grain coats, as well as numerous polymorphs, are not distinguishable by EDS although iron and titanium transition metals and sulfur were commonly detected in clays.

Transmission electron microscopy (TEM) is analogous to traditional light microscopy except that it uses a defocused electron beam to transmit electrons through an extremely thin sample. The sample must be sufficiently thin so that an adequate amount of incident electrons interact but are not blocked as they pass through the sample (Flegler et al., 1993). TEM can be used to discriminate clays on a morphological basis as well as be used to verify a mineral's crystalline nature through selected area electron diffraction (SAED). SAED was performed on suspected clay minerals and the resultant pattern confirmed the crystalline nature of the clay; however, due to time constraints of the building being condemned and the microscope being replaced the crystal spacing was not determined.

C.3 Raman Microscopy

Raman microscopy utilizes a confocal light microscope, in conjunction with a Raman spectrophotometer and accompanying equipment, to perform Raman spectroscopy. Raman spectroscopy measures Raman scattering. Raman scattering is a

form of inelastic scattering that happens to a fraction of photons as they pass through molecules and results in a shift in frequencies (ν) or wavenumbers ($\tilde{\nu}$), of the apparent light (Morris, 1992). The scattered photons may be of lesser (Stokes shift) or greater (anti-Stokes shift) energy than the incident photons depending on whether the scattering molecule gained or lost vibrational energy during the interaction (Struve, 1989). These shifts are symmetric in energy, as they both correspond to the energy difference between the ground and excited vibrational states. However, the Stokes shift is often more prominent in the observed spectrum as most minerals are typically examined at room temperature, which means that the ground vibrational state is much more populated than the excited state.

Electron transitions may be vibrational, electronic, or rotational. Vibrational transitions are the most useful for Raman spectroscopy as every molecule has a vibrational Raman spectrum (Struve, 1989; Morris, 1992). In Stokes-shifted Raman scattering, electrons in the ground state of the material absorb a photon and are promoted to an extremely short-lived "virtual" energy state (Figure C.10) (Long, 1977). The electron instantly transitions downward from this virtual state to an excited vibrational state. As the final state of the electron is higher in energy than the initial state, the emitted photon is less energetic than the absorbed one. The energy difference between the scattered and unscattered/incident light is the energy difference between the initial and final vibrational states. The promotion of an electron to a virtual state in Raman scattering distorts the molecular electron cloud as does the change in vibrational energy upon de-excitation of an electron.

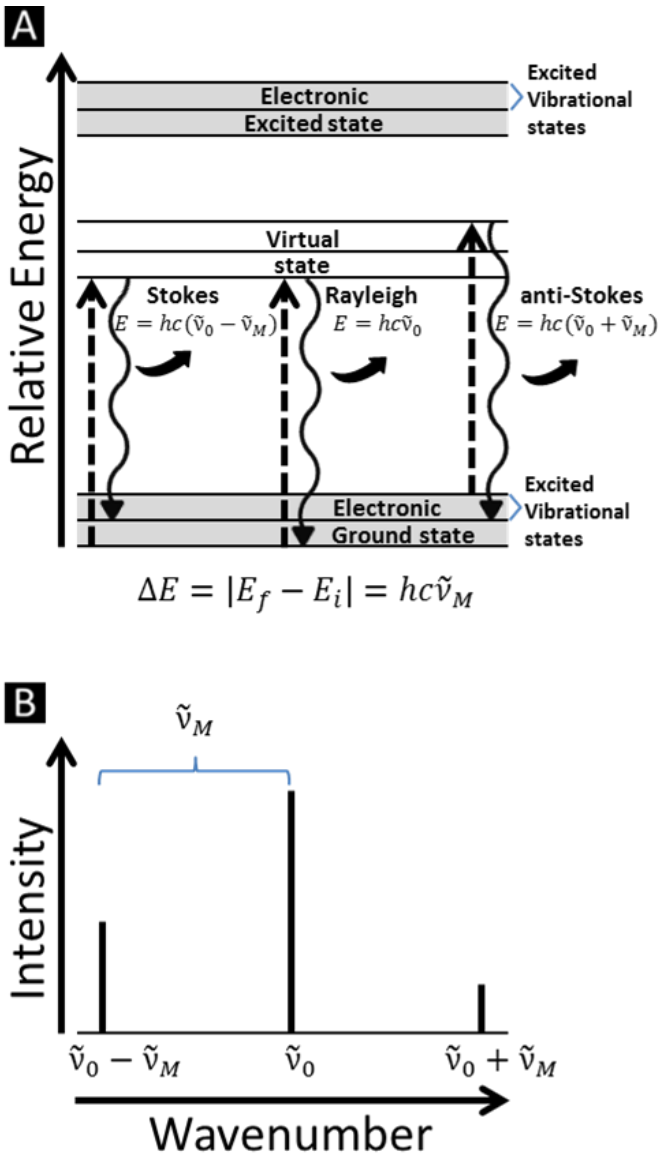

Figure C.10. Raman and Rayleigh light scattering processes. A) An incident photon of wavenumber ($\tilde{\nu}_0$) promotes an electron (dashed arrow) from the ground electronic state to a virtual state. Subsequent de-excitation of the electron (sinuous arrow) results in photon emission (swept arrow). Raman scattered light has slightly different energy and thus wavenumber ($\tilde{\nu}_0 \pm \tilde{\nu}_M$) than the incident photon. The magnitude of energy difference between scattered and incident light is equal to that of final and initial electron vibrational energy states of the molecule. Rayleigh scattering does not involve the electron vibrational states and as such the scattered light is the same as the incident. B) Intensity and wavenumber of scattered light. Rayleigh is the dominant scattering process, with Stokes-shifted Raman light being more intense than anti-Stokes due to relative abundance of molecules in the ground state. After Morris (1992), and Long (1977).

Molecular vibrations that lead to a net change in the polarizability of the molecule, allow for Raman transitions. Such vibrations are Raman-active and are detectable with Raman spectroscopy. Raman scattering occurs in gases, liquids and solids and is capable of providing chemical and structural information about materials via non-destructive means (Morris, 1992). Some bonds have higher polarizability, and solids (particularly crystals) are limited to which bonds can stretch, although intermolecular interactions of the crystal's unit-cell may also contribute to molecular vibrations and influence Raman scattering (Long, 1977). At a practical matter, Raman scattering to "fingerprint" chemical groups (and thus minerals) requires filters and other specialized equipment with computational software for the deconvolution of individual peaks within Raman spectra (Long, 1977; Morris, 1992). Raman spectroscopy uses monochromatic light from a laser as a source of incident photons. Diffraction gratings, spectrometers, and multichannel detectors then measure the slight changes in wavelength of scattered light from Raman-active bonds (Morris, 1992).

C.4 X-ray Diffractometry

XRD and powder XRD are analytical methods typically used to identify crystalline material. X-rays generated from a source, typically copper, are filtered to a monochromatic radiation that is directed towards a sample and scanned over a range of angles while a detector counts the diffracted X-rays from the sample (Suryanarayana and Norton, 1998). The incident X-rays are elastically scattered by the sample resulting in X-rays scattered in random directions. These elastically-scattered X-rays have the same wavelength, and constructive and deconstructive interference occurs. However, due to the periodicity of a crystal lattice and the changing angle of the incident X-rays upon the

sample, at some angle conditions constructive interference of the elastically scattered waves will occur favoring a path of wavefront propagation (Suryanarayana and Norton, 1998; Poppe et al., 2001). Diffraction patterns can be used to characterize minerals due to a mineral's characteristic crystal lattice inherent in its molecular structure (Poppe et al., 2001). The incident X-rays are diffracted according to Bragg's law: $n\lambda = 2d\ sin\theta$ where n = the integer multiple of the wavelength, λ = incident X-ray wavelength, θ = Bragg angle of incident and diffracted X-ray from which constructive interference occurs, and d = interplanar distance between lattice planes (Figure C.11). Samples are scanned over a range of angles by coupled rotation of the detector and specimen holder. This ensures diffraction within a variety of lattice spacings and the resultant X-rays are detected and counted.

Minerals are identified from diffractogram peak patterns where X-ray intensity at specific θ angles can be related to the characteristic interplanar spacing of a mineral's crystal lattice. Polymineralic samples require multiple peak sets to be matched for bulk identification. Organics in samples can obscure low-intensity diffraction patterns of minerals that are weakly detected (low counts) (Poppe et al., 2001). Discrimination of clay mineral species within clay groups is problematic due to similarities in lattice spacing and their shrink/swell capacities. Clay minerals with similar or overlapping peaks must have their shrink/swell and other physical and other chemical properties exploited to change their lattice spacing in order for their mineralogies to be resolved with XRD (Poppe et al., 2001). Precise identification and quantitative analysis of clays with XRD from polymineralic samples require a variety of additional sample preparation procedures

and multiple analyses for accurate identification possibly necessitating electron microscopy for identification of clay species based on morphology (Poppe et al., 2001).

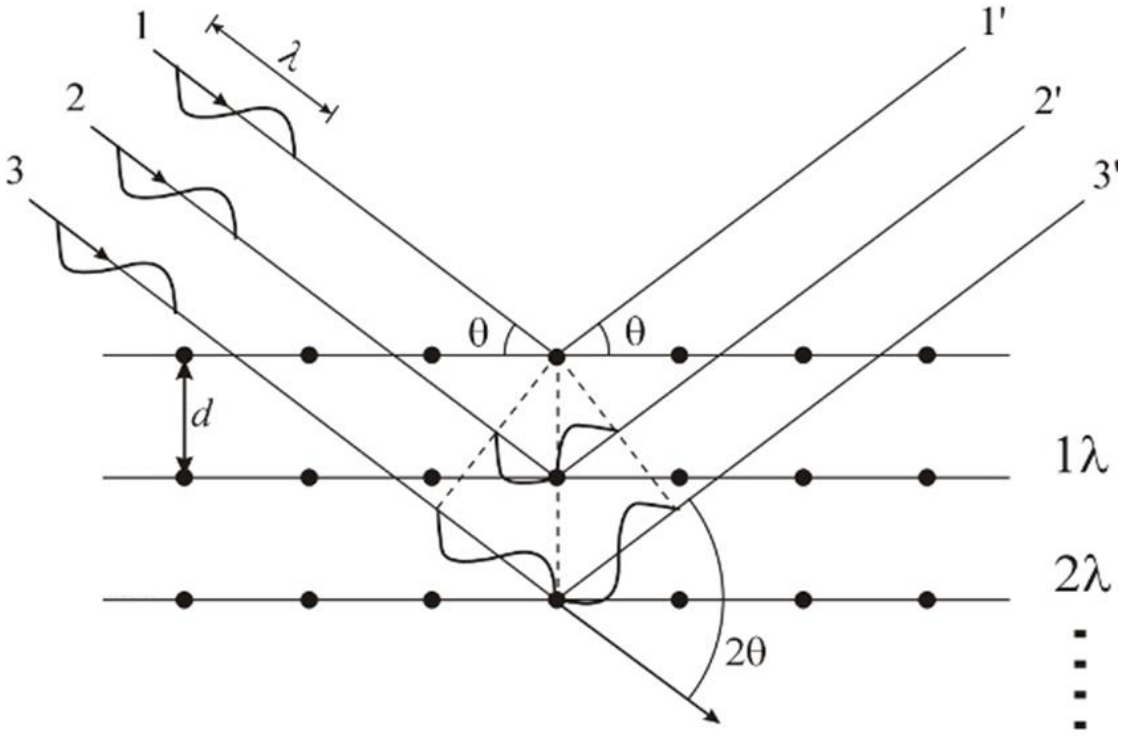

Figure C.11. X-ray diffraction in a crystal. Incident X-rays (left) interact (scattered) with the sample and are diffracted (right). Dashed lines indicate coherent phases of X-ray waves. Modified from University of Leuven, (2010).

APPENDIX D: QFL-Composition Plots and Grain-Size Histograms

This appendix contains QFL-composition plots and apparent grain-size histograms measured during grain-counts. QFL-composition plot diagrams follow McBride (1963), but are modified to better display the quartzose content of the samples. Histograms display grain-size abundancies and are graphically presented with a lower and upper interval within each Udden-Wentworth grade (Udden, 1914; Wentworth, 1922). Bins correspond to grain sizes with the phi scale displayed above the histograms and the μm scale below. These grain-size distribution histograms did not follow the convention of traditional sieve analyses with bins in the phi scale and decreasing in coarseness from the left to the right (Houseknecht, 1993). Because these are apparent grain sizes from thin section, and not based on sieve analysis, histograms display grains in decreasing coarseness from right to left.

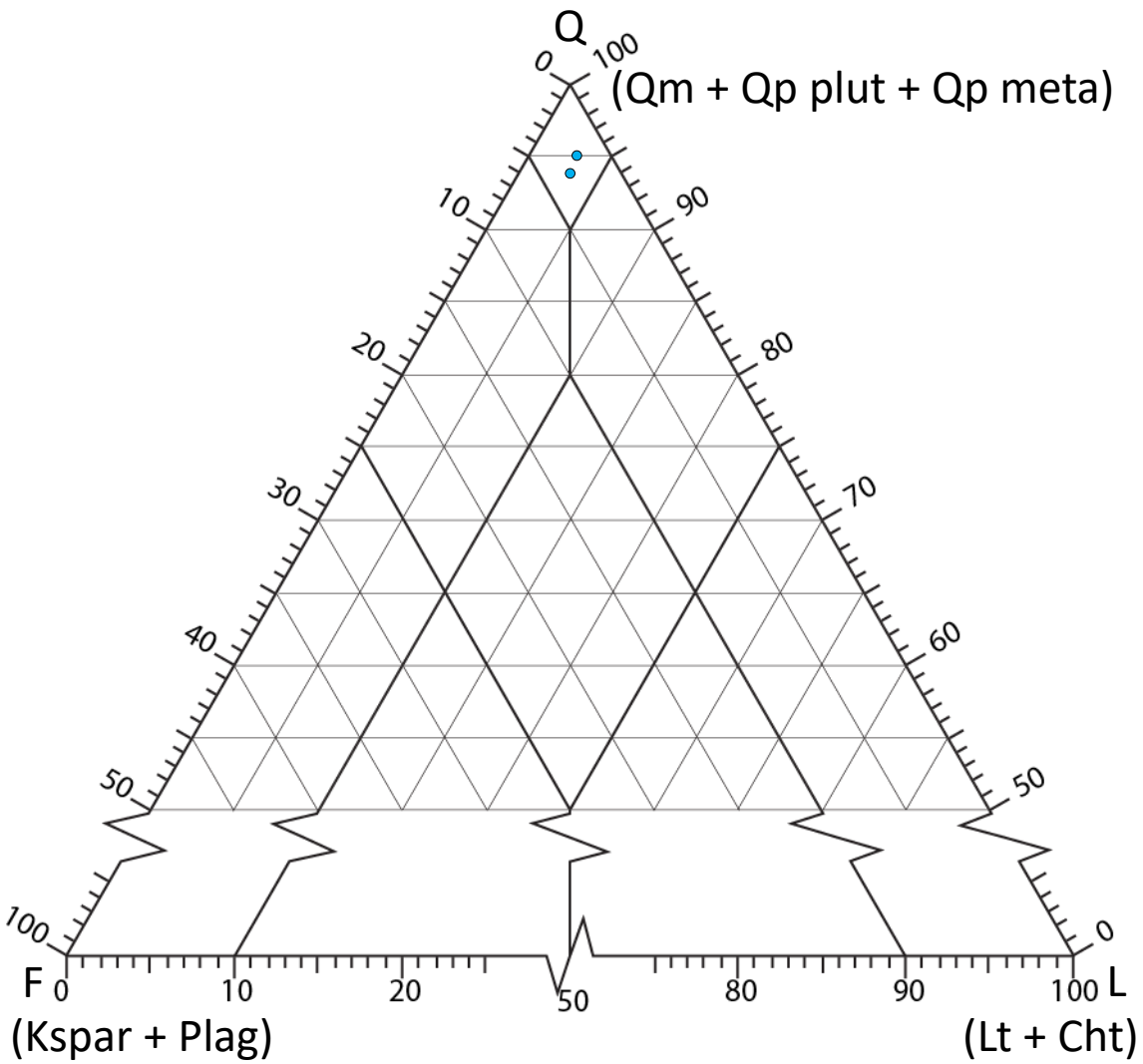

Figure D.1. QFL-composition plot of 104c1-b10 differentiated between reservoir and seal.

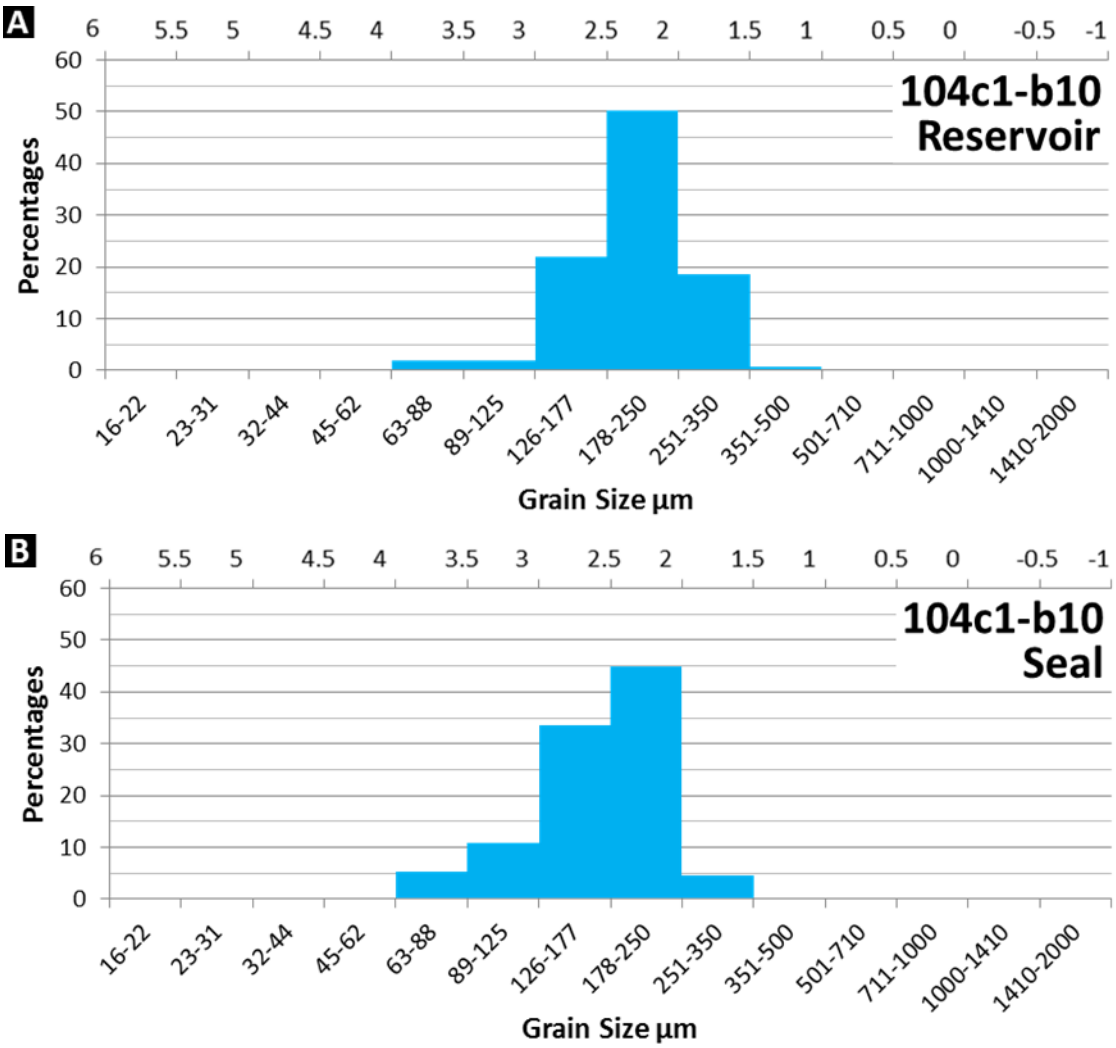

Figure D.2. Framework grain-size distribution of both reservoir and seal sections of 104c1-b10. Grain sample sizes for reservoir (A) and seal (B) are n = 317, and n = 307, respectively.

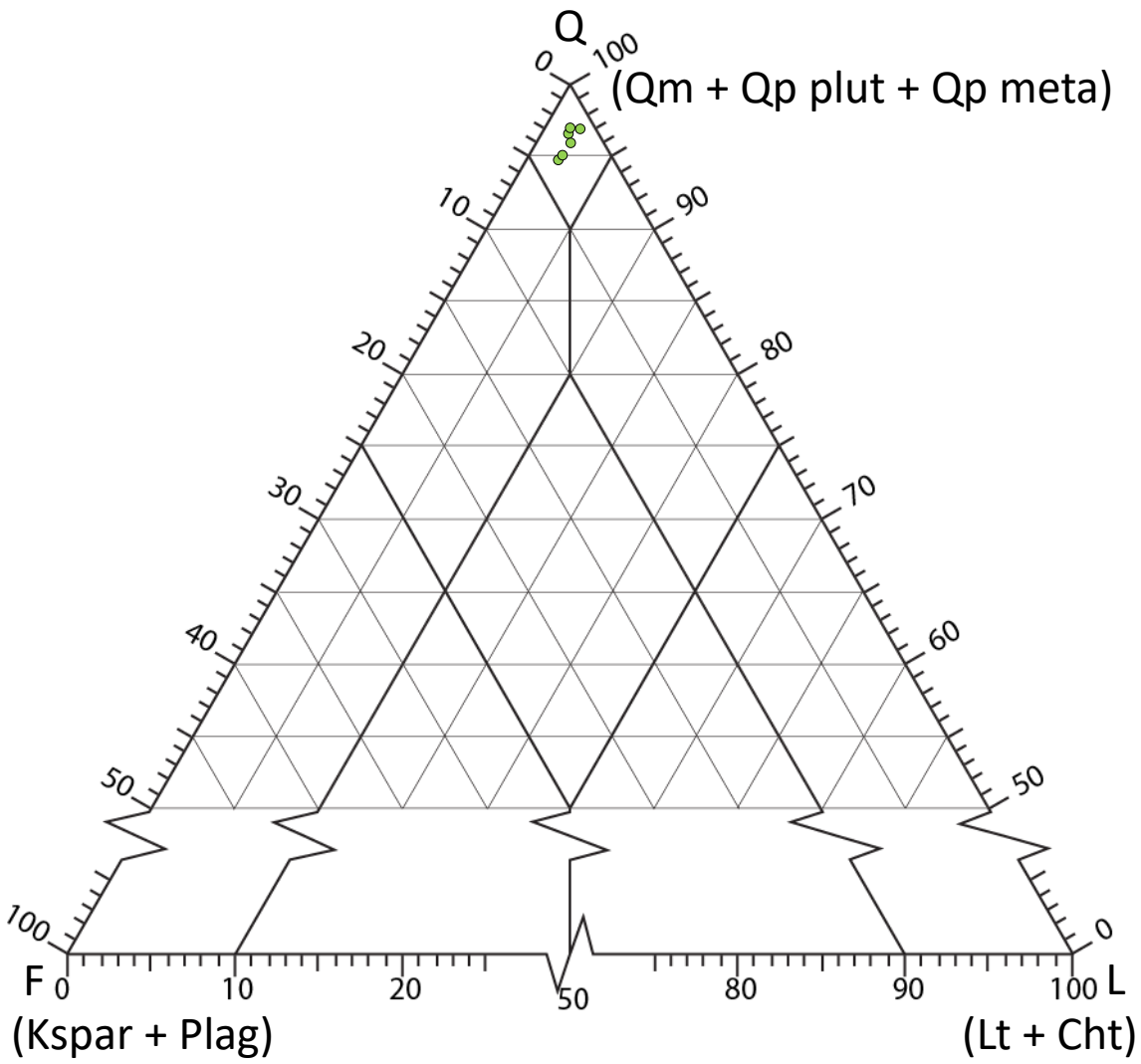

Figure D.3. QFL-composition plot of samples from Core 105.

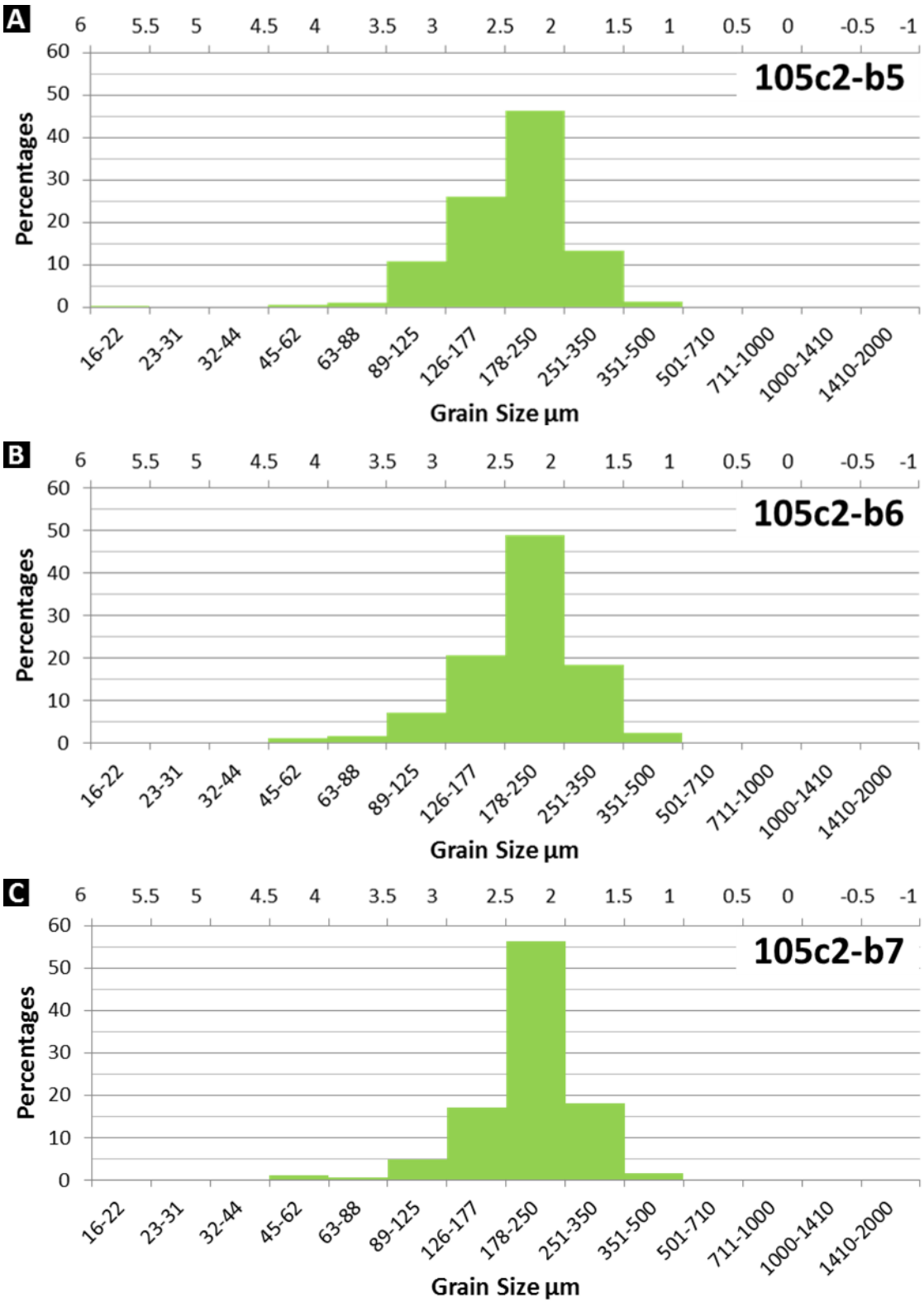
A
6 5.5 5 4.5 4 3.5 3 2.5 2 1.5 1 0.5 0 -0.5 -1
105c2-b5
Percentages
60 50 40 30 20 10 0
16-22 23-31 32-44 45-62 63-88 89-125 126-177 178-250 251-350 351-500 501-710 711-1000 1000-1410 1410-2000
Grain Size µm
B
6 5.5 5 4.5 4 3.5 3 2.5 2 1.5 1 0.5 0 -0.5 -1
105c2-b6
Percentages
60 50 40 30 20 10 0
16-22 23-31 32-44 45-62 63-88 89-125 126-177 178-250 251-350 351-500 501-710 711-1000 1000-1410 1410-2000
Grain Size µm
C
6 5.5 5 4.5 4 3.5 3 2.5 2 1.5 1 0.5 0 -0.5 -1
105c2-b7
Percentages
60 50 40 30 20 10 0
16-22 23-31 32-44 45-62 63-88 89-125 126-177 178-250 251-350 351-500 501-710 711-1000 1000-1410 1410-2000
Grain Size µm

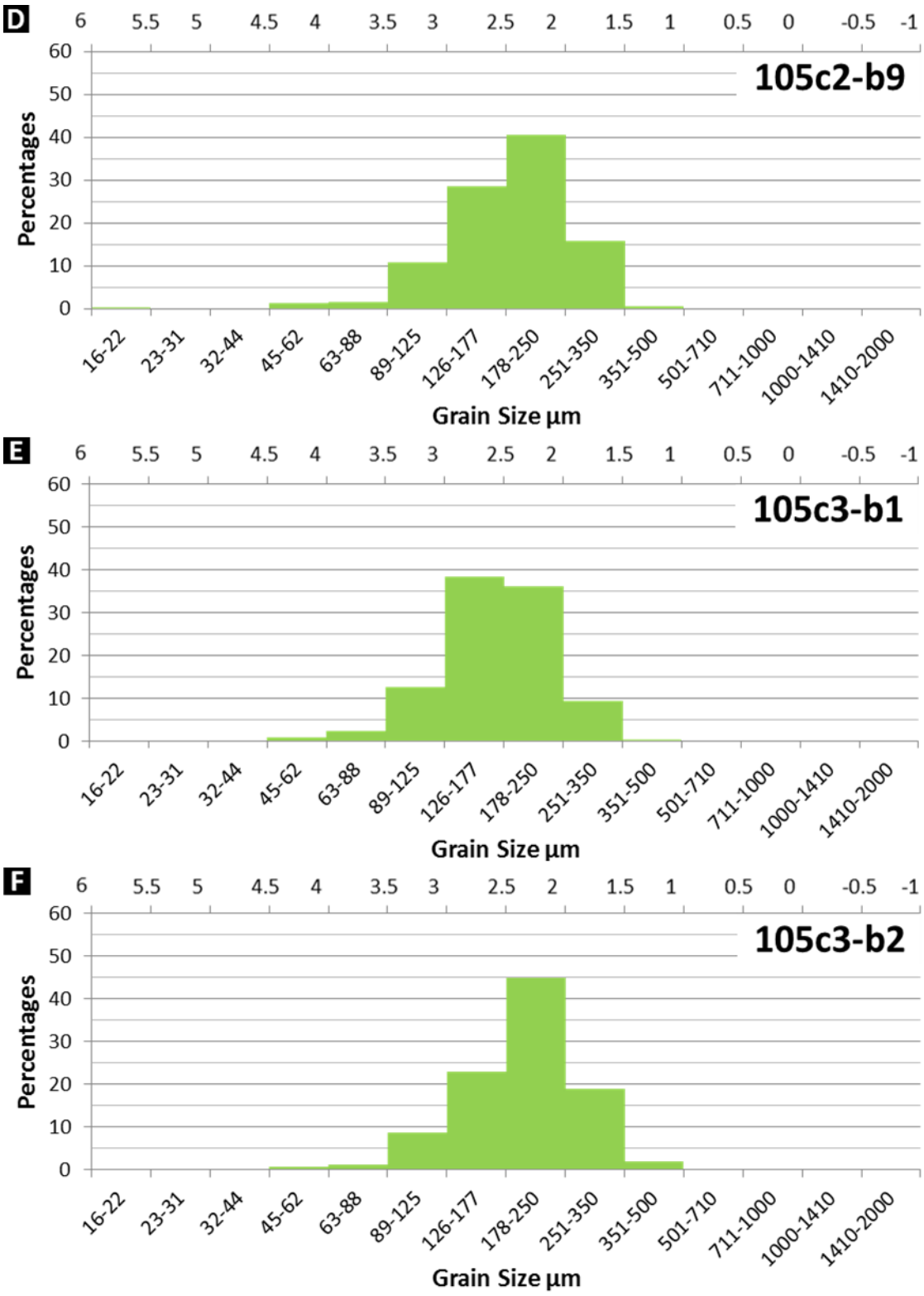

Figure D.4. Framework grain-size distribution from Core 105. Grain sample size for samples 105c2-b5 (A), 105c2-b6 (B), 105c2-b7 (C), 105c2-b9 (D), 105c3-b1 (E), and 105c3-b2 (F) are n = 307, 307, 309, 308, 311, and 306, respectively.

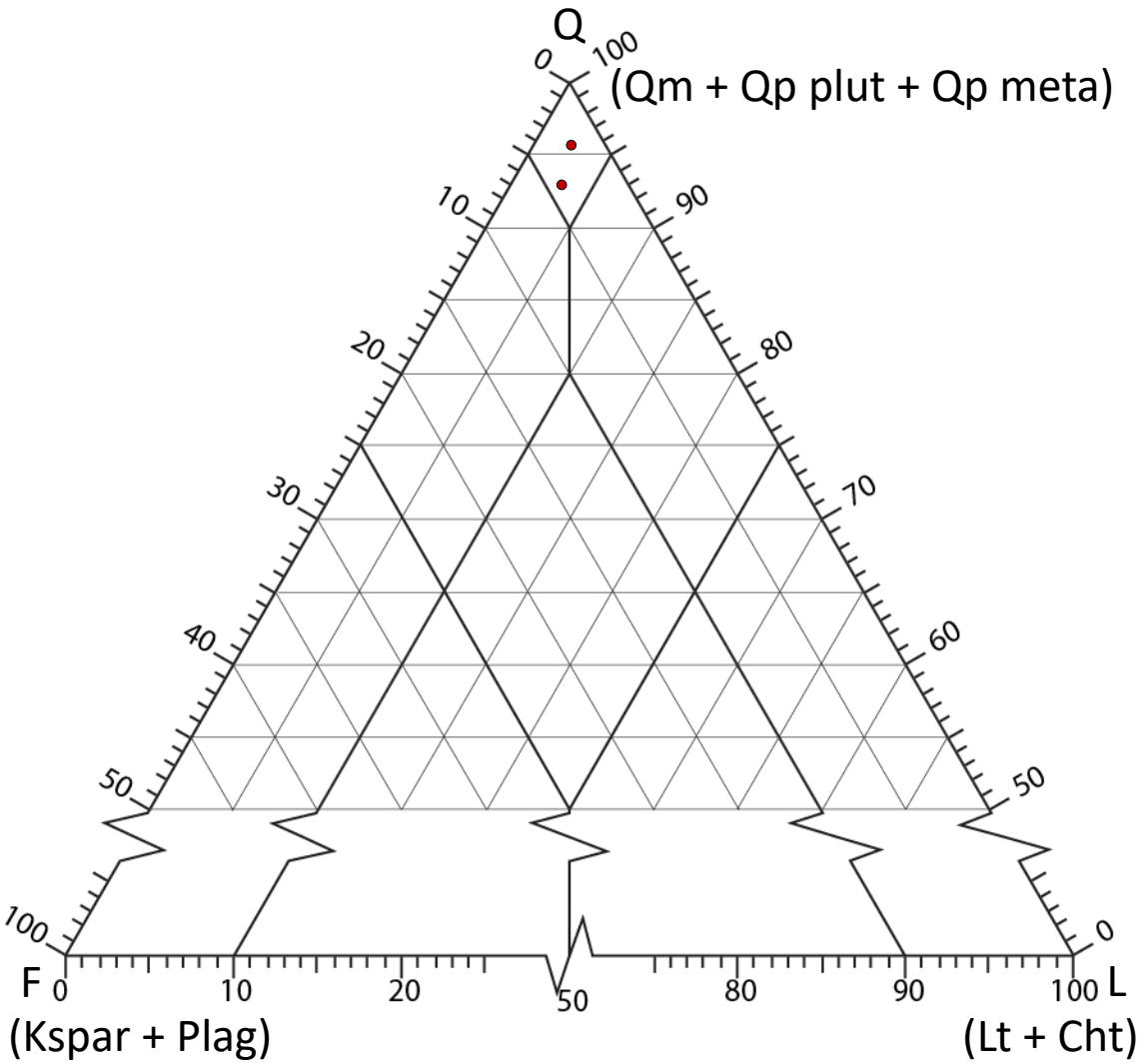

Figure D.5. QFL-composition plot of 106c1-b7 and 106c1-b10.

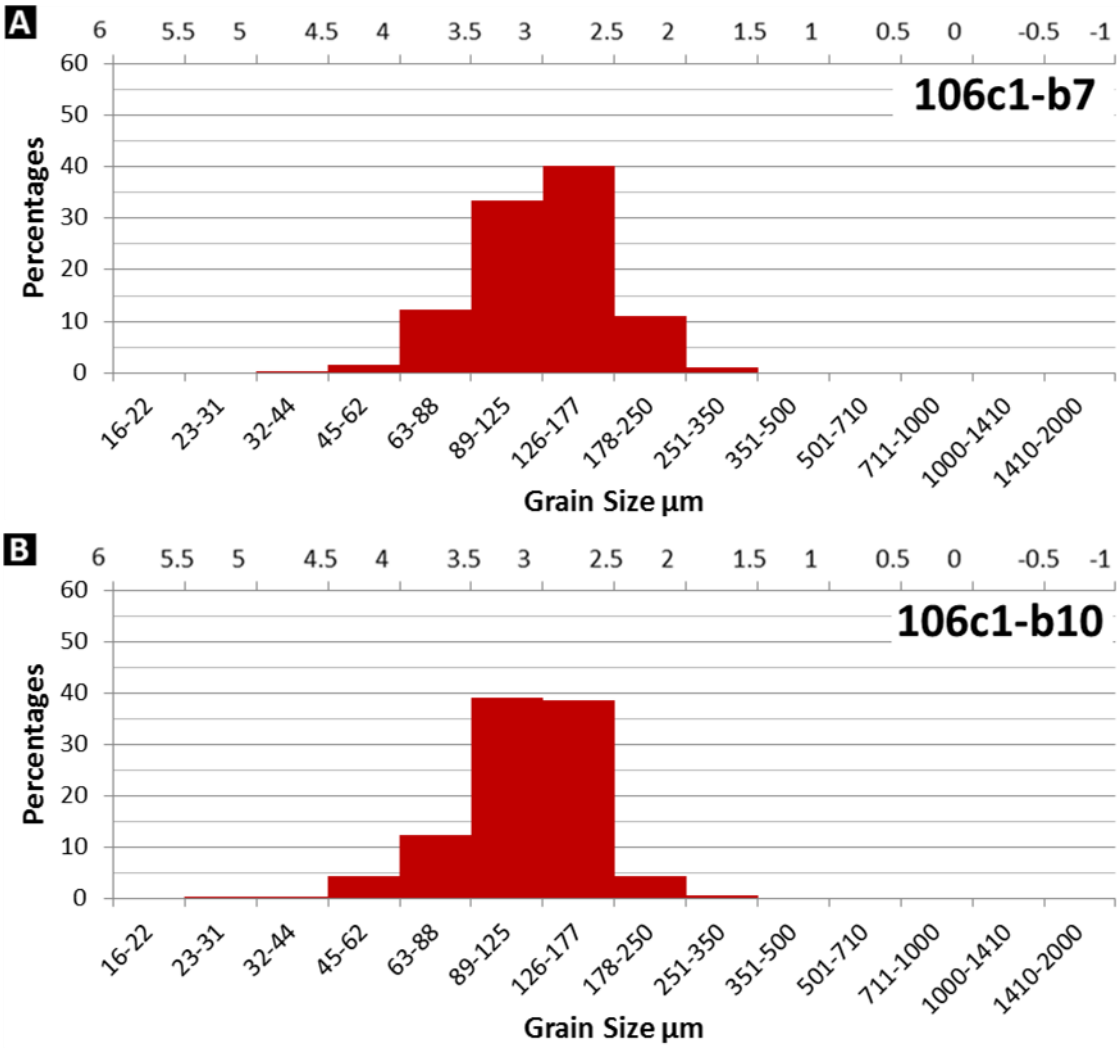

Figure D.6. Framework grain-size distribution of samples 106c1-b7 and 106c1-b10. Grain sample size for 106c1-b7 (A) and 106c1-b10 (B) are n = 311, and n = 325, respectively.

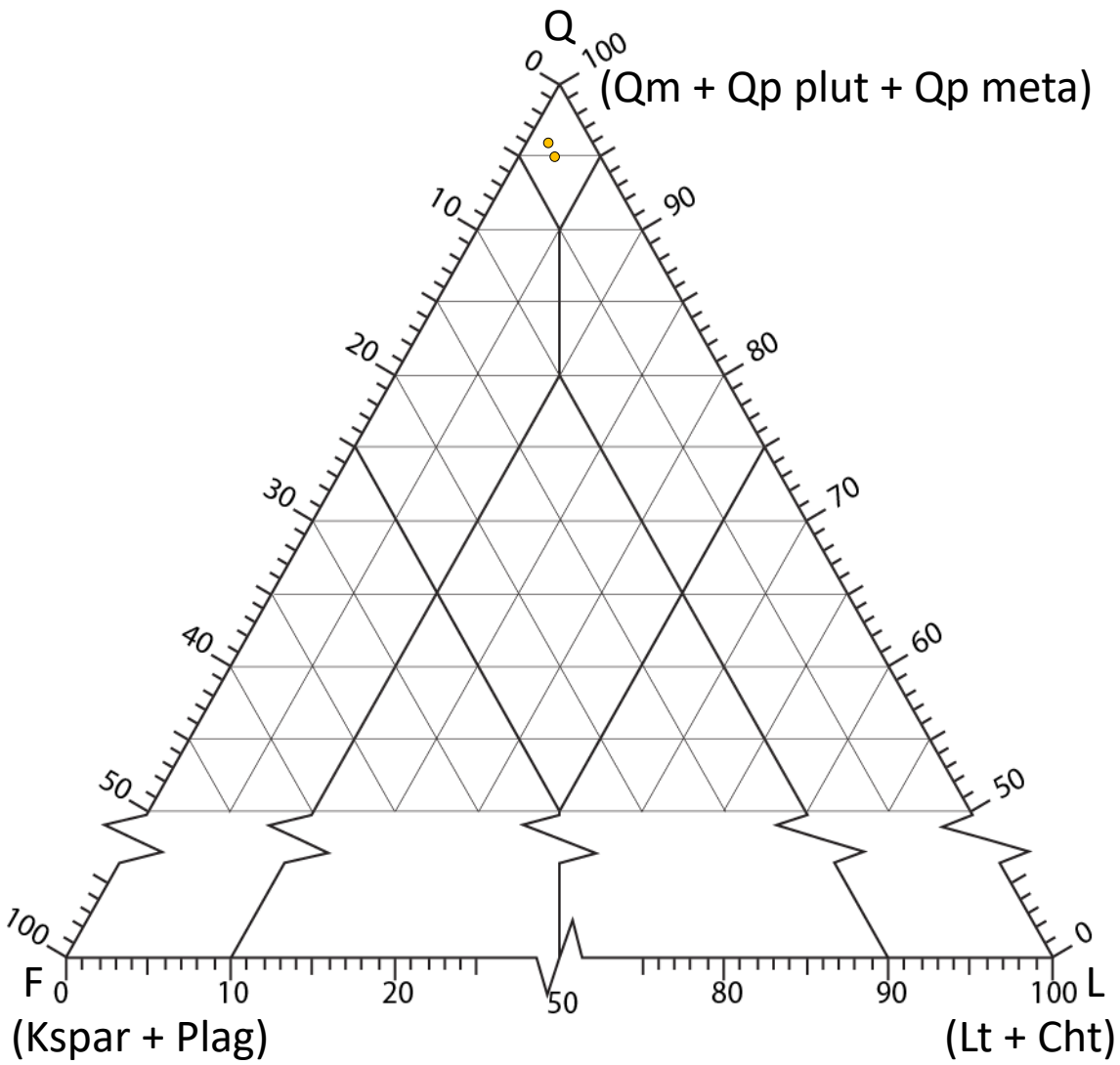

Figure D.7. QFL-composition plot of 107c1-b7 and 107c2-b5.

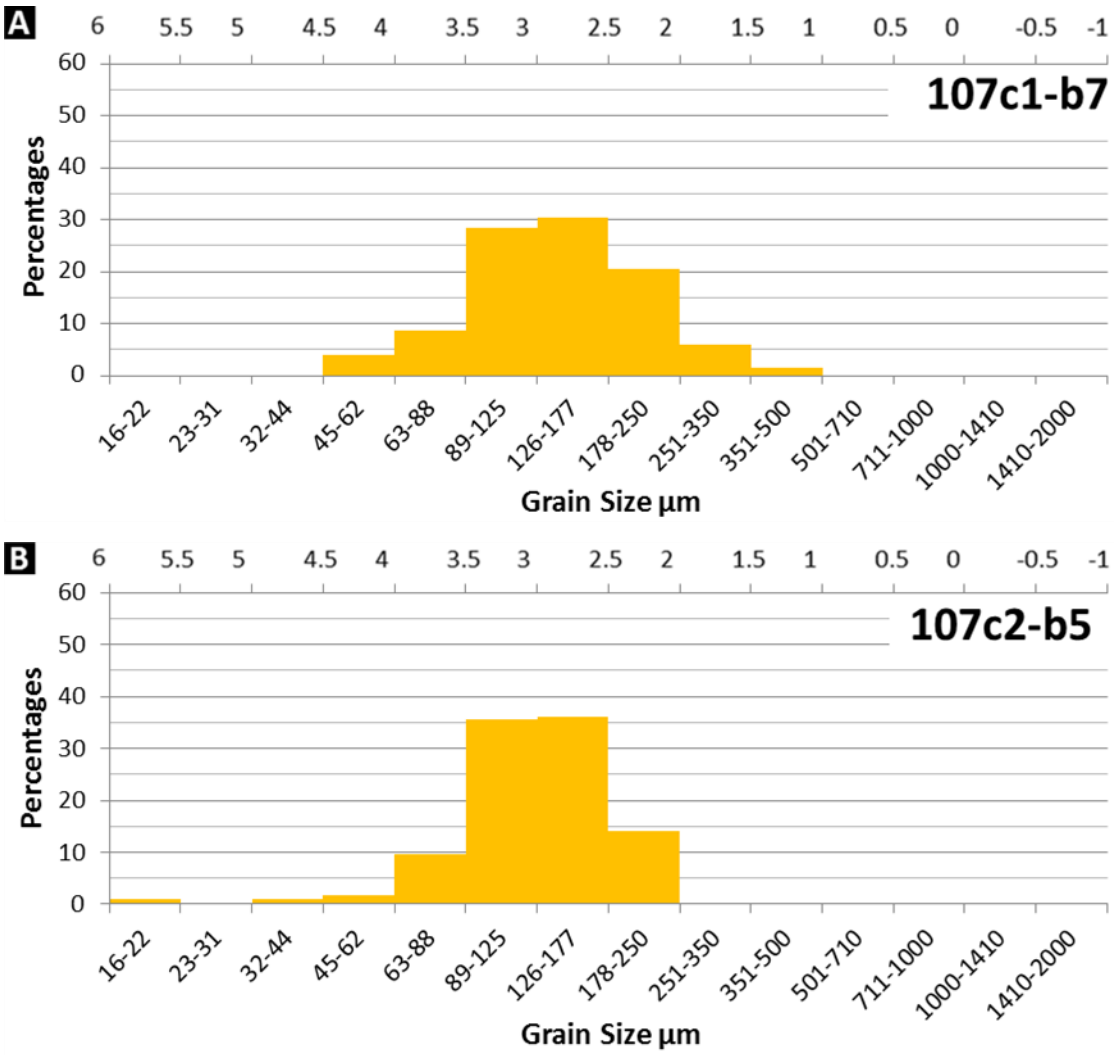

Figure D.8. Framework grain-size distribution of samples 107c1-b7 and 107c2-b5. Grain sample size for 107c1-b7 (A) and 107c2-b5 (B) are n = 320, and n = 325, respectively.

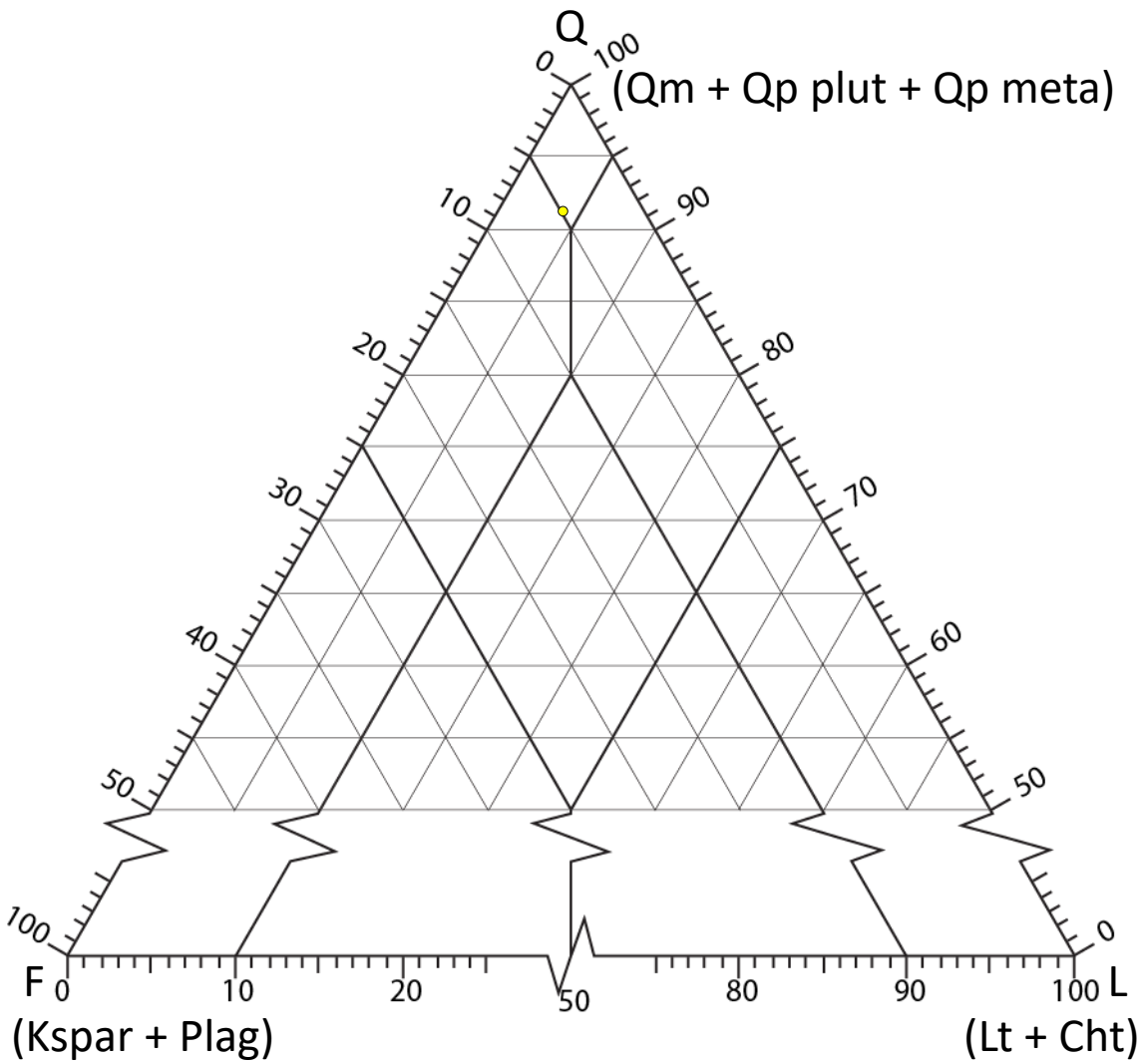

Figure D.9. QFL-composition plot of 108c1-b2, which is Hardinsburg Sandstone.

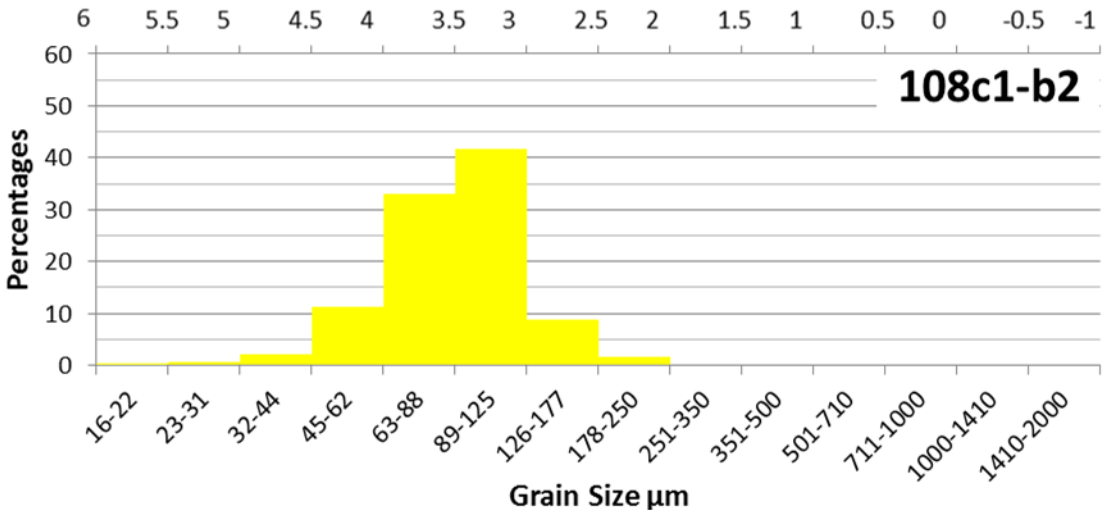

Figure D.10. Framework grain-size distribution of sample 108c1-b2. Grain sample size for 108c1-b2 is n = 362.

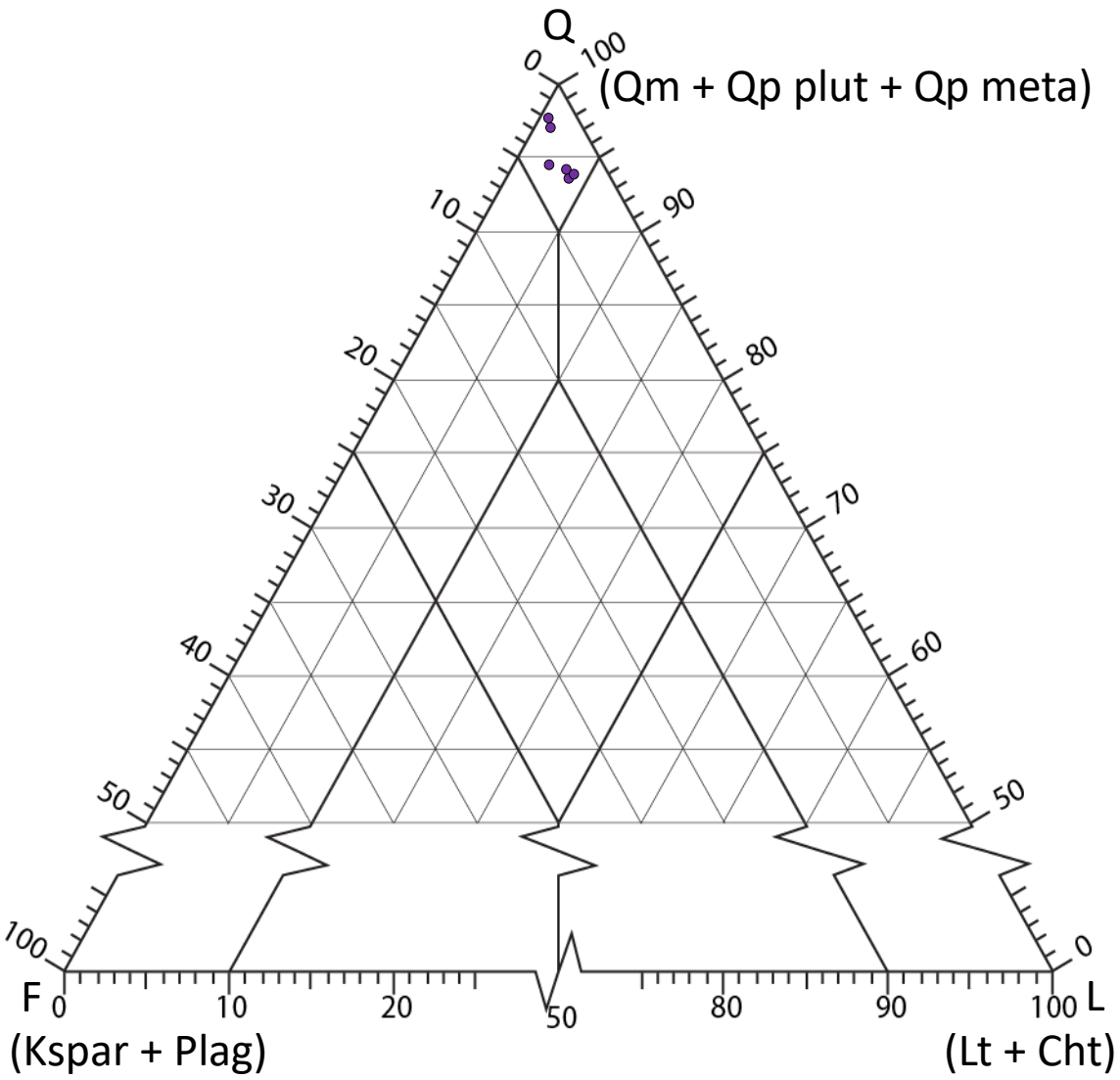

Figure D.11. QFL-composition plot of samples from Core 109.

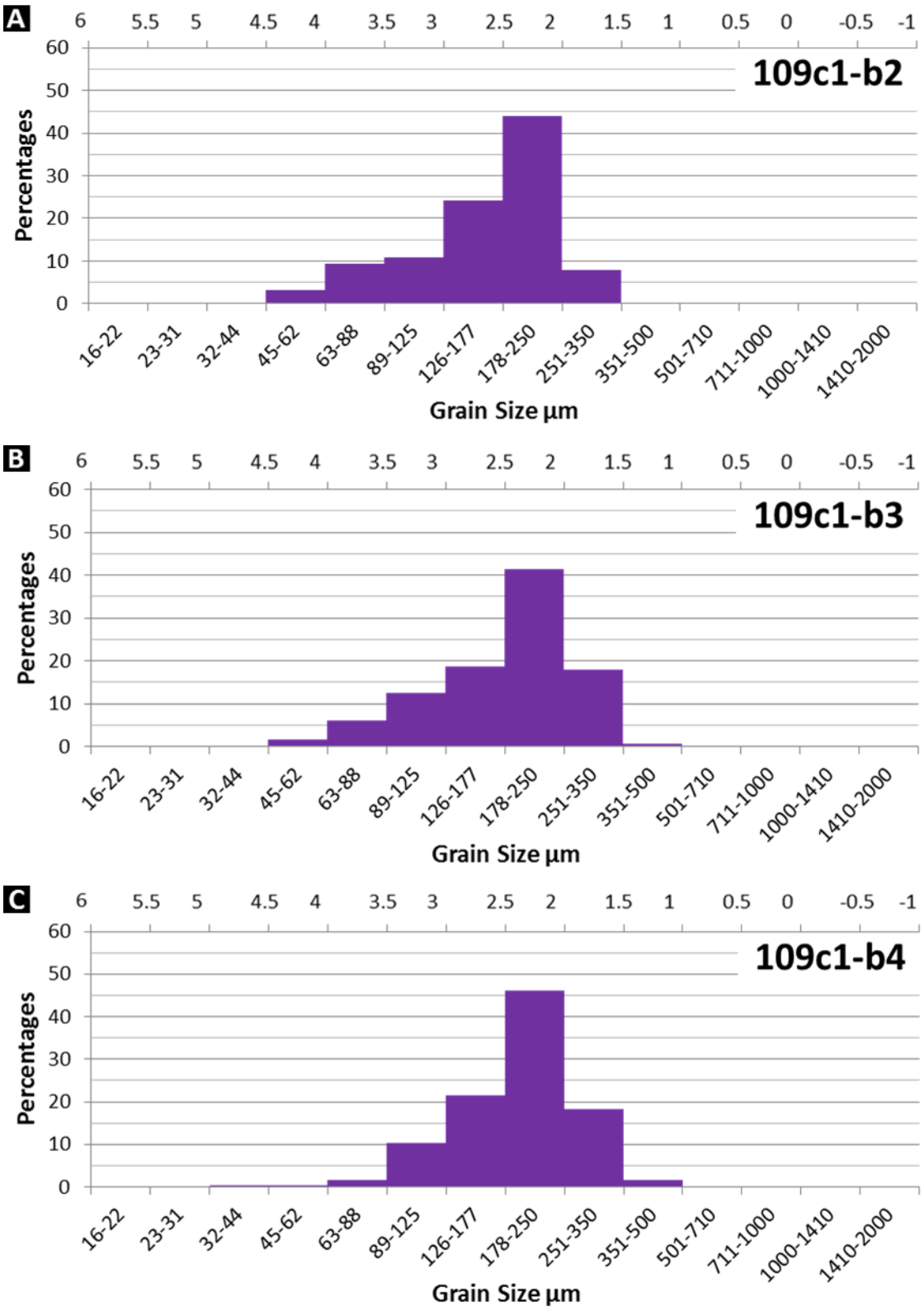
A
6 5.5 5 4.5 4 3.5 3 2.5 2 1.5 1 0.5 0 -0.5 -1
109c1-b2
Percentages
60 50 40 30 20 10 0
16-22 23-31 32-44 45-62 63-88 89-125 126-177 178-250 251-350 351-500 501-710 711-1000 1000-1410 1410-2000
Grain Size µm
B
6 5.5 5 4.5 4 3.5 3 2.5 2 1.5 1 0.5 0 -0.5 -1
109c1-b3
Percentages
60 50 40 30 20 10 0
16-22 23-31 32-44 45-62 63-88 89-125 126-177 178-250 251-350 351-500 501-710 711-1000 1000-1410 1410-2000
Grain Size µm
C
6 5.5 5 4.5 4 3.5 3 2.5 2 1.5 1 0.5 0 -0.5 -1
109c1-b4
Percentages
60 50 40 30 20 10 0
16-22 23-31 32-44 45-62 63-88 89-125 126-177 178-250 251-350 351-500 501-710 711-1000 1000-1410 1410-2000
Grain Size µm

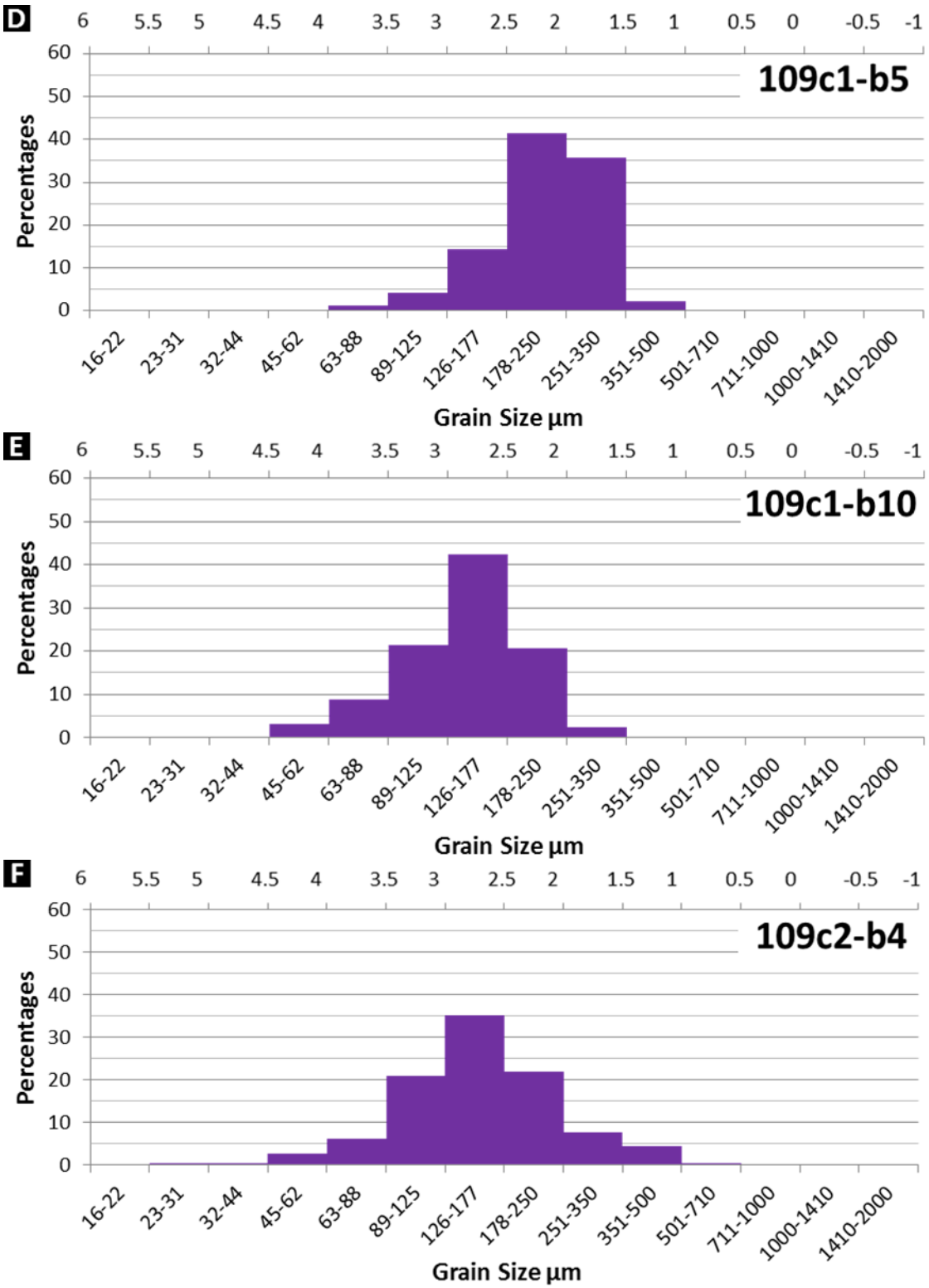

Figure D.12. Framework grain-size distribution of samples from Core 109. Grain sample size for samples 109c1-b2 (A), 109c1-b3 (B), 109c1-b4 (C), 109c1-b5 (F), 109c1-b10 (E), and 109c2-b4 (F) are n = 317, 310, 313, 307, 321, and 315, respectively.